A Cryogenic Scintillation UCN Detector for a Neutron EDM Experiment

Alice A. Lynch
Balliol College, Oxford

Thesis submitted in fulfilment of the requirements
for the degree of Doctor of Philosophy
at the University of Oxford

Trinity Term, 2014

Abstract

The observed imbalance of matter and anti-matter in the universe is one of physics' most fundamental unresolved questions. The leading theories to explain this imbalance require CP violation, and the neutron electric dipole moment (nEDM) is a sensitive parameter in its determination. Many new theories of physics beyond the standard model can be constrained or ruled-out by setting limits on the nEDM. Many next generation nEDM experiments require Ultra Cold Neutrons (UCN), produced in superfluid helium. One such experiment is cryoEDM. This thesis explores various types of UCN detection technologies applicable to cryoEDM or any high-density high-efficiency cryogenic nEDM experiment.

Cryogenic Phonon Scintillation detectors (CPSD) are modified for this application by operating at 500 mK, and by using a titanium transition edge sensor for phonon signal readout. A CPSD is stabilised in the transition using a novel infra-red light feedback system which reduced the response time to $\mathcal{O}(100\ \mu\text{s})$. The detector is characterised and calibrated using an ^{241}Am α source. It was found to operate reliably at this elevated temperature and measure an α spectrum with 11% resolution at 5.5 MeV.

Scintillators are identified as a promising technology for UCN detection at low temperature. Suitable materials that are bright with fast decay times and low γ sensitivity are studied in the temperature range 300 – 6 K. Their light yield to α excitation, their decay time characteristics and spectroscopic properties under VUV excitation are investigated. This study includes the first comprehensive investigation of the luminescence properties of plastic scintillators and of ^{6}LiF/ZnS(Ag) down to 6 K. It is found that there is no degradation of the luminescence or kinetic properties of these materials across the whole temperature range, revealing them as suitable cryogenic detector materials.

Using a plastic scintillator, a prototype UCN detector for operation in liquid helium is designed, manufactured and tested. It is read out using WLS optical fibres to a room temperature photomultiplier. The detector is successfully tested with cold neutrons at the ISIS neutron science facility and found to effectively measure neutrons, with a signal that is clear from background. Recommendations are made for its integration in a cryogenic neutron EDM experiment. This low-cost detector offers a promising method for the passive detection of UCN in a challenging cryogenic environment, with minimal electric interference and low background sensitivity. This technology offers the potential for improved UCN detection efficiency and thus improved sensitivity of the measurement of the neutron EDM.

For Mam and Dad

Acknowledgements

The work presented here is the culmination of many years of education and five years of learning the ropes of research. None of the studies that follow would have been possible without the help of many colleagues and friends. Firstly, thank you to my supervisor Dr. Sam Henry for giving me the opportunity to contribute to this research, his generous time and guidance throughout my time as his student and the writing of this thesis.

I would also like to thank Dr. Vitalii Mikhailik, whose expertise and unwavering dedication has taught me much of the practical skills needed to complete this work and has passed on a tiny fraction of his extensive scintillator knowledge.

Thank you to Prof. Hans Kraus whose vast experience in physics in general, and cryogenic experiments in particular, has been invaluable in advising me along my research journey. A particular thanks for designing the DAQ hardware and software used to perform the experiments presented here. Thanks to all members of the cryoEDM collaboration from Oxford, Sussex, RAL and ILL who have been dedicated to this measurement over many years. It was an exciting experience working at ILL while the experiment was running.

Thank you to Dr. Jeff Sykora from ISIS for generously volunteering his time helping me perform the neutron experiments in Chapter 6, and to Prof. Nigel Rhodes at ISIS, whose expertise helped me solve my research questions, and for donating scintillator samples and resources. Thank you to Dr. Antonin Vacheret in Oxford for volunteering his time to advise me on scintillator readout, and providing me with wavelength shifting fibre and teaching me to use the neutron source.

The harsh concrete facade of the Denys Wilkinson Building in Oxford has been much softened by the wonderful people I have met inside. Sue Geddes and Kim Proudfoot, helpful and supportive in every way, whose welcoming presence and kindness has been a real comfort through the many years here. I am indebted to the staff at the various workshops in the Department of Physics whose expert skills and knowledge have contributed to the realisation of the experiments presented here. Though I cannot list everyone here, many deserve thanks including Mike Tacon, Paul Pattinson and Rick Makin, and thanks to all the staff members in the DWB.

I have shared a working space with many other D.Phil. students and Post-Docs over the years here, who have all made the environment more fun and we have shared in the difficulties of research together, thank you all, it has been fun (occasionally...). A special thanks to Mark Pipe and Markus Horn for all the night-shifts at Hasylab for helping me gather the data that makes up Chapter 5 of this thesis and Mike McCann for his patience explaining the intricacies of cryoEDM.

The work presented here is the culmination of many years of education, following on from my undergraduate at University College Dublin, where my passion for fundamental physics was really lit. Thanks to Prof. Gerry O'Sullivan in particular for passing his passion on.

I have been lucky enough to have this work funded by a number of generous bodies. Thanks to the National University of Ireland for providing me with UCD Travelling Studentship which allowed me to come to Oxford. Thanks to the John Fell Fund for providing further research funds and thanks to DESY for funding a research trip to use their Hasylab facility.

I want to extend a heartfelt gratitude to members of my college, Balliol college. It has provided me with great financial assistance while in Oxford, but moreover with unequalled pastoral support. Thanks to Prof. Tom Melham and to Douglas Dupree for their supportive ear, openness and caring advice.

Much of what I have learned in Oxford has come from sharing the experience with my friends. Without Balliol and the Physics Department, I would not have made some of the best friends I have, that will be part of my life henceforth. They have enriched these years, adding value to the tough times as well as the smooth and been a real solace through the D.Phil process. You are too numerous to list, but I am immensely grateful. Thank you friends!

Especially Natalie, with whom I have shared a journey through physics and life for 8 years now, since the CERN summer school of 2006. We have come a long way, drank a lot of tea, and come out the other end. Words cannot express how thankful I am for your friendship and support.

Mam and Dad have never faltered in their support and belief in me. I am deeply grateful for all the opportunities you have given me, for educating me, and providing unwavering support and love. Thank you for providing a grounding home where I always feel capable. Thanks to all my family and friends in Dublin for reminding me of what is truly important in life.

And finally, Dave, without whom I would have cracked a long time ago.

Contents

1 The Role of Electric Dipole Moments in Matter Anti-Matter Asymmetry 5

1.1 Matter / Anti-Matter Asymmetry 6

1.2 CP Violation and EDMs 9

1.2.1 CP Violation and EDMs 10

1.2.2 Sources of CP Violation in the Standard Model 12

1.2.3 Sources of CP Violation from Beyond the Standard Model 14

1.2.4 Expectation Level of CP Violation in SM Strong Interactions 16

1.3 Limits on the neutron EDM and other EDMs 18

1.3.1 Electron EDM 19

1.3.2 Atomic and Other EDMs 20

1.3.3 Neutron EDM experiments 21

2 The Cryogenic Neutron EDM Experiment 29

2.1 An Overview of the cryoEDM Experiment 29

2.2 The cryoEDM measurement principle 33

2.2.1 The Ramsey Method of Separated Oscillating Fields 33

2.2.2 Extracting d_n 37

2.3 The cryoEDM Experimental Process 40

2.3.1 Production, Storage and Properties of UCN in HE-II 41

2.3.2 The CryoEDM Apparatus 44

2.4 Sensitivity 49

2.4.1 Statistical Uncertainties 49

2.4.2 Systematic Uncertainties 51

2.5 UCN Detectors 53

3 UCN Detection for CryoEDM 55

3.1 Overview of UCN Detection 56

3.2 Solid State Detectors in CryoEDM 58

3.2.1 Performance 61

3.3 Experimental Requirements in a Detector 66

3.3.1 Neutron Count Rate 66

3.3.2 Gamma Background . . . 66
3.3.3 Superfluid Environment . . . 67
3.3.4 Experimental Geometry . . . 68
3.4 Review of Potential Technology . . . 68
3.4.1 Alternatives to Gas Proportional Counters . . . 70
3.4.2 Semiconductor Detectors . . . 70
3.4.3 Cryogenic Phonon Scintillation Detectors . . . 72
3.4.4 Scintillators . . . 74

4 Titanium TES Sensors for α Particle Calorimeter Readout 77
4.1 Cryogenic Phonon-Scintillation Detectors for UCN . . . 78
4.1.1 Pulse Formation Model for Low temperature Calorimeters . . . 80
4.1.2 TES Sensor Readout Circuits . . . 83
4.2 Feasibility Study of Al_2O_3 Ti-TES Calorimeters . . . 85
4.2.1 Calculated Sensitivity to Absorbed α Particles . . . 85
4.2.2 Detector Assembly . . . 86
4.2.3 Detector Readout . . . 88
4.2.4 Data Acquisition & Software . . . 90
4.3 Detector Performance Results . . . 93
4.3.1 Thermometry Calibration . . . 94
4.3.2 Superconducting Transition Curves . . . 94
4.3.3 Operating Point & Stabilisation with LED Heater . . . 95
4.3.4 Calibration from Pulse Height to Energy . . . 100
4.3.5 Energy Spectra & Resolution at 5.5 MeV . . . 106
4.4 Conclusion . . . 107

5 Characterisation of Fast Scintillators at Low Temperature 110
5.1 Shortlisting Suitable Materials . . . 111
5.1.1 Inorganic Scintillators . . . 113
5.1.2 Organic Scintillators . . . 120
5.1.3 Shortlist . . . 124
5.2 Scintillation Response to α at Low Temperature . . . 126
5.2.1 Experimental Setup . . . 127
5.2.2 Analysis methods . . . 129
5.2.3 Results . . . 136
5.3 Luminescence from Vacuum Ultra Violet (VUV) Photons . . . 142
5.3.1 Experimental Setup & Analysis Methods . . . 143
5.3.2 Emission Spectra . . . 147
5.3.3 Excitation Spectra . . . 153

5.4 Decay Time Measurements . . . 156
5.4.1 Plastic Scintillators . . . 157
5.4.2 ZnS(Ag)/^{6}LiF . . . 160
5.4.3 Other Scintillators . . . 162
5.5 Conclusion . . . 163

6 Design Studies for a Prototype UCN Scintillation Detector 165
6.1 Losses in the Signal Transport Process . . . 166
6.1.1 Sources of Photon Loss . . . 166
6.1.2 Transportation of Scintillation Photons . . . 167
6.1.3 Collection of Scintillation Photons . . . 169
6.2 Design Considerations . . . 170
6.3 Experimental Design Investigation . . . 172
6.3.1 Consistancy of Scintillator Pieces . . . 172
6.3.2 Polishing . . . 173
6.3.3 Coupling . . . 173
6.3.4 Sources of Light Yield Variation . . . 173
6.3.5 Wavelength Shifting Optical Fibres . . . 174
6.3.6 Quality & Volume of Scintillator . . . 176
6.3.7 Optical Glue . . . 176
6.3.8 Quantity of Fibres . . . 178
6.3.9 Conclusion . . . 178
6.4 A Prototype Cryogenic Scintillation α Detector . . . 180
6.4.1 Design . . . 180
6.4.2 Characterisation . . . 181
6.4.3 Further Improvements . . . 184
6.5 A Prototype Neutron Detector . . . 189
6.5.1 A Portable Scintillation Neutron Detector . . . 191
6.5.2 Characterisation with AmBe Neutron Source at ISIS . . . 194
6.5.3 Characterisation with Thermal Neutron beamline at ISIS . . . 196
6.6 Recommendations for Further Development . . . 203

A Hasylab Spectra 210
A.1 Plastic Scintillators . . . 210
A.1.1 Emission Spectra . . . 210
A.1.2 Excitation Spectra . . . 213
A.1.3 Decay Times . . . 214
A.2 Cerium Doped Oxides . . . 219
A.2.1 Emission Spectra . . . 219

A.2.2 Excitation Spectra . . . 222
A.2.3 Decay Times . . . 222
A.3 GS20 Neutron Glass Scintillator . . . 226
A.3.1 Emission Spectra . . . 226
A.3.2 Excitation Spectra . . . 228
A.3.3 Decay Times . . . 228
A.4 CaF_2(Eu) . . . 230
A.4.1 Emission . . . 230
A.4.2 Excitation . . . 231
A.4.3 Decay Times . . . 232

B Luminescence Processes in Organic & Inorganic Materials 234
B.1 Organic Scintillators . . . 234
B.1.1 Plastic Scintillators . . . 238
B.2 Inorganic Scintillators . . . 239

Bibliography 241

List of Figures

1.1 Constraints on MSSM parameters by Baryon Asymmetry and EDM limits. . 9
1.2 A particle EDM violates CP symmetry. 11
1.3 Constraints on calculated MSSM parameters from d_n, d_{Tl}, and d_{Hg}. 16
1.4 A SM process generating a neutron EDM of $\mathcal{O}(10^{-32})$ 17
1.5 Historical nEDM and eEDM limits and predicted values from theoretical models. 19
1.6 Experimental apparatus of the nEDM experiment. 23

2.1 The cryoEDM apparatus. 32
2.2 Neutron energy levels due to parallel or anti-parallel E and B fields. 33
2.3 The Ramsey Resonance Procedure. 35
2.4 A neutron Ramsey Curve measured by the nEDM experiment. 36
2.5 Dispersion curves of neutrons and phonons in liquid helium. 42
2.6 UCN storage time as a function of temperature. 43

3.1 Schematic of ^{6}Li Silicon detectors. 59
3.2 Photographs of ^{6}Li Silicon detectors. 61
3.3 Schematic of the layout of the UCN detector guidetube. 62
3.4 ^{6}Li Silicon detector neutron spectra at 300 K with various coating thickness. 63
3.5 ^{6}Li Silicon detector neutron spectra at 430 mK and 300 K. 64
3.6 UCN Spectra measured by ^{6}Li Silicon detectors during Autumn 2010 run. . . 65
3.7 Neutron capture cross section for multiple nuclides. 69
3.8 Micro-trenches etched on Si neutron detector and filled with LiF nanoparticles. 71
3.9 Scintillation UCN detector developed for the PSI neutron EDM experiment. 76

4.1 A thermal model of the phonon detector system. 81
4.2 A CRESST phonon detector pulse, fitted with model. 82
4.3 Schematic of Al_2O_3 Ti-TES detector experimental installation. 87
4.4 Photograph of Al_2O_3 Ti-TES detector experimental installation. 88
4.5 Circuit diagram of Ti-TES electronic readout. 89
4.6 Illustration of the Al_2O_3 Ti-TES detector data acquisition system. 91
4.7 A typical particle event in Al_2O_3 Ti-TES detector. 93
4.8 A typical heater event in Al_2O_3 Ti-TES detector. 93

4.9 Calibration of RuO_2 thermometer. 95
4.10 Superconducting transition curve Ti-TES sensor, with bias currents 1-15 μA 96
4.11 Radiant Intensity of LED as a function of forward current. 97
4.12 Stabilisation of SQUID baseline with LED feedback. 99
4.13 SQUID baseline FT with and without LED feedback. 99
4.14 Stability of detector working point over long time period. 100
4.15 Pulse Height Spectrum from ^{241}Am α and heater events. 101
4.16 Cuts implemented to construct a Standard Pulse. 102
4.17 A Standard Pulse from 5.5 MeV α events. 102
4.18 A Standard Heater Pulse 103
4.19 Comparison of Pulse Height and Amplitude calculated from Standard Pulse fit. 103
4.20 Heater Pulse Amplitude versus time fitted with cubic splines. 104
4.21 A single Heater Pulse Amplitude versus time fitted with a cubic spline. . . . 104
4.22 Conversion from Amplitude to Energy with ^{241}Am source and heater pulses. 104
4.23 The heater transfer function converts Amplitude to Heater Pulse Amplitude. 104
4.24 Calibrated ^{241}Am α particle energy spectrum. 105
4.25 Detector resolution as a function of bias current and operating point. 107

5.1 Photograph of scintillator sample mounted in holder. 128
5.2 Apparatus to measure temperature dependence of scintillation light. 128
5.3 Typical scintillation events from slow and fast materials. 129
5.4 Cutting events using *Time of First Photon* parameter. 132
5.5 *Integral from Peaks* parameter before and after cuts. 132
5.6 ^{241}Am α spectrum before and after cuts with YSO(Ce) scintillator. 132
5.7 The α peak of YSO(Ce) at 293 K and 8 K. 133
5.8 Scintillation emission spectra of multiple materials. 135
5.9 Temperature dependence of scintillation light of plastics. 137
5.10 Temperature dependence of scintillation light of cerium doped materials. . . 140
5.11 Temperature dependence of scintillation light of inorganic materials. 141
5.12 The SuperLumi apparatus at Hasylab, DESY. 144
5.13 The spectrum of the incident VUV photon flux. 145
5.14 Transmission curve response of spectrometer system. 145
5.15 The SuperLumi sample chamber at Hasylab, DESY. 146
5.16 St Gobain BC408 Plastic Scintillator Emission Spectra 148
5.17 ZnS(Ag)/^{6}LiF Emission Spectra. 151
5.18 St Gobain plastic scintillator BC408 excitation spectra. 154
5.19 ZnS(Ag) Excitation spectrum. 155
5.20 BC408 plastic Decay Traces and Fits. 158
5.21 Temperature dependence of BC408 plastic decay times. 158

5.22 Decay traces of ZnS(Ag). 160
5.23 Temperature dependence of ZnS(Ag) decay times. 161

6.1 WLS fibre to PMT coupling device. 175
6.2 PHS for direct coupled (black) and WLS fibre coupled (red) scintillator. . . 175
6.3 Comparison of PHS of small rough piece to larger piece. 177
6.4 Extracted α signal. 177
6.5 Comparing PHS for various fibre configurations. 177
6.6 Photo of 3 WLS fibres glued into scintillator 178
6.7 PHS for 1, 2 and 3 WLS fibres. 179
6.8 Light yield improvements for the α prototype 180
6.9 Scintillation Detector Prototype on Cryogenic Dipstick. 182
6.10 Light yield of the dipstick prototype. 183
6.11 Temperature dependence of the α prototype light yield 184
6.12 Design with WLS fibres in grooves vs. embedded 185
6.13 Comparing the signal for grooves vs. holes 186
6.14 Signal from 4 WLS fibre readout 187
6.15 Comparing 3 WLS fibre signal to 4 fibre signal at 300 K. 187
6.16 Comparing 3 WLS fibre signal to 4 fibre signal at 4.2 K. 187
6.17 4 fibre design: Signal at 300, 77 and 4.2 K. 188
6.18 ^{6}LiF deposited on the surface of the scintillation module. 190
6.19 200 MHz compact USB data acquisition system. 192
6.20 A portable cryogenic scintillation UCN detector. 193
6.21 AmBe Neutron Pulse Height Spectrum. 196
6.22 ISIS thermal neutron beamline flux. 197
6.23 Second Prototype optimised for thermal neutron capture 199
6.24 Comparing the PHS of the first and second neutron detector prototypes. . . 199
6.25 Neutron time-of-flight and wavelength spectra at the ISIS beamline. 200
6.26 Cuts to select cold neutrons. 201
6.27 PHS response of the cryogenic scintillating UCN detector to thermal neutrons. 202

A.1 St Gobain Plastic Scintillator Emission Spectra 211
A.2 Eljen Plastic Scintillator Emission Spectra. 212
A.3 St Gobain plastic scintillator excitation spectra. 212
A.4 Eljen plastic scintillator excitation spectra. 213
A.5 BC400 plastic Decay Traces and Fits. 215
A.6 Temperature dependence of BC400 plastic decay times. 215
A.7 BC418 plastic Decay Traces and Fits. 216
A.8 Temperature dependence of BC418 plastic decay times. 216

A.9 EJ204 Decay Traces and Fits. 217
A.10 Temperature dependence of EJ204 plastic decay times. 217
A.11 EJ254 plastic Decay Traces and Fits. 218
A.12 Temperature dependence of EJ254 plastic decay times. 218
A.13 Emission Spectra of Cerium-activated scintillators. 221
A.14 Cerium activated scintillators' excitation spectra. 223
A.15 Decay time measurements of Cerium doped oxide scintillators. 225
A.16 GS20 ^{6}Li Doped Glass Emission Spectra. 227
A.17 GS20 Excitation spectrum at emission wavelength 400 nm at 300 K and 7 K 228
A.18 GS20 ^{6}Li glass decay traces. 229
A.19 Temperature dependence of GS20 decay time. 229
A.20 CaF_2(Eu) Emission Spectra. 230
A.21 CaF_2(Eu) Excitation spectrum. 231
A.22 CaF_2(Eu) scintillation time scale. 233

B.1 Energy levels of a molecule with π electron structure. 235
B.2 The Stokes Shift. 237
B.3 Energy band structure of an activated crystalline scintillator. 240

List of Tables

1.1 Experimental limits on the EDMs of various particles. 18
1.2 nEDM experiments with UCN around the world. 28

2.1 Neutron energy, velocity, wavelength and temperature ranges. 43
2.2 Fermi potential and critical velocity for some common materials. 44

3.1 UCN detector requirements for cryoEDM. 68

5.1 Requirements for a suitable scintillator 113
5.2 Properties of Common Inorganic Scintillators. 115
5.3 Properties of Some Commercially Available Organic Scintillators. 123
5.4 Properties of Potential Scintillators for UCN α Detector. 125
5.5 OxRop PMT Parameters. 130
5.6 Temperature dependence of scintillation light of plastics. 137
5.7 Temperature dependence of scintillation light of cerium doped materials. . . 139
5.8 Temperature dependence of scintillation light of inorganic materials. 142
5.9 Temperature dependence of Plastic VUV Luminescence. 149
5.10 Temperature dependence of ZnS(Ag)/^{6}LiF VUV Luminescence. 150
5.11 Plastic scintillator decay times at 300 and 6.5 K. 159
5.12 ZnS(Ag)/^{6}LiF scintillator decay times from 300 to 7.5 K. 161
5.13 Decay times of other scintillators. 162

6.1 Parameters to consider during the detector design process. 171
6.2 Sources of Light Yield Variation 174
6.3 Improvements in Light Yield 179
6.4 Light yield results of the prototype α detector tested cryogenically. 183
6.5 Light yield results of further improvements to prototype α detector. 186
6.6 How LiF deposition affect light collection 190

Glossary

BSM Beyond the Standard Model.

CKM Cabibbo Kobayashi Maskawa quark rotation matrix.

CMB Cosmic Microwave Background.

CPSD Cryogenic Phonon Scintillation Detector- developed for dark matter searches.

CPT Charge Parity Time Symmetry: A combination of C-, P-, and Time-symmetries. CPT symmetry is required by Lorentz invariant quantum field theories with Hermitian Hamiltonians.

CP Charge Parity Symmetry: a system is CP-symmetric if it appears the same when particles are replaced with their charge conjugates, and under the inversion of its spatial coordinates.

CRESST The Cryogenic Rare Event Search with Superconducting Thermometers, a direct dark matter search experiment.

DAC Digital to Analogue Converter.

DAQ Data Acquisition.

EDM Electric Dipole Moment.

EUV Extreme Ultra Violet radiation, photons with energy 10 – 124 eV.

FNAL Fermi National Accelerator Laboratory, Illinois, USA.

HEP High Energy Physics.

ILL Institut Laue Langevin, Neutron Research Centre, Grenoble, France.

ISIS A pulsed neutron & muon source at the Rutherford Appleton Laboratory, Oxfordshire.

LHC Large Hadron Collider at CERN.

MCA Multi Channel Analyser - electronics that record the pulse height of incoming events and produces a histogram.

MCS Multi Channel Scalar- electronics that record the counting rate of events as a function of time.

MDM Magnetic Dipole Moment.

nEDM Neutron Electric Dipole Moment.

MSSM Minimal Supersymmetric Model.

ORNL Oak Ridge National Laboratory, Tensessee, USA.

PHS Pulse Height Spectrum.

PID Proportional Integral Differential electronic control system.

PMT Photomultiplier Tube

PSD Pulse Shape Discrimination.

RAL Rutherford Appleton Laboratory, Harwell, Oxfordshire.

SCV Superconducting Containment Vessel- the container in cryoEDM where the neutrons spend most time, where a Ramsey measurement is performed. It holds the E field electrodes and magnetometry.

SM Standard Model of Particle Physics.

SNS Spallation Neutron Source at Oak Ridge National Laboratory, USA.

SQUID Superconducting Quantum Interference Device- a sensitive magnetic flux to voltage converter.

SUSY Supersymmetry- An additional symmetry that transforms between fermionic and bosonic states.

TES Transistion Edge Sensor- a cryogenic thermometer that exploits the strongly temperature-dependent resistance of the superconducting phase transition.

ToF Time of Flight.

UCN Ultra Cold Neutrons, low energy neutrons with E $\sim$neV which can be contained in a suitable vessel.

VUV Vacuum Ultraviolet.

WIMP Weakly Interacting Matter Particle, a dark matter candidate.

WLS Wavelength Shifting.

WMAP Wilkinson Microwave Astronomy Probe- an experiment to measure the CMB.

Introduction

One of the most fundamental cosmological questions yet to be resolved in physics relates to the observed imbalance between matter and anti-matter in the universe today [1] [2]. The Big Bang might be thought to have produced equal quantities of baryons and anti-baryons, annihilating over time to leave only photons. But the complexity of the world we live in is a testament to the asymmetry in the laws of physics that favoured matter over anti-matter. Neither the standard model of particle physics, nor the theory of general relativity provides an obvious explanation for why this should be so.

This asymmetry is intimately linked to charge-parity symmetry (CP) violation in the laws of physics. The Standard Model accommodates CP violation with a non-zero complex phase in the CKM quark mixing matrix, however this is insufficient to explain the magnitude of matter/anti-matter asymmetry observed. Theories of new physics beyond the standard model (BSM) generally have mechanisms which contribute larger amounts of CP violation. The existence of a non-zero electron dipole moment (EDM) of the neutron violates time symmetry, and thus CP by the CPT theorem. It offers a sensitive and model-independent measure of how much CP violation exists in the laws of physics, and may offer the first opportunity to measure CP violation beyond the standard model.

Over the last 60 years, the experimental search for the neutron EDM (nEDM) has grown more and more sensitive, setting ever more stringent upper limits. The current world limit was set by the Neutron Electric Dipole Moment collaboration, with a limit of 2.9×10^{-26} $\mathrm{e} \cdot \mathrm{cm}$. However the aimed sensitivity of the next generation of experiments mean they may be within the range of the predictions made by many viable BSM theories. So the neutron

EDM may offer one of the first indications of physics beyond the standard model, or at least heavily constrain the many theories.

One such experiment, cryoEDM, was begun as a collaboration over ten years ago with the aim to improve on this sensitivity by two orders of magnitude, to 1×10^{-28} e $\cdot$ cm . A major leap forward in next generation neutron EDM searches is the use of Ultra Cold Neutrons (UCN), low energy neutrons which may be bottled and stored for hundreds of seconds. A new method of UCN production by down-scattering in superfluid ^{4}He creates unrivalled neutron densities and therefore an increase in statistical sensitivity. With this method, the experiment must operate at $\sim$500 mK, which introduces significant practical challenges. One of which is the operation of traditional neutron detectors at such low temperature and inside superfluid helium with high detection efficiency.

This thesis presents an investigation of potential technology which could be adapted for use as a cryogenic UCN detector within the cryoEDM experiment or another future cryogenic neutron EDM experiment. The aim is to investigate the possibility of improving the UCN detection capability within superfluid ^{4}He, with improved performance over the current silicon neutron detectors installed in cryoEDM, and contribute to a more sensitive limit on the neutron EDM.

I begin with a discussion of the motivation behind the search for the nEDM, presented in Chapter 1. This focusses on the fundamental questions that underpin the importance and relevance of the nEDM measurement. It gives an overview of the matter/anti-matter imbalance and the role of the nEDM in the determination of CP violation in the laws of physics, along with a review of past, current and future experiments searching for EDMs of various particles. In Chapter 2, the cryoEDM experiment is described in detail, including its measurement principle, the UCN production method in superfluid helium, and the increased sensitivity of this experiment over the previous generation, including efficient UCN detection. A discussion of the current cryoEDM silicon UCN detectors is presented in Chapter 3 in the context of their performance and the opportunity to increase detector efficiency with an alternative technology. The requirements cryoEDM has for a UCN detector are outlined

and a literature review of potential technologies made. Finally, Cryogenic Phonon Scintillation Detectors (CPSD) and Scintillation Detectors are identified for further experimental investigation.

The remainder of the thesis outlines original research I have undertaken to identify and characterise potential cryogenic UCN detector technology and develop a prototype low-temperature scintillation UCN detector. Specifically, Chapter 4 investigates a CPSD, an ultra sensitive detector developed for dark matter searches. The experimental search for dark matter is complementary to nEDM searches, not just in its aims to solve some of the most significant cosmological questions, but in some of its techniques, specifically cryogenic operation. In the chapter, I explore the possibility of adapting a CPSD developed for dark matter to UCN detection. In doing so, the detector is run at a much higher temperature than usual, $\sim$500 mK, and used to measure an α spectrum. This chapter outlines a first use of this type of detector with a titanium superconducting thermometer and thermal stabilisation with infra red light. The detector is thoroughly characterised and calibrated and its suitability as a UCN detector for a cryogenic nEDM experiment is discussed.

Next, Chapter 5 involves research into the low temperature behaviour of scintillators. Scintillators are one of the most commonly used particle detectors, however they can exhibit undesirable temperature dependant effects. A review of available scintillators is made in order to identify potential materials, keeping in mind cryoEDM's detector requirements. Having done this, a shortlist of promising materials is comprehensively investigated in the temperature range 300 – 7 K. By measuring the relative light yield and decay times of the materials, the most suitable material for the UCN detector can be identified, that is both bright and fast at cryogenic temperatures. This work is complemented with a thorough characterisation of the spectral properties of the materials across the same temperature range at the Hasylab synchrotron facility in Germany. This chapter includes a first low temperature study of the scintillation characteristics and luminescence properties of plastic scintillators and of the inorganic material ZnS(Ag). Detailed results from this study are also presented in Appendix A. In Appendix B, the physics of scintillation photon production in inorganic and

organic materials is presented for reference when discussing the low temperature scintillator results.

Having identified a plastic scintillator as the most suitable detector material, I began the process of developing a prototype low temperature UCN detector, which is outlined in Chapter 6. This involves producing a scintillation module that operates within liquid helium and reading out the scintillation photons with wavelength shifting optical fibres. The detector prototype is designed, built and tested at room temperature and 4.2 K with various α and neutron sources, and proven to be an effective and sensitive method to count neutrons in a cryogenic environment.

I conclude this thesis with a discussion of the work performed and its relevance to the field. I include a discussion of the future for cryoEDM and other cryogenic nEDM experiments, suggestions for furthering the research presented in this thesis, and its impact on contributing to the improvement on the limit of the neutron EDM.

In short, the work presented in this thesis represents the research and development of an alternative option for UCN detection within a cryogenic environment for the cryoEDM experiment or any other future cryogenic nEDM experiment.

Chapter 1

The Role of Electric Dipole Moments in Matter Anti-Matter Asymmetry

One of the most significant unsolved questions in physics today is "Why is the universe made up of so much matter, but so little anti-matter?" The current understanding of cosmology indicates that at the Big Bang, equal quantities of matter and anti-matter were produced, and therefore these particles and anti-particles should have annihilated, leaving only photons [3]. And yet the complexity of the universe we live in, of galaxies, stars, planets and life, all made from only matter, clearly shows that at some point, there was an imbalance in the laws of physics such that matter became dominant over anti-matter.

This problem, known as "Baryogenesis", is intimately linked with the electric dipole moments of particles. All theories which seek to explain baryogenesis require a significant source of Charge-Parity symmetry violation in fundamental interactions. The simultaneous transformation of C, P and T, known as CPT, is a fundamental symmetry of physical laws, which holds for all Lorentz invariant quantum field theories [4]. An important consequence of this theorem is that violation in CP must be exactly compensated by a violation in Time symmetry (T), to keep the combination CPT conserved. Thus fundamental particles such as the neutron or the electron found to carry a T-violating electric dipole moment, would be evidence of CP violation. Models of baryogenesis and theories of new physics predicting

CP violation can be tested in ongoing experiments that measure, or set an upper limit on, the EDMs of the neutron and other particles.

The search for the neutron electric dipole moment addresses these issues- which lie at the heart of modern cosmology and particle physics. The current limit on the EDM of the neutron represents one of the most sensitive null measurements in all of physics and has eliminated many theories and extensions to the Standard Model of particle physics (SM).

In this chapter, the matter/anti-matter asymmetry in the universe and its implications are discussed. This is followed by a discussion of CP violation and the role of EDMs in their determination. Sources of CP violation in the SM and from theories of new physics Beyond the Standard Model are outlined and the motivation for the study of the neutron EDM is discussed. Finally a review of experimental searches for EDMs of various particles and atoms is made, with a focus on the neutron EDM, and the historical and current experimental limits on these quantities.

1.1 Matter / Anti-Matter Asymmetry

It is widely accepted that the Big Bang was baryon symmetric [5], where initial baryon number was zero, and thus equal number of baryons and anti-baryons were produced in the early universe after inflation. Given these equal distributions, they should have annihilated almost completely, producing a universe consisting only of photons.

The predicted ratio of baryons to photons (which is equal to the ratio of anti-baryons to photons) from the Big Bang model is $\mathcal{O}(10^{-18})$. However the observed ratio of baryons to photons, η_B/η_γ, is in the range $5.7-6.7\times10^{-10}$ (95% CL) [6], calculated from a combination of theory and observations of D/H measurements [7]. The ratio of anti-baryons to baryons is $< 2.1\times10^{-4}$ (95% CL) [6] [8], the upper limit on which is set by the absence of anti-nuclei among the cosmic rays observed in our galaxy and of any intense γ ray emissions due to annihilations in distant galaxies [9]. Thus the Big Bang model is estimated to be about 9 orders of magnitude off the observed value of η_B/η_γ.

The value of the baryon number in the universe expressed as a ratio to the number of photons can be determined from the Cosmic Microwave Background (CMB) data, which was collected by the Wilkinson Microwave Anisotropy Probe (WMAP) and the Planck Space Telescope [10]; and also from Big Bang Nucleosynthesis calculations. It is currently set at

$$\eta = \frac{\eta_B - \eta_{\bar{B}}}{\eta_\gamma} = 6.064 \pm 0.066 \times 10^{-10} \tag{1.1}$$

which is not compatible with zero. This leaves the interesting question of what happened to all the anti-matter?

There is strong evidence that the universe consists entirely of matter, as opposed to antimatter [11] and the few anti-protons ($n_{\bar{p}}/n_p \sim 10^{-4}$) seen in cosmic rays can be explained by secondary pair processes [12]. The observed dominance of matter over anti-matter is not what we expect from the standard big bang model in combination with the known laws of physics in the SM of particle physics.

The seminal paper by Andrei Sakharov in 1967 [13] proposed that a baryon-symmetric universe could develop into an asymmetric universe if the following three conditions were met:

1. Baryon number violating interactions
2. Thermal non-equilibrium state
3. C and CP violation

This baryogenesis process could then result in substantial amounts of residual matter. Our very existence today requires that all of these necessary conditions for generating a baryon asymmetry have been satisfied at some time in the early Universe.

The first condition, Baryon number violation, can occur within the standard model by non-perturbative effects [14], although it has not been seen experimentally, and may also occur from new physics beyond the Standard Model. One favoured model is through the postulated existence of massive Majorana neutrinos and the process known as “leptogenesis”,

discussed in [15]. The second condition, a state of thermal non-equilibrium, is expected in the early universe. It is the third condition of CP violation that is of interest here, and connected to the search EDM of the neutron. A review of baryogenesis is given by Riotto in [14].

A small amount of CP violation is found in the Standard Model of Particle Physics, however it has been shown by Shaposhinikov [16] that SM processes are not sufficiently effective to account for the observed baryon imbalance. Theories of new physics beyond the standard model can help to resolve this question by introducing new sources of CP violation. One prediction these theories make is of the value of the electric dipole moment of the neutron, a property that is sensitive to the same interactions that are at the cause of CP violation.

For example, Cirigliano et. al [17] have presented a detailed phenomonological discussion of the role of EDM constraints on the Minimal Supersymmetric Model (MSSM), from which Figure 1.1 is taken. In this plot, the parameters μ and M_1 are the masses of the Higgsino and Bino, two of the 4 hypothetical neutralino particle predicted by supersymmetry. Regions in the μ – M_1 phase space which are consistent with observed baryon asymmetry are shown by the black shaded area. Constraints have been made on the calculated values of the masses by LEP and electron EDM measurements, and the next generation of neutron EDM experiments, including cryoEDM, may exclude the entire phase-space region as shown in the figure. nEDM limits are an essential tool for the constraint of the numerous free parameters in Supersymmetry (SUSY) and other BSM models.

Thus the search for the nEDM, is one of the most promising experiments to discover CP violation beyond the SM and a complementary measurement to LHC experiments, other EDM experiments and astrophysical measurements to help to understand baryon asymmetry in our universe.

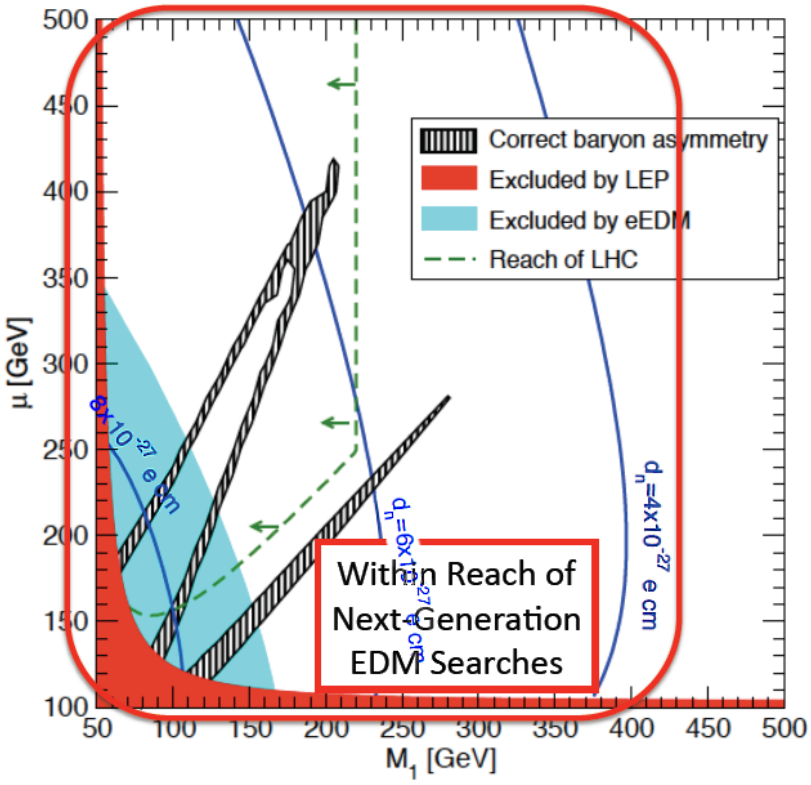

Figure 1.1: MSSM masses of the Higgsino (μ) and Bino (M_1) calculated from Supersymmetric Baryogenesis are constrained by the correct observed Baryon Asymmetry (black shaded area). Indicated are regions of phase space excluded by LEP and the eEDM limit, and within reach of the LHC. The sensitivity aimed for by cryoEDM and other next general nEDM experiments could rule out the entire phase space, as indicated by the blue contours. [17]

1.2 CP Violation and EDMs

The symmetries of three discrete transformations Parity (P), Time (T) and Charge (C) play an essential role in the understanding of our universe. Parity transformation changes the sign of the spatial coordinates so that $\vec{r} \rightarrow -\vec{r}$. Time reversal transformation changes the sign of the time coordinate, t. Charge conjugation transforms a particle into its anti-particle.

It was thought that P was a conserved symmetry in physics until Wu et. al. showed in 1956 that P and C were maximally violated in the weak interaction in the radioactive decay of ^{60}Co [18]. Following this, the neutron EDM became of interest to the nuclear and particle physics community as it offered another system in which to study parity violation. In fact the first limit on the nEDM had been set in 1951 at Oak Ridge using a beam of neutrons, but was not published until after the Wu et. al. paper and its significance realised. It set

$d_n = -(0.1 \pm 2.4) \times 10^{-20}$ e $\cdot$ cm [19], measured using the Ramsey Method with Separated Oscillatory Fields, still used today in cryoEDM and discussed in detail in Chapter 2.

It was subsequently postulated that the combined application of C and P, CP symmetry was a conserved symmetry. Subsequently the experimental search for the neutron EDM became of increased interest to the physics community as is furthermore offered a method of studying CP violation.

CP was thought to be an unbroken symmetry of nature until 1964, when Cronin, Fitch et. al. [20] observed the CP violating decay of long lived Kaons $K_L^0 \rightarrow \pi^+\pi^-$, which proceeds via the weak interaction. Thus CP was discovered to be violated at a small level in the weak interaction and this was then was incorporated into the Standard Model via a complex phase δ in the quark mixing matrix, the Cabibbo-Kobayashi-Maskawa (CKM) Matrix [21]. CP violation has since been measured in weak decays of B mesons [22] and there is evidence for it in the decay of D mesons [23], thus improving the knowledge of the parameters in the CKM Matrix [6]. Observation of CP violation is the main motivation behind the ongoing search for the neutron EDM and EDMs in other systems.

1.2.1 CP Violation and EDMs

An electric dipole moment arises from a non-spherical charge distribution, specifically a distribution with two equal and oppositely charged poles. Two charges of $\pm q$ separated by a distance r will have an EDM of $\vec{d} = q\vec{r}$. For a fundamental spin-$\frac{1}{2}$ particle, any intrinsic EDM must align with its spin vector, the only definable direction associated with such a particle.

A model of a neutron can be constructed having no net charge, but with parallel net electric and magnetic dipole with two counter rotating charges of opposite sign spatially separated, as is seen in Figure 1.2. With the positive charge in an anticlockwise orbit, both the μ and d_n point upwards. Under parity inversion P, consisting of reflection in a mirror, the inverted system has the orbits of the two particles reversed, therefore reversing

the magnetic dipole. The positions of the charges are unchanged, and therefore the electric dipole is unchanged. If then charge conjugation C is applied, the charges are exchanged, thus reversing the electric dipole. This furthermore reverses the direction of the magnetic moment due to the relative flip of the direction of orbits of the two charges. After the application of CP, the model neutron has anti-parallel μ and d_n, and the neutrons properties are no longer CP invariant. An experiment could be constructed to separate particles with μ and d_n parallel and those having μ and d_n anti-parallel.

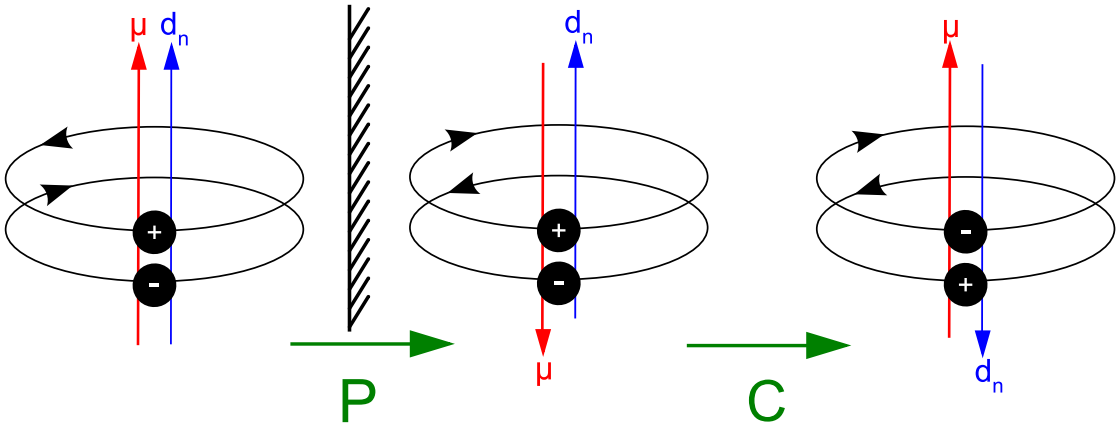

Figure 1.2: A particle EDM violates CP symmetry.

It must be noted that many degenerate systems have electric dipole moments but are not evidence of time-reversal. For example, the ammonia molecule has a finite EDM but does not violate CP or T symmetry as this molecule is described by a degenerate wavefunction. However we assumed that the neutron ground state was completely described by the spin projection quantum number and the spin states are non-degenerate. This is supported by the fact that neutrons obey the Pauli principle.

To date, no permanent EDM of any fundamental particle has been found. A neutron EDM measurement would offer the first experimental indication of CP violation in the standard model independent of meson decays. As a direct measurement, it would offer a method of near-model-independent determination of the amount of CP violation in nature. CryoEDM is a next generation experiment in the nEDM search. The previous incarnation of this experiment (outlined further in Section 1.3.3) currently holds the world limit [24] of

$$|d_n| < 2.9 \times 10^{-26} \mathrm{e} \cdot \mathrm{cm} \tag{1.2}$$

A non-vanishing EDM has been related to concepts beyond the Standard Model, such as additional Higgs fields, right-handed currents or supersymmetric partners. Experimental limits on nEDM have ruled out large swathes of such theories of new physics by its limits on the amount of CP violation allowed in a theory. A review of the role of the neutron and its EDM in fundamental physics is given by Nico and Snow in [25].

As any measurement of a neutron EDM is a measurement of CP violation, we now must consider sources of CP violation in the SM and from theories of new physics.

1.2.2 Sources of CP Violation in the Standard Model

CP violation has been only observed in the Standard Model through weak decays. In the weak interaction, CP violation is observed in the decays of Kaons and other mesons. CP violation was first observed indirectly in the decay of neutral Kaons by Cronin, Fitch et al in 1964 [20]. In this experiment, a beam of neutral Kaons was prepared, which are known to have weak eigenstates of different lifetimes and decay modes: $K_S = \frac{1}{\sqrt{2}}(d\bar{s} - s\bar{d})$, which decays predominantly to 2π (CP +1) and $K_L = \frac{1}{\sqrt{2}}(d\bar{s} + s\bar{d})$, which decays predominantly to 3π (CP –1). In terms of the strange eigenstates K_0 and $\bar{K_0}$, the combinations

$$K_1 = \frac{1}{\sqrt{2}}(K_0 + \bar{K_0}) \qquad CP + 1 \tag{1.3}$$

$$K_2 = \frac{1}{\sqrt{2}}(K_0 - \bar{K_0}) \qquad CP - 1 \tag{1.4}$$

would equal the weak eigenstates K_S and K_L if CP was not violated. In the experiment, the beam of neutral Kaons was allowed to decay away so that only K_L remained, which is expected to be in the CP –1 eigenstate, and thus to decay to 3π. However some rare decays to 2π with CP +1 were seen, thus violating CP. This implied that weak eigenstates are in fact a combination $K_S = K_1 + \epsilon K_2$ and $K_L = K_2 + \epsilon K_1$ with $\epsilon = 2.228 \times 10^{-3}$ [6]. This is known as indirect CP violation, arising from the mixing of the states.

Direct CP violation also occurs in the Kaon sector, where a violation ϵ' occurs in the

decay itself. This direct CP violation comes about via a complex phase in the CKM matrix which describes quark mixing between flavours in weak transitions. A complex phase gives rise to processes that proceed at different rates for particles and antiparticles. Since CP violation through this phase involves flavour mixing of higher generation quarks in multi-loop processes, the calculated neutron electric dipole moment from the weak sector, $d_n \sim 10^{-32}$ $e \cdot cm$, is very small [26] [27].

CP violation has also been observed in neutral B mesons by the Babar [22] and Belle [28] experiments. And recently, evidence of CP violation has been seen in neutral D meson by the LHCb experiment [23] thus indicating CP violation in the charmed sector. These experiments examine rare decay of mesons in order to parametrise the CKM matrix with increasingly high precision, including the CP violating phase factor δ, and results to date are consistent with the standard model.

In principle, CP violation is possible in the strong interaction. A general term in the QCD Lagrangian allows for CP violating effects by

$$\mathcal{L} = -\frac{n_f g^2 \theta}{32\pi^2} G_{\mu\nu} \widetilde{G}^{\mu\nu} \tag{1.5}$$

where n_f is the number of fermions, g is the strong coupling constant, and $G_{\mu\nu}$ is the gluon field strength tensor, and θ is an arbitrary constant angle where $0 \leq \theta \leq 2\pi$. For a non-zero θ, this term is C even and P odd, thus violating CP symmetry. As $G_{\mu\nu}$ couples to quarks, the neutron is directly influenced by this θ mechanism, which might lead to a measurable EDM of the neutron. Calculations have shown that for such a contribution, $d_n \sim \mathcal{O}(10^{-16}\ \theta)$ $e \cdot cm$ [29] [30] [31]. While there is no reason within the SM for CP to be conserved in the strong sector, experimental evidence to date indicate that it is. In fact, it is experimental limits on the EDM of the neutron that set the strongest constraint, $|\theta| < 0.7 \times 10^{-11}$ [32].

This number is expected to be $\mathcal{O}(1)$ by naturalness arguments, and there is no reason for it to be fine-tuned to such a small value. This problem is known as the *Strong CP problem* and is considered one of the important unsolved problems in physics. Peccei and Quinn have

proposed an elegant solution [33] whereby a new symmetry is spontaneously broken, giving the CP violating term a vanishingly small value. It promotes θ to a field and predicts a particle, the axion, to date unobserved, despite ongoing searches [34].

θ has been estimated by renormalisation of the quark mass matrix at the two-loop level to give $\theta \approx 10^{-16}$ rad from which the contribution to the nEDM can be calculated as $d_n(\theta) \approx 10^{-32}$ e $\cdot$ cm , which is comparable to the contribution from the weak interaction.

In the standard model, CP violation is not observed in electromagnetic interactions [35]. CP violation by the gravitational force has not been observed, but is a topic of study in quantum gravity [36] and of experimental investigation using cooled anti-hydrogen [37].

The CP violation seen from the standard model via the CKM matrix however does not account for the observed baryon asymmetry in the universe. It occurs due to highly suppressed flavour changing processes, and so the observed baryon asymmetry from the CKM matrix is $\eta < 10^{-26}$, many orders of magnitude smaller than is measured, $\eta \sim \mathcal{O}(10^{-10})$, Eq. (1.1). Hence theories of new physics beyond the Standard Model that are proposed seek to reconcile this with allowed CP violating processes.

1.2.3 Sources of CP Violation from Beyond the Standard Model

Most extensions to the Standard Model contain possible sources of CP violation. Sources of CP violation above and beyond what is provided by the standard model are abundant in supersymmetric theories, and other theories of new physics beyond the standard model.

A general supersymmetric extension to the standard model postulates the existence of a fermionic superpartner particle for every boson and vice versa, the only difference being their spin. As particles with equal mass but different spins have not been observed, SUSY must be a broken symmetry, giving the SUSY partners much higher masses than their standard model partners. SUSY is a promising theory as it could provide a particle physics basis for explaining both the unsolved problem of baryogenesis and also of dark matter in the universe.

As these theories introduce extra fields and extra couplings, they may also introduce CP violating interactions. Generally, imaginary phases in the squark (quark supersymmetric partner) and gluino (gluon supersymmetric partner) mixing parameters allow for first order contributing interactions to CP violation, and therefore predict a larger nEDM.

In order to evaluate the contribution to CP violation from these interactions, one has to know the masses of the squarks and the couplings, which depend on the details of the supersymmetric breaking for the particular model of SUSY. Many models lead to values of the nEDM of $\mathcal{O}(10^{-23} - 10^{-24})$ which is incompatible with the current experimental limit of $|d_n| < 2.9 \times 10^{-26}$ e $\cdot$ cm and thus have been ruled out [38].

Experimental limits of nEDM and other EDMs impose severe constraints on the parameters in SUSY models. The experimental limits aimed for by cryoEDM experiment are within the measurement realms of promising SUSY theories. CryoEDM has the capacity to measure any new physics if such theories predict an nEDM within the sensitive range, or to rule out certain models of SUSY. An example of the constraints on MSSM parameters is given by Pospelov and Ritz in Figure 1.3 [39]. Without getting into details of MSSM and its symmetry breaking, the figure can be explained by saying that the breaking mechanism allows for dozens of new CP violating phases. However, constraints and parameterisations can reduce this to two phases, θ_A and θ_μ, where A refers to the boson couplings in the theory, and μ is a term which gives Dirac mass to the higgsino. Given expressions for the EDMs of the neutron, Thallium atom and Mercury atom derived within the MSSM theory, which depend on the values of the CP violating factors, θ_A and θ_μ as well as the Supersymmetric breaking scale of M_{SUSY} and the ratio of Higgs vacuum expection values tanβ, one arrives at a set of constraints on the allowed values of θ_A and θ_μ. This is plotted in Figure 1.3 for $M_{SUSY} = 500$ GeV and tan$\beta = 3$. A full review of CP violation in SUSY is given by Khalil in [40] and the implications of EDM limits on SUSY theories given by Abel and Lebedev in [41].

Other theories of new physics also have implications for CP violation and the nEDM. In the neutrino sector, the PMNS matrix which parameterises neutrino mixing in the same

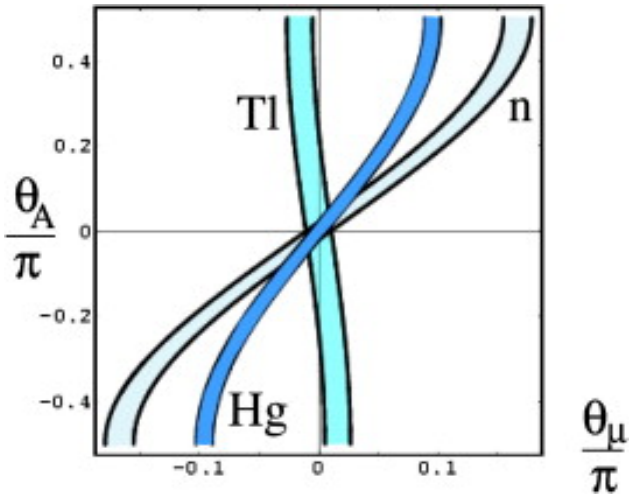

Figure 1.3: The combination of the three most sensitive EDM constraints, d_n, d_{Tl}, and d_{Hg}, for MSSM parameters $M_{SUSY} = 500$ GeV, and $\tan\beta = 3$. The region allowed by EDM constraints is at the intersection of all three bands around $\theta_A = \theta_\mu = 0$ [39].

manner as the CKM matrix for quark mixing, also allows for CP violating phases. Further theories of new physics include multi-Higgs theories and left-right symmetric models which may produce CP violation, and so an nEDM measurement is potentially sensitive to them. These theories and the role EDMs play in their parameterisation are discussed by Ramsey-Musolf and Su in [42].

1.2.4 Expectation Level of CP Violation in SM Strong Interactions

An example of a Feynman diagram of one process producing a quark EDM within the SM is shown in Figure 1.4. In order to generate a complex amplitude in a weak interaction, at least two charged current transitions, not related by complex conjugation, must occur. This is CP violating due to the factor of δ in the CKM matrix, and in the diagram given in Figure 1.4, $V_{cs}V_{cd}^* \neq V_{cd}V_{cs}^*$, which is not real.

The predicted d_n is very small in these SM interactions due to these high order flavour changing diagrams; calculations predict it to be 10^{-31} to 10^{-32} e $\cdot$ cm [26] [27], several orders of magnitude beyond the reach of any experiment being considered at present. This offers the considerable advantage of a background-free environment: a measurement of a non-zero

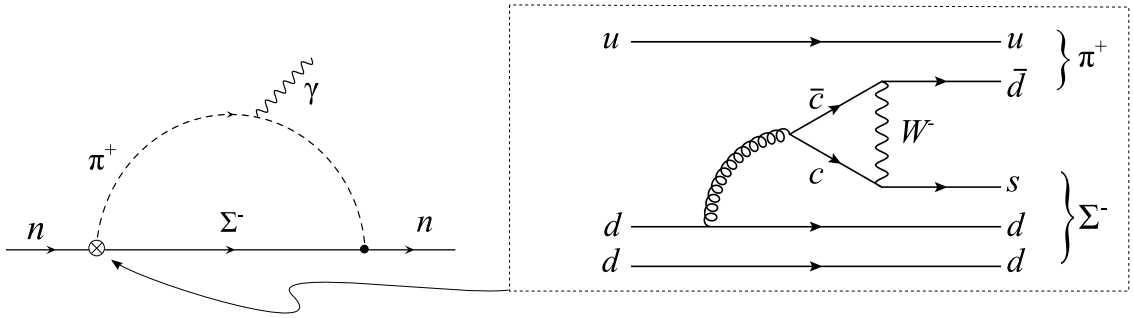

Figure 1.4: A so-called "Strong Penguin" Feynman diagram depicting a SM process generating a neutron EDM of $\mathcal{O}(10^{-32})$. The neutron appears to spontaneously emit a photon. A constituent quark of the neutron emits a gluon which creates a c and $\bar{c}$ pair, creating a s and $\bar{d}$ upon exchange of a W^-. These quarks in combination with the other consituent quarks form a π^+ and a Σ^-. The process is then reversed to give back the neutron but not before the π^+ has radiated a γ, carrying away some of the neutron's momentum.

value would be an unequivocal proof of new physics beyond the Standard Model.

Models of new physics including left-right symmetric models, non-minimal models in the Higgs sector, and SUSY models allow for CP violating mechanisms not found in the SM, including lower order terms that do not change flavour. Lower order non-flavour changing interactions in these extensions typically give rise to neutron EDM contributions, which are of the order of $(10^{-25} - 10^{-27})$ e $\cdot$ cm .

Thus there is a natural and reasonable expectation that the values of the nEDM may lie at levels just beyond current experimental limits and within the realm of detection with the technology of next generation nEDM experiments. This leaves the exciting possibility of at least ruling out models, if not detection and confirmation of new physics.

Complimentary searches for electric dipole moments in other systems, such as leptons and atoms, are important as they can strongly constrain models in different ways. For example atoms may be particularly insensitive to flavour-changing parameters and the electron insensitive to strong CP violation. A thorough review of the role of EDMs as probes of new physics is given by Pospelov and Ritz in [39], and a thorough theoretical review given by Dubbers and Schmidt in [43].

1.3 Limits on the neutron EDM and other EDMs

As the search for permanent electric dipole moments is currently among the most promising methods to find new sources of CP-violation, it is not surprising that around the world more than 30 different experiments are searching for electric dipole moments in different systems. As the various sources of CP violation beyond the Standard Model predict different values to the electric dipole moments of various particle species, it is valuable to have a collection of EDM measurements of these different particle species for model differentiation. This includes the search for a permanent electric dipole moment of the muon, proton and the electron from heavy paramagnetic or diamagnetic atoms and molecules.

Figure 1.5 shows the experimental limit on both the neutron and electron EDMs over the last fifty years, on the left hand side. It also shows the expected ranges for the neutron and electron electric dipole moments in various popular theories on the right hand side. It is clear that certain theories have already been ruled out, and others give differing ranges for the EDM values for both particles.

The present limits on EDMs of the neutron, electron and mercury atom are already remarkably stringent. Table 1.1 shows the current best limits on the EDM of various particles, the experiment that obtained the results, the year it was published and the method by which it was obtained.

Particle	Experiment/Institution (Date)	Method	Limit / e cm
Neutron	nEDM (2006)	Stored Neutrons	2.9×10^{-26} [24]
Proton	University of Washington (2009)	Inferred from Hg	7.9×10^{-25} [45]
e	The ACME Experiment (2013)	ThO beam	8.7×10^{-29} [46]
μ	muon g -2 Brookhaven (2009)	Storage Ring	1.8×10^{-19} [47]
τ	BELLE (2003)	$e^+e^- \rightarrow \tau\tau$ events	4.5×10^{-17} [48]
Hg^{199}	University of Washington (2009)	Absorption spectrum	3.1×10^{-29} [45]

Table 1.1: The current best experimental limits on the EDMs of various particles.

Comprehensive review papers on the topic is available by Abele at [49] and by Pospelov

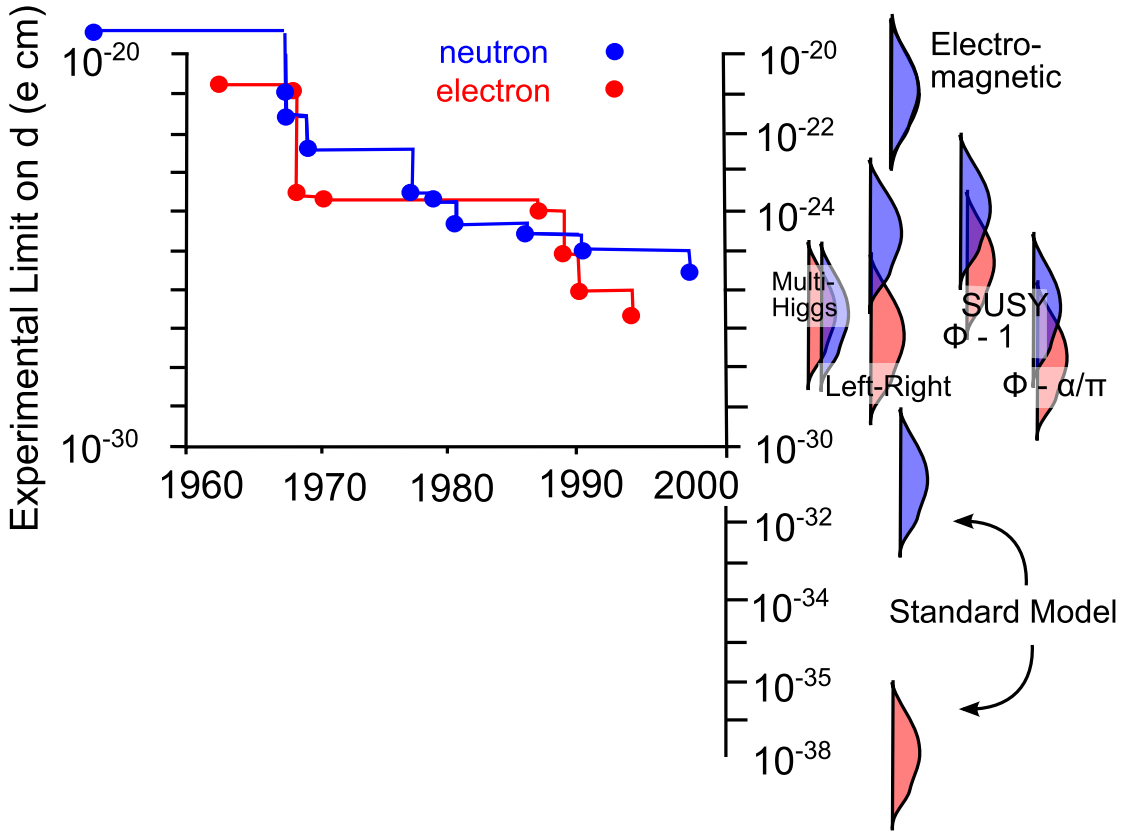

Figure 1.5: Neutron (blue) and electron (red) EDM limits over the last 50 years, and the predicted values from theoretical models [44].

and Ritz at [39].

1.3.1 Electron EDM

The measurements of the EDMs of the electron and neutron have similar principles but have various technical distinctions. Electron EDMs experience a theoretically determinable enhancement factor by being bound in paramagnetic atoms or molecules and can be produced in higher densities than free neutrons, however the Standard Model prediction for its EDM is up to seven orders of magnitude lower than that of the neutron. It also probes CP violation in the leptonic sector rather than the hadronic sector.

In heavy paramagnetic atoms, the relativistic treatment of their interaction with an external electric field leads to a measurable electron EDM, which grows with atomic number as Z^3. Exceptionally high internal effective electric fields, $\mathcal{E}_{eff}$, can be used to precisely probe

for d_e via the energy shift $-\vec{d_e} \cdot \vec{\mathcal{E}_{eff}}$. Valence electrons travel relativistically near the heavy nucleus, making $\mathcal{E}_{eff}$ up to a million times larger than any static laboratory field.

The current limit-holding experiment, by the ACME collaboration [46] used a beam of spin aligned thorium monoxide (ThO) polar molecules, to place an upper limit of $d_e < 8.7 \times 10^{-29}$ e $\cdot$ cm. With this molecule, an effective field of 84 GV/cm was obtained. The Ramsey Method of Separated Oscillatory Fields is also used on this beam of molecules. A previous limit holding experiment, held by Hudson et. al at Imperial College London [50], of $d_e < 10.5 \times 10^{-28}$ e $\cdot$ cm used the molecule YbF which had an effective field of 14.5 GV/cm.

Many competing experiments are in operation, using molecules including ThO, YbF, and PbO. Reviews of lepton EDMs are available by Bernreuther and Suzuki [51] and by Commins [52].

1.3.2 Atomic and Other EDMs

In heavy diamagnetic atoms, EDMs become measurable due to the finite size of the nucleus. For the diamagnetic atom ^{199}Hg, Griffith et. al. [45] set a limit of $d_{Hg} < 3.1 \times 10^{-29}$ e $\cdot$ cm from which they could extract the EDM of the proton, $d_p < 7.9 \times 10^{-25}$ e $\cdot$ cm. They could also extract d_n and d_e to a sensitivity of only factor of $\sim$2 less stringent than the world limits. Many collaborations worldwide are measuring the EDMs of various atoms, including Xe, Cs and Ra. A thorough discussion of this topic is given by Ginges and Flambaumin in [53].

The μ EDM is measured essentially as a by-product of magnetic moment measurements by the $\mu(g-2)$ collaboration at Brookhaven. A new generation $\mu(g-2)$ experiment is in preparation at Fermilab National Laboratory (FNAL) [54]. The τ-lepton EDM was measured by the BELLE collaboration at KEK (Japan), a precision flavour physics experiment using B mesons to investigate CP violating parameters [48]. An experiment to directly measure the EDM of the proton has been proposed by Brookhaven National Laboratory (BNL) using a proton storage ring [55].

All these complementary measurements seek to place ever more stringent constraints on various theories of new physics beyond the standard model, and theories of CP violation in different sectors.

1.3.3 Neutron EDM experiments

Norman Ramsey first recognised the significance of the neutron EDM for the investigation of CP violation [56]. The first neutron EDM measurements were done by Ramsey and Purcell in the 1950s at Oak Ridge National Laboratory (ORNL), USA [19]. Ramsey invented the method of separated oscillatory fields, a type of nuclear magnetic resonance, which was subsequently applied to the invention of atomic clocks and for which he won the Nobel Prize in Physics in 1989 [57]. This method is used to measure the nEDM by applying RF magnetic field pulses to a beam of polarised neutrons which is close to the resonance neutron magnetic resonance frequency. A period of free precession in the presence of a static electric field then occurs, followed by a further RF pulse. The presence of any EDM will cause a shift in Larmor precession frequency due to a coupling of the EDM with the E field, $\vec{d_n} \cdot \vec{E}$. This shift manifests as a finite probability that some neutrons have flipped spin. The intensity of neutrons passing through a spin analyser in response to the E field is counted by a neutron detector. In early experiments, this was a BF_3 proportional counter. This *Ramsey Resonance* method is outlined in full detail in Chapter 2.

The early experiments were done with a beam of cold neutrons, which can be produced in high density. However the high velocity of the neutrons means the observation time is short. There is also the complication of a velocity dependant systematic effect, $\vec{v} \times \vec{E}$, which produces a B field in the rest frame of the neutron, mimicking an EDM signal. The best result obtained with a beam of neutrons was $d_n < 3 \times 10^{-24}$ e $\cdot$ cm.

From the 1980s, advancement in techniques meant that ultra-cold neutrons (UCN) could be bottled and stored for much longer times. The kinetic energy of these neutrons ($< \mu$eV), is low enough for them to reflect from certain materials, such as Beryllium or Copper. If the so-called Fermi-Potential of a material is low enough, the neutron will elastically scatter off

the surface, rather than passing through it or being absorbed by it, as is the case with higher energy neutrons. Thus UCN can be stored for hundreds of seconds, increasing exposure to the electric field, allowing the sensitivity of the method to increase, and also removing the $\vec{v} \times \vec{E}$ effect. This however is at the cost of neutron density and thus statistics, as UCN production methods cannot match the number density of cold neutron beams. The first nEDM results using bottled UCN by Altarev et al in 1980 [58] set a limit of $d_n < 1.6 \times 10^{-24}$ e·cm. Experiments using these stored UCN began at Institut Laue Langevin (ILL) in France and Petersburg Nuclear Physics Institute (PNPI), Russia, eventually becoming limited by neutron statistics from the UCN sources of the time.

Thorough reviews of the subject and the historical measurements are given by Ramsey [59] and [60], Pendlebury [61] and Golub and Lamoreaux [62].

The Room Temperature nEDM experiment

The room temperature neutron EDM experiment was a collaboration between the University of Sussex, Rutherford Appleton Laboratory (RAL) and the Institut Laue Langevin. It ran from 1996 to 2002, measuring a final limit of $d_n < 2.9 \times 10^{-27}$ e · cm [24], which is the best in the world.

It utilised the ILL ultra-cold neutron source in Grenoble, which guides cold neutrons from a liquid deuterium cold source to a neutron turbine serving as generator of UCN [63]. The source delivered a UCN density to the experiment of 50 cm^{-3}. The nEDM experiment stored $\sim 10^4$ UCN per batch.

The measurement was made with spin-polarized UCN stored in a quartz cell permeated by uniform B field and uniform high E field of 10 kV/cm. The terms $-\vec{\mu_n} \cdot \vec{B}$ and $-\vec{d_n} \cdot \vec{E}$ are added to the Hamiltonian determining the states of the neutron. Given parallel E and B fields, the Larmor frequency $\nu_{\uparrow\uparrow}$ with which the neutron spin polarization precesses about the field direction is

$$\nu_{\uparrow\uparrow} = 2\vec{\mu_n} \cdot \vec{B} + 2\vec{d_n} \cdot \vec{E} \tag{1.6}$$

The polarity of the E field is flipped relative to the B field, resulting in a shift in Larmor frequency,

$$\nu_{\uparrow\downarrow} = 2\vec{\mu_n} \cdot \vec{B} - 2\vec{d_n} \cdot \vec{E} \tag{1.7}$$

The experiment measured with the highest possible precision any shift in the precession frequency $\nu = \nu_{\uparrow\uparrow} - \nu_{\uparrow\downarrow}$ as the applied $\vec{E}$ field alternates between being parallel and then anti-parallel to $\vec{B}$. A schematic of the apparatus is shown in Figure 1.6.

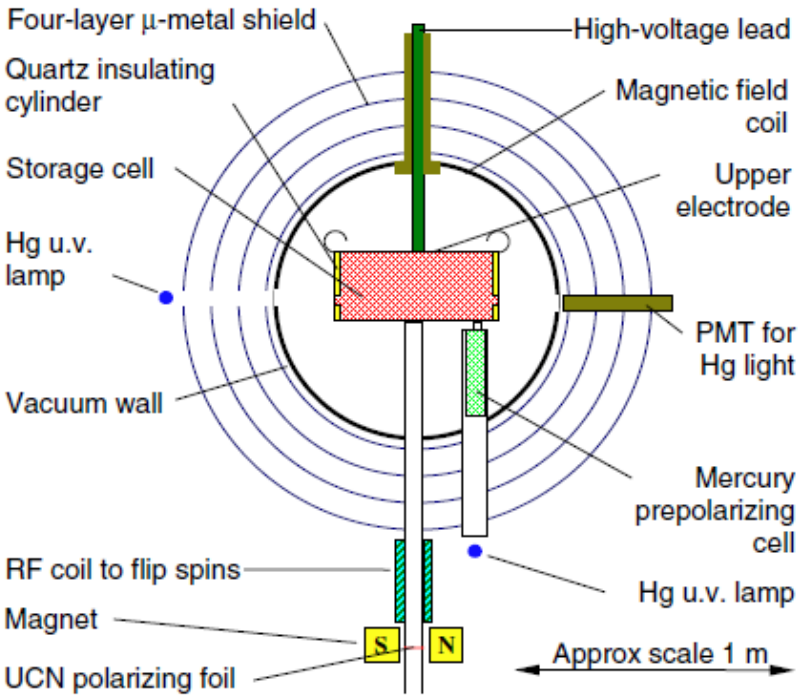

Figure 1.6: Experimental apparatus of the nEDM experiment [24].

The precession frequency ν of the neutrons was measured using the Ramsey Method with Separated Oscillatory Fields. During the storage period, the neutrons interacted coherently with two short (∼2 s) intervals of oscillating magnetic field having a chosen frequency close to the Larmor frequency. The two intervals were separated by a long period $T \sim 120 - 150\ s$ of free precession. The last step was to count the number of neutrons $N_{\Uparrow}$ and $N_{\Downarrow}$ which finish in each of the two polarization states. The neutron detector was a ^{3}He gas proportional counter.

The dominant systematic error in earlier experiments was due to fluctuations in the magnetic field. An EDM of 1×10^{-26} e · cm would produce a change in precession frequency

on reversal of $\vec{E}$ of 1×10^{-7} Hz for a field strength of 10 kV cm^{-1}. This frequency shift corresponds to a magnetic field of around 2 fT for a neutron. Given that the earth's magnetic field is $\sim$50 μT, it is immediately clear that magnetic field control is crucial to minimising systematic uncertainty in an nEDM experiment.

For this reason, the nEDM storage volume was situated within four layers of mu metal, giving a shielding factor of about 10^4 to external magnetic field fluctuations. Moreover, they developed a ^{199}Hg co-magnetometer based upon the storage of polarized atoms simultaneously with and in the same cell as the neutrons. Another significant systematic error involved a geometric phase arising when the trapped neutrons experience a gradient $\delta B_{0_z}/\delta z$ in the presence of an E field [64]. Both these systematics remain of concern to contemporary EDM experiments and cryoEDM.

Ultimately, the room temperature nEDM experiment was limited by statistical uncertainty. Although methods were suggested to improve the UCN density at the turbine source, orders of magnitude increases in intensity required the development of new UCN production methods. The method proposed relied on the inelastic scattering of 9 Å cold neutrons in superfluid ^{4}He, causing the cold neutrons to downscatter to UCN. UCN densities created in the helium might be as high as 10^5 cm^{-3} [61]. This method was used to develop the cryoEDM UCN source, which has been outlined in Chapter 2.

Contemporary nEDM experiments

As well as cryoEDM, there are currently at least six other collaborations around the world trying to measure the electric dipole moment of the neutron. They all aim for an improvement of the current best limit by at least an order of magnitude in sensitivity. Although having different approaches on experimental techniques, most of these experiments use a refined method of the room temperature approach that was just described. Essential to most of the experiments is the development of new UCN sources to increase the UCN density to $10^3 - 10^4$ cm^{-3} and therefore the statistical sensitivity.

Another cryogenic experiment is the **SNS nEDM** experiment currently under construction at the Spallation Neutron Source (SNS) at ORNL in the USA. The main advantage of a cryogenic experiment is the novel UCN production method where cold neutrons at 9 Å inelastically scatter in superfluid ^{4}He and downscatter to UCN [65] [66]. Furthermore, a polarised cold neutron remains in the same polarisation state after downscattering, producing polarised UCN. This is the same production method used for cryoEDM has been well studied and can produce UCN densities of up to 10^4 cm^{-3} [67].

The SNS collaboration intends to use the same vessel for production, storage, precession and measurement, in order to minimise losses due to UCN extraction transport. It proposes to use a Ramsey Resonance method similar to cryoEDM, as will be described in detail in Chapter 2. It proposes to use the novel method of a dilute solution of polarized ^{3}He to act as a UCN spin analyzer, detector and magnetometer. The ^{3}He nuclei act as a co-magnetometer, like the ^{199}Hg nuclei in the ILL experiment. The ^{3}He nuclei also act as a neutron spin analyzer: For neutron spin opposite to the ^{3}He spin, the neutron capture cross section is almost 200 times larger than for parallel spins. Finally, the ^{3}He nuclei act as a counting process: in the reaction n + ^{3}He $\rightarrow$ ^{3}H + ^{1}H + 0.764 MeV, the products produce ultraviolet scintillation photons in liquid helium, which can be wavelength shifted to the visible region and then transported to outside the cryostat for detection with Photomultiplier Tubes (PMTs), as was demonstrated in [68].

A further advantage of performing the experiment in liquid helium is that higher electric fields can be held across this fluid than across an evacuated volume. The SNS experiment aims to have a sensitivity of 5×10^{-28} e $\cdot$ cm. A review of EDM experiments with a focus on the SNS experiment was made by Laroreaux and Golub in 2009 [69]. Details of the proposal are available at [70], and a status report from 2007 at [71].

At Paul Scherrer Institut (PSI) in Switzerland, the room temperature nEDM experiment, described on page 22, is being upgraded and installed at the 1.3 MW proton beam. The **PSI nEDM** experiment will be an optimised version of the room temperature in vacuum approach. The proton beam hits a dedicated small spallation target which in turn feeds a

solid D_2 UCN converter. As well as an improvement on neutron statistics from this new source, the collaboration intend to also improve on systematics by installing an array of laser optically pumped Cs magnetometers to monitor and stabilise the magnetic field and its gradients. It will also gain in sensitivity due to a larger experimental volume and polarization product [72].

A new detection system was constructed for the nEDM experiment at PSI. The former experiment used the ^{3}He gas counter which is too slow for the high counting rates (up to 10^6 UCN/s) expected at PSI. A new type of high counting rate UCN detector based on ^{6}Li doped glass scintillator was developed. The scintillation light is measured by 9 PMTs in 9 separate channels to allow for the counting rate per channel to be decreased within the capability of the PMT [73]. They have reported that it shows efficiency similar to ^{3}He counters [74]. The UCN source was described by Anghel et al [75] and tested under full power in 2010. With all the planned improvements and the improved source, it aims to improve on the present limit by a factor of 100, and intents to run through the 2010s. A status report is available at [76].

A second nEDM experiment is being constructed at ILL, a collaboration between PNPI-Joffe-Physical Technical Institute-ILL. The **PNPI-ILL nEDM** experiment is a room temperature multichannel spectrometer which consists of four double chamber units. It is an upgraded version of the previous PNPI experiment and is now installed at the ILL UCN turbine source. Many discrete Cs magnetometers are used to monitor the magnetic field and to compensate magnetic field fluctuations with magnetic field gradients. It has already released a result of 5.5×10^{-26} e $\cdot$ cm in 2013 [77]. With present operating conditions of this experiment, a limit three times better than the current limit can be obtained in three years of running. The collaboration intends to upgrade to a superfluid He UCN source at PNPI, Gatchina, Russia [78] [79].

Another European collaboration are developing a room temperature nEDM experiment for use at the FRMII research reactor and neutron source operated by Technische Universitat Munchen (TUM). The **FRMII nEDM** experiment aims to have a precision of 10^{-28} e $\cdot$ cm.

It too is a room temperature EDM experiment which utilises a ^{199}Hg spin polarized vapor to act as a co-magnetometer. A large scale and sophisticated system is currently being realised for a highly magnetically shielded experimental room and a sophisticated magnetic field compensation system [80].

A proposal for a future experiment foresees a collaboration between the Research Center for Nuclear Physics (RCNP) in Japan and TRIUMF in Canada. The **RCNP-TRIUMF nEDM** collaboration have already demonstrated a superfluid UCN source [81] at RCNP. The proposed UCN source at TRIUMF would will utilise the superfluid-helium downscattering method and provide the world's highest density source, with the proposed EDM experiment being constructed later in this decade. [82]. The proposal is available at [83].

A different experimental approach to measure the nEDM is to derive an EDM using dynamical diffraction from noncentrosymmetric perfect crystals. The neutron can experience interplanar electric fields of the order of $E_g \sim 10^9$ V/cm. This **Crystal Diffraction nEDM** experiment is trading the long observation time of UCN for the high electric field inside the lattice of non-centrosymmetric crystals. A cold neutron beam is reflected from a quartz crystal close to the Bragg condition and the spin rotation due to a possible EDM of the neutron is measured. The sensitivity of the experiment needs to be improved to reach the same sensitivity as current UCN based experiments. A prototype experiment was carried out at ILL [84].

A summary of the competing next generation UCN neutron EDM experiments is presented in Table 1.2, outlining the collaboration, location, the type of neutron source (He-II being superfluid helium, SD_2 solid deuterium etc.) and the proposed sensitivity.

There is a worldwide competition of ambitious and challenging neutron and atomic physics EDM experiments, with various routes to setting ever stringent limits on theories of new physics. As outlined in this chapter, the EDMs are one of our best chances to pinpoint the scale of new physics in this century. The neutron EDM has been described by Ellis as a "sensitive cosmological seismometer" [88] in relation to baryon asymmetry. The subsequent focus of this thesis will be the experimental aspects of the cryoEDM experiment.

Collaboration	Location	Source	Proposed Sensitivity / e cm
CryoEDM	ILL	He-II	1×10^{-28} [85]
ORNL	SNS	He-II Spallation	2×10^{-29} [70]
PSI	PSI	SD_2 Spallation	5×10^{-28} [86]
PNPI	ILL	LD_2 UCN Turbine	3×10^{-28} [87]
TUM	FRMII	SD_2	5×10^{-28} [80]
RCNP	TRIUMF	He-II Spallation	1×10^{-28} [83]

Table 1.2: nEDM experiments with UCN around the world.

Chapter 2

The Cryogenic Neutron EDM Experiment

As the predicted neutron EDM is very small in the Standard Model ($\sim 10^{-32}$) and in BSM theories ($\sim 10^{-24} - 10^{-28}$), any attempt to measure or place an upper limit on it requires extremely sensitive measurement techniques. A commonly used analogy contextualises the sensitivity and ambition of this experiment: if the neutron was the size of the earth, the current nEDM limit would correspond to an electric dipole separated by 1.5 μm. Thus large neutron numbers are required to increase the statistical sensitivity, combined with efficient detection of said neutrons, and precise control of systematic effects from electric and magnetic fields. This chapter will focus on the techniques used in cryoEDM to measure the nEDM and an overview of the experimental subsystems.

2.1 An Overview of the cryoEDM Experiment

The cryoEDM experiment is one of the next generation neutron EDM experiments worldwide. It is situated at the Institut Laue Langevin in Grenoble, France, taking advantage of the most intense neutron beam in the world, providing 1.5×10^{15} n s^{-1} cm^{-2}. The experiment uses the cryogenic technique of cold neutron down-scattering in superfluid ^{4}He, as was intro-

duced in the last chapter. It is a collaboration between the University of Sussex, Rutherford Appleton Laboratory, University of Oxford, ILL, and Kure University, Japan.

CryoEDM aims to measure the nEDM by detecting a change in neutron precession frequency when in alligned B and E fields or anti-alligned fields. A neutron possesses a magnetic dipole moment (MDM), μ_n, which in a magnetic field, will precess around the axis of the B field at the Larmor frequency. Analogously, any electric dipole moment of the neutron d_n, in an electric field, will precess about the axis of the E field. As both the MDM and EDM are aligned with the neutron's spin, if aligned electric and magnetic fields are applied, the precession frequency ω will be a sum of the terms from the MDM and EDM,

$$H = \hbar\omega = |2\mu_n B \pm 2d_n E| \tag{2.1}$$

Therefore, EDM can be measured by detecting the change in neutron precession frequency, $\Delta\omega$, between the B and E fields being parallel or anti-parallel:

$$d_n = \frac{\hbar\ \Delta\omega}{4E} \tag{2.2}$$

This is the underlying principle of the cryoEDM experiment and most contemporary EDM experiments, and is discussed at length in Section 2.2. The measurement of this shift in precession frequency is done using the method of separated oscillatory fields, developed by Norman Ramsey with molecular beams in 1950 [57]. This is discussed in detail in Section 2.2.1, but in short, the method applies static and AC B fields tuned to spin flip polarised neutrons. The frequency of the AC B field is varied resulting in a distribution of neutron spins counts as a function of frequency. Any shift in this distribution under the reversal of the E field may be due to a coupling of the nEDM to the field. This method requires a spin polarised neutron source, a spatially and temporally homogeneous static B field, a tunable AC B field, a high voltage E field, a neutron spin analyser and neutron counter.

Figure 2.1 shows a schematic diagram of the cryoEDM apparatus, with the passage of the UCN through the system marked in red. A beam of polarised cold neutrons enters the

apparatus (1.) and are down-scattered in the superfluid source to produce polarised UCN (2.). These UCN are then contained within the walls of the guidetubes, and diffuse through a 90° turn and vertical drop into the main body of the apparatus (3.). This turn allows any remaining cold neutrons to be lost at the end of the source tube, so that spurious counts from cold neutrons will not contribute. The UCN diffuse to the Ramsey Cell at the left of the figure, where the resonance B fields and high voltage E field are applied (4.). Following the resonance, the UCN diffuse back through the system (5.) to the right, where a valve now allows them to travel vertically downwards into the detection area (6.). Here spin analysis and counting is performed (7.). Locations of all the various components and subsystems of the experiment are also marked in black. During their travel through the system, the UCN polarisation is maintained with holding fields. The Ramsey Cell region is surrounded my multiple layers of magnetic shielding. A full discussion of the apparatus and the role of each subsystem is described in Section 2.3.2.

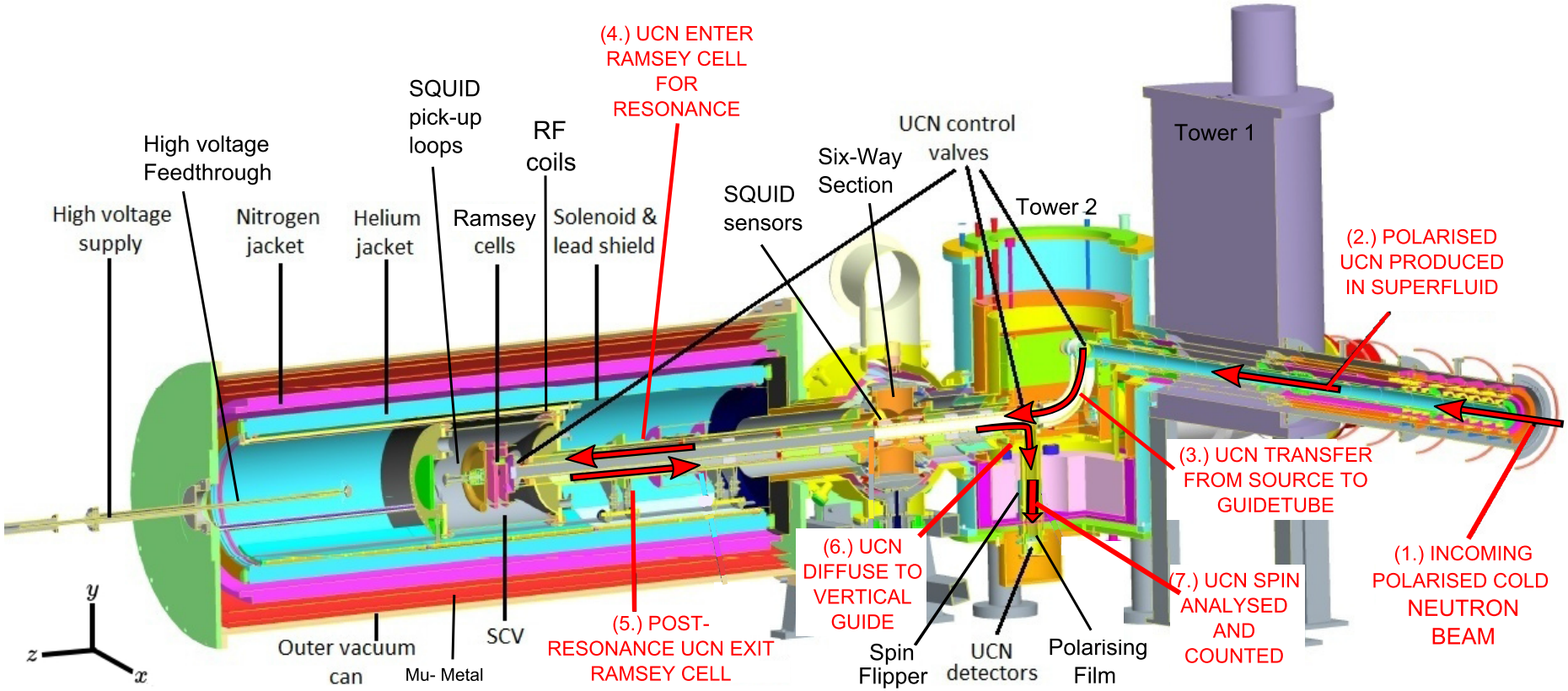

Figure 2.1: An illustration of the cryoEDM apparatus, showing the various sub-sections. The polarised cold neutron beam enters the superfluid UCN source volume on the right of the figure (1.). The cryostat cooling the superfluid volume is marked *Tower 1*. Polarised UCN are produced (2.) and contained by the guidetubes, and diffuse from the source through a 90° turn to remove any remaining cold neutrons (3.). UCN travel through the *Transfer Section* and *Six-Way section* to enter the measurement region of the experiment on the left hand side of the figure. The *Ramsey Cells*, Superfluid Containment Vessel (*SCV*), AC coils, solenoid, lead and mu-metal shields are arranged in concentric layers. High voltage is applied from room temperature with a feedthrough to the Ramsey Cells at the extreme left. UCN are held in the Ramsey Cells while resonance fields are applied (4.). SQUID magnetometers are mounted within the 6-way section, with their pick-up loops inside the SCV. UCN then diffuse from the Ramsey Cells (5.) towards a vertical guidetube, which has become accessible by a valve (6.). The spin flipper, polarising film and neutron detectors are located in this vertical tube under the neutron guides centre-right, where the UCN are spin analysed and counted (7.).

2.2 The cryoEDM measurement principle

The interaction of a neutron's magnetic dipole moment with a B field, and any electric dipole moment with an E field causes a shift in energy levels, which depend on the relative orientation of the fields. This is illustrated in Figure 2.2.

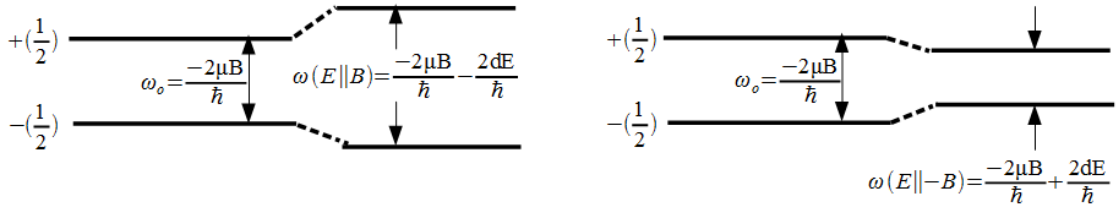

Figure 2.2: The shift in energy levels of the neutron when an E field is applied parallel to the B field (left) and anti-parallel to the B field (right)

From Eq. (2.1), the neutrons precession frequency in such fields is dependant on d_n, and any shift in precession frequency that occurs between the two relative alignments of the electric and magnetic fields would be a signal of an EDM. It is important to have a very homogeneous and well-controlled magnetic field to minimise any false EDM signal, and high electric field to maximise sensitivity to any shift. With an E field of 10 kV cm^{-1} a nEDM of 1×10^{-26} e·cm would cause a frequency shift of 1×10^{-7} Hz. If the neutrons were to experience a magnetic field change of 2 fT during the resonance cycle, the same frequency shift would occur. Therefore magnetic shielding, a high degree of magnetic control and highly sensitive magnetic measurements are of utmost importance to minimise these systematic effects.

2.2.1 The Ramsey Method of Separated Oscillating Fields

The cryoEDM experiment is based on the method of separated oscillatory fields developed by Norman Ramsey with molecular beams in 1950 [57]. The Ramsey resonance process as applied to neutrons is illustrated in Figure 2.3. In cryoEDM, polarised UCN are filled from the UCN source into the storage vessel, the Ramsey Cell, with their spins precessing about a static holding field B_0 and in an applied E field, marked as (1.) in Figure 2.3. An AC magnetic field B_{RF} is applied for a time t to the UCN, perpendicular to the static field and

at a frequency resonant with the precession. In the spin's rotating reference frame, this field appears static and perpendicular to the spin polarising field, causing the spin to precess around it. The resultant motion of the neutron due to the two precession components is a spiral, rotating between the spin-up and spin-down state. The magnitude and application time of the AC field is chosen so that the spin is flipped by $\pi/2$ and is rotating in a plane perpendicular to the static field. This is known as a $\pi/2$ pulse, or the rotating field. This is marked as (2.) in Figure 2.3.

After the pulse, the neutrons are allowed to precess freely for a time $T \gg t$ under the influence of the static magnetic and electric fields, marked as (3.) in Figure 2.3. A second $\pi/2$ pulse, coherent with the first, can then be applied for the same time t. If the frequency of B_{RF} is exactly the Larmor frequency, and no additional phase has built up, the two pulses will exactly add up and the UCN will all be in the opposite orientation to which they began. This is marked as (4.) in Figure 2.3.

However, if the frequency of the rotating magnetic field is not resonant with the precession frequency during the period of free precession, a phase difference will be introduced between the applications of the rotating field relative to the spin. This additional phase may have been due to a coupling of d_n to E, as in Eq. (2.1). The second $\pi/2$ pulse will result in a superposition of up and down spin states, which is dependent on the phase shift. Measuring the relative populations of spin-up and spin-down particles will yield the value of the phase shift and so the precession frequency.

The resulting pattern of neutron counts in the initial spin state is seen in Figure 2.4. This shows the number of spin-up counts on the y-axis, from a polarised neutron source after a Ramsey cycle, as a function of the applied field frequency. Each point corresponds to a measurement cycle applied to a batch of UCN as described above, where the AC B field has a frequency ω, given by the x-axis value. The periodic dependence on the applied frequency is clear, with the fringes in polarisation caused by the Ramsey resonance. The central minimum is at the neutron's precession frequency. The outer envelope is defined by the *Rabi resonance*, where an AC pulse is applied with no period of free precession.

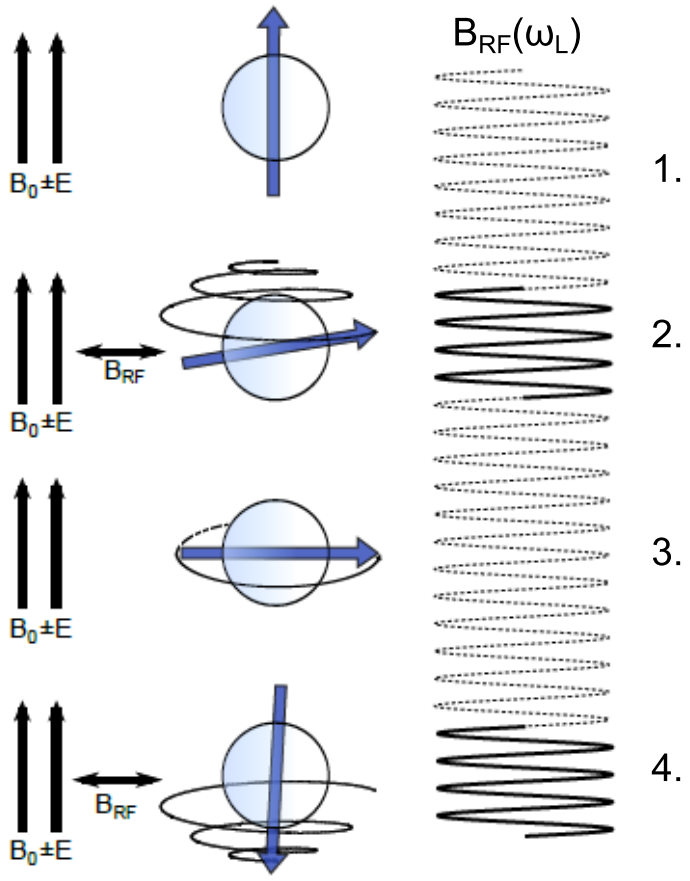

Figure 2.3: Shown is an illustration of the measurement procedure for a Ramsey resonance: 1. A spin polarised (spin-up) neutron precesses in a magnetic field; 2. An AC pulse is applied to the neutron to rotate the spin into an intermediate state; 3. The neutron has a period of free precession during which a phase shift relative to the AC signal may accumulate; 4. The AC pulse is applied a second time to complete the rotation of the spin; The neutrons' spin-state is now dependent on the phase shift introduced during free precession, and is ready for spin analysis.

Under the influence of an electric dipole moment the pattern in Figure 2.4 would shift to a higher (or lower) frequency for a parallel (or anti-parallel) field configuration. The maximum sensitivity on such a frequency shift of the neutrons is achieved at the steepest slope of the pattern. Here a small change in frequency would lead to a large difference in the observed count rate.

While the position of the central minimum of the resonance curve will yield the neutron precession frequency, it is impractical to obtain a resonance curve in each field configuration over a very long measurement period. Once a resonance curve has been measured, the applied frequency is chosen such that the experiment is conducted in a region of the resonance

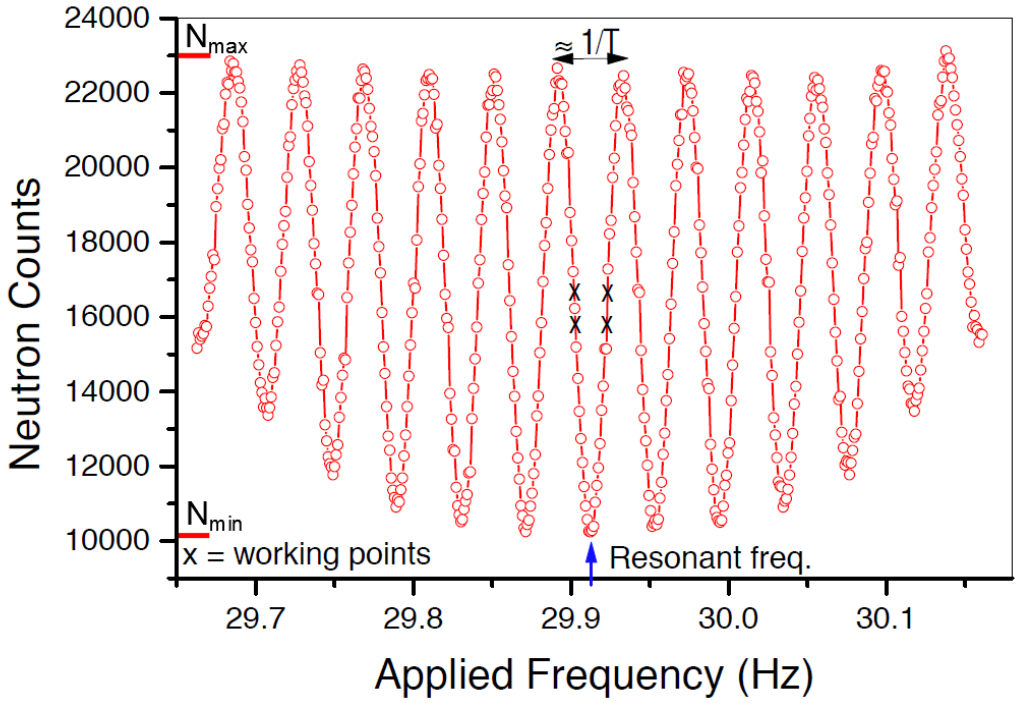

Figure 2.4: Shown is an example experimental curve showing how the neutron spin-up count varies with the frequency of an applied AC magnetic field. Clearly visible are Ramsey fringes giving a resonance frequency of 29.91 Hz. The regions of the curve the experiment operates in are labelled with 'X'. This curve was recorded with the room temperature nEDM experiment [89].

where $\delta N/\delta\omega$ is maximum, thus producing the largest change in neutron counts for change in precession frequency. As the curve is symmetric, by changing the frequency of the applied field by a small amount the operating point can be moved to the point on the resonance curve where the gradient is exactly opposite. Measurements taken at these points can be combined to cancel certain systematic effects, which are associated with changing the polarity of the electric field. For example, if the signal from the neutron detector is affected by the field polarity to cause a shift in neutron counts, the opposing gradients would produce a false EDM in opposite directions, which can be cancelled upon summation. These points are marked with an X in Figure 2.4, and the experiment is run at these points over a long time, accumulating statistics.

2.2.2 Extracting d_n

When separated oscillatory fields are used with an initial AC pulse of time τ and free precession time T, the full equation for probability for a neutron to flip spin as a function of AC pulse frequency ω, as measured in Figure 2.4, is given by Ramsey in [90] as:

$$P = 4\,sin^2\,\Theta\,sin^2\frac{a\tau}{2}\left[cos\frac{(\omega_0-\omega)T}{2}cos\frac{a\tau}{2} - cos\,\Theta\,sin\frac{(\omega_0-\omega)T}{2}sin\frac{a\tau}{2}\right]^2 \tag{2.3}$$

where Θ is given by

$$cos\,\Theta = (\omega_0-\omega)/a$$
$$sin\,\Theta = -2b/a$$
$$a = \sqrt{(\omega_0-\omega)^2+(2b)^2}$$

and where ω_0 is the resonance frequency, and 2b the magnitude of the AC B field multiplied by the gyromagnetic ratio of the neutron, $\gamma_n = 1.833 \times 10^8$ rad s^{-1} T^{-1}.

For neutrons near resonance, in the approximation $b \gg \Delta\omega\ (= \omega_0 - \omega)$ this leads to

$$P = sin^2(a\tau)cos^2\left(\frac{\Delta\omega T}{2}\right) \tag{2.4}$$

which is just the product of a diffraction factor corresponding to a total passage time 2τ in the oscillating field region and an interference factor introduced by virtue of a passage time T through the region of free precession. Since $T \gg \tau$ for a $\pi/2$ pulse it can be shown that [91] :

$$P \approx -cos(\Delta\omega T) \tag{2.5}$$

Therefore the number of neutrons expected with a precession frequency ω_0 rotated by an AC field with frequency ω, applied for a time τ with a period of free precession of $T \gg \tau$ is given by

$$N = N_{ave}\big(1 \pm \alpha\,cos(\Delta\omega T)\big) \tag{2.6}$$

for spin-up and spin-down respectively. N_{ave} is the average population of the two states, (denoted by $N_{\Uparrow}$ and $N_{\Downarrow}$) and α is the visibility averaged over the two spin states, of the

central resonance fringe:

$$\alpha_{\Uparrow} = \frac{N_{\Uparrow max} - N_{\Uparrow min}}{N_{\Uparrow max} + N_{\Uparrow min}} \tag{2.7}$$

with a similar expression for $\alpha_{\Downarrow}$. The visibility is effectively a measure of the polarization that can be achieved and maintained throughout the measurement period.

The difference then between spin-up counts and spin-down is given by

$$\Delta N = 2N_{ave}\,\alpha\, cos(\Delta\omega T) \tag{2.8}$$

Assuming the electric and magnetic fields are either parallel or anti-parallel, the precession frequency is $\omega_0 = \omega_B \pm \omega_E$ respectively and thus $\Delta\omega = (\omega_B \pm \omega_E) - \omega$

$$\Delta N = 2N_{ave}\,\alpha\, cos\Big[\big((\omega_B \pm \omega_E) - \omega\big)T\Big] \tag{2.9}$$

Using the cosine summation rules to expand this gives

$$\Delta N = 2N_{ave}\,\alpha\,\Big(cos\big[(\omega_B - \omega)T\,\big]\, cos(\omega_E T) \mp sin\big[(\omega_B - \omega)T\,\big]\, sin(\omega_E T)\Big) \tag{2.10}$$

Subtracting these counts from aligned ($\uparrow\uparrow$) and anti-aligned ($\uparrow\downarrow$) fields gives

$$\Delta N_{\uparrow\uparrow} - \Delta N_{\uparrow\downarrow} = 4N_{ave}\,\alpha\, sin\big[(\omega - \omega_B)T\big] sin(\omega_E T) \tag{2.11}$$

As the experiment is looking for a small change in frequency with the application of the electric field, the experiment is carried out at operating points on the resonance curve where the sensitivity is highest, that is, where the slope is the greatest. At this point $(\omega - \omega_B)T = \pi/2$ and so $sin\big[(\omega - \omega_B)T\big] = 1$. As the EDM is small, $\omega_E T \ll 1$ so $sin(\omega_E T) = \omega_E T$. Thus we have

$$\Delta N_{\uparrow\uparrow} - \Delta N_{\uparrow\downarrow} = 4N_{ave}\,\alpha\,\omega_E T \tag{2.12}$$

As $\omega_E = 2d_nE/\hbar$ this leads to

$$\Delta N_{\uparrow\uparrow} - \Delta N_{\uparrow\downarrow} = 4N_{ave}\,\alpha\,\frac{2d_nE}{\hbar}T \tag{2.13}$$

where $4N_{ave}$ is the total number of neutrons in both spin states in both field alignments, i.e. N. This gives an expression for d_n

$$d_n = \frac{\hbar(\Delta N_{\uparrow\uparrow} - \Delta N_{\uparrow\downarrow})}{2EN\alpha T} \tag{2.14}$$

The statistical uncertainty on this number can also be determined. Assuming the statistical uncertainties on the electric field, polarisation and measurement time are small, the dominating effect will be uncertainties in the neutron counting, which will be Poisson distributed. Thus the uncertainty will be given by

$$\big(\sigma(d_n)\big)^2 = \left(\sigma(\Delta N_{\uparrow\uparrow} - \Delta N_{\uparrow\downarrow})\frac{d\,d_n}{d(\Delta N_{\uparrow\uparrow} - \Delta N_{\uparrow\downarrow})}\right)^2 + \left(\sigma(N)\frac{d\,d_n}{dN}\right)^2 \tag{2.15}$$

And as $\sigma(\Delta N_{\uparrow\uparrow} - \Delta N_{\uparrow\downarrow}) = \sigma(N) = \sqrt{N}$, Eq. (2.15) simplifies to

$$\big(\sigma(d_n)\big)^2 = \left(\frac{\hbar}{2E\alpha T}\right)^2\left[N\cdot\left(\frac{1}{N}\right)^2 + N\cdot\left(\frac{\Delta N_{\uparrow\uparrow} - \Delta N_{\uparrow\downarrow}}{N^2}\right)^2\right] \tag{2.16}$$

As $N \gg \big(\Delta N_{\uparrow\uparrow} - \Delta N_{\uparrow\downarrow}\big)$, the second term in the bracket can be ignored giving

$$\big(\sigma(d_n)\big)^2 = \left(\frac{\hbar}{2E\alpha T}\right)^2\frac{1}{N} \tag{2.17}$$

or

$$\sigma(d_n) = \frac{\hbar}{2E\alpha T\sqrt{N}} \tag{2.18}$$

2.3 The cryoEDM Experimental Process

The advantages of operating in superfluid helium become clear when examining the parameters that the EDM are dependant on, given in Eq. (2.14) and its uncertainty, given in Eq. (2.18). Having a neutron storage volume filled with liquid helium means most of these parameters can be improved.

The storage time of the UCN is ultimately limited by the lifetime of the free neutron, 880.1 ± 1.1 s [6] [92], after which is decays by beta emission $n \rightarrow p^{+}e^{-} + \bar{\nu}_e$. This lifetime is under idealised conditions, set by dedicated lifetime experiments. There are many modes of storage loss which reduce the UCN storage time from this limit to tens of seconds. This is primarily due to upscattering of the UCN to higher energies which cannot be contained, by interacting with impurities in the volume or on the surface, and also losses of UCN through gaps in the guidetubes.

At low temperature, any impurities on the surfaces of the neutron containment volume are cold, and so are less likely to scatter the UCN to high energy [91]. This improves the lifetime of the neutrons when stored, which is also has a linear dependence on the resolution of d_n. The low temperature allows superconducting magnetic shielding to be used, making use of the Meissner Effect whereby superconductors expel external field. This increases the stability of the magnetic environment that the neutrons are contained in, and thus reducing effects which may depolarise the neutrons.

However the most significant reason for operating the experiment at cryogenic temperatures is the UCN production method of down-scattering cold neutrons in superfluid helium. This method can produce a density of UCN much higher than other methods, thus increasing the statistical sensitivity and the value of N.

2.3.1 Production, Storage and Properties of UCN in HE-II

The process of UCN production by down-scattering in superfluid helium was first described by Golub and Pendlebury in 1975 [65] [66], known as the "Superthermal UCN Production Method".

At low energies neutrons lose energy when entering a superfluid with the creation of phonons, while at higher energies the ^{4}He excitations are rotons. The Feynman-Landau phonon-roton dispersion curve, shown in Figure 2.5, describes the energy-momentum relationship of the quasiparticles in the superfluid helium. The energy of the excitations in the superfluid are plotted in blue versus their momentum. The linear part of this corresponds to phonons and the minimum at higher-k to rotons. The dispersion relation for free neutrons is shown on the same plot in red, a parabolic function in wavevector Q, which intersects the superfluid phonon curve at $Q = 0.7$ Å^{-1}. Exchange of energy and momentum between a free neutron and a single phonon in the superfluid can take place only at the intersection point of the two dispersion curves, i.e., only neutrons at a wavelength of 8.9 Å ($Q = 0.7$ Å^{-1} $E =$ 1 meV $T = 12$ K) can be transformed into the UCN energy range (mK) by single phonon emission [93].

ILL provides cryoEDM with a cold neutron beam, which has a low energy tail of UCN. However the number of UCN in this beam is quite small, and not sufficient for the UCN densities desired for a highly sensitive nEDM measurement. Therefore, the superthermal UCN production method offers an efficient method of getting high UCN densities. To make use of this method the volume must be cooled below 0.7 K at least, this ensures that the thermal population of phonons is not large enough to scatter a significant number of UCN back to higher energies, at which they would no longer be storable. The probability of this thermal up-scattering process is proportional to the Boltzman factor $e^{-\Delta E/T}$ and is highly suppressed as the change in neutron energy Δ E = 12 K is much larger than the superfluid temperature, 0.7 K. This is illustrated in Figure 2.6, where the UCN storage time is plotted as a function of temperature. There is a sharp rise in storage time below 0.7 K where the phonon up-scattering of UCN is no longer dominant. The cryoEDM cryostat cools the

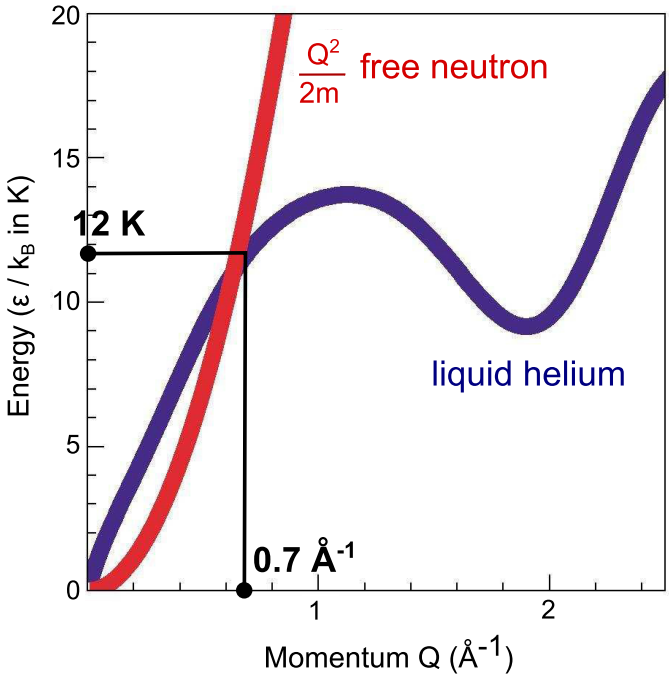

Figure 2.5: Dispersion curves for superfluid ^{4}He (blue) and free neutrons (red) ($E = h^2k^2/2m$). At the temperature and pressure of cryoEDM these intersect at the point where a neutron's wavelength is approximately 9 Å. Therefore it is possible that neutrons with this momentum can produce a single 12 K phonon with the same energy and momentum, scattering to very low energies, in the mK range (equivalent to ∼100 neV).

apparatus to ∼500 mK, below the temperature threshold for UCN storage of 0.7 K.

Golub and Pendlebury noted three further features of ^{4}He which make it ideal as a medium for UCN production and storage: it has zero neutron absorption cross section; its critical energy for total reflection is about 10 times smaller than that of most of the common wall materials; As a boson with zero magnetic moment, ^{4}He scatters neutrons in a purely coherent manner and the initial UCN polarisation is preserved.

ILL provides cryoEDM with a 9 Å cold neutron beam with a flux of $\mathcal{O}(10^7$ n cm^{-2} s$^{-1})$. Cold neutrons are those with energies lower than thermal neutrons, $E < 25$ meV. Ultra cold neutrons are defined as neutrons which can be stored in bottles of certain materials. The energies, velocities and wavelength of these neutrons are given in Table 2.1.

The cold neutrons are polarised before entering the superfluid volume and before down-scattering to UCN. The strong nuclear interaction is spin dependant, and by using a magnetisable material in a very strong magnetic field, the two spin states of neutron will experience

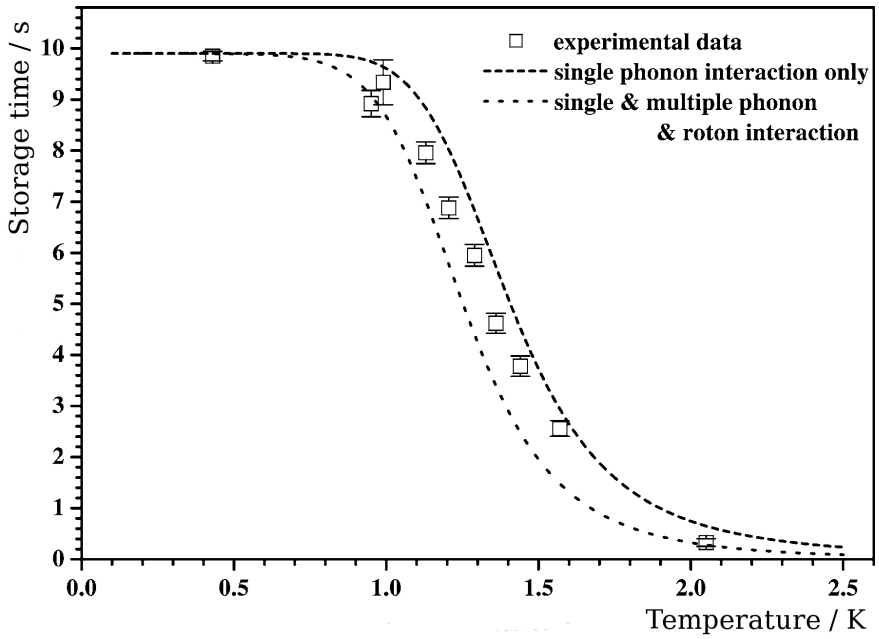

Figure 2.6: The storage time of UCN as a function of temperature. Below 0.7 K the storage time is flat, above this temperature the storage time drops to zero. This is the reason cryoEDM must be operated below 0.7 K [67]. Losses due to UCN interactions with impurities on the walls causes the storage time to top out at 10 s in this case.

	Energy	Velocity (m/s)	Wavelength (Å)	Temperature
Thermal	25 meV	2200	1.8	290 K
Cold	300 neV – 25 meV	7.65 – 2200	520 – 1.8	3 mK – 290 K
UCN	<300 neV	<7.65	>520	<3 mK

Table 2.1: Neutron energy, velocity, wavelength and temperature ranges.

a significantly different potential barrier. This allows cold neutrons of one polarisation to be reflected from the material and the other to escape. The polariser in cryoEDM is about 3 m long and made of successive layers of magnetised iron and silicon. The Fe layers are not perfectly magnetically saturated, resulting in the polarisation efficiency of a single layer to about 90%. Multiple layers sandwiched with Si result in the neutron polarisation at the exit to be 95%.

UCN reflection by materials is caused by the coherent strong interaction of the neutron with atomic nuclei. It can be quantum-mechanically described by an effective potential which is commonly referred to as the *Fermi Potential*, V_F. The corresponding velocity is called the critical velocity, v_c, of a material. Ultra cold neutrons have long wavelengths, much longer than the range of the potential well of the nuclei of the material, and thus are scattered.

A detailed quantum mechanical approach to this scattering is given in [91]. Neutrons are reflected from a surface if the velocity component normal to the reflecting surface is less than or equal to the critical velocity. As the Fermi potential of most storage materials is below 300 neV, the kinetic energy of incident neutrons must not be higher than this value to be reflected under any angle of incidence, especially for normal incidence. The kinetic energy of 300 neV corresponds to a maximum velocity of 7.6 m/s or a minimum wavelength of 52 nm. Only materials with a Fermi potential of ∼250 neV or higher can be used to store UCN. The Fermi potentials of some commonly used materials are given in Table 2.2.

Material	V_F (neV)	v_c (m/s)
Beryllium	252	6.89
BeO	261	6.99
Nickel	252	6.84
Diamond	304	7.65
Graphite	180	5.47
Iron	210	6.10
Copper	168	5.66
Aluminium	54	3.24

Table 2.2: Fermi potential and critical velocity for some common materials.

Some other properties of UCN are that they can be described as a very thin ideal gas with a temperature of 3.5 mK, due to their low density, and the influence of gravity is significant, as a result of their low kinetic energy. Thus, the trajectories are parabolic and the kinetic energy of UCN can be transformed into potential (height) energy with ∼102 neV/m. The magnetic moment of the neutron, produced by its spin, interacts with magnetic fields. The total energy changes by ∼60 neV/T. Modelling of the UCN properties in cryoEDM has been performed in [94].

2.3.2 The CryoEDM Apparatus

A schematic diagram of the cryoEDM apparatus was presented in Figure 2.1, with the locations of all the various subsystems of the experiment marked.

UCN Production

The UCN source is on the right of the figure. The polarised cold neutron beam enters the superfluid helium volume (1.) and production of UCN begins (2.). UCN are trapped by Copper-Berylium guidetubes and any remaining cold neutrons which do not down-scatter are not contained in the volume and leave the volume at the far end. The production is monitored with a detector in the base of the source volume. Once the source has achieved the required UCN density, the source valve is opened, and the UCN diffuse into the main section of the experiment (3.), all filled with superfluid helium. The source valve is closed and the source refilling process begins again for the next batch of UCN.

Cryogenics

All the volumes in which the neutrons move are filled with superfluid ^{4}He at $\sim$500 mK. This is done with a ^{3}He cryostat cooling approximately 50 litres of isotopically pure superfluid ^{4}He (marked Tower 1 on Figure 2.1), to fill the source volume, several guide sections, the Ramsey Cell, and the large superfluid containment vessel (SCV) surrounding the cells. The ^{3}He isotopes are removed from the liquid helium using a method known as superleaks, which utilises the fact that the point at which ^{4}He turns to superfluid (T= 2.17 K) is above that which ^{3}He turns to superfluid (T = 2.5 mK) [95].

Storage

Once leaving the source volume, the CuBe guidetubes guide the UCN to the Ramsey Cells, which is the heart of the experiment, where the resonance process takes place (4.). The Ramsey Cells consist of two 250 mm diameter ceramic cylinders with pure beryllium electrodes acting as end caps, separated by 45 mm. Each cell is capable of storing the UCN for hundreds of seconds during a measurement. Each cell is exposed to the same magnetic field, but with different electric fields applied across them (+E, 0, or -E) to reduce systematic uncertainties. The measurement assembly is held in a container known as the superfluid

containment vessel (SCV). R&D is ongoing to produce the most suitable SCV which is superfluid tight, mechanically robust and free from magnetic inhomogeneities.

Magnetic Field

Surrounding the SCV is the superconducting solenoid. This is a NbTi magnet which is cooled by concentric liquid helium and liquid nitrogen canisters. It provides the main static magnetic field, B_0. The experiment requires a spatially homogeneous and temporally stable magnetic field parallel to the symmetry axis of the apparatus with no radial or azimuthal components. The stored UCN will sample all parts of the Ramsey cells and hence any spatial inhomogeneities will result in different precession frequencies in different parts of the cells. This in turn leads to a dephasing of the neutrons during the free precession part of the Ramsey cycle. The AC magnetic field is produced by two pairs of coils on a carbon fibre former outside the SCV but inside the solenoid. For a $\sim \mu$T static field, the resonance frequency is around 145 Hz.

Surrounding the solenoid is a cylindrical superconducting lead shield, that provides dynamic shielding against external field perturbations. Flux penetration through the lead is approximately zero due to the Meissner effect. It is 2.68 m long and coaxial with the experimental volume. The final layer of shielding is provides by an almost 4π coverage of the experimental volume with three layers of high magnetic permeability mu-metal. Stray magnetic field lines travel though this material more favourably than into the experimental volume. Outside this shielded region, the neutrons are subject to external magnetic field from the environment. Given cryoEDM is located in an active neutron scattering laboratory, there are plenty of large magnetic fields generated by neighbouring experiments. To preserve the neutron polarisation from the source to the shielded region, and after the resonance process as they travel to the detectors, there are a set of guide field coils at intervals along the guides. Details of the magnetic systems are provided in [96].

Magnetometry

Monitoring the magnetic environment is crucial. The false EDM induced by a change in the magnetic field during a measurement is given by

$$\sigma(d_n) = \frac{\mu_n \sigma(B)}{2E} \tag{2.19}$$

where μ_n is the magnetic moment of the neutron and $\sigma(B)$ are the fluctuations in the magnetic field. This will dominate the counting statistics when

$$\sigma(B) > \frac{\hbar}{\mu_n \alpha T \sqrt{N}} \tag{2.20}$$

For the expected values $\alpha = 0.9$, T = 300 s, and N = 4.5×10^5 this is approximately 60 fT. The magnetic field stability must be significantly below this for the experiment to be limited by neutron statistics. The magnetic shielding goes a long way to providing homogeneity, but some temporal variation will still exist. The temporal variation in magnetic field can be monitored and the Ramsey resonance data corrected for any shift in field. The experiment uses two types of magnetometers for diagnostics, SQUIDs and fluxgates. The ^{199}Hg co-magnetometer in the room temperature nEDM experiment described in Section 1.3.3 could not operate in the cryogenic environment of cryoEDM, and so a new system was developed.

Fluxgates are magnetometers that can operate in cryogenic temperatures and have resolutions of the order 0.1 nT [97], which is insufficient for the needs of the experiment. Therefore they do not operate as the primary magnetometer for the Ramsey Cell region, but as a diagnostic tool for various parts of the experiment. Superconducting Quantum Interference Devices (SQUIDs) are magnetometers based on a superconducting loop containing Josephson Junctions that measure extremely small magnetic field changes. They have been shown to have resolutions as good as 0.3 fT Hz$^{-\frac{1}{2}}$ [98]. As SQUID sensors measures the flux only through its sensing region, multiple SQUIDs are required to sample the field enough to give a good spatial resolution. The sensing regions are loops of superconducting wire and so

many can be accommodated in the experimental volume. These so-called "pick-up loops" are mounted in various regions in the SCV to measure the magnetic field and magnetic field gradient, and extrapolate it to the Ramsey Cell region. The magnetometry system is the responsibility of the Oxford group, and significant work has gone into developing a stable, reliable and sensitive system within the constraints of the experiment. A detailed discussion of magnetometry for cryoEDM is available in [99].

Electric Field

The UCN in the Ramsey cell must be exposed to as high electric field as possible to achieve maximal sensitivity to d_n. An electric field of 40 kV cm^{-1} is applied to the beryllium electrodes of the Ramsey Cell. A retractable HV feedthrough connects an external room temperature high voltage supply to the Ramsey Cell electrode. The development of the high voltage system is discussed in [100] along with the study of high voltage breakdown in liquid helium.

Neutron Detection

Finally, after going through the resonance process in the Ramsey cells, the valve to the cells is opened and they are emptied (5.). The neutrons diffuse along the guidetube and a valve allows them to travel to a vertical quartz guidetube (6.) which contains a spin-flipping solenoid, a spin analyser and neutron detectors. The analyser consists of a magnetised iron layer, which decreases the material's potential barrier for aligned spins allowing them to pass through to the detector (7.). The potential barrier for anti-aligned spins is increased by the magnetised iron, and so these are rejected and scattered back into the volume. The detectors are purpose built lithium coated cryogenic silicon detectors [101] [102]. An incoming neutron reacts with the lithium layer through the reaction $^6Li + n \rightarrow {}^4He + {}^3H$. Either the α particle or triton reaction products can enter the silicon causing an ionisation current. This current, the output of the detector, is read through a multi-channel analyser. CryoEDM has had two detector configurations during its development. One large detector with a spin analysing Fe layer counts all neutrons in the spin up state. Once this state has been measured, the spin-

down state is then flipped using the spin flipping solenoid and passed through the analyser again to count their numbers. The other configuration consists of having an open detector with no Fe layer to count spin up and spin down neutrons, as well as a detector with the magnetised Fe layer which counts only spin up neutrons. These detectors are discussed at length in Chapter 3 and the bulk of the work in this thesis concerns the development of detectors.

2.4 Sensitivity

Extracting a value for the EDM is in principle simple: A straight line fit to the corrected frequency as a function of the applied electric field E yields a gradient that is directly proportional to the EDM. As either a precision-measurement experiment, or, in the absence of a signal, a limit-setting experiment, the uncertainty is of great importance, both statistical and systematic.

2.4.1 Statistical Uncertainties

The statistical uncertainty on d_n was given in Eq. (2.18) as:

$$\sigma_{d_n} = \frac{\hbar}{2\alpha E T\sqrt{N}}$$

It is inversely proportional to the visibility of polarisation α, the magnitude of the E field applied across the Ramsey cells and the free precession time T during the Ramsey resonance. The design of the experiment has been done with maximising this parameters in mind.

The larger electric field that can be sustained in liquid helium than in vacuum brings an improvement in sensitivity of cryoEDM over the room temperature nEDM experiment of a factor of 4. The electric field in cryoEDM is expected to be at least 40 kV cm^{-1}.

Ultimately the measurement time T is limited by the lime time of the UCN by β decay, $n \rightarrow p + e + \bar{\nu_e} + 782$ keV, which has a half-life of $\tau_\beta = 886.3 \pm 1.2$ (stat) $\pm$ 3.2 (sys) s [103].

However in practice, there are other significant factors which lead to neutron losses. In particular, surface contamination by hydrogen, in the form of water molecules or otherwise, is problematic and must be minimised as this has a large neutron capture cross section and also causes inelastic up-scattering. The operation of the experiment at cryogenic temperatures significantly decreases the likelihood of up-scattering. The improved lifetime of the neutrons to 260 s (from 130 s in the room temperature experiment) when stored in cryogenic conditions, is expected to produce an improvement in sensitivity over the room temperature experiment of a factor of 2.

The polarisation visibility parameter α is essentially a measure of how well the polarisation of the neutrons has been produced and maintained throughout the experiment. The operation of the superconducting magnetic shield improves the stability of the magnetic environment and is expected to produce an improvement in sensitivity over the room temperature experiment of a factor of 2.

The statistical sensitivity is inversely proportional to the square root of the number of neutrons counted in the resonance. Significant improvement on UCN production has been made in cryoEDM by comparison to the previous room temperature experiment. This has increased the number of neutrons per batch from 14,000 to 140,000 thus improving the sensitivity by a factor of $\mathcal{O}(\sqrt{10})$.

Of course, with the high density of neutrons being used in the experiment, must come a high performance neutron detector. The number of neutrons counted is given by

$$N = \epsilon N_{guide} \tag{2.21}$$

where ϵ is the efficiency of the detection system, and N_{guide} is the number of neutrons entering the detection guidetube. It is therefore essential to have the detection efficiency as close to 1 as possible to take advantage of all the neutrons that have been produced and guided through the measurement system. The statistical uncertainty on d_n is proportional to $\sqrt{\epsilon}$. The ^{6}Li coated Si detectors in use currently show an efficiency of only 41% and so this is an

area where improvements could be made to gain a factor of up to $\sqrt{2.4}$ in sensitivity. The investigation into alternative detectors with an eye to improving detection efficiency is the focus of this thesis.

2.4.2 Systematic Uncertainties

The possibility of detecting a false EDM due to systematic effects has been studied at length and taken into account in the design of cryoEDM. Many of the systematic effects known in the room temperature nEDM experiment and previous experiments will also exist in cryoEDM. The most serious are those which are correlated with the direction of the electric field and can escape the precaution of cancellation by the separated Ramsey cells and symmetric operating points discussed in Section 2.2.1.

However there are many constant systematic uncertainties that can be removed if the EDM is deduced from the quantity

$$\hbar(\omega_{\uparrow\uparrow} - \omega_{\uparrow\downarrow}) = |2\mu_n|(B_{0\uparrow\uparrow} - B_{0\uparrow\downarrow}) - 4d_nE \tag{2.22}$$

where $\omega_{\uparrow\uparrow}$ and $\omega_{\uparrow\downarrow}$ are the precession frequencies of the neutrons observed with the magnetic and electric fields aligned and anti-aligned respectively, and $B_{0\uparrow\uparrow}$ and $B_{0\uparrow\downarrow}$ are the modulus of magnetic fields applied to the neutrons when the magnetic and electric fields aligned and anti-aligned respectively. In the notation given, the relative alignment of the magnetic and electric fields is averaged over both combination of field orientations that produce it, i.e. $\uparrow\uparrow$ is the average of $\uparrow\uparrow$ and $\downarrow\downarrow$, and $\uparrow\downarrow$ is the average of $\uparrow\downarrow$ and $\downarrow\uparrow$.

The expected systematic effects have been well studied in the lifetime of this experiment and are considered manageable.

$v \times E$ Effect: In considering the motion of a particle through a background electric field, it is important to take account of the fact that it is experiencing both electric and magnetic

fields. The Lorentz transformation of these fields to the moving reference frame is given by

$$\begin{aligned}\vec{B}' &= \gamma\left(\frac{\vec{B}-\vec{v}\times\vec{E}}{c^2}\right) - \frac{\gamma^2}{c^2(\gamma+1)}\vec{v}(\vec{v}\cdot\vec{B}) \\ &\approx \vec{B} - \frac{\vec{v}\times\vec{E}}{c^2}\end{aligned} \tag{2.23}$$

Systematic effects can arise if the background magnetic field, electric field and $v \times E$ field have components that are at right angles to one another. This may arise if the fields are not perfectly aligned, and extra terms can arise inducing first and second order effects in $v \times E$. The cross product of $v \times E$ will produce a magnetic field with a non-zero component along the axis of the E field, which changes with the polarity of E and change the neutrons precession frequency. The extra contribution to the B-field seen by the neutrons will result in a frequency shift ($\delta v \propto \delta B'$) directly proportional to the applied electric field. Simulations have shown that this effect can be minimised to $\sim 2 \times 10^{-28}$ e $\cdot$ cm [104].

Geometric Phase Effect: The combination of the $v \times E$ effect and of a non-zero axial gradient in the background field B_0 can result in a rotating magnetic field in the neutron's reference frame. The interaction of the neutrons with this field is complicated and is treated fully in [104]. The resulting false EDM with expected magnetic gradients of 3 nT m^{-1}, a false EDM of 2.4×10^{-27} e $\cdot$ cm . would be produced. This is unacceptably large and sets of coils are placed around the experimental volume designed to trim the field such that the gradients are as low as 0.1 nT m^{-1}. This leads to a false EDM of 8×10^{-29} e $\cdot$ cm with the magnetic field trimmed.

High voltage ripple: The high voltage generator used to create the electric field across the experiment is produced by a Cockroft-Walton generator, driven with an AC voltage at 10 kHz. The driving voltage is generated from the mains supply, which operates at 50 Hz. If a small fraction of either of these frequencies were transmitted through the generator, they would cause a ripple on the otherwise DC voltage. This would cause an AC magnetic field perpendicular to the static B and E field, creating a shift in the Larmor frequency. A 0.6

% ripple in the high voltage on the 10 kHz frequency would cause a false EDM signal of 1×10^{-28} e $\cdot$ cm to be observed. A 0.08 % ripple on the 50 Hz frequency would cause a false EDM signal of 1×10^{-28} e $\cdot$ cm to be observed [99]. The specification of the HV supply is better than this requirement.

Leakage currents: Leakage currents from the HV stack that flow on the surface or through the material of the storage cells are a potentially significant source of spurious signals as they would produce magnetic fields which are correlated with the background electric field. Axial currents do not contribute to a spurious EDM signal. Azimuthal currents, on the other hand, can create a magnetic field component parallel to B_0 and therefore give a false EDM signal, by changing the neutron's precession frequency. Such effects can be sought by looking for correlations between the EDM signal and the measured stack leakage and a correction applied.

2.5 UCN Detectors

In the room temperature nEDM experiment, the neutrons were detected with a proportional counter containing ^{3}He, in which the neutrons were detected via the reaction $n + {}^3He \rightarrow {}^3H + p$ which releases 764 keV of energy, detected as an ionisation signal. This detector requires a window of 100 μm aluminium foil. The efficiency of the detector was about 80% for UCN. Such a detector is not compatible with cryogenic use- while the ^{3}He reaction still holds with liquid ^{3}He, the principle of proportional gas counters does not. Furthermore, a mechanically robust window to operate in a cryogenic environment would be significantly thicker than 100 μm, resulting in significant UCN loss.

The collaboration designed solid state UCN detectors that are more suited to the environment, as were described briefly in Section 2.3.2. While they offer an elegant solution to the significant experimental constraints of cryoEDM, the silicon sensors have shown a large background signal, obscuring the α peak from the reaction $n + {}^6Li \rightarrow {}^4He + {}^3H$. This

has reduced their operating efficiency to 41%. Efforts are in motion to improve this with improved shielding, electrical noise reduction and other background suppression techniques. However in parallel, this thesis is an in-depth investigation of alternative methods of detecting UCN within the constraints of the cryoEDM experiment and whether other technology could provide a more efficient detection system.

Chapter 3

UCN Detection for CryoEDM

High efficiency detection of ultra cold neutrons in cryoEDM is a key element to maximising the sensitivity of the experiment. As non-ionising particles, low energy neutrons cannot be detected using the usual methods employed for ionising particle detection. Instead detectors typically make use of neutron capturing processes, which emit ionising reaction products that can be readily detected. The very low energy of UCN make them ideal candidates for a capture processes, as the capture cross section is extremely high at low energy. The challenge lies in operating a detector in a superfluid helium environment, at cryogenic temperatures within the constraints of the cryoEDM apparatus.

This chapter will give an overview of neutron detection methods and UCN detection in particular. The solid state silicon detectors designed for cryoEDM that are currently operational in the experiment are discussed- their strengths, and shortcomings, and the motivation behind the investigation of alternative methods of UCN detection. The experimental requirements in a UCN detector for cryoEDM are outlined and finally a review is made of potential technology that may be developed for use in this experiment and cryogenic nEDM experiments in general, and which are researched further in this thesis.

3.1 Overview of UCN Detection

UCN detectors use the same methods as thermal neutron detectors. Most commonly, they make use of the absorption reactions ^{3}He(n, p)^{3}H or ^{10}B(n, α)^{7}Li in a ^{3}He or BF_3 gas filled proportional counter. The absorption cross sections of these nuclides are high for low energy neutrons (below about 0.5 eV), and these gas counters have minimal sensitivity to γ particle background due to their low density. While the neutrons themselves do not cause ionisation in materials, the high energy ionising reaction products do, and are measured via their ionisation tracks in a gas proportional counter. Information on the captured neutron's energy is not contained in the reaction products' energy, or other properties. The absorption reactions of interest are:

$$^3_2He + ^1_0n \rightarrow ^3_1H\,(0.191\,MeV) + ^1_1p\,(0.573\,MeV) \qquad (\sigma = 5330\,b) \tag{3.1}$$

$$^{10}_5B + ^1_0n \rightarrow ^7_3Li^*\,(0.84\,MeV) + ^4_2\alpha\,(1.47\,MeV) \qquad (\sigma = 3840\,b) \tag{3.2}$$

$$^6_3Li + ^1_0n \rightarrow ^3_1H\,(2.73\,MeV) + ^4_2\alpha\,(2.05\,MeV) \qquad (\sigma = 940\,b) \tag{3.3}$$

where σ is the thermal neutron cross section for the reaction.

The choice of absorption reaction is influenced by the cross section, the energy emitted by the reaction and the natural abundance, or ease of enrichment, of the given nuclide. A typical BF_3 gas filled proportional tube can be optimised with ^{10}B enrichment and with suitable density and geometry to produce over 90% neutron detection efficiency at thermal neutron energies (0.025 eV) [105]. They have a low stopping power for γ rays or high energy electrons produced by γ, due to the relatively low atomic mass and density, and thus low sensitivity to γ background. ^{3}He is also used in proportional gas counters. It has a huge neutron capture cross section, however because of their lower atomic mass, the ranges of the reaction products are relatively long. There is then an optimisation trade-off between increasing the size of the counter and therefore in detection efficiency versus the cost. The lower energy reaction products of ^{3}He make discrimination more difficult than in a BF_3

detector, as the products' pulse height may of similar size to the γ background, and so is more difficult to separate in a spectrum. Furthermore, there is an increasing move away from ^{3}He due the high cost and global supply shortage.

Unfortunately gas counters are unsuitable for application in cryoEDM, as the detector must function in-situ within a cryogenic environment. It is at an operating temperature of less than 1 K, where the compounds are no longer gaseous and the principle of detection no longer applies. They also need windows to contain the mixture, which then restrict their efficiency and use, as windows can cause large neutron losses at UCN energies. Of course, ^{3}He is liquid at 0.5 K, and there is ongoing research in other collaborations as to how to exploit this as a cryogenic UCN detector [106]. When a UCN is captured by a ^{3}He nucleon in the superfluid helium, the reaction products, a proton and a tritium, create ionisation in the superfluid helium, which causes the helium to emit UV scintillation light, emitting the equivalent of 22 photons / keV, at 80 nm. The transport and detection of extreme ultra violet (EUV) photons is challenging as traditional optics cannot be used, and they must be wavelength shifted. The integration of such a technology would involve significant redesign of the cryoEDM apparatus, and so has not been a focus of this research.

None the less, absorption reactions can still be exploited, as long as the technology used to count the reaction products is compatible with cryoEDM in solid state form at 0.7 K. ^{3}He is a noble gas, so no solid compounds can be fabricated. However boron can be made into solid state layers and thus exploited with a different technology. Furthermore, the absorption reaction ^{6}Li(n, α)^{3}H is sensitive to neutrons, and while lithium is not available in any stable gaseous compound for proportional counters, it is available in stable solid compounds.

While the ^{6}Li capture cross section is much lower than for ^{10}Bo (σ = 3840 b) or ^{3}He (σ = 5330 b), the reaction products have a much higher energy, offering a real advantage where discrimination against γ rays is concerned. ^{6}Li can be incorporated in crystalline compounds LiI or LiF, and a crystal of suitable size and density of enriched ^{6}LiI has essentially 100% neutron conversion efficiency for neutrons of thermal energies and below [105].

One of the main differences between UCN detection and detection of higher energy neu-

trons is accounting for the Fermi Potential, V_F, for UCN, as was described in Section 2.3.1. The Fermi Potential of a given material must be low enough to allow the passage of UCN when considering it as a detector material. Another major difference is that absorption cross section for these capture cross sections goes from $\mathcal{O}$(kb) to $\mathcal{O}$(Mb) for UCN. Advantageously, a small amount of detection material is sufficient for UCN capture and thus the thickness of a detector can be small. This has the added convenience of reducing background sensitivity to γ rays and high energy neutrons.

Either the ^{10}B or ^{6}Li reactions may be exploited at low temperature in conjunction with a solid-state detector. In this case, a thin film of the absorbing material, e.g. ^{6}LiF, is deposited on a charged particle detector, and the charged decay products, for example, the α particle (2.05 MeV) and the triton (2.73 MeV), are detected. The current cryoEDM detectors exploit this ^{6}Li reaction in conjunction with a silicon charged particle detector and their development and performance are described further in the following section. An overview of various solid state neutron detector technology is given in Section 3.4.

3.2 Solid State Detectors in CryoEDM

The UCN detectors currently in use in cryoEDM are ORTEC ULTRA ion implanted silicon detectors, designed for α spectroscopy [107]. These are a silicon p–n diode, with an ion implanted Boron p-type layer and Arsenic n-type layer. They have been modified by the cryoEDM collaboration with the deposition of a ^{6}LiF neutron conversion layer, thus operating as surface barrier charged particle detectors. A thin film of ^{6}LiF of surface density 600 μg cm^{-2} has been deposited onto the Si wafer by sputtering, so that the charged products of the ^{6}Li reaction given in Eq. (3.3), namely the α particle and the triton, are identified as an ionisation signal in the silicon detector. The R&D program for developing these detectors optimised the deposition thickness to obtain a maximum UCN detection efficiency of 85% at room temperature [101]. This layer can be kept very thin due to the large capture cross section of ^{6}Li (940 barns for 25 meV thermal neutrons [108] and $\mathcal{O}$(Mb) for UCN [101]). The

layer must also be thin enough to allow the escape of the α particle and triton, which have a range of $\sim$1.5 mg cm^{-2} and $\sim$7.8 mg cm^{-2} in LiF respectively. On top of this, a coating of iron of thickness 1500 Å has been deposited for polarisation analysis. The iron atoms in this layer are magnetically polarised by a permanent magnet in order to allow the passage of only one spin polarisation.

The ionisation signal in the silicon diode produces a voltage pulse signal whose magnitude is proportional to the energy deposited. The α and triton particles are emitted back to back and isotropically, but due to the thin film nature of the ^{6}Li layer, only one of the charged particles enter the detecting bulk below, stopping in less than 1 mm and creating an ionisation signal. This process is illustrated in Figure 3.1. A pulse height spectrum will then show two peaks corresponding to the 2.05 MeV α and 2.75 MeV triton. For 100% efficiency, the particle counts in both peaks in the spectrum must be measured in entirety. Tests at room temperature have shown a 300 mm^2 detector, with 600 μg cm^{-2} ^{6}LiF evaporated directly onto the active silicon face, to have 82% UCN counting efficiency relative to a ^{3}He gas counter with a 100 μm aluminium entrance window, which has an efficiency close to 100% [101]. This was for UCN in the 230 – 300 neV energy range.

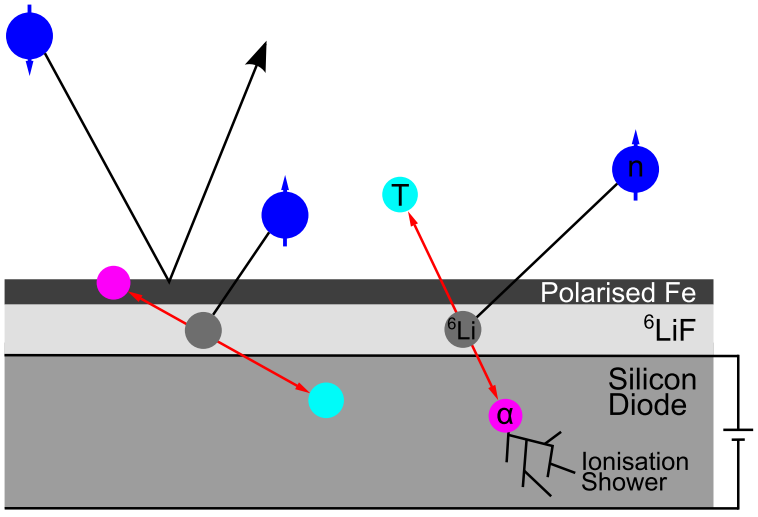

Figure 3.1: Schematic diagram of the detection of neutrons by the ^{6}LiF thin film Silicon Diode detectors. Polarised Fe allows only one spin state of neutron to pass, which is then captured by a ^{6}Li nucleus in the LiF layer. The reaction products, triton and α, are emitted back to back isotropically, with one entering the silicon detector and producing an ionisation signal.

The spin polarisation of the UCN can be analysed by measuring the transmission through,

or reflection from, a magnetically aligned iron layer. The technique is described in [89]. This is carried out with the use of two different detector configurations. One detector has a magnetically aligned iron layer deposited on top, which is achieved with a permanent magnet of ∼60 mT. This counts, say the spin up states, $N_{\Uparrow}$. Another detector does not have an iron layer and detects neutrons of both polarisations, acting as a normalisation standard. This counts $N_{\Uparrow} + N_{\Downarrow}$. $N_{\Downarrow}$ is then the difference between these detector counts. The polarisation can then be calculated as

$$P = \frac{N_{\Uparrow} - N_{\Downarrow}}{N_{\Uparrow} + N_{\Downarrow}} \tag{3.4}$$

The value of the neutron EDM, d_n, can then be calculated according to Eq. (2.14), with the value for the total number of neutrons in both spin states in both field alignments given by $N = (N_{\Uparrow} + N_{\Downarrow})_{\uparrow\uparrow} + (N_{\Uparrow} + N_{\Downarrow})_{\uparrow\downarrow}$, where $\Uparrow$ represents spin orientation and $\uparrow\uparrow$ represents E and B field alignment. The uncertainty of the neutron EDM, $\sigma(d_n)$, is calculated from Eq. (2.18), with the same value of N. It is clear from Eq. (2.14) and Eq. (2.18) that the neutron count must be maximised for increased sensitivity to d_n. Considerable effort has gone into producing a source with as high UCN numbers as possible, as was discussed in Section 2.3.1. A process of R&D was carried out to develop these detectors for cryoEDM in the early stages of the experiment, with ^{10}Bo and ^{6}Li conversion layers of different thickness tested [101] and optimised for use at low temperature [102]. The ORTEC silicon detector is readily available commercially, easily modified for neutron sensitivity and easy to install in the cryoEDM apparatus.

Unfortunately, upon cooling to cryogenic temperatures, the signal is reduced, and the α peak in the pulse height spectrum is not visible under noise and background signal, with only the triton peak clearly visible and available for neutron counting. This means the 82% detection efficiency reported at room temperature is now reduced to 41%, this halving causing a factor of $\sqrt{2}$ reduction in nEDM sensitivity according to Eq. (2.18). Furthermore, the detectors have not survived multiple cycling from room temperature to liquid helium temperature. Silicon detectors are also susceptible to radiation damage over time which inhibits their charge collection and degrades their energy resolution [101].

Although the detectors function sufficiently to count UCN, and have been satisfactory during the development phase of the experiment, one would prefer to have as high a neutron counting efficiency as possibly during the exploitation phase of the experiment. While a program of research continues to try to improve the performance of the silicon detectors, the research described in this thesis has been carried out in parallel, to determine if there are other feasible technologies for UCN detection in cryoEDM, which may result in a higher detection efficiency.

3.2.1 Performance

Multiple sizes of detector with varying iron layer configurations have been produced and installed in cryoEDM over the development of the experiment, some are pictured in Figure 3.2. In the Autumn 2010 run, there were six ORTEC detectors installed in the apparatus. Two small area detectors acted as flux monitoring detectors within the source tube section of the experiment, and were of $\sim$100 mm^2 surface area. These detected both cold and ultra cold neutrons coming through a 3 mm diameter hole in the bottom of the source volume.

Figure 3.2: Various configurations of ^{6}LiF Silicon UCN detectors developed for cryoEDM. The configuration on the right of four detectors, two with magnetised iron foils, and two open, was installed in 2010. The large size detector (left) and the three small detectors (centre) have been investigated in earlier experimental runs.

Four further detectors of 900 mm^2 active surface area were mounted on a single CF100 flange, as on the photograph on the right hand side Figure 3.2. This is placed on the bottom

of a vertical 70 mm diameter cylindrical quartz guide tube as illustrated in Figure 3.3 and previously described in Section 2.3.2 and Figure 2.1. Two of these were intended to see UCN of both spin states while another two had a 1500 Å iron foil on top of the ^{6}LiF film. This foil was magnetised by a permanent yoke magnet to allow the passage of only one spin direction neutrons, that opposite to the initial spin state of the cold neutrons upon entering the superfluid UCN source, as outlined in Section 2.3.1. Thus one spin state, say $N_{\Uparrow}$, is measured by the iron covered detectors, and the other, say $N_{\Downarrow}$, is measured by the difference in signal between the open and covered detectors.

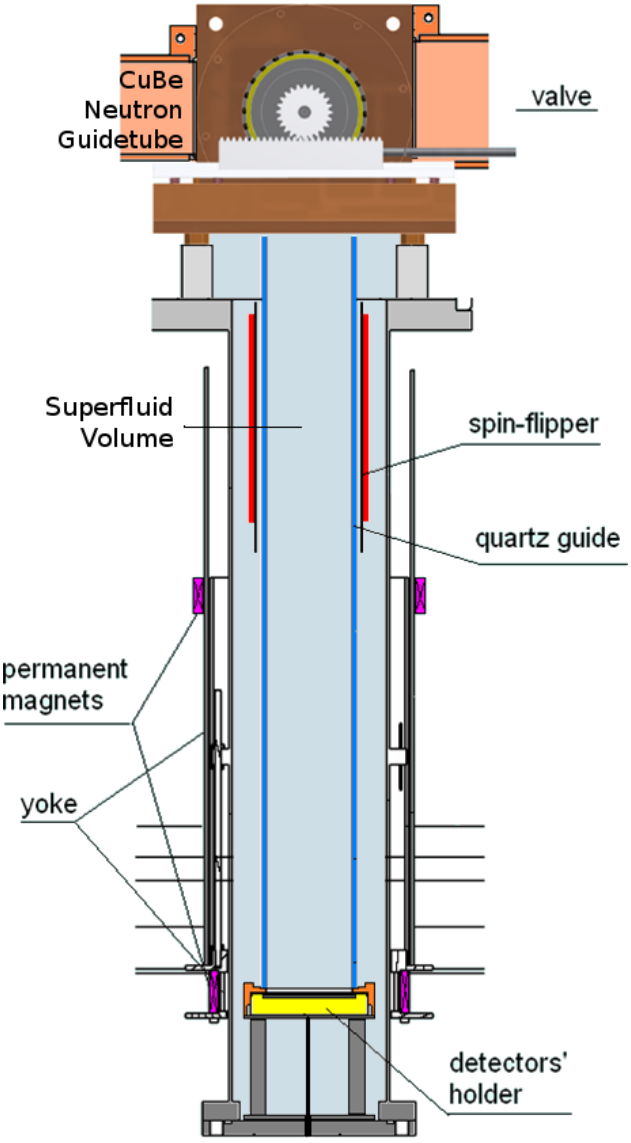

Figure 3.3: Schematic of the UCN detectors and guidetube under the transfer section, showing the layout of the detectors, magnet, spin-flipper and guidetubes.

The voltage pulses from the detectors are amplified and sent to a Multi-Channel Scalar (MCS) and a Multi-Channel Analyser (MCA), counting the number of pulses and pulse height, and recorded.

The room temperature spectra as optimised during the original detector R&D in [101] are shown in Figure 3.4. The thickness of the ^{6}LiF layer was investigated, and the final chosen thickness was 600 μg cm^{-2}. The thicker layers show widening of the peaks and a movement to lower detected energy. The reaction products have to penetrate a larger layer of converter and thus are subject to scattering and energy loss before detection in the silicon. The α peak is much wider and poorer resolution than the triton peak, as well

as being at half the detected energy. As α particles lose energy at a higher rate than tritons, their range is shorter.

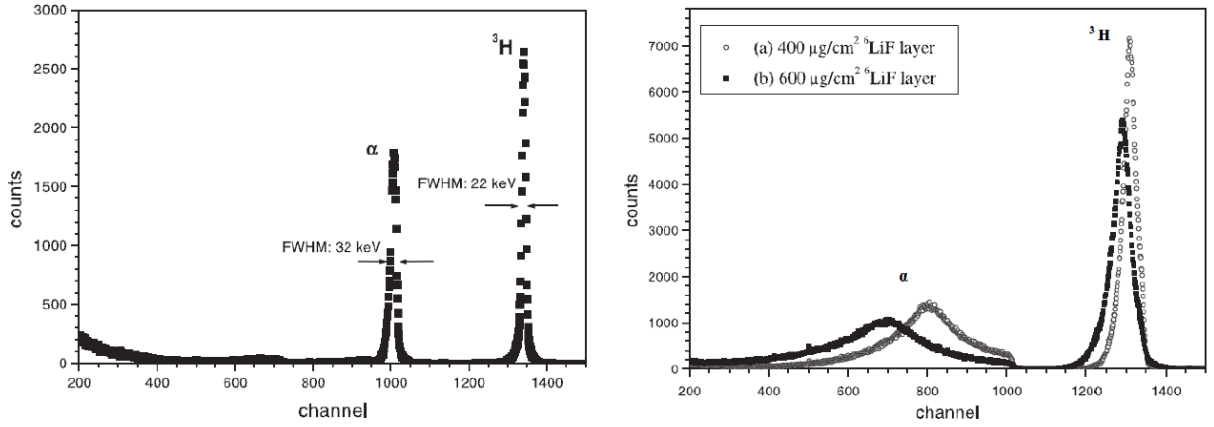

(a) 10 $\mu g/cm^2$ ^{6}LiF converter

(b) 400 and 600 $\mu g/cm^2$ ^{6}LiF converter

Figure 3.4: Neutron-generated pulse height spectra from ORTEC silicon detectors with ^{6}LiF converter of different thickness at room temperature [101].

The deterioration of performance at low temperature was seen during the development of these detectors, and is shown in Figure 3.5. It can also be seen by examining typical pulse height spectra from the Autumn 2010, displayed in Figure 3.6. These spectra are taken from analysis carried out by Katsika in [96]. This plot shows MCA spectra for the four installed detectors- *UCN1* (red dots) and *UCN2* (purple dots) are open and *UCN3* (green dots) and *UCN4* (blue dots) are iron coated. We expect to see both α and triton peaks in each of these plots but only the latter is clearly visible. In all four cases the presence of γ background or electronic noise seems to dominate the low pulse height area where the α peak is expected. For the detector in Figure 3.6 marked *UCN1 Open detector* (red dots) it affects the triton peak as well, which is only at half the voltage value measured by detector *UCN4* (blue dots).

In a semiconductor, at low temperature (below ∼40 K for Si), negligible intrinsic electron-hole-pairs exist as there is insufficient thermal energy to excite them, and the donor electrons are bound to the donor atoms This is known as the ionization (or freeze-out) region of a semiconductor. As conductivity depends on the density and mobility of carries, this region corresponds to very low conductivity. In a doped semiconductor, some small residual conductivity can be observed even at very low temperature, due to the overlap of wavefunctions

of the electron/hole and the impurity site, and tunnelling from one site to another may occur [109].

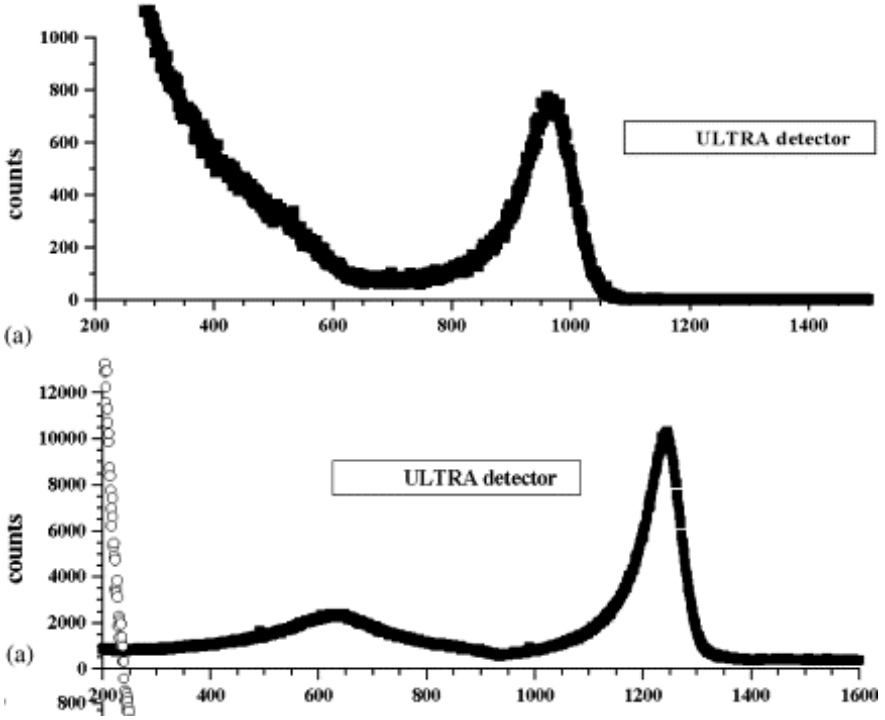

Figure 3.5: Neutron-generated pulse height spectra from ORTEC silicon detectors with ^{6}LiF converter as measured during the development phase [102]. The spectrum at the top is within superfluid at 430 mK and below is taken 300 K after having been taken out of liquid helium (bottom). At low temperature the α peak is buried in noise, however this recovers once warmed up.

Research is ongoing to improve the performance, in particular if the noise floor can be lowered with reduced electrical interference and shielding from background γ, perhaps the small signal can be resolved. Not only is the efficiency of the detectors affected by this problem, and thus the sensitivity of the EDM measurement, but as both the α and triton peak are not clearly visible in the open detector, it also means that measurements of the neutron polarisation are unreliable. Analysis by Katsika in [96] has attempted background subtraction on these signals to correct the counts in the open detector. Work continues to minimise electrical interference between elements of the apparatus, but this is further motivation for the development of an alternative detector, particularly one which is less sensitive to electrical interference, and which has no electrical components inside the main experimental apparatus, such as a scintillation detector.

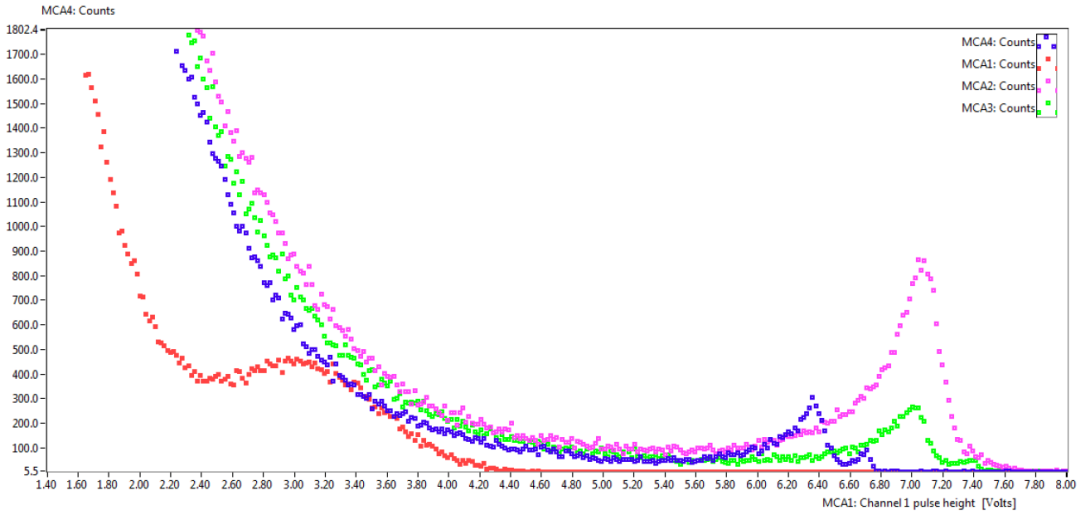

Figure 3.6: Typical MCA spectra for the *UCN1* (red dots), *UCN2* (purple dots) open detectors and the *UCN3* (green dots) and *UCN4* (blue dots) iron detectors for run at 0.7 K [96]

In summary, the current silicon UCN detectors exhibit a number of deficiencies, which lead to a UCN detection efficiency of only 42%. The detectors have low conductivity at these extreme low temperature, which results in the α particle signal being indistinct from detector noise and background, immediately losing half the UCN detection efficiency. Furthermore they are sensitive to γ background, which contributes to a significant background signal, from which the α or triton signal cannot be distinguished. The detectors have also had some mechanical failures, not surviving multiple temperature cycles from room temperature to 0.5 K. Finally, they are sensitive to radiation damage which over time inhibits charge collection. With these drawbacks in mind, an investigation into alternative UCN detection technology has been undertaken in this thesis. The particular constraints of the cryoEDM experiment must be acknowledged, and any potential alternative detector technology assessed for compatibility with the experiment's aims and apparatus.

3.3 Experimental Requirements in a Detector

A high neutron detection efficiency, of at least ∼50%, preferably significantly higher, is required to improve on the ORTEC Ultra Silicon detectors. With a thin film conversion layer, in order to count all neutrons, both the α and triton peaks must be fully measured and distinguished from background. Alternative detector geometries [110] and surface structure [111] have been reported in the literature, enabling both particles to enter the detecting body, described further in Section 3.4. In such a geometry, where both particles enter the detection volume, only one must be counted for full neutron detection efficiency. An alternative detector should have low sensitivity to γ background, or be capable of distinguishing these events from signal events. The detector must have sufficiently high repetition rates in order to deal with the design specification neutron count rates [85]. It must integrate with the current apparatus and the challenging engineering constraints of the cryogenic environment. All its properties must retain their requisite values at low temperature.

3.3.1 Neutron Count Rate

The detector must have sufficiently high repetition rates at the operating temperature of 0.7 K in order to deal with the design specification neutron count rates [85]. 4.5×10^5 UCN per batch are expected from the cells at the detector surface. Assuming most of these diffuse to the detector within the first second of the batch, the detector must be able to resolve neutron counts arriving every ∼2 μs. For a single cell detector, this corresponds to count rates of ∼500 kHz. Alternatively, the interaction area can be segmented to reduce the interaction rate.

3.3.2 Gamma Background

The PF2 guide-hall at the ILL, where cryoEDM is situated, is a noisy γ environment. While the neutron beam is on, at cryoEDM or neighbouring experiments, neutron scattering from

nearby equipment may produce a high flux of fast neutrons, and γ background.

An ideal detector would be sufficiently insensitive to γ background so that the signal is low relative to the UCN signal. This could be optimised with the choice of low atomic number Z materials to minimise γ energy deposition in the detector. Alternatively, the background may be removed if the detector has the ability to distinguish a γ event from a neutron event, for example through pulse shape discrimination (PSD) techniques. Particles of different type may cause a different pulse shape in a detector due to different underlying physical interactions, allowing signal and background to be clearly identified and separated. Ensuring the signal from the neutron capture events is distinguishable from background is essential for maximisation of neutron detection efficiency.

3.3.3 Superfluid Environment

Crucially, a suitable detector must be compatible with the cryogenic superfluid environment of cryoEDM. The area in which the detector was installed was shown in Figure 3.3. The UCN diffuse from the Ramsey Cell along the copper beryllium guidetube and at the valve move downwards into the quartz detector tube via the force of gravity. This whole area is filled with superfluid helium at 0.7 K. This is a challenging experimental environment and the characteristics of many instruments change or lose functionality at low temperature. The magnitude of the signal may weaken, the speed of the signal may slow, or the thermal contraction may cause them to fail altogether. A new detector for cryoEDM must be proven to work at low temperature.

Furthermore, not only is the environment one of low temperature, but of superfluid. This adds the extra difficulty of producing super-fluid tight feed-throughs for the signal to travel from the detector to data acquisition outside the experiment, passing through layers of superfluid, vacuum, cryogens and shielding. The electrical signals produced by the silicon detectors are read out electrically through stainless steel coaxial cabling. These firstly travel through a superfluid feed-through, and subsequently through multiple layers of cryogenic shielding and vacuum cans until the signal is presented to a room temperature feed-through.

3.3.4 Experimental Geometry

Any feasible alternative detector would have to integrate into the cryoEDM apparatus as was described in Section 2.3.2 and illustrated in Figure 2.1 and Figure 3.3. Ideally the detector could be installed on a flange which connects to the bottom of the vertical guidetube. Detector power and readout would need to physically fit into the space already allocated to the current detectors. Cables would need to be routed through either a) a superfluid feedthrough and further cryogenic and vacuum feedthroughs to outside the experiment underneath the transfer section; or b) through the superfluid volume but outside the neutron guidetubes to the cryostat area, where there could be a cryogenic, but non-superfluid, feedthrough.

These detector requirements are summarised in Table 3.1. With these in mind, a literature review of available detection technology for UCN, thermal neutrons and for α radiation was undertaken. We can review the suitability of various other technologies that are used for neutron detection or particle detection more generally, and assess their suitability for this application. This is outlined in the following section.

UCN Detector Requirements for cryoEDM
Neutron count rate of 500 kHz
Compatible with neutron conversion via thin film ^{6}Li layer or other
Low γ sensitivity
Low temperature superfluid compatible
Integration with existing apparatus

Table 3.1: UCN detector requirements for cryoEDM.

3.4 Review of Potential Technology

Detection technology developed for slow neutrons with energies below 0.5 eV may be suitable for UCN detection, provided it meets the other criteria outlined in Section 3.3. At low energies, neutron capture cross-sections tend to be proportional to $1/v$ (i.e. to $1/\sqrt{E}$) where v is the neutron velocity. This can be derived from the Breit Wigner Formula [112]. Capture cross sections are usually quoted at E = 25 meV, thermal neutron energy, and will be

significantly higher for UCN. For example, ^{6}Li capture given in Eq. (3.3) has a cross section of 940b for thermal neutrons, and $\mathcal{O}$(Mb) for UCN [101]. Figure 3.7 shows the neutron capture cross section trend as a function of energy for numerous isotopes.

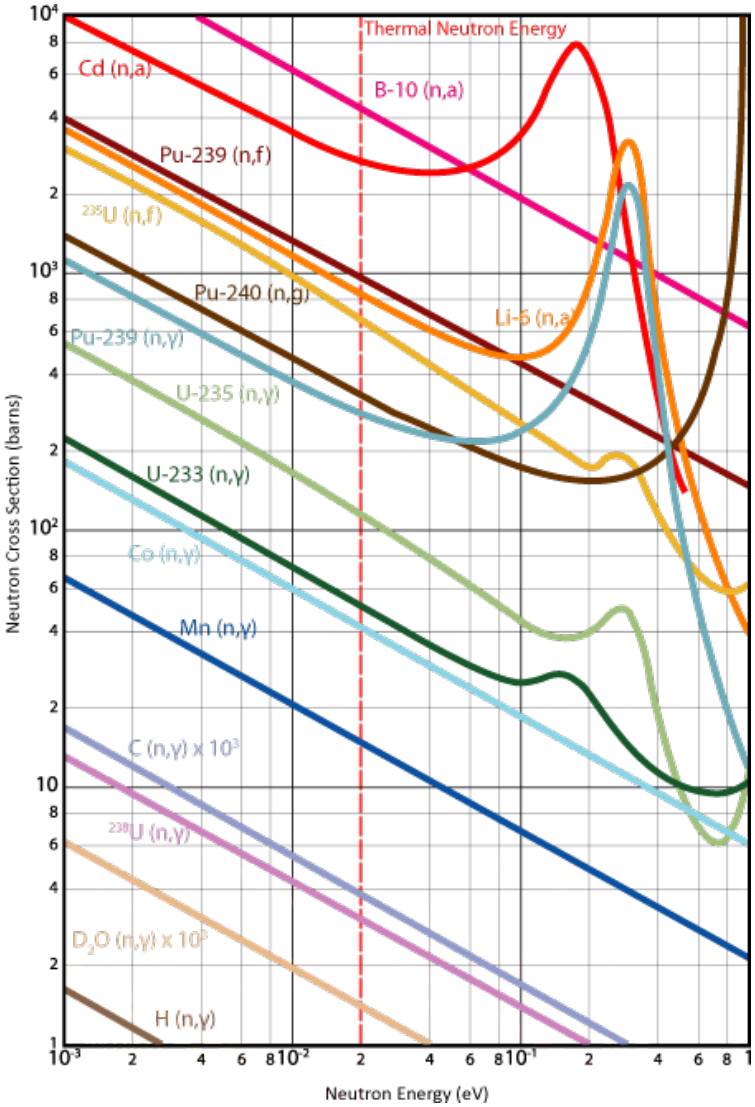

Figure 3.7: Neutron capture and fission cross-section in thermal region, showing ^{10}Bo in pink and ^{6}Li in orange [113].

To search for alternative neutron detection technologies applicable to cryoEDM, we can look to the vast pool of particle physics detection knowledge that has been built up over the last decades for fundamental particle physics experiments, at colliders, neutrino experiments or dark matter searches, neutron scattering and imaging facilities, as well as the nuclear power industry, and defence industry.

In particular, the global shortage of ^{3}He has led to a lot of investment in and develop-

ment of alternative neutron detectors in the last few years. Neutron detection is an area full of innovation and fast development. Reviewed here are various neutron detection methods reported in the literature and a discussion of their suitability for application for UCN detection for cryoEDM. An in-depth presentation of the current status of alternative neutron detection methods is available at [114].

3.4.1 Alternatives to Gas Proportional Counters

Although ^{3}He gas filled proportional counters remain the most commonly used neutron detector, the high cost and global shortage of ^{3}He seen in the last decade has led to significant investment in the development of alternative neutron detector technology. In particular, there has been significant development of solid state detectors, making use of ^{6}Li, ^{10}Bo capture as well as other technologies. It is a relatively young research area, that has really come about since the increase in border security in the US and globally after the September 11 terrorist attacks. Neutron detectors have been systematically installed at borders, causing a depletion in the US stockpile of ^{3}He from 200,000 L in 2001 to 50,000 L in 2010, and a twenty fold increase in cost per litre of the gas. Consequently, the research area of finding alternatives to ^{3}He neutron detection very active and growing, and showing lots of innovation.

Gas proportional counters with ^{10}Bo are also widely used for thermal neutron detection, and are thoroughly reviewed in [105]. Gas counters will not be applicable to cryoEDM due to the cryogenic nature of the experiment.

3.4.2 Semiconductor Detectors

Silicon UCN detectors have not only been developed for the cryoEDM experiment, but have also been reported by the PNPI nEDM group [115]. An innovation in the latter case is the use of a sandwich construction, made from two silicon plates with a ^{6}LiF converter placed between them. They have reported UCN transmission coefficients of over 70% through 100 μm of Al and 375 μm of Si wafer, for UCN above 150 neV. They reported a 75 – 80% detection

efficiency for UCN with energies of 200 – 300 neV. The Fermi Potential of silicon is 50 neV and so UCN with energies above this are not reflected by the first layer of Si, but enter the bulk, and interact with the ^{6}LiF layer in the middle. Such a sandwich construction could be applied to the cryoEDM silicon UCN detectors. If both reaction products entered one of the two silicon wafers, any concealment of the α peak due to γ background or noise would not cause loss of UCN detection efficiency, as long as the triton peak was fully measured.

Semiconductor neutron detection is an area of research showing fast innovation over the last years, as part of the move away from ^{3}He detectors. In particular, the development of silicon detectors with 3D micro-structures etched onto their surfaces and then filled with the ^{6}LiF neutron converter have been reported by [116] and [117]. They have shown neutron detection efficiencies for thermal neutrons increase from 5% to 42%, reported by Bellinger in [118], as the capture rate increases for both neutrons and the reaction products. An example of such a structured surface is shown in Figure 3.8.

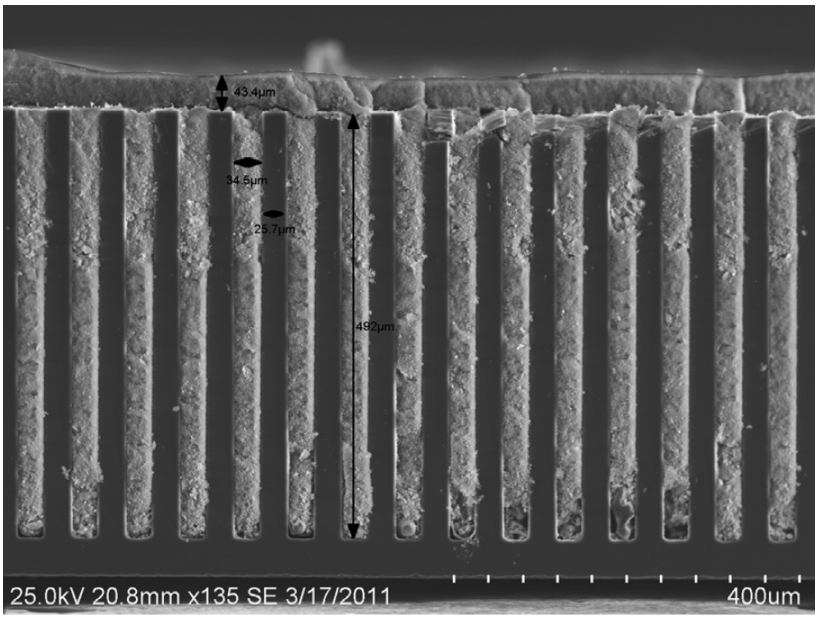

Figure 3.8: Figure from McGregor [119], reporting a silicon neutron detector (black) with 492 nm deep trenches etched and filled centrifugally with LiF nanoparticles (grey).

Such detectors have been reported by Uher et. al [116], Bellinger et. al [117] and reviews given by McGregor [119] and Caruso [111]. This is an elegant solution that could be applied to UCN detection with the benefit of the increased UCN capture cross section potentially leading to much higher UCN detection efficiencies than that reported for thermal

neutrons. However it is a technology that has been heavily invested in with significant resources and expertise. It involves advanced etching techniques on semiconductor surfaces, complex electrode layout and nanoparticle ^{6}LiF production, and therefore has not been researched further as a potential cryoEDM UCN detector.

Furthermore, research is ongoing in the development of semiconductors that are themselves directly sensitive to neutrons. One technique relies on the drifting of neutron sensitive isotopes into the structure of the traditional semiconductor, such as ^{6}Li in Si or ^{10}Bo in Ge. Another area of ongoing research involves the development of semiconductors where it itself constitutes a neutron sensitive isotope. However this technology is in an immature state, only a handful have shown the most basic electrical, electronic, structural and chemical properties, combined with the processability needed to fabricate a structure. A review of this area is reported by Caruso [111].

3.4.3 Cryogenic Phonon Scintillation Detectors

Cryogenic detectors are widely used in the research area of rare event detection for dark matter experiments and neutrinoless double beta decay experiments, as well as in astronomy for infra-red detection. For these type of experiments, low energy events are expected and so it is critical that the detectors have a very low energy threshold. Operation at cryogenic temperatures minimises the thermal noise that would otherwise hide their signal. They also have excellent energy resolution, and can be used to discriminate electron and nuclear recoils on an event by event basis.

These particle detectors operate at very low temperature, typically below 100 mK, taking advantage of the low thermal noise, and the superconducting properties of materials. The detectors allow nuclear recoil reactions to be distinguished from electronic recoil reactions, by measuring two of three types of signal- phonon, scintillation or ionisation. It is precisely this ability to discriminate between neutron (nuclear) and γ (electronic) interactions which would be of great advantage as a neutron detector for cryoEDM.

The Oxford group has a pool of expertise, knowledge and resources accumulated from the development of cryogenic detectors for dark matter detection, in particular Cryogenic Phonon Scintillation Detectors (CPSDs) for the CRESST experiment [120], cryogenic scintillation detectors [121] and the operation of Photomultiplier Tubes at cryogenic temperatures [122]. This is a natural area to investigate further for the application of neutron detection for cryoEDM.

The detectors, operating below 1 K, have two modes of signal generation. Firstly, a particle interacting with the absorber crystal will produce phonons. The crystal is maintained at cryogenic temperature to maximise the heat capacity and thus the temperature change due to phonon generation due to deposited energy. Secondly, the cryogenic phonon channel is combined with conventional ionisation or scintillation measurements to provide discrimination of nuclear recoils from electron recoils.

The phonon channel of the CRESST-type CPSD detectors is read out using superconducting transition edge sensors (TES) which are very sensitive to changes in temperature due to phonon generation. The absorber crystal is also a scintillator, and a fraction of the deposited energy produces scintillation photons, which escape the crystal and are counted by a light detector. The ratio of the phonon signal to the light signal varies with the particle interaction, and is used to discriminate between γ, α and neutrons. This method is well established and used by the CRESST dark matter experiment.

The CPSD have used different target materials/scintillators operating at low temperature, and had many of the same detector requirements as was outlined for a neutron detector in Section 3.3. Scintillators with high scintillation yield at low temperature were investigated by the group [123] [124] as part of CPSD development, however there are some crucial differences in requirements for a UCN detector. Rare event searches do not require fast decay times and therefore they can use scintillators which are traditionally considered "slow". This is not the case for cryoEDM due to the high neutron event rate. For dark matter searches, high radiopurity is essential, but this is not necessary for cryoEDM. The research on scintillators for dark matter searches has investigated a number of good cryogenic scintillators

including $CaWO_4$, $ZnWO_4$ and $CaMoO_4$, however all of these are too slow for the cryoEDM application, and so an alternative crystal must be found. There are a large number of compounds, such as NaI(Tl) [125] and CsI(Tl) [126], that are known to be good scintillators at room temperatures, but their light yield decreases substantially with temperature or decay time slows, thereby making them unsuitable for cryogenic applications. This is discussed at length in Chapter 5.

The readout of the TES sensors has been done using SQUIDs, by measuring a change in resistance due to the temperature change, through a SQUID input loop. The sensor is stabilised within its superconducting transition, which results in a very large change in resistance for a small change in temperature. If such a detector could be developed with an appropriate fast scintillator and a superconducting transitions edge sensor at a temperature near the operating point of cryoEDM, 0.7 K, it could be a feasible neutron detector. As the extremely low energy threshold (and thus low thermal noise) required by rare event searches is not required in cryoEDM, it may be possible to operate a CPSD at this higher temperature. A feasibility study of this kind of detector has been carried out and discussed in detail in Chapter 4.

3.4.4 Scintillators

Aside from gas proportional counters, scintillation detectors are in increasingly widespread use as thermal neutron detectors. Scintillation detectors are one of the most widely used type of charged particle detectors in particle physics, particularly in calorimetry. They are also being deployed widely at neutron scattering facilities such as the ISIS neutron scattering facility at RAL in Oxfordshire, and the neutron scattering facility at ILL, replacing ^{3}He detectors. As a solid state detection medium, it is an obvious candidate to investigate for application in cryoEDM. For low energy neutrons, rather than the neutron interacting with the scintillating material directly, they are usually loaded with the conversion nuclide, ^{6}Li or ^{10}Bo. The ionising reaction products then generate scintillation photons which are then read out as the signal.

Large area scintillation detectors have been built as part of many collider particle physics experiments and long baseline neutrino detectors. Plastic scintillator is used by the Atlas, CMS and LHCb experiments at the LHC, CMS also uses $PbWO_4$ scintillating crystals, and plastic is also used by the MINOS and T2K long baseline neutrino experiments. The design and readout of scintillation detectors is a mature field and research published in the literature gives a wide possibility of detector designs that could be adapted and tested for use at low temperature and for integration with cryoEDM. This is studied in Chapter 6.

The thin-film conversion layer process, as exploited by cryoEDM's silicon detectors, may still be used with a scintillator, thereby removing the need to have a loaded scintillator. This opens up a vast array of scintillators which could be used in conjunction with a conversion layer for UCN detection, provided they met the detector requirements outlined in Section 3.3. A combination of traditional scintillator detection technology and the low temperature scintillation studies carried out for CPSD could be applied to develop a scintillating cryogenic neutron detector. A study of the characteristics of potential scintillating materials at low temperature is carried out in Chapter 5.

A number of scintillators have been developed for thermal neutron detection, which combine ^{6}Li or ^{10}Bo nuclei in a scintillators. These include lithium glass scintillators, developed by Advanced Scintillation Technologies with natural Li, enriched ^{6}Li or depleted ^{6}Li. Boron doped plastic scintillators are available from St Gobain and Eljen technologies ([127] [128]) with ^{10}Bo quantities up to 5% by weight. The scintillator ZnS(Ag) mixed with ^{6}LiF has been used in segmented scintillation detectors developed for use at the ISIS neutron scattering facility, and are read out with wavelength shifting fibres and PMTs [129].

^{6}Li doped glass scintillators have been used by the PSI EDM group to develop a room temperature UCN detector [74] [110]. They report that by using a sandwich of ^{6}Li depleted scintillator with low UCN capture, and ^{6}Li enriched scintillator, both the α and triton reaction products can be counted. Zenner [72] gives details of the 9 part segmented UCN detector capable of rates up to 1.75×10^5 n s^{-1}. The detector has 9 square 28×28 mm^2 detection surfaces for a total detection area of 635 cm^2. Each detector segment consists first

of a 57 μm thick layer of glass scintillator GS30 that is depleted in ^{6}Li and so is insensitive to neutrons. They report it to have a Fermi potential of 101 neV and thus UCN with energies above this can pass through it to the next layer. Next is a 117 μm thick layer of enriched ^{6}Li glass scintillator GS20 which captures the UCN. This geometry allows the detection of both the back-to-back reaction products that the thin-film method cannot. As the range of the α and triton in the enriched glass is longer than the UCN mean free path, one of the reaction products will often escape. The sandwich structure with the depleted scintillator is a solution to this loss. Finally, a light guide transports the light to a PMT for conversion to electrical signal. They report 85% UCN detection efficiency relative to a ^{3}He gas counter at the PSI nEDM experiment [130]. A schematic and photograph is depicted in Figure 3.9.

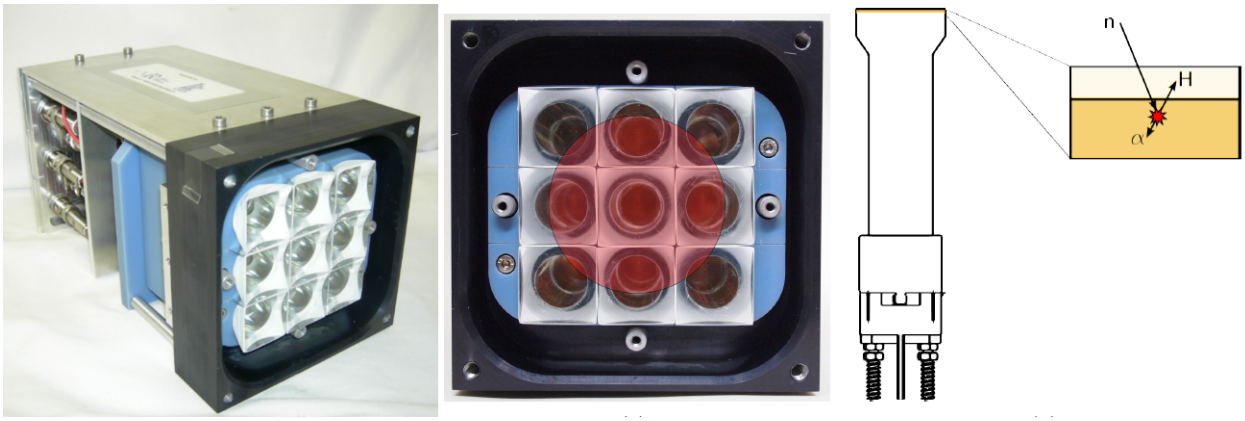

Figure 3.9: UCN detector developed for the PSI neutron EDM experiment consisting of 9 scintillation modules. Figure shows the detector as a whole on the left, face on in the middle with the UCN guidetube area overlaid in red, and a schematic of the detector on the right. Figures from [73] and [72].

Such a detector principle could be applied to the cryoEDM provided it was proven and optimised to work at cryogenic temperatures. The light yield and decay time of the relevant scintillators would need to be tested and reach the necessary requirements. A full review of scintillators that may be suitable for cryogenic use is discussed in Chapter 5 and low temperature characterisation of such scintillators carried out. The light collection method would need to be compatible with low temperature and the physical constraints of the cryoEDM experiment. For cryoEDM, it is clear that scintillation based neutron detectors are one of the most promising alternative detectors. A design study and protoype development is undertaken and reported in Chapter 6.

Chapter 4

Titanium TES Sensors for α Particle Calorimeter Readout

Cryogenic Phonon Scintillation Detectors have been developed as ultra-sensitive low temperature WIMP detectors, and may be adaptable for use as a UCN detector at low temperature. They are capable of distinguishing between interaction type, such as α, γ or neutrons, by examining the ratio of energy deposited in the scintillation and phonon channels. This would offer the significant advantage of background veto capability. Those used in the CRESST dark matter experiment operate at $\sim$10 mK, and use a tungsten transition edge sensor as an ultra-sensitive thermometer to measure the phonon signal. In this chapter, CPSD are described, and preliminary research is undertaken to investigate their feasibility as an α particle calorimeter, and ultimately a UCN detector via the ^{6}Li(n, α)^{3}H reaction. The phonon channel of such a detector is investigated with a titanium TES thermometer, which operates at a much higher temperature than tungsten, 350 mK, close to the operating temperature of cryoEDM, $\sim$500 mK. An alloy with a transition temperature of $\sim$500 mK could be manufactured in future for the best temperature compatibility.

The operation of these detectors is not without significant challenges. They must be thermally stabilised in a very narrow temperature range within the superconducting transition, and so could not be in a large heat bath of liquid helium. They must operate in a

vacuum so that the phonon signal is collected by the TES sensor and not lost to the environment. This may be particularly difficult for cryoEDM as the detector could not operate directly in the superfluid helium, but would require the UCN to travel through a vacuum tight window, introducing the potential for UCN losses. None the less, their high sensitivity, PSD capability and operation at low temperature suggest they may still be an appropriate technology for UCN detection at low temperature, and worth investigating further.

The aim of this chapter is to experimentally assess the feasibility of operating CPSD as UCN detectors for cryoEDM and characterise their behaviour at their transition temperature, 350 mK, close to the working temperature of cryoEDM. This characterisation includes a first use of a titanium transition edge sensor as the CPSD temperature sensor, the optimisation of this CPSD as an α detector rather than a rare low-energy event detector, and a novel method of temperature stabilisation using infra-red light emitting diode (LED) pulses delivered to the surface of the TES. The prototype Ti-CPSD detector is operated close to the cryoEDM temperature, it is calibrated, and the measurement of an ^{241}Am α spectrum is carried out, and optimisation of detector bias current and working point is investigated and the detector resolution measured. The relative merits and challenges of this technology is discussed in the context of operation within, and integration with the cryoEDM apparatus.

4.1 Cryogenic Phonon-Scintillation Detectors for UCN

Cryogenic Phonon Scintillation detectors are an established technology used primarily in experiments to detect low energy weakly interacting particles in rare decays, in particular WIMP dark matter candidates. These highly sensitive devices essentially act as calorimeters in which a particle interacts with an absorber crystal, depositing its energy, ΔE, to produce a population of phonons. These thermalise in the absorber and are collected in the TES thermometer, where the energy is transferred to the electrons of the thermometer, to give a temperature rise,

$$\Delta T = \frac{\Delta E}{C} \tag{4.1}$$

where C is the heat capacity of the device. This temperature rise is read out as a change in its electrical resistance. In order to maximise the sensitivity, C must be minimised. The phononic heat capacity contribution dominates at low temperature, and $C \propto T^3$, thus operation at cryogenic temperature is advantageous, utilising a superconducting TES as the method of reading out the signal, ΔT. The TES sensor is operated in the narrow temperature range within the superconducting transition, where a small change in temperature produces a large change in resistance– $\frac{dR}{dT}$ is very large– thus making it a highly sensitive detector.

If the absorbing material is simultaneously a scintillator, the interaction may produce both phonons and scintillation light. The scintillation photons are measured by a light detector physically separated from the absorber. Analysis of the ratio of energy produced by the interaction in the phonon channel to the light channel yields the capability of distinguishing types of interaction and particle [131]. This would be advantageous in a UCN detector, as the background γ rays could be easily vetoed from a UCN spectrum. As cryoEDM is already operating at sub-kelvin temperatures, integrating cryogenic detectors may be an elegant solution to increasing the UCN detection efficiency. It must meet the criteria set out in Chapter 3 in order to be feasibly integrated with the cryoEDM apparatus. In particular, a titanium TES sensor operates close to the working temperature of cryoEDM, with the nominal transition of titanium being $\sim$400 mK, and thus stabilising it at an operating point inside this transition would not cause undue heat load onto the experiment. Although the integration of a vacuum can into the detector area to hold a CPSD detector would be possible, the UCN would have to travel through a neutron window. These are typically thin membranes made of aluminium or some other low-Fermi-potential material which allow the passage of UCN, with transmission efficiencies that vary greatly from 20% to 90% [132], [133] [134]. In order to exceed the detection efficiency of the current silicon detectors, the CPSD would require a high transmission UCN window to be developed and installed.

4.1.1 Pulse Formation Model for Low temperature Calorimeters

These CPSD detectors have been theoretically modelled by Probst in [135], a diagram of which is shown in Figure 4.1. The electron system of the thermometer and the phonon system of the absorber are characterised by their heat capacities, C_e and C_a, and by their temperatures, T_e and T_a. The temperature of the thermometer, T_e is what determines its resistance and therefore produces the signal. The electron system and the phonon system of the thermometer are considered separately, but coupled by a weak thermal conductance of $G_{ep} \propto T^5$. This is the strongest temperature dependence of all the thermal links: G_{ab}, the conductance between the absorber and the heat bath, is proportional to T^3 and G_{eb}, the conductance between the electron system of the thermometer and the heat bath, is proportional to T. The heat capacity of the phonon system of the thermometer is negligible.

An interaction in the absorber crystal causes non-thermal phonons to fill the crystal. These are efficiently absorbed by the free electrons of the thermometer, which quickly thermalise the phonon energy across the electron system of the thermometer. This corresponds to a heating of the thermometer electron system due to an input power $P_e(t)$, creating a fast non-thermal component to the signal. Part of the energy thermalised by the electrons radiates back as thermal phonons across the interface into the absorber, which induces the slow thermal component. The power input due to this is represented by $P_a(t)$. Due to the reduction of the thermal coupling, G_{ep}, as temperature decreases, at low temperatures the energy flow from thermometer to absorber is impeded and the slow component is suppressed. This model can be summarised by two coupled equations.

$$C_e\dot{T}_e + (T_e - T_a)G_{ea} + (T_e - T_b)G_{eb} = P_e(t) \tag{4.2}$$

$$C_a\dot{T}_a + (T_a - T_e)G_{ea} + (T_a - T_b)G_{ab} = P_a(t) \tag{4.3}$$

where T_b is the temperature of the heat bath.

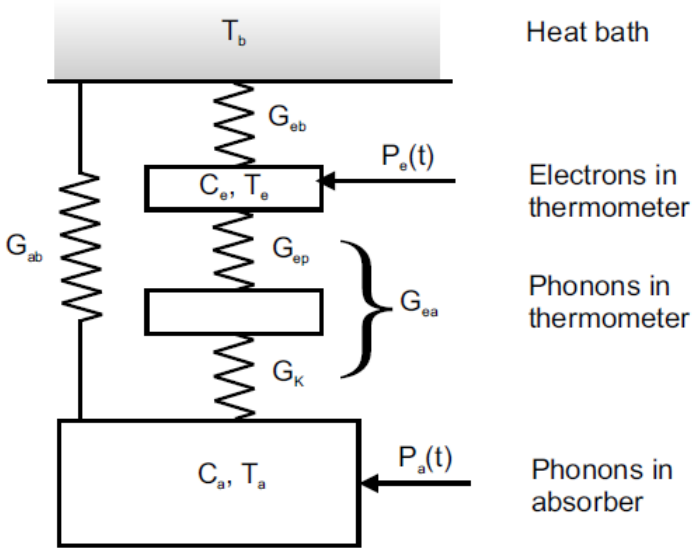

Figure 4.1: A thermal model of the phonon detector system.

The non-thermal power inputs are

$$P_e(t) = \Theta(t) P_0 e^{-t/\tau_n} \tag{4.4}$$

$$P_a(t) = \frac{1-\epsilon}{\epsilon} P_e(t) \tag{4.5}$$

The Θ step function represents the assumption that a uniform density of high frequency phonons is essentially present immediately after the particle interaction. The initial power input into the thermometer is P_0, and ϵ is the fraction of the high frequency phonons which are thermalised in the thermometer. The time constant τ_n represents the lifetime of the non-thermal phonon population introduced by $P_e(t)$ and $P_a(t)$, and is given by

$$\tau_n = \left(\frac{1}{\tau_{film}} + \frac{1}{\tau_{crystal}} \right)^{-1} \tag{4.6}$$

where τ_{film} and $\tau_{crystal}$ are the time constants for thermalisation in the thermometer and crystal respectively. With the initial condition $T_a(t = 0) = T_e(t = 0) = T_b$, these equations

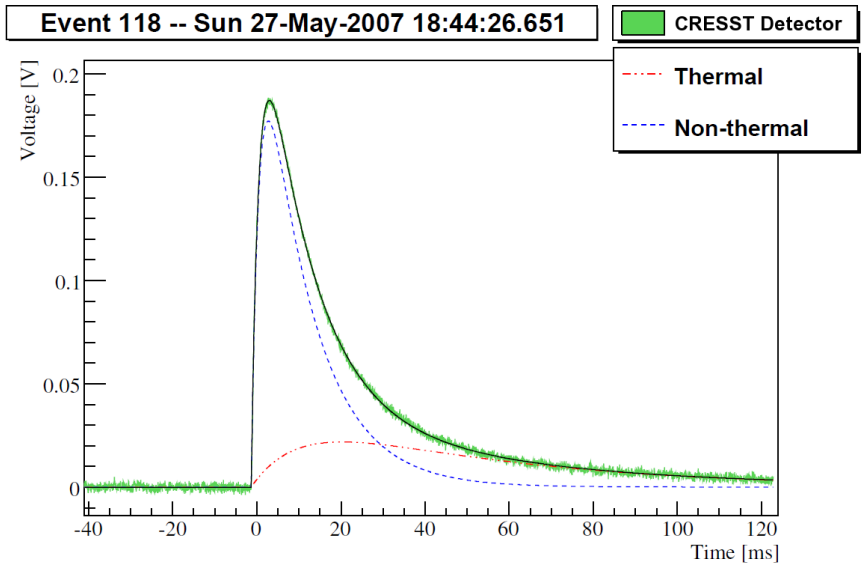

Figure 4.2: An 85 keV pulse in a CRESST phonon detector (green). The solid black line is a fit of Eq. (4.7) to the pulse, and the dashed lines show the thermal and non-thermal contributions [136].

yield the following solution for the thermometer signal $\Delta T_e(t) \equiv T_e(t) - T_b$:

$$\Delta T_e(t) = \Theta(t) A_n \left[(e^{-t/\tau_n} - e^{-t/\tau_{in}}) \frac{A_t}{A_n} (e^{-t/\tau_t} - e^{-t/\tau_n}) \right] \tag{4.7}$$

The solution consists of two components, a non-thermal component with amplitude $\mathrm{A_n}$ and a rapid rise and fall time, and a thermal component with amplitude $\mathrm{A_t}$, with a slower characteristic time. τ_n is the mean phonon lifetime, τ_{in} the intrinsic time constant of the thermometer, and τ_t the thermal relaxation time constant of the absorber. The pulse shape predicted by this model matches experimental data very well [135]. This can be seen from a typical CRESST pulse, and the fitted model, as analysed by McGowan in [136] and displayed in Figure 4.2.

The detectors developed for CRESST have a characteristic time of $\mathcal{O}(10\,\mathrm{ms})$, which would be much too slow for the repetition rates needed in cryoEDM. The time of the phonon signal depends on the dissipation time of heat in the crystal, and is dependant on the parameters τ_n (the mean phonon lifetime), τ_{in} (the intrinsic time constant of the thermometer), and τ_t (the thermal relaxation time constant of the absorber) from Eq. (4.7). Thermal feedback may be used to lower this recovery time, to cool the crystal more rapidly in response to the pulse.

In this chapter, a thermal feedback system is investigated that uses infra-red LED light to stabilise the detector, resulting in faster response time of $\mathcal{O}(100\ \mu s)$. Furthermore, the selection of absorber may influence the decay time parameters significantly. For example, the CDMS-II dark matter experiment uses Phonon-Ionisation cryogenic detectors with a germanium absorber, demonstrating a 200 μs phonon detector decay time [137]. Multiple small absorbers could be operated as separate modules, reducing the interaction rate by possibly a factor of 10. This is discussed further in Section 4.3.3.

4.1.2 TES Sensor Readout Circuits

The thermometer is typically operated in a readout circuit that detects a change in current corresponding to a change in temperature through the following relation

$$\Delta I = \frac{\delta I}{\delta T} \cdot \Delta T \tag{4.8}$$

$$= \frac{\delta I}{\delta R} \cdot R_0 \cdot \alpha \cdot \Delta T \tag{4.9}$$

where R_0 is the resistance of the thermometer at the operating point and the parameter α is given by:

$$\alpha = \frac{1}{R_0} \cdot \frac{\delta R}{\delta T} \tag{4.10}$$

The steepness of the superconducting transition gives rise to a very large positive α.

The equation for the rate at which the temperature T of the absorber changes is given by a sum of all power inputs and outputs

$$C\dot{T} = P_{ext} - P_{link} + P_{elec} \tag{4.11}$$

where C is the heat capacity of the detector, T its temperature, and P_{ext}, P_{link} and P_{elec} the power flow caused by a particle interaction in the detector, the power flow from the detector to the constant temperature bath via the thermal link and the power input by the readout current through the resistive temperature transducer. The electrical power can be expanded

to give:

$$P_{elec} = P_0 + \left.\frac{\delta P}{\delta T}\right|_{T_0} \cdot \Delta T \tag{4.12}$$

Variation of P_{elec} with ΔT gives rise to electrothermal feedback whose strength is governed by the sign and magnitude of $\delta P/\delta T$. The configuration of the electrical readout circuit and the detector biasing scheme controls these values. The three modes of electrical biasing correspond to constant current, constant voltage of constant power, given by:

$$\left(\frac{\delta P}{\delta T}\right)_{T_0} = +\alpha P_0 \qquad \text{Constant Current} \tag{4.13}$$

$$= -\alpha P_0 \qquad \text{Constant Voltage} \tag{4.14}$$

$$= 0 \qquad \text{Constant Power} \tag{4.15}$$

where $P_0 = I_0^2 R_0$.

As $\alpha > 0$ for TES sensors, constant current readout is susceptible to "thermal runaway", where an increase in temperature causes an increase in current, causing further joule heating ($I_0^2 R$). This mode is usually avoided. In constant voltage mode, thermal runaway is avoided as the absorption of power causes the thermometer resistance to rise, thereby reducing the electrical heating power (V_0^2/R). Furthermore, in constant voltage mode, the time constant of the system is shortened and the linearity and dynamic range of the detector are improved. Although this mode has not been implemented here, it would offer another method to potentially lower the detector time constant and become more viable as a fast UCN detector.

The third mode of operation, and that which is implemented in these experiments and in CRESST detectors, is one of constant power. In this mode, there is no change in heating power with temperature, so thermal runaway is not a problem, the time constant does not change with read-out power, and they are easier to stabilise inside the superconducting transition [138] [139]. With this mode, an external method of temperature stabilisation is needed and is implemented here with the infra red LED light.

4.2 Feasibility Study of Al_2O_3 Ti-TES Calorimeters

The feasibility of operating a Al_2O_3 Ti-TES CPSD at 350 mK for application as a UCN detector for cryoEDM was investigated experimentally. A proof-of-principle experiment was performed by installing a phonon detector module in an Oxford Instruments K400 Dilution Refrigerator cryostat. The absorber crystal is aluminium oxide, with a thin-film titanium thermometer, with a superconducting transition at ∼350 mK (the exact temperature depends on the alloy). The detector was cooled, the titanium transition characterised, the detector was stabilised at an operating point inside the transition, and an α spectrum was measured.

4.2.1 Calculated Sensitivity to Absorbed α Particles

The sensitivity of the detector to a particle of known energy can be calculated according to Eq. (4.1). At low temperature, the Debye model for predicting the phononic contribution to heat capacity at low temperature is an accurate approximation [140]. It correctly predicts the low temperature dependence of the heat capacity of insulating, crystalline solids where other contributions, such as conduction electrons, are negligible. It gives the following relationship between heat capacity C_V and temperature:

$$C_\mathrm{V} = \frac{12\pi^4}{5} N k_\mathrm{B} \left(\frac{T}{\Theta_D}\right)^3 \tag{4.16}$$

where N is the number of atoms in the sample, k_B is the Boltzmann constant, T is the temperature of the material and Θ_D is the Debye Temperature of the material. The Debye temperature is characteristic of a particular material, it is the temperature of a crystal's highest normal mode of vibration, and is 1030 K for Al_2O_3. For N = 1 mole of Al_2O_3, operating at the transition temperature of titanium, 350 mK (for this particular alloy, as measured in Section 4.3.2), $C_\mathrm{V} = 2.62 \times 10^{-7}$ J K^{-1}. For a 4 g absorber crystal, as was used in this experiment, an α particle of energy 5.5 MeV will cause a temperature rise in the absorber of 8.6 $\times 10^{-5}$ K, assuming all its energy is deposited and converted into phonons.

A typical titanium transition width is 30 mK, which was confirmed by the measurement of the transition of this particular titanium film in Section 4.3.2. It has a superconducting transition temperature of T_c = 350 mK, with a transition size of 6 Ω, giving an average gradient, $\frac{dR}{dT}$ of 200 Ω K^{-1}. Thus a 5.5 MeV α will cause a change of resistance of $\sim 17\ m\Omega$.

Given the set-up of the circuit, as in Figure 4.5, a change in current through the SQUID input line ΔI due to a change in resistance of ΔR, is given by:

$$\Delta I = I_0 \frac{R_T}{(R_T + R_R)^2} \Delta R \tag{4.17}$$

and thus for R_T = 6 Ω and R_R = 700 mΩ

$$\Delta I = 2.3 \times 10^{-3} I_0 \tag{4.18}$$

The resolution of the detector can be estimated by the noise contributions to the system. This is dominated by thermal Johnston noise of both the film and the reference resistors, which goes as

$$i_n = \frac{\sqrt{4kT\Delta f R_R} + \sqrt{4kT\Delta f R_T}}{R_R + R_T} \mathrm{pA}/\sqrt{\mathrm{Hz}} \tag{4.19}$$

and by intrinsic SQUID noise, which is of the order 3 $pA/\sqrt{Hz}$. A bandwidth of 250 kHz, for a detector at 350 mK with $R_R = 700\ m\Omega$ and $R_T = 6\ \Omega$, yields a Johnston contribution of 0.85 nA and a SQUID contribution of 1.5 nA, added in quadrature yields a detector resolution of 1.7 nA. From Eq. (4.18), the detector must be biased at at least $I_0 = 0.75\ \mu A$ to resolve an α particle of 5.5 MeV.

4.2.2 Detector Assembly

A detector module was fabricated, consisting of an absorber crystal of Al_2O_3 of dimensions 10 x 20 x 1 mm with a titanium transition edge sensor deposited onto the surface of the crystal in order to measure phonons. Two superconducting Al contact pads were sputtered onto the surface of the Ti film at opposite ends, as well as one Au contact pad at the centre.

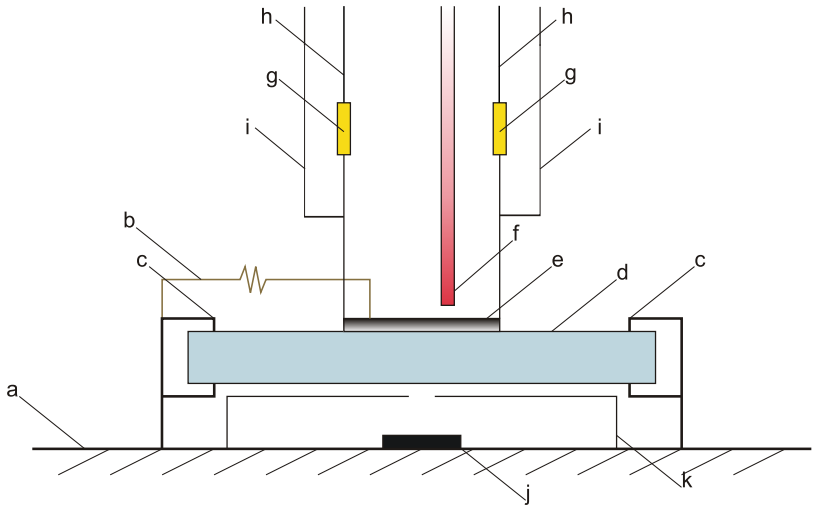

Figure 4.3: Schematic of Al_2O_3 Ti-TES detector experimental installation, including LED and optical fibre temperature stabilisation.

These pads are used for bonding the electrical and thermal contacts. Al wires are bonded to the Al pads to form the superconducting readout circuit, as described later in Section 4.2.3. The other ends of these Al wires are bonded to a readout pad, which connects to the readout circuit, as illustrated in the schematic diagram of the experimental installation, Figure 4.3. One end of a Au wire is bonded to the Au pad, and the other to the copper detector holder, which provides a weak thermal link and a central ground connection.

The detector was installed in the copper detector holder, and held in place with copper clamps. This holder was firmly bolted to the experimental plate of an Oxford Instruments Kelvinox 400 dilution refrigerator, as seen in the photograph in Figure 4.4. Underneath the detector, an ^{241}Am source was installed, exposing the absorber to 5.5 MeV α particles and 60 keV γ particles. A source collimator was later installed to reduce position dependence of the detector resolution.

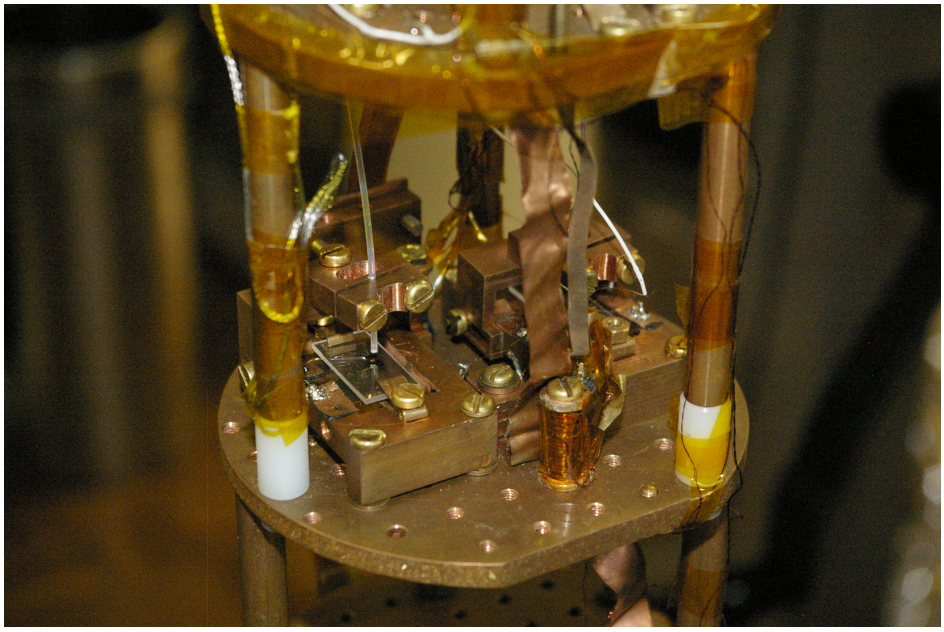

Figure 4.4: Photograph of the Al_2O_3 Ti-TES detector installed on the experimental plate of an Oxford Instruments Kelvinox 400 dilution refrigerator.

4.2.3 Detector Readout

The change in resistance of the TES sensor is read out as a change in current through a SQUID input coil. As illustrated in the circuit diagram in Figure 4.5, the sensor is biased by a constant input current I_0, which then flows in parallel through the TES and through two balanced reference resistors, of total value $R_R = 588\ m\Omega$, in series with the SQUID input coil. The reference resistors are strongly thermally linked to the mixing chamber in order to reduce thermal Johnston noise. A particle interaction in the absorber crystal will cause a resistivity pulse of the form given by Eq. (4.7) in the TES sensor, which will change the fraction of current in the SQUID input coil branch of the circuit. This current pulse causes a magnetic flux pulse in the SQUID input coil, and is read out of the SQUID system as V_{sq}. The current through the SQUID input coil is given by

$$I_{sq} = I_0 \frac{R_T(T)}{R_T(T) + R_R} \tag{4.20}$$

A SQUID operates as a magnetic flux sensor, converting flux through a SQUID coil to an output voltage, with a periodic transfer function. In order to linearise this function, and

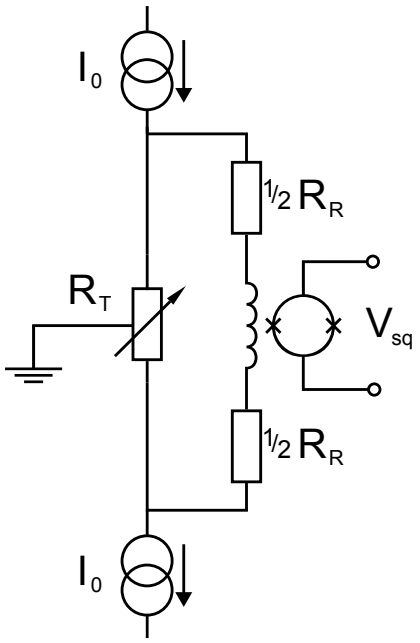

Figure 4.5: Diagram of Ti-TES electronic readout circuit, operated in constant power mode.

widen the available dynamic range, the SQUID is run in so-called "flux-locked loop mode" [141]. In this regime, the flux is kept constant through the loop, and the necessary feedback voltage to do this is read out as the signal, V_{sq}. This voltage depends on a feedback resistor in the flux-locked loop circuit, R_f, and the mutual inductance of the feedback coil and the SQUID coil, M_f. These parameters essentially determines the gain or flux to voltage transfer function, N, in units of V/Φ_0. The voltage across the feedback resistor then depends linearly on the applied flux.

Thus the relationship between the current, I_{sq} and the voltage readout by the data acquisition system (DAQ), V_{sq}, is linear and given by

$$V_{sq} = N(\Phi + n\,\phi_0) \tag{4.21}$$

where Φ is the magnetic flux in the input loop, $\phi_0 = h/2e = 2.07 \cdot 10^{-15}$ Wb is the magnetic flux quantum, n is an integer, and N is the gain of the system. The dynamic range can be changed by changing R_f. The constant of proportionality relating the current through the input coil, I_{sq}, and the magnetic flux in the squid loop, Φ, is simply the mutual inductance of the two, $\Phi = MI_{sq}$. There can always be an arbitrary current offset added to the signal given

by $\frac{Nn\phi_0}{M}$. The gain N, is dependant on the value of the feedback resistor in the flux-locked loop feedback coil, and relates the squid voltage to the current in the feedback loop. This feedback current/voltage is then the value that is read out of the system, V_{sq}. As SQUIDs have very low current noise of $\sim 3\ pA/\sqrt{Hz}$, and have a low input impedance, they are a most suitable device to read out the resistance of the Ti film.

The cables carrying the output voltage of the SQUID, V_{sq}, leave the cryostat and enter a pre-amplifier (PFL), which then connects to the SQUID control unit, known as the PCI. The output of the control unit is filtered and recorded, if triggered, in a 12-bit transient recorder, with a $\pm$ 10 V range, installed in a CAMAC crate. When the signal reaches $\pm$ 10 V, the control hardware resets it to zero. The filter is an anti-aliasing low-pass 8 pole Bessel filter, with a cut-off frequency of half the sampling frequency, which can be controlled by the DAQ software. V_{sq} also provides an input to a trigger unit, and an input to the operating point stabilisation system, described in more detail in Section 4.2.4 and outlined in Figure 4.6.

4.2.4 Data Acquisition & Software

A schematic diagram of the data acquisition and stabilisation system can be seen in Figure 4.6. The CAMAC crate is interfaced with custom software, known as DaqClient, which can control the sampling rate, record length and filtering settings. The data is recorded in binary format, which is then analysed using custom software, called OxRop, based on C++ and the ROOT data analysis package.

For pulse acquisition, the time base of the transient recorder was set to 4 μs with a record length of 2048 samples. These parameters were chosen such that the full decay of the α and heater pulses were within the event length, and that the shape of the rise time could be fully resolved. The pre-trigger region is set to one-quarter of the record length. It is from this region that the value of the SQUID baseline is calculated (the average value of the signal is recorded as the pulse parameter *Baseline Offset [V]*), and from the post-trigger region that the parameters related to the pulse shape are calculated. Following each complete record, there is a dead time in which the trigger is inactive, to allow for read-out time and

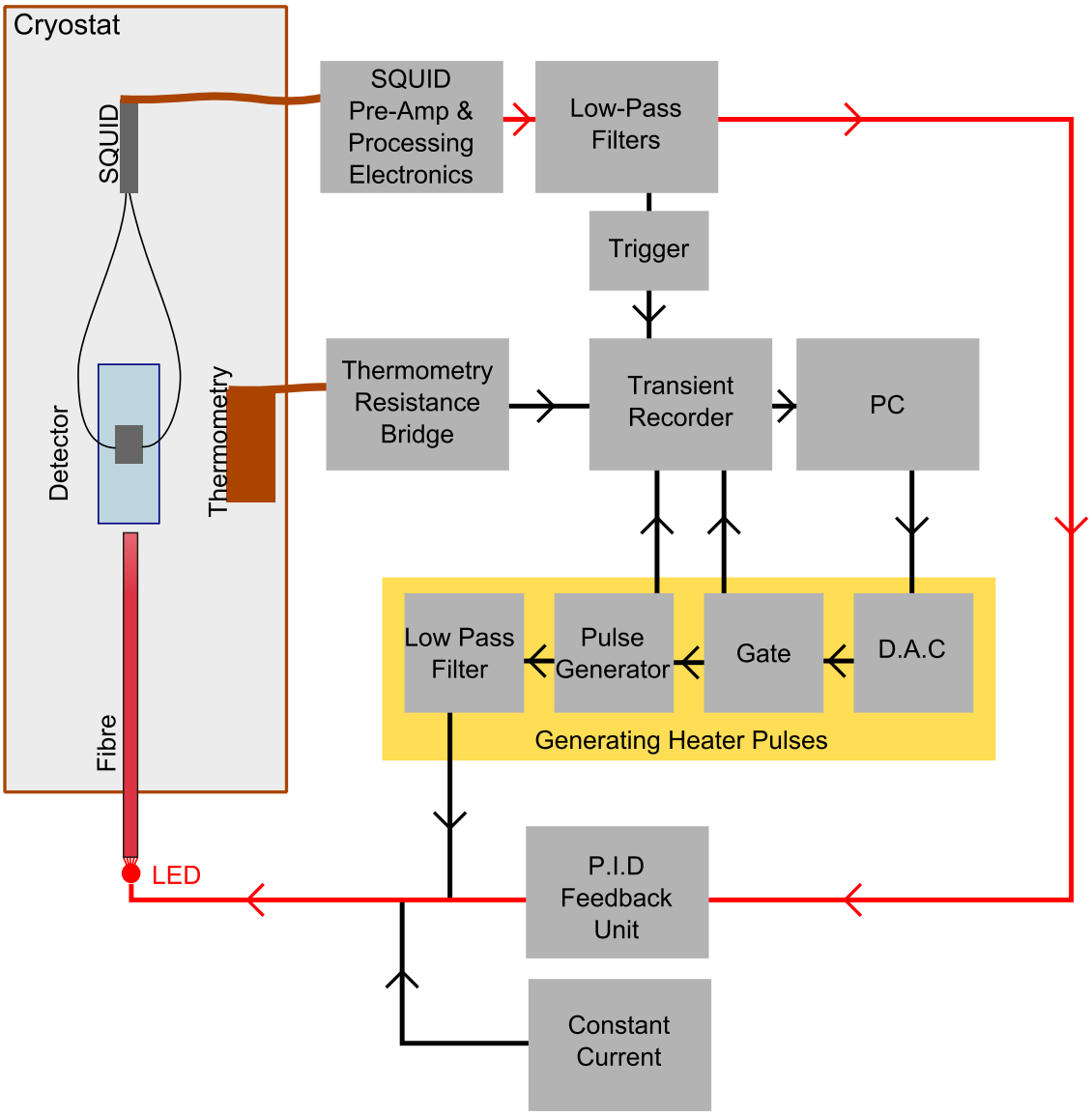

Figure 4.6: Schematic of the data acquisition system. The signal from the SQUID leaves the cryostat and is amplified and processed in a SQUID control unit (PFL and PCI). The output signal from this is filtered with an anti-aliasing low-pass 8 pole Bessel filter, with a cut-off of half the sampling frequency, which can be controlled by the DAQ software. The signal is used as an input to a PID (Proportional-Integral-Differential) unit to control the intensity of the LED (this feedback signal is in red). If triggered, the SQUID signal is recorded by a 12-bit CAMAC transient recorder (TR). Heater Pulses are generated by a software-controlled DAC (Digital-to-Analogue-Convertor), a gate and a pulse generator unit. A sum of a constant current to power the LED, the feedback signal and heater pulse signal are sent to the LED for stabilisation and characterisation of the detector. A PC records the signals from the SQUID, from the thermometry and signals generated for the feedback loop.

pre-trigger time for a subsequent pulse. The raw data for every triggered event is written to disk for later analysis. In addition to V_{sq}, the thermometer resistance, the heater pulser voltage (described in Section 4.3.3), and other voltages related to the trigger and pulser units are recorded. A typical particle event is seen in Figure 4.7 and a typical heater event in Figure 4.8.

The stabilisation of the detector in its transition is done with IR light from an LED sent to the detector via an optical fibre. The LED is powered with a DC current to provide a minimal base level of heating. In addition to that, the intensity is moderated depending on the output signal from the SQUID. This signal is processed through a Proportional-Integral-Differential (PID) control unit, before being added to the DC current. A third current signal is sent to the LED; pulses of controlled magnitude are sent on a regular basis to the LED as a method of characterising the position within and linearity of the superconducting transition. To produce these pulses, a software controlled digital-to-analogue converter (DAC) outputs a reference voltage to a commercial Camac Tail Pulse Generator module. The magnitude and frequency of the pulses are controlled by software, while the rise and decay time is controlled by the Tail Pulse Generator. This is discussed in more detail in Section 4.3.3, however it is already clear from comparing the particle event in Figure 4.7 to a typical CRESST event in Figure 4.2 that the feedback system has shortened the characteristic decay time from $\mathcal{O}$(10 ms) to $\mathcal{O}$(100 μs).

OxRop is a data analysis package that has been developed originally for the CRESST dark matter search, but now services a variety of data types, including PMT data analysis, SQUID magnetometry data analysis, and data from the EDELWEISS dark matter experiment. OxRop is implemented in C++ and based on the ROOT framework, and it inherits all of ROOT's graphical capabilities and classes. With an object oriented structure, OxRop has over 250 classes, providing the facility for users to write analysis macros which can be run on demand. It also provides an extensive Graphical User Interface for monitoring, visualising and analysing data. Full details are described in [142]

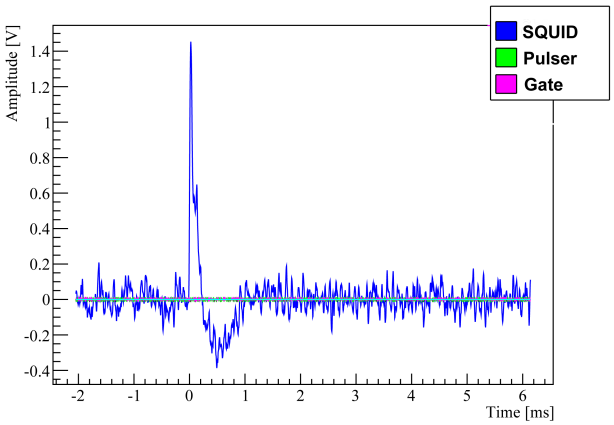

Figure 4.7: A typical particle event. Thermal feedback with an LED heater has shortened the characteristic decay time to $\mathcal{O}(100\ \mu s)$. The stabilisation system attempts to correct for the signal pulse causing a negative overshoot.

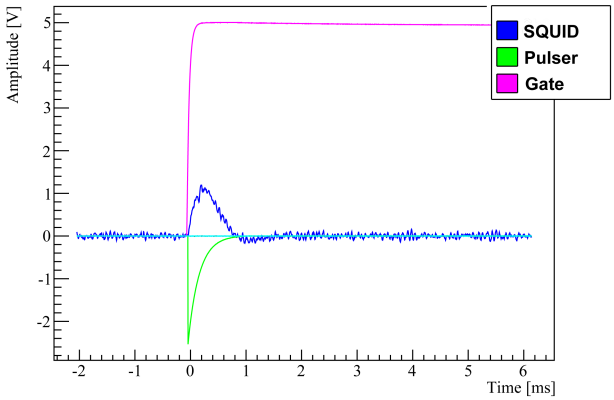

Figure 4.8: A typical heater event. An output current pulse (green) is sent to the LED, and the SQUID response is seen in blue. These events have characteristically slower rise and fall time and show much less overshoot.

4.3 Detector Performance Results

To characterise the sensitivity of the Ti-TES sensor to particle pulses at its transition temperature, a working point is established within the superconducting transition and thousands of α particle events and heater pulse events are recorded. The detector is stabilised at a chosen working point inside the transition with a particular bias current, the choice of which is described below. The linearity of the response is characterised using infra-red heater pulses from the LED/optical fibre heater, which is described in Section 4.3.3. The particle pulses from the α source are recorded concurrently.

The working point is defined by the temperature and the applied bias current, and affects the detector performance. To determine the optimal choice of working point, the superconducting transition of the film was measured as a function of detector bias current. A choice of a large bias current will produce large pulse amplitude, thus producing a very sensitive detector. However unwanted effects occur at high bias current, including approaching the critical current, self heating effects, and flattening of the transition, where it becomes broader and less steep.

4.3.1 Thermometry Calibration

In the temperature region of interest, resistance thermometry is a simple and suitable solution for temperature measurement. A high purity copper strip connects the cryostat mixing chamber to the experimental plate, where is is firmly anchored. At this anchor point, a ruthenium oxide, RuO_2, thermometer and a copper film resistive heater are firmly thermally anchored within a heat-sinking copper block. The purpose of these is to measure the temperature as the experiment cools, to measure the superconducting transition of the Ti-TES and to use with a Picowatt AVS-47 AC Resistance Bridge feedback unit for approximate temperature stabilisation. The resistance of the sensor is measured using a 4-point resistance measurement technique with an AC resistance bridge which regulates the power input to the resistive heater, using a PID (Proportional Integral Differential) temperature controller.

A calibrated Oxford Instruments Cernox sensor is firmly thermally anchored to the mixing chamber of the cryostat directly, to which the RuO_2 sensor is cross-calibrated in the 100 mK – 1 K region. The following expression was fitted to the data in Figure 4.9,

$$R(T) = R_0 exp\left[\left(\frac{T_0}{T}\right)^a\right] \tag{4.22}$$

as given in [95]. This fit yielded a power relationship of $a = 0.281 \pm 0.058$.

4.3.2 Superconducting Transition Curves

Extensive sweeps of the temperature range encompassing the superconducting transition were made, recording the output V_{sq}, at multiple bias currents. This was subsequently converted to resistance according to Eq. (4.20). The width of the transition constrains the dynamic range of the detector. The sensitivity, and ultimately the resolution, depend on the slope of the transition. The shape of the transition was measured with bias currents in the range 0.1 – 25 μA. A selection of the transitions are plotted in Figure 4.10. They exhibited some small broadening and flattening with high bias current, due to self-heating and due to dependence of transition temperature on the field in the superconductor. For clarity, the

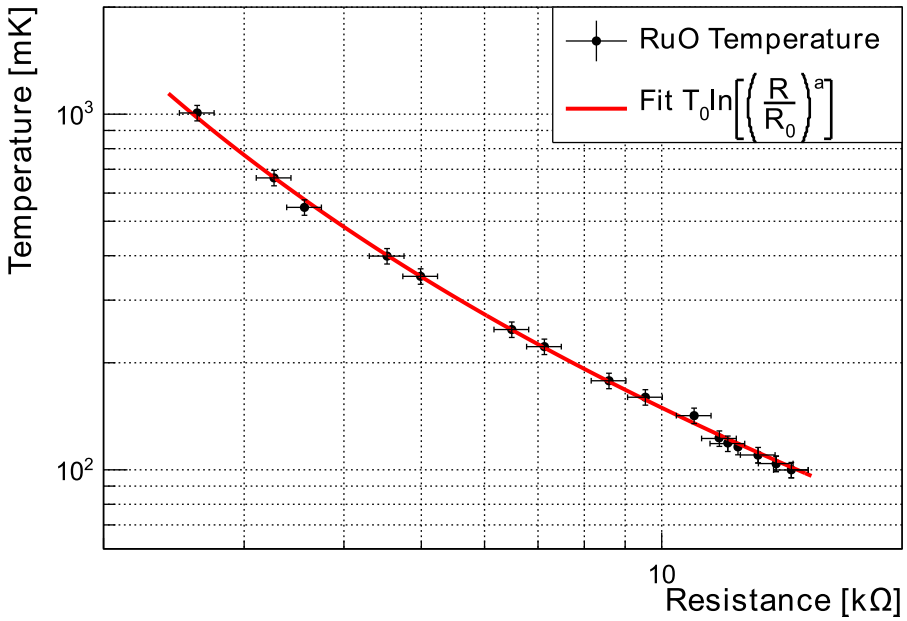

Figure 4.9: Temperature dependence of a RuO_2 resistive thermometer, fitted to the inverse of Eq. (4.22).

temperature axis is enlarged in the inset to display this effect. A temperature hysteresis was seen between cooling and warming, and this is displayed as error bars in the inset of Figure 4.10.

The number of bias currents were selected and optimised by trial and error, taking into account the transition curves recorded, as well as ease of stabilisation and establishment of operation point (see Section 4.3.3). At each established working point, an α spectrum was recorded.

4.3.3 Operating Point & Stabilisation with LED Heater

The detector is roughly stabilised at a working point within the transition, using the resistive thermometer and heater on the experimental plate. Infra-red light is transported from outside the cryostat to the TES sensor via an optical fibre. This fibre is positioned 1 mm above the film inside the cryostat. The LED, at room temperature, is powered by a current source as part of the PID control unit. The stability of the operating point is controlled entirely by hardware, providing a modulation current to the LED circuit. The control circuit

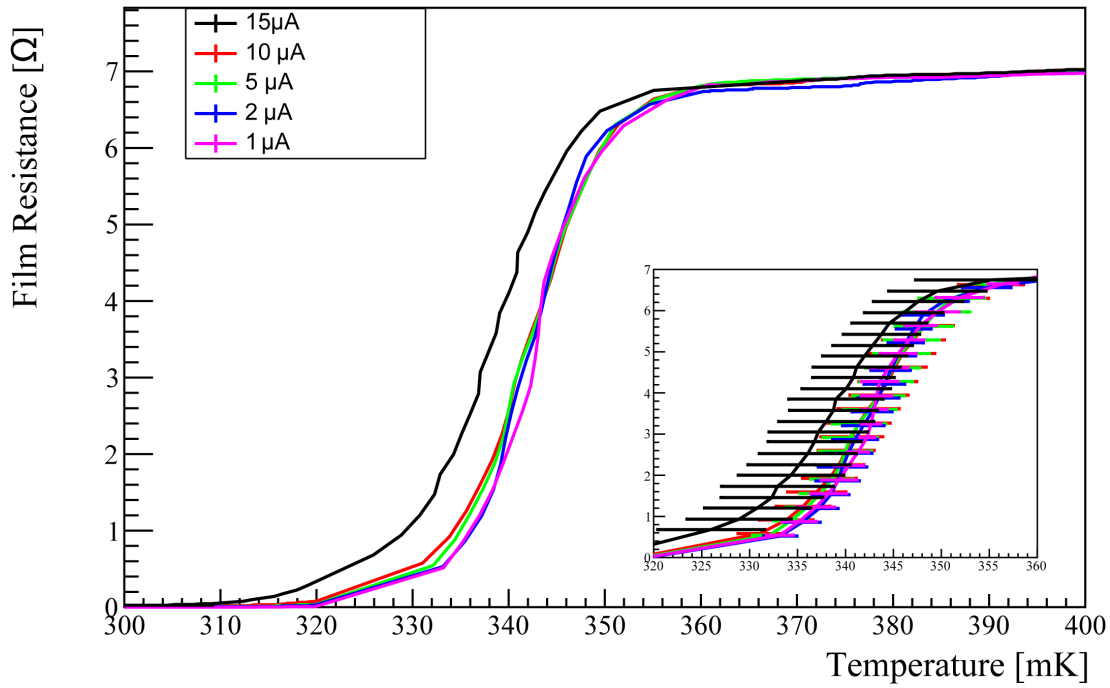

Figure 4.10: Superconducting transition curve, R vs. T, of Ti-TES sensor, with detector bias currents 1 – 15 μA. Inset: the temperature axis is expanded to illustrate the broadening of the transition with bias current. The error bars indicate the width of the hysteresis.

schematic was outlined in Figure 4.6. There are three signals which are input into the PID control unit which contribute to the current supplied to the LED. The first, a DC current provides enough power to overcome the LED band gap. This just switches on the LED and brings the detector into the superconducting transition. The second, a signal proportional to the filtered output from the SQUID, provides an extremely sensitive measurement of, and feedback to, any deviations from working point due to thermal fluctuations. The third, a pulser signal of controlled, varying magnitude, provides a method of characterising the position within and linearity of the superconducting transition. This is a key element for calibrating and characterising the sensitivity of the Ti-TES, and is described in more detail in Section 4.3.4. A software controlled digital-to-analogue converter (DAC) outputs a reference voltage to a commercial Camac Tail Pulse Generator module. The magnitude and frequency of the pulses are controlled by software, while the rise and decay time is controlled by the Tail Pulse Generator.

The standard method of operation point stabilisation is by using resistive gold heaters

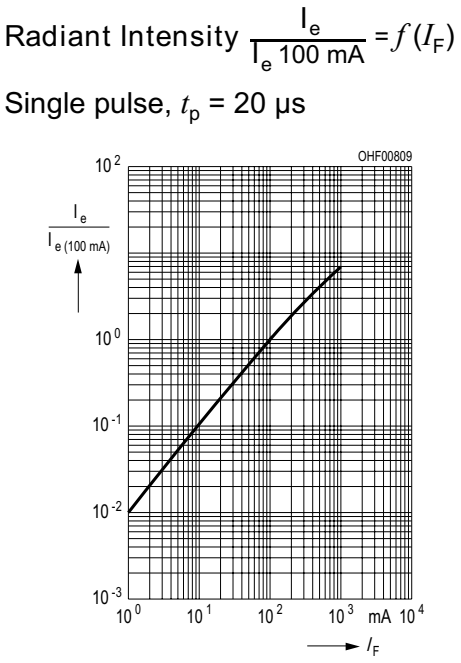

Figure 4.11: Radiant Intensity of LED as a function of forward current [144].

deposited on the sensor, and modulating the power input to these heaters. This is documented by the CRESST experiment in [120]. The method described here, of stabilisation with infra-red light, has been documented by the ROSEBUD dark matter experiment, [143], however there are little details of the success of this novel stabilisation method in the literature. The experiments described here investigate the advantages, disadvantages and efficacy of the method.

The infra-red LED is an OSRAM Opto Semiconductors SFH 4503 High Power Infra-Red emitter [144]. The current supplied was in the 10 – 50 mA region, and has an approximately linear forward-current to radiant intensity relationship, as displayed in Figure 4.11. The absorption and reflectivity of the Ti-TES sensor was not investigated, all that is required for this application is that as sufficient IR radiation is absorbed to heat the film.

In order to investigate the dependency of the sensitivity and resolution on applied bias current, a working point was established at multiple bias currents in the range 5 – 35 μA. A limitation of the control system is the inability to take account of SQUID resets, which occur at when the signal reaches $\pm$10 V, or due to a noise spike, or due to SQUID quantum

flux losses. Thus after each reset, the control system establishes a new working point. This limits continuous comparable data to less than one hour on average. Another limitation of the system is that the entire SQUID output signal is used as the feedback control input, not just its DC baseline. This means that the system attempts to correct for the detector's response to actual particle pulses and to heater pulses. This overcompensation is seen as a dip in the pulse below the baseline after the pulse has decayed. This can be clearly seen in the event in Figure 4.7, and the pulse shape no longer conforms to the model outlined in Section 4.1.1, and plotted in Figure 4.2. The CRESST experiment has an advanced detector stabilisation system with more controllable hardware and software. Ideally such as system should be implemented here if this detector is to be used for cryoEDM. Furthermore, an investigation of filtering on the feedback signal could improve the overshoot. Implementation of an improved stabilisation system was beyond the scope of these investigatory experiments.

Despite these operational limitations, it is clear on inspection of the particle event in Figure 4.7 that the feedback system has provided a shortening of the characteristic decay time of the detector, reducing its decay time from $\sim$10 ms in CRESST type detectors to $\sim$100 μs. As is, this is still at least a factor of 100 times too slow for the repetition rates expected in cryoEDM. However if the decay time could be reduced further by investigating alternative crystals and/or an alternative detector design that is segmented, it may be a feasible option.

As a stabilisation device, and within a stable period where no SQUID resets or quantum flux losses occurred, the LED stabilisation performed well. Figure 4.12 shows the baseline of the SQUID without stabilisation in black, as it fluctuates wildly due to thermal fluctuations of the cryostat. The red trace shows the SQUID baseline once feedback had been implemented. Figure 4.13 shows the spectral density of the signal before and after stabilisation was implemented, showing a suppression of low frequency fluctuations by $\mathcal{O}(10^3)$. Fluctuations above 100 Hz however are of similar magnitude. The infra-red radiation inside the cryostat showed no major adverse affects on the operation of the cryostat, and the temperature of the mixing chamber remained relatively stable.

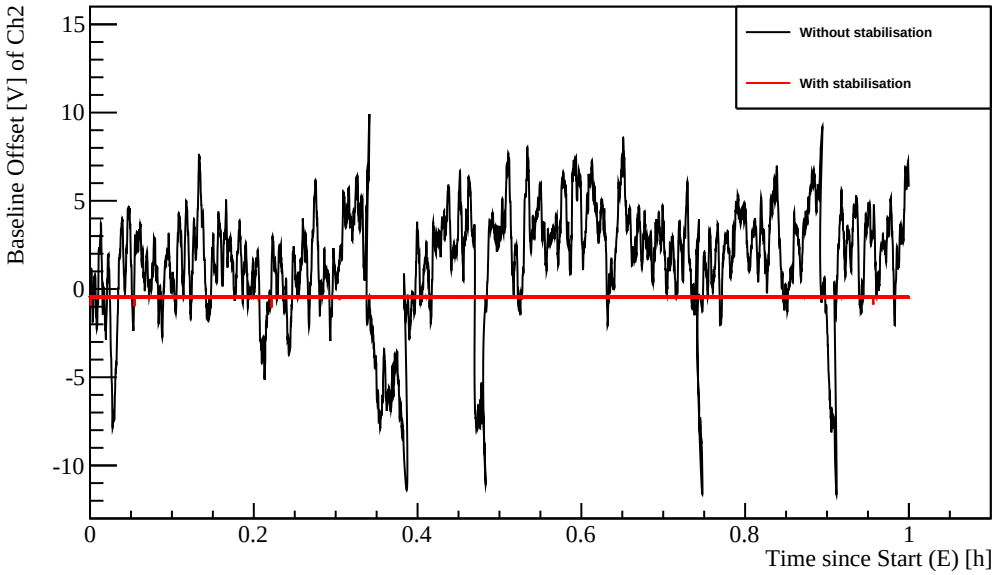

Figure 4.12: Comparison of the stability of the SQUID baseline with and without the LED feedback.

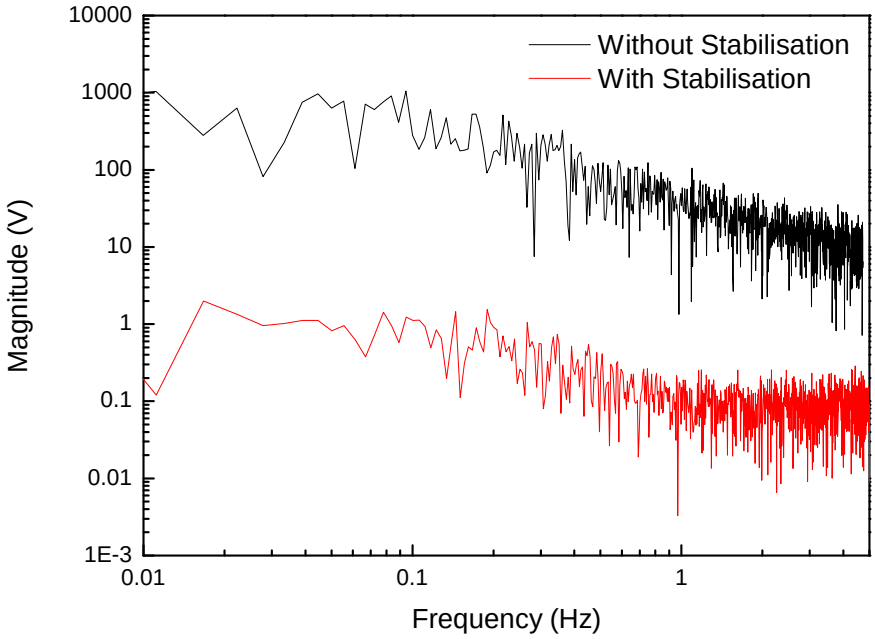

Figure 4.13: Comparison of the spectral density in the low frequency domain of the signal with (black) and without (red) LED feedback indicates a suppression of fluctuations at 1 Hz by $\mathcal{O}(10^3)$.

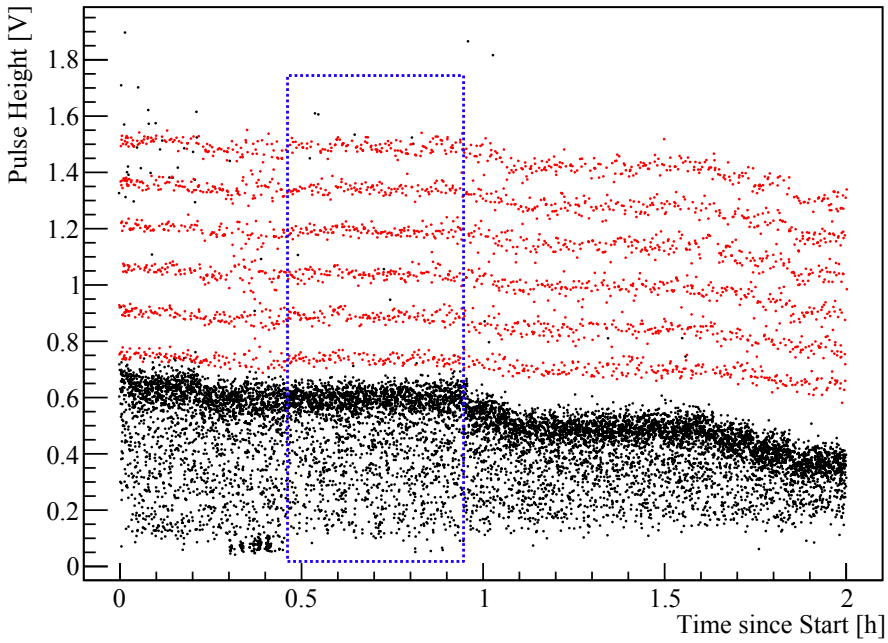

Figure 4.14: Monitoring of the sensor response to Heater Pulses (red) is a sensitive measurement of the stability of the working point. Stable periods can be selected for analysis together (blue). Pulses due to the ^{241}Am source are in black.

Furthermore, LED heater pulses are regularly injected into the system, and the response of the sensor to these pulses monitored over time. This gives a sensitive measurement of any deviations from the working point. Heater pulse events are monitored, and the response *Pulse Height* is used as a cut parameter to select stable periods for analysis. Figure 4.8 shows a typical heater pulse event, with the input pulse voltage to the LED shown in green and the SQUID response shown in blue. The amplitude of the injected voltage pulse from the pulser unit is recorded in the parameter *Test Pulse Amplitude [V]*. These heater pulse events are also used to measure the linearity of the superconducting transition, discussed in Section 4.3.4. Figure 4.14 shows the response of the TES to the heater pulses in red, as a function of time over a two hour period, with a stable period in blue selected for analysis.

4.3.4 Calibration from Pulse Height to Energy

The following section describes the analysis involved in extracting the recoil energy of a given event from the recorded pulse. The functional relationship between the amplitude

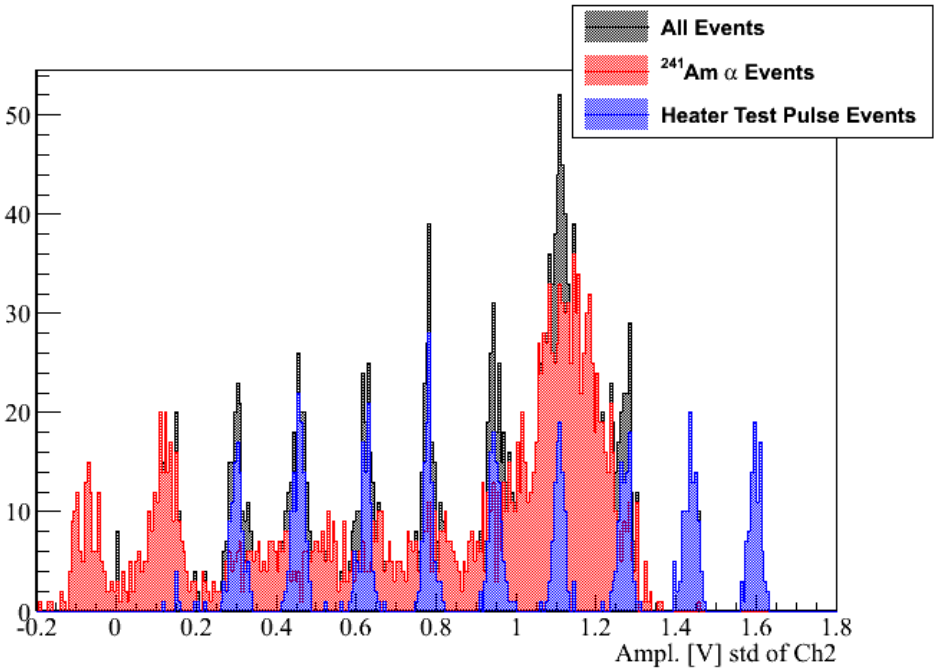

Figure 4.15: Spectrum constructed from the Pulse Height [V] parameter of all events (black), ^{241}Am α events (red) and heater events (blue)

of the pulse and the recoil energy must be accurately determined. For each event, the parameter *Pulse Height [V]* is calculated from a moving average of the signal, and set as the maximum voltage of this average above the baseline. This is done for all events, both particle and heater events. Figure 4.15 shows a rudimentary spectrum constructed from the Pulse Height parameter for both types of events.

However, calculating the pulse height simply by subtracting the baseline from the maximum voltage systematically overestimates the amplitude due to noise on the pulse. For a more accurate estimation of amplitude, a large number of pulses of the same energy, in this case selected from the ^{241}Am 5.5 MeV α peak, are averaged to create a *Standard Pulse*, with a zero baseline and normalised to 1 V. An automatic routine was implemented to select suitable events to average. This includes a cut on parameters *Peak Position [ms]* and *Left-Right Baseline [V]*. This cut removes spurious events caused by pile-up or events triggered purely on noise. A rudimentary Pulse Height Spectrum is then constructed, and events within one sigma of the peak of the spectrum are automatically selected to create the Standard Pulse, as displayed in Figure 4.16. Figure 4.17 shows a typical Standard Pulse for the 5.5 MeV α events.

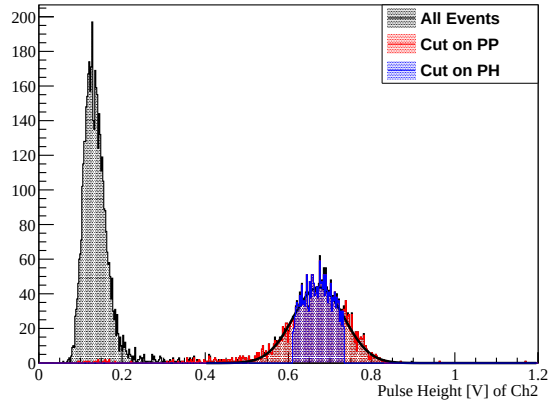

Figure 4.16: Cuts implemented to Pulse Height Spectrum (black- no cuts; red- cut on peak position). Events within 1 σ of the fitted Gaussian peak (blue) are chosen to construct the *Standard Pulse*.

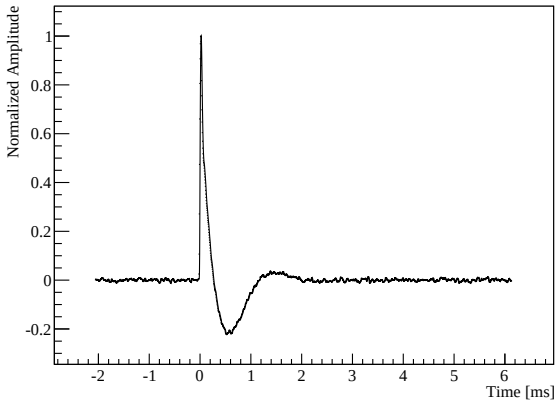

Figure 4.17: A Standard Pulse calculated from 5.5 MeV α pulses within the blue event selection, left.

Finally the normalised Standard Pulse is then fitted to all the particle pulses, and fitting parameters calculated, including a scaling factor, i.e. *Amplitude [V]*. This produces a more robust measurement of the amplitude of the pulse.

The amplitude parameter is only proportional to the energy deposited if one assumes linearity of the superconducting transition of the thermometer. This linearity is approximately true. Furthermore, the amplitude in a linear scheme is constant under fluctuations of operating point, which is not the case for a non-linear thermometer response. Accurate calibration requires the shape of the transition to be measured and the operating point monitored as the particle events are being recorded. This is done by injecting heater pulses via the LED & optical fibre, to the TES sensor, and recording the response. These heater pulses are sent at regular intervals with multiple energies within the approximately linear range of the transition, and essentially simulate particle events of various energy. The injected *Test Pulse Amplitude [V]* is linearly proportional to energy, thus they can be used to convert measured pulse height of a particle pulse to recoil energy. First, the amplitude of the response to these heater pulses is evaluated using a Standard Pulse, as before. A standard pulse is created from heater pulse events with energy near that of the ^{241}Am α events, and can be seen in Figure 4.18, which is then fitted to all heater pulse events. The difference between the

simple Pulse Height parameter for heater events and the calculated pulse Amplitude from the standard pulse fitting procedure can be seen in Figure 4.19.

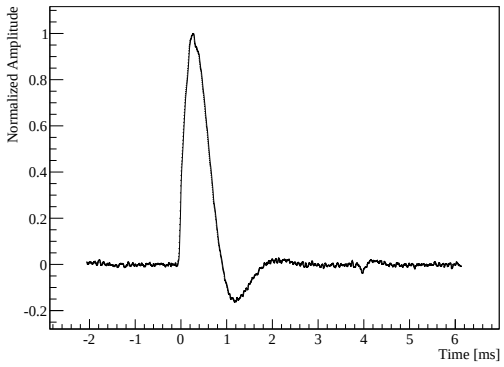

Figure 4.18: Standard Heater Pulse averaged from heater pulse events with energy near that of the ^{241}Am α events.

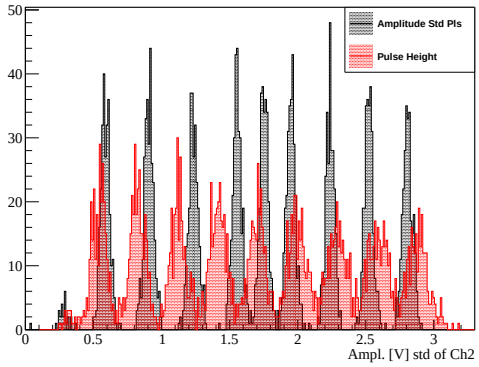

Figure 4.19: Comparison between the simple *Pulse Height* (red) and the calculated *Amplitude* (black) from the standard pulse fitting procedure for heater events.

The amplitude of these events is then plotted against time, and a cubic spline is fitted to define the time dependency of the Heater Pulse Amplitude, Figure 4.20. A set of heater pulses with one given amplitude is presented with an enlarged y-axis in Figure 4.21. The spread in response voltage is due largely to the resolution of the detector, and fluctuations as a function of time are minimal.

At a particular time, T, a polynomial interpolation can be done to define the transfer function between *Amplitude [V]*, and equivalent injected *Test Pulse Amplitude/Energy [V]* for any arbitrary amplitude. For particle pulse occurring at time T, with amplitude A, the equivalent Test Pulse Amplitude can be calculated from this polynomial, i.e the amplitude of a heater pulse that would have created a response with amplitude A. The 5.5 MeV ^{241}Am α line is then used to calibrate the heater. As the injected Test Pulse Amplitude is linearly proportional to energy, the constant of proportionality is extracted by calculating the equivalent Test Pulse Amplitude for the α peak, Figure 4.22. For any injected heater pulse the equivalent particle energy can be calculated with this method, Figure 4.23, and a particle and heater pulse energy spectrum made, as seen in Figure 4.24. Thus for any particle interaction of any energy in the calibrated range, *Amplitude [V]* is converted to *Energy [keV]*, from a combination of the heater pulses and calibration sources.

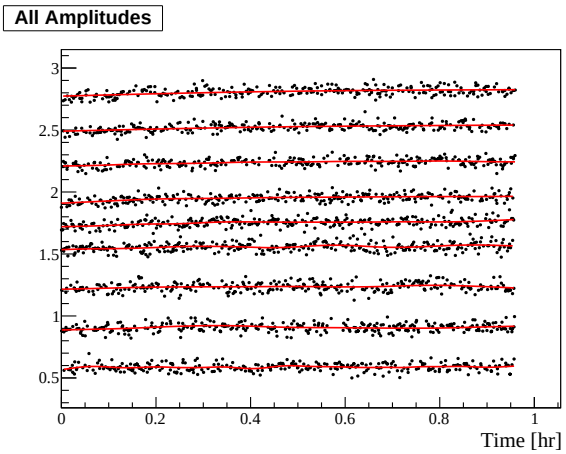

Figure 4.20: Cubic Splines fitted to Heater Pulse Amplitudes, for all sets of injected Test Pulse Amplitude.

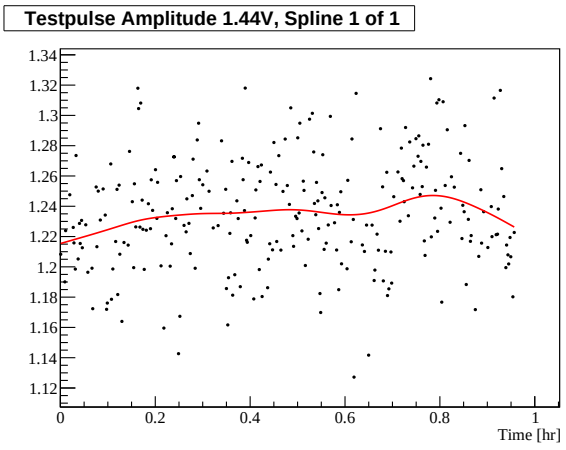

Figure 4.21: A cubic spline fitted to heater Pulse Amplitudes, at a single injected Test Pulse Amplitude.

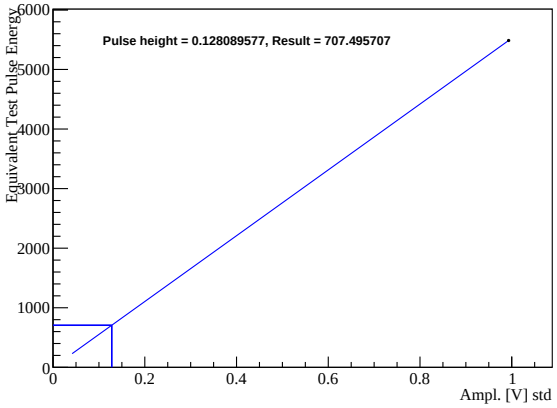

Figure 4.22: With a known transfer function from Amplitude to equivalent Heater Pulse Amplitude, and a calibration point (5.5 MeV ^{241}Am α), particle pulse Amplitude is converted to Energy [keV]

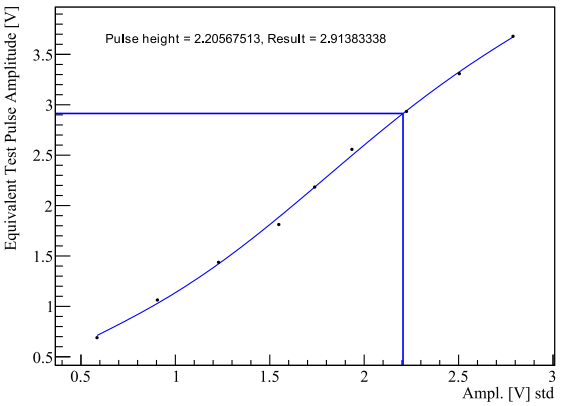

Figure 4.23: At a particular time, T, a polynomial interpolation defines the transfer function from Amplitude to equivalent Heater Pulse Amplitude.

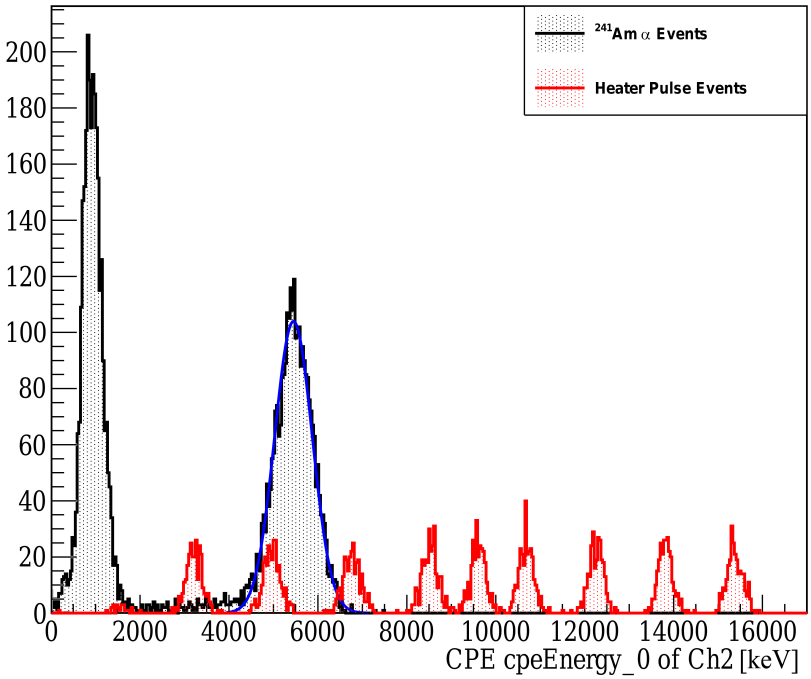

Figure 4.24: Calibrated ^{241}Am α particle energy spectrum (black) with the 5.476 MeV peak fitted with a Gaussian (blue). The low energy peak is due to noise. The equivalent energy spectrum of injected heater pulses is seen in red.

4.3.5 Energy Spectra & Resolution at 5.5 MeV

The calibration routine was implemented for data sets recorded at multiple working points, with bias currents in the range 5 – 35 μA. A calibrated energy spectrum was recorded at 16.6 μA and is displayed in Figure 4.24. A Gaussian is fitted to the peak and the resolution, given by the full width at half maximum, is calculated as 17.9% at 5.476 MeV, for this particular working point.

This procedure was repeated for many working points and bias currents to investigate the dependency of resolution on bias current. One would expect to see an improved resolution with increased detector bias current, however with an uncollimated source, there is no trend seen. In this configuration, the resolution is dominated by the position dependency of the detector. Phonons may not be fully thermalised in the absorber, but may also have thermalised in the detector clamps. Thus particles which had interacted near the centre of the absorber will have more thermalised phonons in the absorber. To test this hypothesis, a collimator was installed between the source and the absorber, so that all α particles would interact with the crystal very close to its geometrical centre. In this case, there is some trend of improving resolution with increasing bias current, although not very significant. Refer to Figure 4.25, to see this dependency. For a given bias current, the resolution seems to vary largely with the stability of the working point, for example varying from 19% to 40% with a bias current of 22.5 μV. The best measured resolution was 11% at 27.5 μV.

It is clear from the results that the resolution at a given bias current is dependant on the operating point within the superconducting transition, and the stability of this operating point. After a SQUID reset, the hardware re-stabilises at a new operating point, and thus a different pulse height - energy relationship. An improvement in the stabilising electronics and software would be necessary to increase the resolution further and to improve the ease of operation.

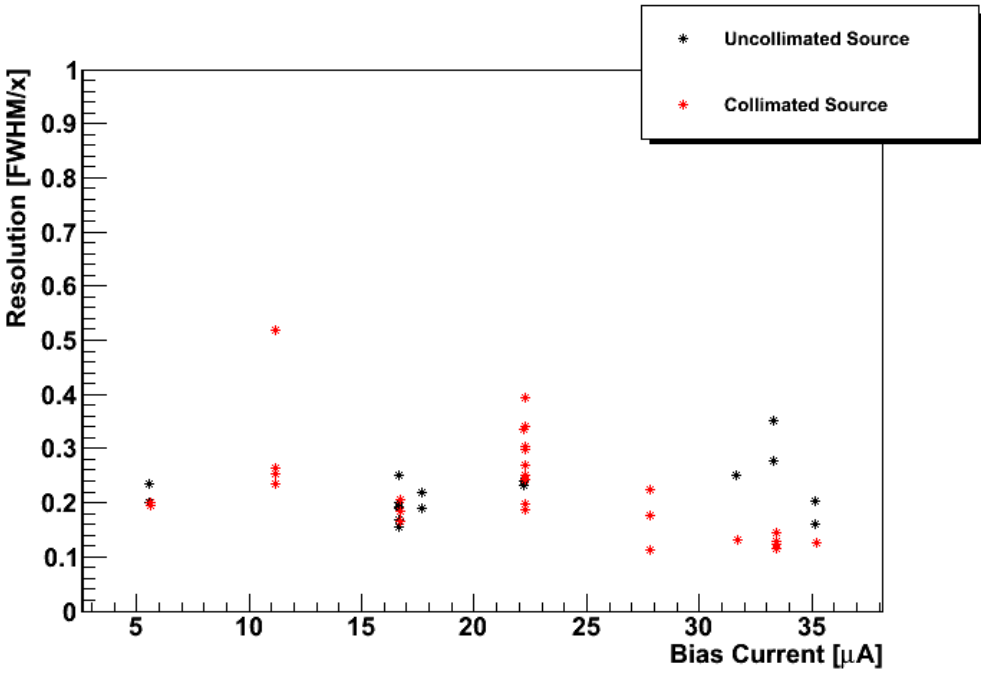

Figure 4.25: Fractional resolution at 5.476 MeV for Al_2O_3-Ti TES detector to α particles, and its dependency on detector bias current. The multiple points at a given bias current are recorded at different operating points in the transition.

4.4 Conclusion

This experimental demonstration has proven that the phonon channel of a CPSD detector with a titanium TES sensor can be operated at the transition temperature of titanium, 350 mK. It has been stabilised in the transition with the novel method of using infra red light via optical fibre. The detector has been able to measure an ^{241}Am α spectrum at 5.5 MeV with a best resolution of 11%.

For these detectors to be viable as a UCN detector in cryoEDM, they must meet the requirements as outlined in Table 3.1. It has been demonstrated that they will function at 350 mK and could easily be adapted to work at the cryoEDM operation temperature of ∼500 mK. The combination of a ^{6}Li UCN conversion film would be the most suitable method, as the detection of the MeV energy reaction products would be much easier than the neV energy UCN. These detectors have excellent intrinsic resolution and pulse shape discrimination capabilities, and the α and triton from the ^{6}Li reaction would be well clear from any noise. Further research would be required to demonstrate these capabilities with

installation of a separate light detecting module to capture the scintillation light.

A success of this demonstration was the integration of thermal feedback with an infra-red LED, which significantly shortened the detector response time. This module has a phonon pulse decay time $\sim$100 μs, which would allow a neutron count rate of 10 kHz. Although this is 50 times slower than required for the neutron count rates expected at cryoEDM, further improvements would be possible. Multiple small absorbers, such as the one presented here could be operated as separate modules, reducing the interaction rate by possibly a factor of 10. Investigation into different absorber materials may also improve the decay time. Operation in constant voltage bias mode is also known to shorten the response time [139], and this could be investigated.

For operation over longer time scales, more reliable operation and an improvement in resolution, a more advanced software based stabilisation system would be required. Squid resets, flux jumps or noise spikes need be identified as such, and the operation point maintained. Limitations met in this demonstration due to outdated and non-adaptable control hardware meant that stable working points were usually limited to 1 hour or less, depending on the noise environment in the laboratory. This resulted in limited statistical sets from which a spectrum could be constructed. This would need to be rectified for feasible integration into the cryoEDM experiment and straight-forward detector operation.

As the operation of SQUIDs is challenging, and correcting for SQUID resets and flux jumps would need to be implemented in a new stabilisation system, it may be worth investigating other low temperature readout methods instead. The very low impedance of TES sensors requires a low impedance readout circuit, such as that provided by a SQUID. However there are alternative high impedance cryogenic thermal sensors available, such as a semiconductor thermistor. They have a large negative temperature coefficient α from Eq. (4.10). That, coupled with their high impedence of $\mathcal{O}(\mathrm{M}\Omega)$ means can be operated in constant current mode (Eq. (4.15)), with the signal read out as a change in current. These sensors do not require as precise stabilisation as a TES, and do not require SQUIDs. For example, NTD-Ge sensors with Germanium absorber crystals at 20 mK are currently used

in the Edelweiss dark matter experiment [145] [146].

While there is lots of scope for investigation of improvements to CPSD to make them more suitable for cryoEDM, the major drawback remains that they must be run in a vacuum. Integration of a further vacuum can into the restricted experimental volume in cryoEDM would be difficult, but not impossible. However the transport of the UCN from the superfluid volume into a vacuum region would require a window, which immediately introduces significant losses. Ultimately, gains in detection efficiency due to the ability of the CPSD to reject γ background and clearly detect the α and triton reaction particles of the UCN capture on ^{6}Li would be heavily offset by losses of UCN in the aluminium window entering the detection volume. Although gains are being made in the efficient transmission of UCN through appropriate windows in current research, these detectors are not the best option available as an alternative UCN detector for cryoEDM.

Although CPSD are a capable, promising and interesting technology, ultimately their complexity mean they are less suitable for this application than say a simple scintillation detector. For these reasons, it was decided that CPSD would not be a viable detector to replace the solid state detectors and would be unlikely to offer any improvement in UCN counting efficiency, particularly due to losses at any windows and its inability to deal with high count rates.

Pure scintillation based detectors may offer a simpler solution, with fast repetition rates and the capability of being run within the superfluid volume. The search for an alternative UCN detector for cryoEDM was now focussed on identifying a scintillator suitable for this application, which may meet the requirements laid out in Chapter 3.

Chapter 5

Characterisation of Fast Scintillators at Low Temperature

Scintillators have been identified as one of the most promising technologies as a low temperature solid state ultra cold neutron detection method for cryoEDM. Scintillators are often used as a stand-alone detection mechanism in room temperature experiments in particle and nuclear physics. However we know from their use in CPSD that the properties of many conventional scintillators change markedly upon cooling, and in particular significant slowing of their decay time and reduction in their light yield, known as quenching, may render them ineffective for this application. In this chapter, an outline of the necessary properties of scintillation materials suitable for a cryogenic UCN detector is made, followed by a review of commercially available scintillation materials, focusing on these properties. A comprehensive study of the scintillation light yield to α particles as a function of temperature to 6 K is made. A spectral study of their luminescence under VUV (vacuum ultraviolet) excitation at low temperature reveals the emission energy levels and allows for an understanding of the underlying physics of the given material. Finally an analysis of the temperature dependence of the decay time kinetics of the potential materials is made. A discussion of their relative merits at low temperature leads to the conclusion of the most suitable material(s) for use in the prototype low temperature UCN detector developed in the following chapter.

5.1 Shortlisting Suitable Materials

Over the last decades, there has been extensive development of, and investment in, fast scintillators with $\mathcal{O}(ns)$ decay times that retain high light output, and high stopping power. This has been motivated largely by the advancement of medical imaging technology, such as Positron-Emission-Tomography (PET) and Single Photon Emission Computed Tomography (SPECT), and also in high-luminosity hadron colliders for high energy particle physics (HEP) research. While each application has significantly different detector requirements, and thus scintillator requirements, there are some common basic specifications they all generally meet. These are a fast response time (<100 ns), a high light yield (>10,000 photons per MeV γ), a high density ρ, and a high atomic number Z (as photoelectric absorption $\propto \rho Z^n$, n = 4–5) [126]. Published studies of novel scintillators have focused around optimising these requirements.

The requirements in a scintillator for a cryoEDM neutron detector were outlined first in Chapter 3. These requirements are not always similar to that for which the materials have been developed for, and so the relative merits must be assessed. A common thread throughout the search for better scintillating materials, across all applications, is a **high light output**. It is important that the number of photons produced is large, as typically only a small percentage of the photons created in the scintillation event are detected due to low light collection efficiency in many detection systems. The brightest scintillators emit up to 80,000 photons / MeV γ interaction. For a UCN scintillation detector, the conversion processes described in Section 3.1 will be used, for example in a ^{6}LiF thin film or ^{10}B loaded scintillator. Ensuring the light signal remains high for these heavy ionisation products will mean the signal is more clearly distinguished from any low energy γ background.

Many inorganic and organic commercially available scintillators have **fast sub-microsecond decay times**, and it is a strong focus in the development of novel scintillators to produce faster and faster decay times, in the ns region. Cerium-doped Halides or Oxides are common commercially available inorganic fast scintillators developed for medical imaging, which have a decays times less than 100 ns. Plastic scintillators are also very fast with

decay times of ∼1 ns. They offer the huge advantage of ease of moulding or machining, and although they have a reduced light output relative to many inorganic crystals [105], they are widely used in areas such as large area calorimeters in particle physics. In cryoEDM we require fast neutron counting rates of 500 kHz, as described in Section 3.3.1, and so a suitable scintillating material must have a decay time of <1 μs to be able to cope with these repetition rates without pile-up becoming a problem. This decay time is relatively slow compared to the current scintillation research focusing on sub–ns scintillators, which allows a wide range of materials to be considered.

For medical imaging and HEP detectors, high density and high Z materials are required for stopping power of high energy photons and particles. As cryoEDM is concerned about the relatively low energy decay daughter products of ^{6}Li(n,α)^{3}H, these requirements are of less relevance to us, as outlined in Chapter 3. In fact, the very high ionizing power of heavy ions often induces quenching effects which result in a reduced light output. A suitable scintillator for this application should retain its **high light output when excited by α particles**. Furthermore, we wish to reduce sensitivity to background γ radiation, and so focus on the **lower density** scintillating materials to reduce the photoelectric absorption cross–section, rather than the typical high density materials for medical imaging. This was taken into account during the material review.

Often, many scintillators low light output at room temperature and an increased light output when cooled. This is known as temperature quenching, and significant progress has been made in scintillator development to reduce this effect in order to maintain a high light output and enable the use of common scintillators without the need to cool to low temperature. However for our requirements, it is precisely the **low temperature luminescence characteristics** that are of importance, and must be quantified in order to choose the most suitable material. Decay time slowing is commonly exhibited by materials upon cooling. We must ensure that there are no low temperature quenching effects that decrease the light output or slow the decay time at cryogenic temperature. A search for any published low temperature studies of suitable materials was done, focusing on materials that remain fast

with high light output upon cooling.

Scintillators may have a fast and a slow component to their light output, (see Appendix B for mechanism). The high $\frac{dE}{dx}$ of heavy ions can result in a reduction of the fast component relative to the slow component, increasing detector dead-time. However, as long as the slow component remains less than one microsecond, this may actually be a beneficial characteristic, as the overall decay time constant varies with the type of incident particle. Such scintillators enable **pulse shape discrimination (PSD)**, i.e. particle identification based on the signal's decay characteristics, and background γ events may be rejected using this method. A search for any published pulse shape discrimination studies of suitable materials was done.

All these considerations are summarised in Table 5.1. With these in mind, and the requirements outlined in detail in Chapter 3, a literature review of potentially suitable materials has been made and is presented in the following sections.

Considerations for a Suitable Scintillator
(1.) Light output >10000 photons / MeV
(2.) Decay time <1 μs
(3.) High sensitivity to α / low quenching factor
(4.) Low sensitivity to γ / low atomic weight
(5.) No degradation in qualities at low temperature
(6.) Potential for pulse shape discrimination

Table 5.1: Requirements for a suitable scintillator

5.1.1 Inorganic Scintillators

A table of commonly used inorganic scintillation materials is listed in Table 5.2 which is adapted from that published in Knoll [105]. This includes alkali halides, slow scintillators, non-activated fast scintillators, cerium activated fast scintillators and glass scintillators. All these materials rely on the crystal lattice of the material to produce scintillation photons. The luminescence mechanism is outlined in Appendix B. They often rely on a dopant atom to provide a luminescence centre in the crystal which boosts its scintillation efficiency

greatly above that of the intrinsic crystal. This table is a useful reference which indicates the light output per MeV for γ interaction, decay time(s) and density (relative to water). It also indicates the pulse height in a PMT which also takes into account how well the given scintillator's emission spectrum is matched to a Bialkali–Cathode PMT sensitivity spectrum.

Alkali Halides

Alkali Halide crystals, such as NaI(Tl) and LiI(Eu) offer some of the brightest scintillators available. Inorganic scintillators' light output is typically measured as % NaI(Tl), due to its historical dominance as the brightest scintillator available. They have remained dominant in the field as they offer high light yield and a large crystal size at low cost. As well as having high light output, they have moderate decay times of <1 μs at room temperature, and relatively low density. CsI(Tl) shows good $\alpha - \gamma$ PSD capabilities, as tabulated in Table 5.2. Of particular interest is LiI(Eu) which is used as a low energy neutron detector. Unfortunately low temperature studies indicate significant slowing of the decay times of these materials at cryogenic temperatures, as well as a reduction in light yield [147] [126]. Furthermore, the surfaces of these materials are highly hygroscopic and thus can be very difficult to work with. They often come pre-packaged in an air tight container. This introduction of a material barrier is not desirable when dealing with neutron irradiation as there will be neutron losses as they absorbed in said material. These materials are concluded to be unsuitable for further application to this project.

Slow Inorganic Crystals

Other slow inorganic crystals include BGO and $CaWO_4$ and are tabulated in Table 5.2. These have high density and thus high sensitivity to γ radiation, and have been employed in X-ray counting, PET scanners, and dark matter searches. They also exhibit decay times at cryogenic temperatures much slower than the required counting rates for cryoEDM [148] [149]. Two interesting materials in this category are ZnS(Ag) and CaF_2(Eu).

Table 5.2: Properties of Common Inorganic Scintillators [105]

	Specific Gravity	Wavelength of Max Emission (nm)	Refractive Index	Decay Time (μs)	Abs. Light Yield in Photons/MeV	Relative Pulse Height with Bialk. PMT
Alkali Halides						
NaI(Tl)	3.67	415	1.85	0.23	38,000	1.00
CsI(Tl)	4.51	540	1.80	0.68 (64%), 3.34 (36%)	65,000	0.49
CsI(Na)	4.51	420	1.84	0.46, 4.18	39,000	1.10
LiI(Eu)	4.08	470	1.96	1.4	11,000	0.23
Other Slow Inorganics						
BGO	7.13	480	2.15	0.30	8,200	0.13
$CdWO_4$	7.90	470	2.3	1.1 (40%), 14.5 (60%)	15,000	0.4
$CaWO_4$	6.1	420	1.94	8	15,000	
SrI_2(Eu)	4.6	435		1.2	85,000	
ZnS(Ag)(polycrystalline)	4.09	450	2.36	0.2		1.3[1]
CaF_2(Eu)	3.19	435	1.47	0.9	24,000	0.5
Unactivated Fast Inorganics						
BaF_2 (fast component)	4.89	220		0.0006	1400	na
BaF_2 (slow component)	4.89	310	1.56	0.63	9500	0.2
CsI (fast component)	4.51	305		0.002 (35%), 0.02 (65%)	2000	0.05
CsI (slow component)	4.51	450	1.80	multiple, up to several μs	varies	varies
CeF_3	6.16	310, 340	1.68	0.005, 0.027	4400	0.04 to 0.05
Cerium-Activated Fast Inorganics						
GSO	6.71	440	1.85	0.056 (90%), 0.4 (10%)	9000	0.2
YAP	5.37	370	1.95	0.027	18,000	0.45
YAG	4.56	550	1.82	0.088 (72%), 0.302 (28%)	17,000	0.5
LSO	7.4	420	1.82	0.047	25,000	0.75
YSO	4.54	420		0.070	24,000	
LuAP	8.4	365	1.94	0.017	17,000	0.3
$LaCl_3$(Ce)	3.79	350		0.028	46,000	
$LaBr_3$(Ce)	5.29	380	2.05-2.10	0.026	63,000	
Glass Scintillators						
Ce activated Li glass[2]	2.64	400	1.59	0.05 to 0.1	3500	0.09
Tb activated glass[2]	3.03	550	1.5	~3000 to 5000	~50,000	na
For comparison, a typical organic (plastic) scintillator:						
NE102A	1.03	423	1.58	0.002	10,000	0.25

1. *for α particles*
2. *Properties vary with exact formulation.*

Source: Data from References within Knoll [105].

ZnS(Ag)

ZnS(Ag) is an α counter with a very high scintillation efficiency and a light output comparable to NaI(Tl). Zinc sulfide activated with Ag^+ ions is one of the oldest known scintillators, known for its exceptionally bright blue light output under excitation with high energy photons, electrons or ions. It is one of the most efficient scintillators, with ∼20% of absorbed energy converted into visible emission, resulting in a high light yield equivalent to 75,000 photons/MeV γ [150].

It is typically used in thin films as it is opaque to its own scintillation, and is commonly used in thin screens for α detection. It shows excellent sensitivity to α particles with low sensitivity to γ radiation. The α/β ratio for a scintillator is the ratio of the light signal to incident α and β (or γ, which produces an e^-/β upon interaction) radiation of the same energy. For ZnS(Ag), this ratio is ∼2, indicating it is twice as sensitive to α radiation as it is to γ. This is particularly promising for our application, as light yield is typically reduced for heavy ion interactions compared to γ interactions in many scintillators. As such, it is worth considering this inorganic phosphor that is known to be an efficient heavy ion converter.

When mixed with ^{6}LiF, it has been used in detectors at large scale neutron facilities such as the ISIS neutron spallation source in Oxfordshire, JParc neutron spallation source in Japan, and SNS spallation source at ORNL, USA [129] [151] [152], in conjunction with fibre optic readout to produce position sensitive detection. It has also been developed in other commercial systems, such as by the Mars Project that provides high performance, yet cost effective, detector systems of neutrons for defence and industry [153] [154].

It has a fast component to the decay time of $\mathcal{O}$(100 ns) at room temperature. However it also exhibits longer decays times of 1 μs and phosphorescence of up to a millisecond and above. This slow phosphorescent component corresponds to the thermal release of electrons from traps into the conduction band, and varies with the manufacturing process of the sample. With electron or γ excitation there is a fast component of ∼10 ns, allowing for pulse shape discrimination [155]. To ameliorate the problem of the slow component, an

alternative segmented detector design could reduce the count rate to the necessary value, as its light yield is so high, as detailed in Chapter 3. This is demonstrated in neutron detectors at neutron scattering facilities, such as by Wang et. al at SNS at ORNL [152]. Rates of 35,000 counts per second for neutron counting have been demonstrated using a pixelated ZnS(Ag)/^{6}LiF scintillator read out with WLS fibres coded to multiple PMTs.

Its scintillation properties have been studied at length at room temperature [156][157], however no low temperature properties have been published to date due to a lack of motivation for cryogenic application. This material warrants further study for this application and a sample was obtained from the detectors group at ISIS.

CaF_2(Eu)

CaF_2(Eu) is notable as a non-hygroscopic inert inorganic scintillator. Its luminescence properties at room temperature meet requirements (1.) and (2.) in Table 5.1 and it has a low density and low atomic weight and so has a low sensitivity to γ radiation, especially when used in thin films. Eu^{2+} provides the activation centre, with the 5d – 4f electron transition producing luminescence centred at 435 nm. Its relatively long decay time of 900 ns has inhibited its widespread use, however if this decay time does not become slower at low temperature, it is within a suitable range for cryoEDM.

It has been used in studies of bolometers for neutrinoless double–β decay experiments [158] and WIMP searches [159] and has shown $\alpha - \gamma$ discrimination capabilities when combined with measurements from a phonon channel [160]. The light yield of CaF_2(Eu) when irradiated with α and γ particles has been studied to mK temperature as part of research for double–β decay bolometers for the experiment Cuore [159]. Although this paper showed the light yield at 20mK reduced by $\sim$50% from that at room temperature, it is likely that this is due to a slow component to the luminescence being undetected by the apparatus, causing a measured reduction in light yield [161].

No studies of the decay time characteristics at low temperature are known to be published,

and a sample was obtained for Hilger Crystals [162] to complete a thorough study of its suitability as a low temperature heavy ion scintillator.

Unactivated Fast Inorganic Crystals

The unactivated fast inorganic crystal BaF_2 has a emission component in the UV with a decay time of less than 1 ns. It also has a component with 630 ns which dominates at low temperature and slows to many μs. At high count rates, the build-up of the slow component intensity creates a persistant signal that may interfere with clean detection of the fast component. For this reason it is not suitable in our application. Unactivated CsI also has a fast decay component however the light output is weak. At low temperature this becomes much brighter; however, the decay time slows to over 1 μs [163], and so is not being studied further.

Cerium has commonly been used as an activator in other inorganic crystal scintillators, providing the luminescence centre. However it also acts as an intrinsic scintillator in Cerium Halides. These materials include CeF_3, $CeCl_3$ and $CeBr_3$ which have been developed for X– and γ–ray spectroscopy due to the relative high atomic number of cerium (Z = 58). As well as this unsuitable quality, these crystals, like the alkali halides, are hygroscopic. While they have promise for high energy spectroscopy, they are less suitable for cryogenic heavy ion or UCN detection.

Cerium Activated Fast Crystals

When incorporated in crystals as an activator, cerium acts as the luminescence centre that causes the scintillation light emission. The energy deposited in the crystal by the impinging radiation is transferred to the cerium ion activator site, Ce^{3+} where it undergoes a transition from the 5d to 4f states [105]. The cerium decay time is in the 20 – 80 ns range, depending on the host crystal. Rare earth halides and rare earth oxides are the most common host crystals for cerium activation. They are often combined with lanthanum, gadolinium

and lutetium which results in a high effective Z and density, and has led to them being exploited in PET scanners. These cerium-doped orthosilicate materials include LYSO(Ce) *($Lu_{1.8}Y_{0.2}SiO_5(Ce)$)*, YSO(Ce) *($Y_3Al_5O_{12}(Ce)$)* and LSO(Ce) *($Lu_2SiO_5(Ce)$)*, which show good light yield and decay times, as listed in Table 5.2, and this remains true even at low temperature [164].

Lutetium has a high atomic weight, so the materials not containing this element would be more suitable for cryoEDM application. Natural Lu contains 2.6% ^{176}Lu which undergoes radioactive decay, adding an undesirable intrinsic background. Thus YSO(Ce) is of most interest, with a relatively low density of 4.45 g/cm^3. Samples of LYSO(Ce) and YSO(Ce) were obtained from Crytur [165] for further investigation. Their luminescence characteristics have been studied comprehensively to low temperature and their fluorescence mechanisms well understood. A review of the role of cerium in these crystals is available in [166], and studies of LYSO(Ce) and YSO(Ce) to low temperature available in [167] [168] and [169] [170] respectively.

Yttrium Aluminium Garnet *($Y_3Al_5O_{12}$)*, known as YAG, has a long history doped with neodymium as a laser material. However when grown as a single crystal doped with cerium as an activator, it becomes a useful scintillation material. It has a light yield of about 50% NaI(Tl) and is unusual in that it emits primarily in the green band, at 550nm, a longer wavelength than most scintillators. This creates difficulty for matching it to the sensitivity of PMTs, but may be read out with semiconductor photodiodes. What is interesting about this material is that it shows multiple components to its decay. It has decays times of 88 ns and 302 ns at room temperatures, where γ radiation primarily excites the faster component, and α radiation primarily excites the slower component. Thus it is a promising material for pulse shape discrimination and γ background suppression [171]. It also has a relatively low densities for a cerium-activated single crystals at 4.55 g/cm^3. A sample of YAG(Ce) was obtained from Crytur [165] for further study. It too is a well studied and characterised material and a low temperature study is available at [172].

Glass Scintillators

Glass scintillators containing ^{6}Li and activated with cerium are commercially available and widely used in neutron detectors, as was discussed in Chapter 3. They can be bought enriched to over 95% with either ^{6}Li or ^{7}Li for maximal or minimal neutron sensitivity. The cerium activator produces fast scintillation light typical of Ce^{3+} sites as seen in the fast crystals discussed above. The light output is low, with only ∼3500 photons/MeV for fast electrons or γ, and lower by a factor of 10 for α particles or neutrons [173]. This very low light yield may limit the material to high efficiency read out methods where a large fraction of the photons are counted. None the less, it is of interest due to its fast decay time, ease of manufacture into arbitrary shapes and its embedded ^{6}Li content. It also has a low density, so if kept thin, the γ sensitivity may be reduced. It has been used as a neutron monitor at the ISIS neutron facility [174] and it has been investigated as a room temperature UCN detector material [74]. Ban et. al. report promising results with this material as an efficient UCN detector. They have kept the thickness small effectively reducing γ sensitivity and used sandwiches of enriched and depleted ^{6}Li glass to minimise edge effects, where only one reaction product is captured. A sample was obtained from the Neutron Detectors Group at the ISIS factility for further investigation at low temperature.

5.1.2 Organic Scintillators

Organic scintillators are most widely used in the form of liquids or plastics. The luminescence occurs due to transitions in the energy level structure of a single molecule and thus is not dependent on the physical state, as inorganics depend on the crystal lattice. The luminescence mechanism is described in Appendix B. This is extremely practical as the flourescent molecule can be developed into a solid polycrystalline material, a plastic, a liquid or a vapour.

While polycrystalline solid organic materials have been widely and historically used for particle detection, the materials are fragile and difficult to obtain in large sizes and show

variation in scintillation efficiency depending on the orientation of the radiation relative to the crystal axis due to anisotropy [105]. Common materials in this category are Anthracene, Stilbene and p-terphyenyl. Anthracene has the highest scintillation efficiency of any organic scintillator, and materials' light yield are often compared to it.

More commonly, an organic scintillator is dissolved in a solvent to produce a solid **liquid scintillator** or a solvent that is then polymerized to produce a **plastic scintillator**. Liquids are often deployed in large volume detectors such as neutrino experiments or fast neutron detectors. Liquids have been excluded from this review as the difficulties of containing a liquid once again would require the incorporation of a neutron window into the design, and would likely freeze. Plastics are formed by dissolving the appropriate organic scintillator, typically some polyphenyl hydrocarbon such as n-terphenyl (PPP), PBD, butyl PBD, PPO or POPOP, in an aromatic plastic base such as PVT, Polystyrene or Polymethylacrylate (PMMA). They can be shaped, fabricated, moulded or machined with ease and so have become extremely popular and useful. The different plastic scintillators are manufactured by varying the solvent material, the solute materials and its concentration and any wavelength shifting chemical to promote efficient transfer of energy from the absorber molecule to the scintillating molecule. This process of producing a plastic scintillator with the desired luminescent characteristics is outlined in detail in [126].

There is a large selection of commercially available plastic scintillators available, with various decay times in the range of 0.7 ns to a few hundred ns, different attenuation lengths in the order of 100 – 200 cm, different peak emission wavelength, usually in the blue region, different stopping power often increased by loading with lead for γ stopping power or boron for neutron conversion. They have been widely adopted in particle physics measurements due to the ease of manufacture on a large scale and their affordability, and significant work has been done to improve the attenuation properties and also their hardness to radiation damage [175]. No studies of their scintillation light output and decay time properties at low temperature have been published, and so have been undertaken in this thesis.

A table of commonly used plastic scintillation materials is shown in Table 5.3 which is

adapted from that published by Knoll in [105]. The two leading manufacturers are Eljen and St Gobain, and the manufacturer name of the material is given in columns 2 and 3. The light output is given as % Anthracene, where NaI(Tl) = 230% Anthracene for comparison to Table 5.2. Plastic scintillators meet the requirements for high light output, fast decay time and low density and thus insensitivity to γ radiation as stated in Table 5.1.

Samples of the materials highlighted in yellow were obtained for further testing, to determine their relative sensitivity to α radiation, their low temperature characteristics and whether they exhibit pulse shape discrimination potential. Samples of St. Gobain BC400, a general purpose material, BC408 with longer attenuation length, and BC418 an ultra-fast premium plastic with short attenuation length were obtained. Samples of Eljen EJ204, a general purpose scintillator with the highest scintillation efficiency, delivering both a fast decay time and good attenuation length, and EJ254, which is loaded with natural Boron (5% by weight) were also obtained. The isotopic fraction of ^{10}B in natural boron is 19.9%, and hence the sample contains nearly 1% of ^{10}B. The neutron capture reaction on the boron ^{10}B(n,α)^{7}Li was described in Eq. (3.2) in Section 3.1 and has a Q value of 2.34 MeV shared by the α and lithium particles. This energy is fully captured in the plastic to produce a scintillation signal approximately equivalent in amplitude to that of a 76 keV electron.

Plastic scintillators are used in a wide variety of particle physics detectors. Interleaved with lead or steel absorbers, the Atlas and CMS experiments at the LHC use large plastic scintillator sheets in their hadron calorimeters, as did CDF at the Tevatron, and the T2K neutrino experiment in Japan uses plastic scintillator sheets read out by wavelength shifting fibres in multiple parts of its detector systems. Recent studies have shown pulse shape discrimination capabilities of plastic scintillators between fast neutrons and γ by increasing the concentration of the fluor solute [176]. However for low energy neutrons, plastics doped with ^{10}B are available or a thin film ^{6}LiF layer may be deposited for conversion as described in Chapter 3. As tests have shown loaded glass scintillators to be effective UCN detectors at room temperature [74], it follows that these loaded plastics should be investigated in a similar fashion for low temperature. Despite their ubiquitous use, no comprehensive low temperature

Table 5.3: Properties of Some Commercially Available Organic Scintillators [105]

NE	Eljen	St. Gobain	Light Output %Anthracene[a]	Wavelength of Max Emission (nm)	Decay Constant (ns)	Attenuation Length (cm)	Refractive Index	H/C Radio	Density	Loading Element % by weight or dist. feature	Softening or Flash Point (deg C)	Uses
	Crystal											
	Anthracene		100	447	30		1.62	0.175	1.25		217	
	Stilbene		50	410	4.5		1.626	0.858	1.16		125	
	Plastic											
NE-102A	EJ-212	BC-400	65	423	2.4	250	1.581	1.103	1.032		70	General purpose
NE-104	EJ-204	BC-404	68	408	1.8	160	1.58	1.107	1.032	1.8 ns time constant	70	Fast counting
Pilot F	EJ-200	BC-408	64	425	2.1	380	1.58	1.104	1.032		70	TOF counters, large area
NE-110	EJ-208	BC-412	60	434	3.3	400	1.58	1.104	1.032	Longest attn. length	70	General purpose, large area, long strips
		BC-420	64	391	1.5	110	1.58	1.100	1.032	1.5 ns time constant	70	Ultrafast timing, sheet areas
NE-111A	EJ-232	BC-422	55	370	1.4	8	1.58	1.102	1.032	1.4 ns time constant	70	Very fast timing, small sizes
		BC-422Q	11	370	0.7	<8	1.58	1.102	1.032	Benzephenone, 1%	70	Ultrafast timing, ultrafast counting
NE-103	EJ-260	BC-428	36	480	12.5	150	1.58	1.103	1.032	Green emitter	70	Photodiodes and CCDs; phoswich detectors
NE-108		BC-430	45	580	16.8	NA	1.58	1.108	1.032	Red emitter	70	Silicon Photodiodes and red-enchanced PMTs
		BC-436	52	425	2.2	NA	1.61	0.960 D:C	1.130	Deuterium, 13.8%	90	Thin discs
NE-115	EJ-240	BC-444	41	428	285	180	1.58	1.109	1.032		70	Phoswich detectors for dE/dx studies
NE-142	EJ-256	BC-452	32	424	2.1	150	1.58	1.134	1.080	Lead, 5%	60	X-ray dosimetry (<100 keV)
	EJ-254	BC-454	48	425	2.2	120	1.58	1.169	1.026	Boron, 5%	60	Neutron spectrometry, thermal neutrons
NE-105	EJ-252	BC-470	46	423	2.4	200	1.58	1.098	1.037	Air equivalent	65	Dosimetry
		BC-490	55	425	2.3		1.58	1.107	1.030	Casting resin	70	General purpose
		BC-498	65	423	2.4		1.58	1.103	1.032	Applied like paint	70	β, λ detection

1. *NaI(TI) is 230% on this scale*

study of the luminescent properties of plastic scintillators was found. Temperature studies of plastic scintillator solute chemicals have been performed to 100 K, and show little variation in light yield as a function of temperature [126]. Comprehensive studies of light yield and decay time of commercially available plastic scintillators have not been published, and so have been undertaken for this thesis.

5.1.3 Shortlist

A detailed table of the short-listed scintillators, their properties and published studies relevant to our requirements are outlined in Table 5.4. This includes the manufacturer's quoted *Decay Time*, *Output Peak Wavelength*, and *Light Yield*. In the following tabulated data, following convention, light output for inorganic crystals is typically quoted as % NaI(Tl) which gives approximately 38000 photons / MeV for incident γ. Similarly, light output for organic scintillators is typically quoted as % Anthracene. 100 % NaI(Tl) is equivalent to 230% the light output of Anthracene [105]. Furthermore, if a low temperature study or a pulse shape discrimination study has been published, a reference is quoted. The tables details the types of Plastic Scintillator chosen, the cerium-activated inorganic scintillators, the phosphor ZnS(Ag) and the inorganic crystal CaF_2(Eu).

Following this review, samples of all the promising scintillators outlined in Table 5.4 were obtained and low temperature studies of their response to α radiation at low temperature were performed and described in Section 5.2 and low temperature luminescence studies with vacuum-ultraviolet photons performed and detailed in Section 5.3.

Table 5.4: Properties of Potential Scintillators for UCN α Detector

Material	Decay Time [ns]	λ [nm]	Density	LY[1]	LTS[2]	PSD[3]	Manufacturer	Comment
LYSO(Ce)	46	415-420	7.1	40-75 % N	[177] [164]		Crytur	High light yield, density & sensitivity to γ. Undesirable internal radiation due to ^{176}Lu.
YSO(Ce)	45	425	4.54	80 % N	[169] [170]		Crytur	Lower density than LYSO.
YAG(Ce)	70	550	4.56	40 % N	[178]	[171]	Crytur	Lower density than LYSO.
GS20 Glass	98	395	2.64	20-30 % A	[179]	No [180]	AST	Ce activated glass scintillator with ^{6}Li for neutron detection.
ZnS(Ag)	110/1000	450	4.09	300 % A		[155]		Phosphor: Opaque to its own emission, thin film deposition needed. Excellent $\alpha - \gamma$ discrimination. Slow component 1 μs.
CaF_2(Eu)	1000	435	3.19	50 % N	[181]	[182] [183] [184]	Hilger	Low Z and low sensitivity to γ. Slow component 1μs.
BC400	2.4	423	1.032	65 % A			St Gobain	General purpose plastic scintillator. Large size & affordable.
BC408	2.1	425	1.032	64 % A			St Gobain	Plastic. $\alpha/\beta/\gamma$. Large size & affordable.
BC418	1.4	391	1.032	67 % A			St Gobain	Premium ultra-fast plastic.
EJ204	1.8	408	1.032	68 % A			Eljen	High efficiency plastic sensitive to $\alpha/\beta/\gamma$
EJ254	2.2	425	1.026	48 % A			Eljen	Plastic loaded with 5% B for neutron capture on ^{10}B.

1. *Light Yield where % N refers to NaI(Tl) and % A refers to Anthracene.*
2. *Low Temperature Study*
3. *Pulse Shape Discrimination*

5.2 Scintillation Response to α at Low Temperature

Having assessed the prospective materials for a low temperature scintillation detector for cryoEDM, a comprehensive study of their properties can now be undertaken.

Firstly, a study of the α scintillation response at low temperature of the shortlisted materials will give a good indication of their usefulness as cryogenic UCN detector materials. As the UCN will likely be detected using the ^{6}Li(n,α)^{3}H conversion reaction, the 2.73 MeV ^{3}H and 2.05 MeV α will be detected by the scintillation material. A study of the materials' relative light yield at low temperature can rule out any materials that exhibit temperature quenching effects.

This method was undertaken at Oxford and the facilities allow for measurements in the 300 – 6 K temperature region. The measurement of the decay times of scintillators slower than ∼50 ns can also be made. A full description of the apparatus and data reduction techniques is outlined below in Section 5.2.1 and the results of these experiments in Section 5.2.3. The apparatus used for these experiments can only cool to ∼6 K, however the response of many scintillators below 10 – 50 K becomes stable. Typically, at high temperatures (>250 K) the light output is dominated by thermal quenching: as the probability of non-radiative decays increases strongly with temperature, the emission intensity is relatively low. This often increases in the range 20 – 250 K as non-radiative modes are suppressed and traps filled [121]. It is seen empirically that the temperature dependence of organic scintillators is not strong [126]. Therefore it is fair to assume that a scintillator whose light yield is stable in the region <50 K, will remain so down to 500 mK.

Secondly, a complementary measurement of the luminescence properties when excited with Vacuum Ultra Violet radiation was also undertaken at the SuperLumi station at the Hasylab Photon Science facility at DESY (Deutsches Elektronen-Synchrotron) laboratory. This facility allows for the spectroscopic properties of the materials to be studied, which may reveal the underlying physical processes and crystallographic energy levels governing the light yield and kinetic properties of a given material. This equipment also allows for

study in the 300 – 6 K region and decay time analysis for fast scintillators <100 ns. The facility's equipment and spectroscopic measurement capabilities are outlined in Section 5.3 and the results of measurements taken there outlined in Section 5.3.2, Section 5.3.3 and Appendix A.

Using these experimental tools, it is possible to consider the various scintillators and evaluate their worth as potential neutron detector materials, as well as understand the underlying physics contributing to their luminescence. A discussion of the decay times from both measurement processes are discussed in Section 5.4. Finally the relative merits are weighed up in the conclusion, Section 5.5.

5.2.1 Experimental Setup

The scintillation response of the materials listed in Table 5.4 to incident α radiation was measured as a function of temperature. A sample of each scintillator from Table 5.4 was cut with dimensions $5 \times 5 \times 1$ mm^3 with one 5×5 mm^2 face mechanically polished to a level of specular reflection. The sample was placed in a helium-flow optical cryostat [185] with an optical quartz windows to allow the detection of light, which is capable of cooling to ∼6 K. The sample was excited by α particle radiation from an ^{241}Am source of 33 kBq with energies of 5.578 MeV (84.45%) and 5.535 MeV (13.23%), which is also placed inside the cryostat. The scintillator is secured in a sample holder, as seen in the photograph in Figure 5.1. The sample holder is constructed so that the sample is held, glued on a copper prong, at the focus of a spherical mirror. The α particles impinge on the rear face of the crystal, and scintillation light that escapes the crystal is reflected towards the cryostat window and the photomultiplier tube, as illustrated in the schematic Figure 5.2.

In order to reduce pile-up, the event rate was decreased by placing an 0.1 mm stainless steel aperture between the source and the sample. This also collimates the particles so that they impinge on the crystal surface with approximately the same momentum, and thus minimises any effects due to absorption position. The PMT is external to the cryostat, and scintillation light travels from inside the cryostat through the optical windows to the

Figure 5.1: Photograph of a sample mounted in the holder.

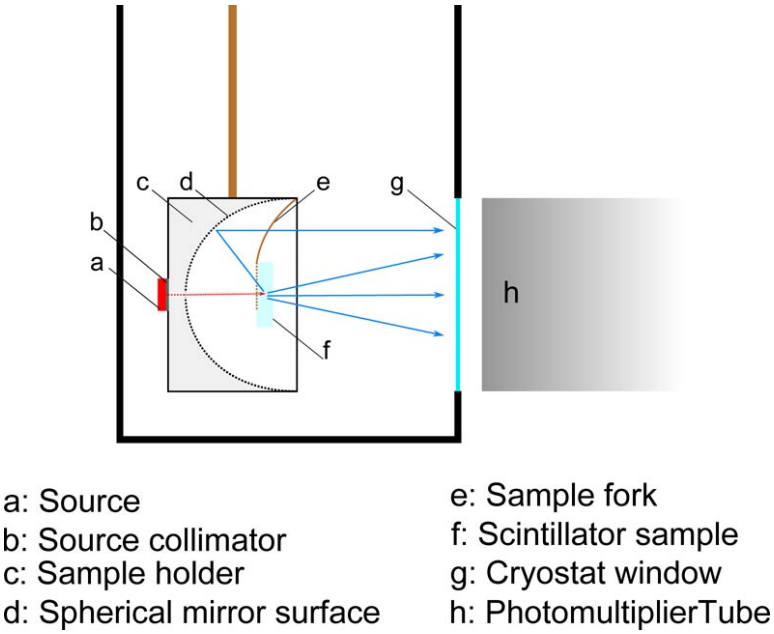

Figure 5.2: Schematic drawing depicting the experimental set-up to measure the temperature dependence of scintillator luminescence to α radiation.

PMT face. It is an Electron Tubes blue-green-sensitive photomultiplier 9125BQ [186]. The signal produced by the PMT is first fed to a custom build fast pre-amplifier with integration constant of 2.2 ns, and then is passed in parallel to a 8-bit transient recorder and an integrating amplifier. Event selection for triggering is carried out by processing the integrated and amplified signal in hardware. The integrating amplifier produces a signal which is a measure of the total energy detected, and is fed into a single channel analyser (SCA). The discrimination thresholds of the SCA are then manually set to reduce the number of pulses with low and very high amplitudes that are associated with electronic noise and cosmic muon events respectively, which acts as the input signal for the lower and upper threshold for triggering the recording of events by the transient recorder (TR). The TR is a LeCroy TR8818A

module with a sampling interval up to 20 ns and with 8-bit resolution. It can record up to 16 KB of data per record. Further details of this experimental set-up are available in [187].

5.2.2 Analysis methods

All scintillation events recorded by the TR are stored in binary data file by custom-made DAQ software, as was described in Section 4.2.4, and analysed using the OxRop software package. This software has tailor-made set of C++ classes to represent the individual record, scintillation event, photon pulses etc. Each *Event* is an array of floating point numbers, of the same size as the record length, representing the PMT signal as a function of time, and a collection of events is known as an *Event List*.

For pulse acquisition, the time base of the transient recorder was set to 20 ns with a record length chosen such that all photons generated in the scintillation event were within the event length. The pre-trigger region is set to one-quarter of the record length. Typical scintillation events are seen in Figure 5.3. The slow scintillator $CaWO_4$ in Figure 5.3a has a nominal decay time of 8 μs and individual photons can be resolved, whereas the fast scintillator EJ204 Plastic in Figure 5.3b has a nominal decay time of 1.8 ns and essentially all photons arrive within the first time bin.

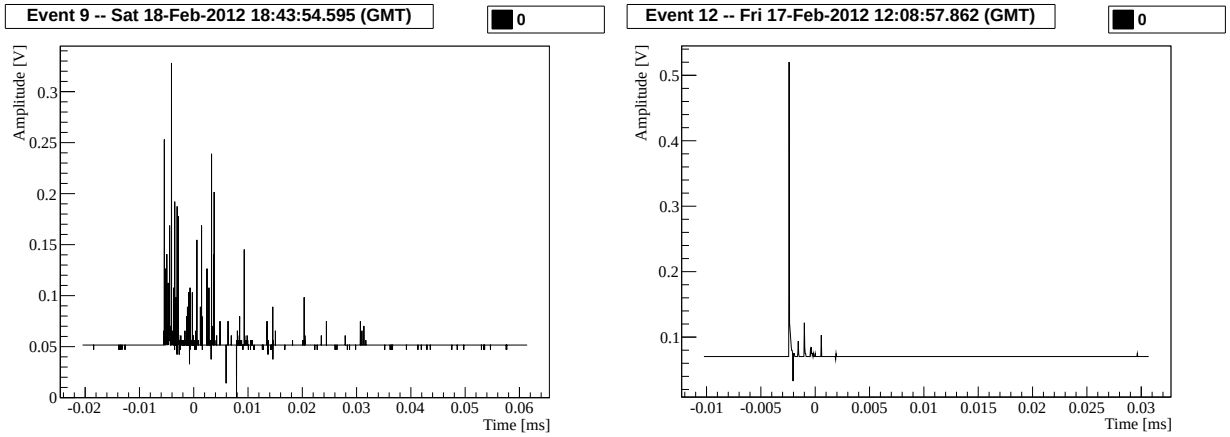

(a) $CaWO_4$ (b) EJ204 Plastic

Figure 5.3: Typical scintillation events from (a) slow scintillator $CaWO_4$ and (b) fast scintillator EJ204 Plastic.

A series of routines are part of the OxRop software to determine analysis parameters

associated with the scintillation events. Notable parameters calculated are described in Table 5.5.

Name (Unit)	Description
Number of Photons (E)	Total number of photons found in event.
Time of First Photon (samples)	Time in the event in which the first photon is counted.
Baseline (V)	Calculated from pre-trigger & non-photon signal regions.
RMS Baseline (V)	Root mean squared of the baseline.
Integral from peaks (μVs)	Integrated signal calculated from photon peaks
Tau (μs)	Event decay time calculated assuming a single exponent

Table 5.5: OxRop PMT Parameters.

The first iteration of the value of the PMT baseline is calculated from the pre-trigger region, and the parameters related to the PMT pulse are calculated from the post-trigger region, in the same fashion as described in Section 4.2.4 for phonon pulses. OxRop contains a photon pulse recognition algorithm, which calculates when the signal has sufficiently deviated from the baseline to be labelled a photon pulse. The *Baseline* and the *RMS Baseline* are also found. The photon finding algorithm counts individual photons (*Number of Photons*) and also attempts to identify and count where a pulse may contain multiple unresolved photons, as is the case with most of the fast scintillators we are considering here, as depicted in Figure 5.3b. All of these parameters associated with a particular event are calculated and stored.

The integral of the signal due to all the photon peaks in each event is also calculated, *Integral from Peaks*, which is a good figure of merit for comparing the amount of light measured per α event in different crystals. This parameter should be proportional to the photons measured, and thus to the energy deposited in the sample, even when individual photons cannot be resolved, and is a more reliable comparative parameter than *Number of Photons*. This means the light yield of fast scintillators, where individual photos are not resolved due to the 20 ns sampling time, can be compared to that of slow scintillators, where individual photons arrive >20 ns apart. For slow scintillators, where individual photons are measured, decay time analysis can be done, where as for fast scintillators, the information on the rate of photon emission is lost in the slow sampling rate. A single exponential is

fitted to the photon arrival time distribution to give the decay time parameter, *Tau*. For fitting of data with a multi-component exponent, a routine was written which combines all photons from all events in a given event list, which may be thousands of events, to produce a histogram which can be fitted with any choice of function.

To select events for scintillation analysis, a number of hard and soft cuts are implemented to remove noise and to create a level playing field from which to compare the calculated light yield of different scintillators. An automatic routine was implemented to perform these cuts. Events which have a particularly noisy baseline due to equipment faults, such as from interference or overheating, are removed by a hard cut on *RMS Baseline*. Events containing noise or dark counts which arrive before the trigger time are removed with a hard cut on *Time of First Photon*. As the trigger input is taken when an integrated signal of the event is larger than a threshold, the exact time between when the first photon is detected and when the trigger is produced depends on many factors including the record length and sampling rate, the pulse height of the photons, the number of photons, the decay constant and the noise of the PMT. Thus the cut is determined visually, when the peak in the *Time of First Photon* spectrum is distinct from noise, as illustrated in Figure 5.4. Determining a cut visually may lead to bias, and a final analysis when running as particle detector should involve an automatic method of determining the cut limit. A simple method could involve finding the minimum of a running average and choosing the corresponding x as the cut limit.

If these events are not identified and removed, it will introduce an error in the results, particularly in the decay time analysis. Decay time characteristics of the scintillation process are calculated with respect to the time of the first photon in a record, and so it is important that the first photon must be correctly identified as being a part of the scintillation event, and not noise. A comparison of the *Integral from Peaks* spectrum before and after the removal of such events is illustrated in Figure 5.5, removing most spurious events where the full energy have been not deposited or measured in full.

Following the application of the cuts, a histogram of the Integral from Peaks of the final event sample is made, equivalent to the Pulse Height Spectrum typically quoted in

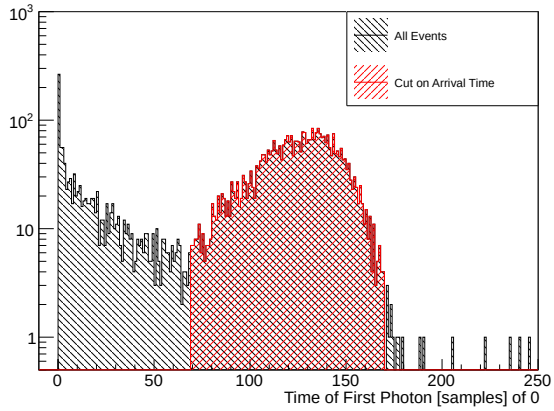

Figure 5.4: Histogram of the parameter *Time of First Photon*, with all events shown in black and those selected by a hard cut shown in red.

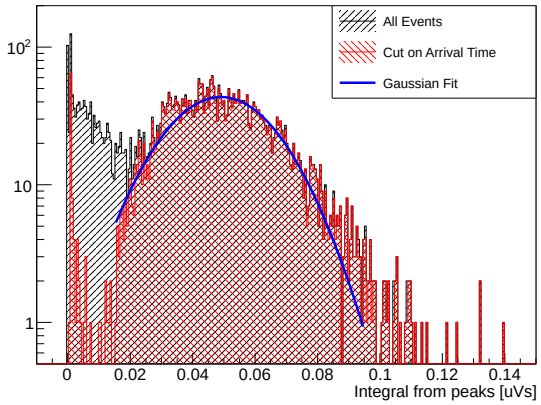

Figure 5.5: Histogram of the parameter *Integral from Peaks*, before (black) and after (red) a cut on *Time of first photon* was implemented.

detector/scintillator papers. This histogram typically shows a broad peak which is fitted by a single Gaussian, and attributed to the energy released by the α particles, Figure 5.6. For an α particle of $\sim$5.5 MeV the peak position in the peak integral histogram is proportional to the measured light for the sample under investigation. Thus, by measuring the variation of the peak position as a function of temperature, one can monitor the change of the light yield with temperature. The peak integral histogram after cuts due to α excitation for a sample of YSO(Ce) at 292 K and 8 K can be seen in Figure 5.7.

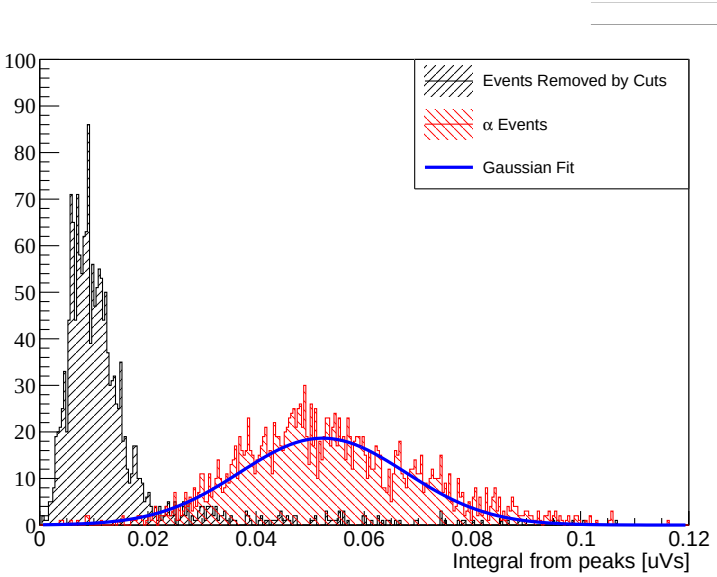

Figure 5.6: YSO(Ce) – A typical *Integral from Peaks* histogram with a Gaussian fit to α peak (red) after background events (black) have been removed by cuts.

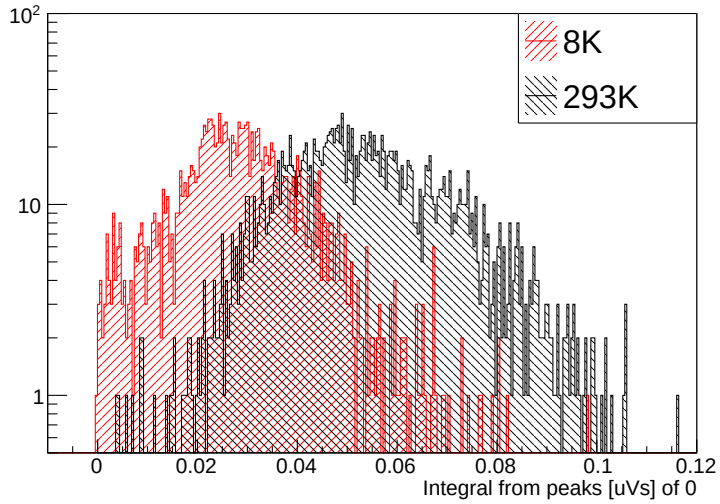

Figure 5.7: The α peak of YSO(Ce) at 293 K (black) and 8 K (red).

The spectral sensitivity of the PMT can be seen in the inset of Figure 5.8a. In this figure, the PMT quantum efficiency is compared with X-ray luminescence spectra of plastic scintillators. This is repeated for cerium-doped materials in Figure 5.8b and other scintillators in Figure 5.8c. It is clear that the measured scintillation light yield of a given sample will depend on the overlap between its emission spectrum and the quantum efficiency spectrum of the PMT. To compare different scintillator samples with different emission spectra, a spectral correction must be made. This correction was made using measured emission spectra if available (see Section 5.3), or using published data from the sample manufacturer.

The peak position of the signal measured (PP) in a given event is proportional to the product of the intrinsic light yield (LY) that is produced in the crystal and the spectral response of the scintillator and detector. This spectral response is the convolution of the scintillator emission spectrum, $I(\lambda)$, and the spectral sensitivity of the PMT, $S(\lambda)$:

$$PP = kLY \int I(\lambda)S(\lambda)d\lambda \tag{5.1}$$

where k is a constant of proportionality that takes into account the light collection efficiency of the setup. In these experiments, k remains approximately constant from sample to sample, given the fixed geometry. Some variation will be present due to surface preparation and different optical properties of the samples. The relative light yield of all the samples presented

here are taken relative to the well-studied inorganic crystal, $CaWO_4$. Thus one obtains an expression for the light yield of each crystal, relative to the reference material, $CaWO_4$, which can then be objectively compared.

$$LY_x = \frac{PP_x}{PP_{CaWO_4}} \frac{\int I_{CaWO_4}(\lambda)S(\lambda)d\lambda}{\int I_x(\lambda)S(\lambda)d\lambda} LY_{CaWO_4} \tag{5.2}$$

Details of these results are outlined below, in Section 5.2.3.

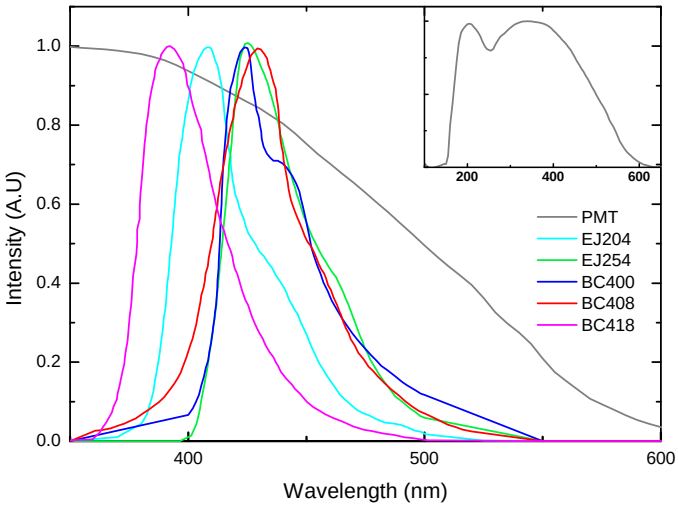

(a) Plastics

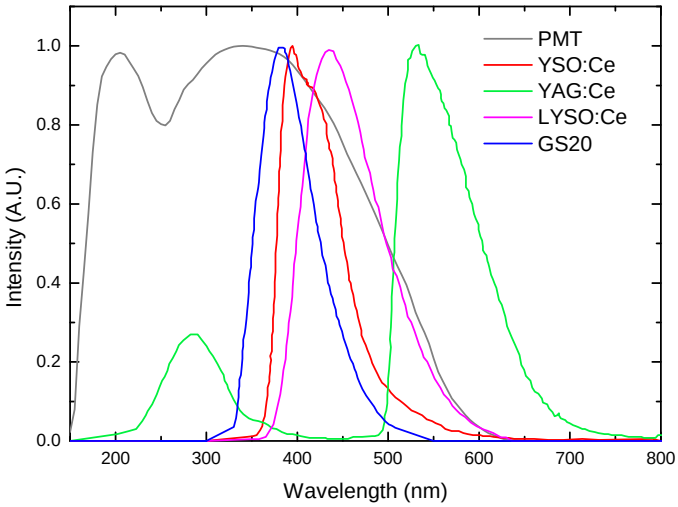

(b) Cerium

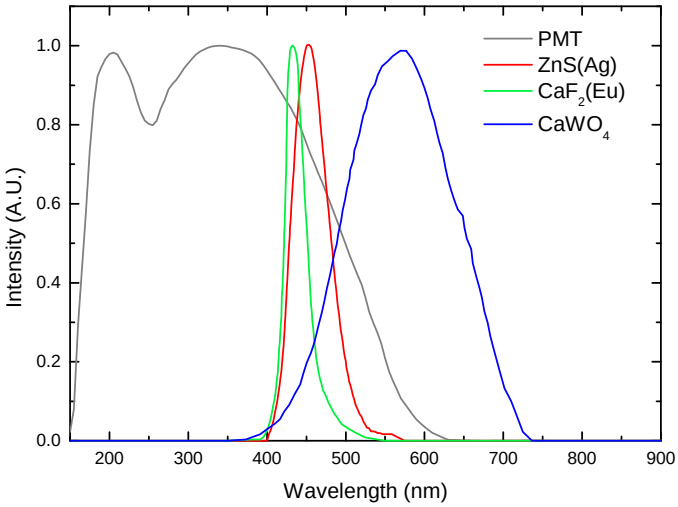

(c) Others

Figure 5.8: The emission spectra of (a) Plastic; (b) Cerium-activated; (c) other scintillators compared to the quantum efficiency of the PMT. The insert in 5.8a shows an expanded wavelength axis with the full PMT quantum efficiency for clarity.

5.2.3 Results

Measurements are recorded at regular temperature intervals from room temperature, 300 K to cryostat base temperature, ∼7 K. Enough events are collected to produce a measurable α peak in the *Integral from Peaks* spectrum following cuts. The spectral correction and comparison to $CaWO_4$ as was outlined above by Eq. (5.2) is done for every temperature point, and the relative light yield is plotted as a function of temperature. Errors plotted show statistical error on the mean from the Gaussian fit to the α peak in the *Integral from Peaks* spectrum.

Plastic Scintillators

Light yield results from plastic scintillators are plotted in Figure 5.9 and summarised in Table 5.6. In general, the light yield is quite constant for all the plastics across the temperature range, with EJ204 and BC408 remaining brightest at 7 K at 0.43 and 0.40 LY($CaWO_4$). BC408 in particular has a very stable scintillation light output the whole temperature range.

The energy transfer process in plastic scintillators has been widely studied for many years, with a comprehensive overview given by Birks [126] and also by Moser [188]. In general, plastic scintillators consists of a mixture of an aromatic base plastic, a primary fluorescing chemical and a secondary wavelength shifting fluor. The base plastic of the materials studied here is Polyvinyl Toluene (PVT), however the particular mixture of fluorescing chemicals is proprietary and not publicly known. The specific mixture creates the characteristic spectral, light yield and decay time characteristics of a given scintillator. When ionising radiation is stopped by the base plastic, energy is transferred to the fluorescing chemicals by a non radiative mechanism known as Forster transfer. It results from the interaction of the donor and acceptor molecular electric dipole moments, giving an energy transfer probability which is inversely proportional to the sixth power of the intermolecular separation [126]. The transfer probability also depends on the weighted frequency overlap integral between the base emission spectrum and primary fluor absorption spectrum. Thus early observations

led to the erroneous assumption that radiative transfer was the dominant energy transfer mechanism. Finally, the energy is transferred radiatively between the primary fluor and the spectrum shifter with subsequent emission of the shifter typically blue. An overview of the scintillation mechanism is given in Appendix B.

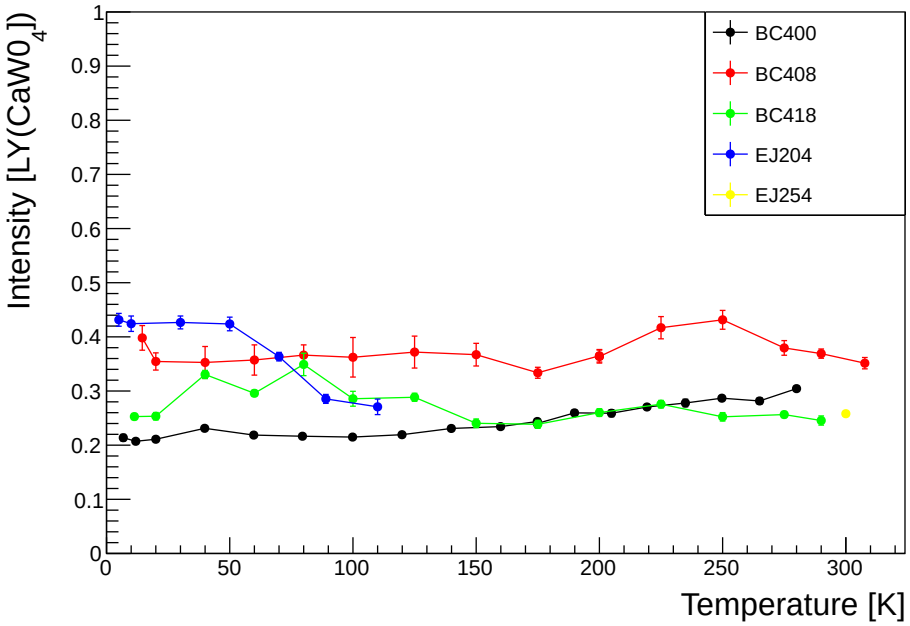

Figure 5.9: The temperature dependence of the light output response to α radiation of plastic scintillators in the 300 – 7 K range, relative to that of $CaWO_4$ at 300 K.

Scintillator	300 K	200 K	100 K	7K
BC400	0.31	0.26	0.22	0.21
BC408	0.35	0.36	0.36	0.40
BC418	0.25	0.26	0.29	0.25
EJ204	-	-	0.27	0.43

Table 5.6: Plastic scintillator light output at various temperature, (unit is fraction of $CaWO_4$ light output at room temperature)

The α scintillation results presented here indicate that there is little temperature dependence to the efficiency of the energy transfer. BC400 shows the largest light yield decrease of 32% from 300 to 7 K, however this is still relatively small in comparison to the temperature changes of the light yield of some typical inorganic crystals, such as NaI(Tl) or CsI [126], whose light yield depends on the energetic structure of the crystal lattice. BC408 was quite stable across the entire temperature range, increasing by 14% from 300 K to 7 K. As each

commercial scintillator is an unknown mixture of base plastic, primary fluor and secondary wavelength shifting fluor, we can only speculate as to the exact nature of the processes occurring. Nonetheless we can assume that the changes in light output are due to some change in efficiency of absorption or scintillation of the primary fluor with temperature, or a change in the efficiency of energy transfer to the wavelength shifter with temperature, or a change in the Forster transfer between the base plastic and primary fluor with temperature. These results show that plastics remain useful α scintillators at low temperature, and in this regard are an ideal candidate for a low temperature UCN detector, meeting requirements (1.) and (5.) from Table 5.1, EJ204 and BC408 in particular showing the highest light output at 7 K. The response is stable across the whole temperature range down to 7 K, and most likely remain bright down to 500 mK.

Ce activated materials

The temperature dependence of the scintillation response of the cerium activated scintillators, YSO(Ce), LYSO(Ce) and YAG(Ce) GS20 glass, measured using α particle excitation is shown in Figure 5.10 and summarised in Table 5.7.

For LYSO(Ce), there is little change over the temperature interval 300 – 7 K, with a 10% larger light yield of 0.33 LY($CaWO_4$) measured at 7 K relative to 0.3 LY($CaWO_4$) at room temperature. The luminescence from LYSO(Ce) is caused by the doping ions of Ce^{3+}, which creates luminescence centres in the crystal. The Ce^{3+} ion has one electron in the 4f shell, and the light emission is based on the electronic transition from the lowest excited 5d energy level to the 4f ground level. This is discussed further in the context of VUV excitation studies in Section **??** and in general in Appendix B. High energy ionising radiation, such as this ^{241}Am α radiation, causes excitation of the crystal lattice which migrates to the cerium emission centres, which then emit scintillation photons. The results presented here show that the process remains efficient and thus bright to 6.5 K and no temperature quenching effects are seen. This is consistent with γ scintillation studies reported in [189], where little temperature variation in light yield was found below room temperature down to 200 K.

For YSO(Ce) it is found that there is a reduction in light yield of 46% over the temperature interval 300 – 7 K from 0.52 LY($CaWO_4$) at 300 K to 0.28 LY($CaWO_4$) at 5 K. YSO(Ce) shares the same Ce^{3+} luminescence mechanism as LYSO(Ce), however in this crystal, there is clearly a reduction in mobility of electron-hole pairs with decreasing temperature, which leads to a reduction in light output.

The most variation was seen in YAG(Ce) in the temperature interval 300 – 7 K. The base temperature light yield was 19% lower than at room temperature, (0.18 versus 0.2 LY($CaWO_4$)) but rose to a maximum of 170% the room temperature value at 150 K.

It is unusual to see such a temperature response, with the intensity initially rising in the range 300 – 150 K before steadily dropping again as the material cools to base temperature, and such a broad change in intensity over such a wide temperature range. Usually thermal quenching results in a rapid change in intensity over a short temperature range, caused by temperature dependent non-radiative processes [126]. One might expect the electron-hole pairs created in the scintillation event to become less mobile at lower temperatures, increasing the time needed for them to reach the Ce^{3+} ion and raising the probability of non-radiative recombination. However in this case, there is more complicated mechanism at work. A steady drop in scintillation intensity was also seen in [172] over the broad range from room temperature to 50 K, under γ radiation.

Scintillator	300 K	190 K	90 K	7K
YSO(Ce)	0.52	0.41	0.34	0.28
LYSO(Ce)	0.30	0.42	0.31	0.33
YAG(Ce)	0.22	0.31	0.27	0.18
GS20	0.20	-	-	-

Table 5.7: Cerium Activated scintillator light output at various temperature, (unit is fraction of $CaWO_4$ light output at room temperature)

While the drop in light yield of the cerium orthosilicate scintillators does not render them useless, as some light is still produced, the relative light yield at 7 K is lower than the best plastic materials, BC400 and EJ204. This, coupled with the more significant variation over a range of temperatures, and their higher γ stopping power makes them a less suitable

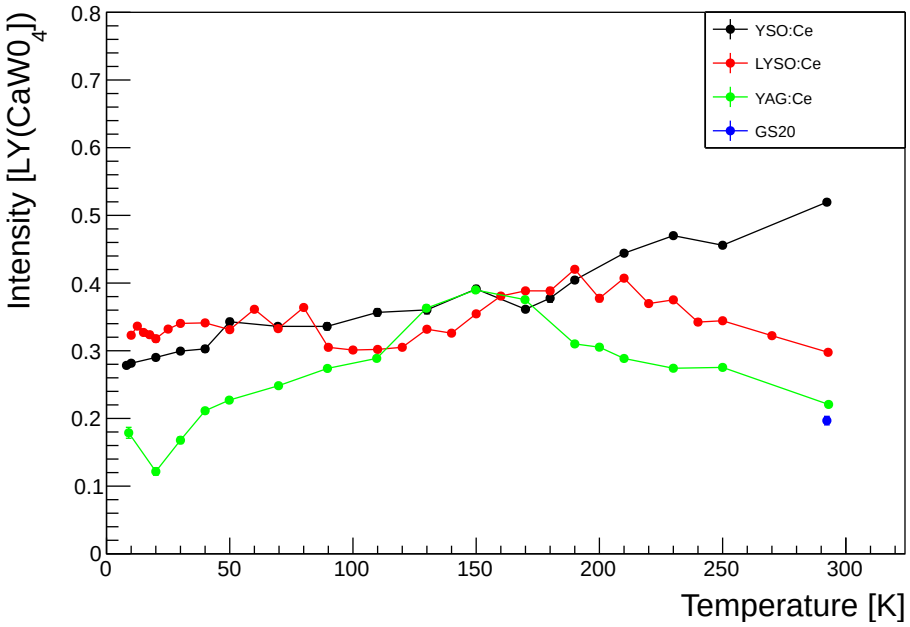

Figure 5.10: The temperature dependence of the light output response to α radiation of Cerium-doped scintillators LYSO(Ce), YSO(Ce), YAG(Ce) and GS20 Cerium glass in the 300 K – 7 K range, relative to that of $CaWO_4$ at 300 K.

candidate for a cryogenic UCN detector. Furthermore, as single crystals they are more costly than plastics, and more difficult to machine for the desired detector geometry.

The light yield of the cerium activated glass scintillator, GS20, was 20% $CaWO_4$ at room temperature. However it was insufficiently bright below room temperature to measure an α peak distinct from PMT noise, and thus it is not useful as a cryogenic scintillator.

Studies of the temperature dependence of the scintillation properties of cerium activated ^{6}Li glass have been published by Spowart in [190] and [179]. Spowart compared the UV luminescence of lithium glass to scintillation with β particles and found that below 50 K the scintillation light yield had reduced by over 50% whereas the UV luminescence light yield had remained constant. It was postulated that for charged-particle excitation by either ^{6}Li (n, α)^{3}H with thermal neutrons or β irradiation, the end product is the formation of electron-hole pairs in the glass dielectric, an ionic conductor. It was proposed that energy transfer from the lithium detection sites to the Ce^{3+} luminescent centres is phonon assisted, and that the phonon population $\propto T^3$. This model agrees with the findings here that the scintillation light yield to α was not measurable with our apparatus when the temperature

was reduced.

Others

The temperature dependence of the scintillation responses of ZnS(Ag)/^{6}LiF and CaF_2(Eu) to α particle excitation are plotted in Figure 5.11. For ZnS(Ag)/^{6}LiF, it is found that the scintillation response under α particle excitation shows little change over the temperature interval, 300 – 10 K, with a measured reduction of 14% from 2.1 LY($CaWO_4$) at room temperature to 1.8 LY($CaWO_4$) at 10 K.

Similarly, the scintillation response of CaF_2(Eu) to α particle excitation is quite stable over the same temperature range, showing an increase of 18% from 1.1 LY($CaWO_4$) at room temperature to 1.3 LY($CaWO_4$) at 6 K. This is consistent with γ and UV excitation in this temperature range [191] [181].

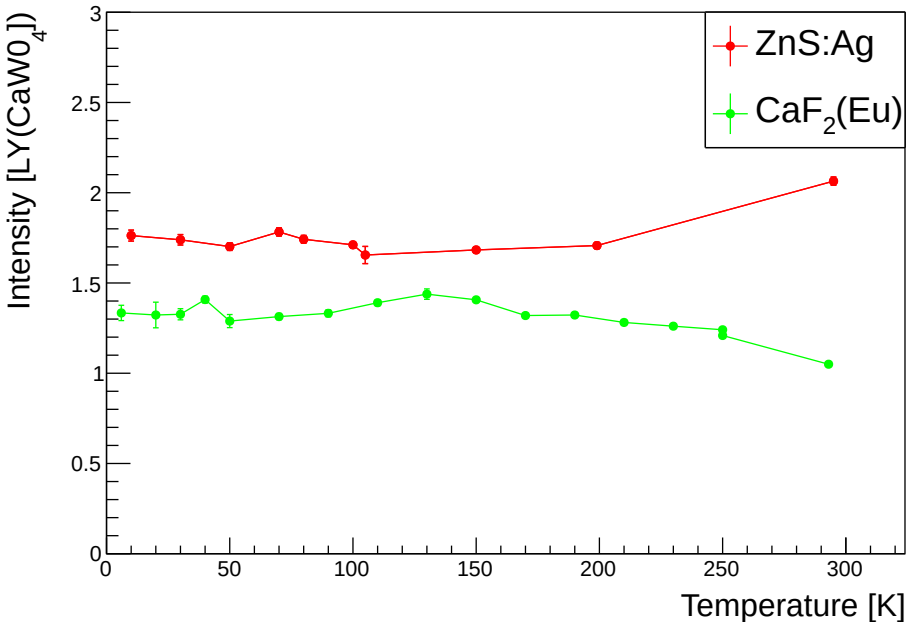

Figure 5.11: The temperature dependence of the light output response to α radiation of CaF_2(Eu) and phosphor ZnS(Ag) in the 300 K – 10 K range, relative to that of $CaWO_4$ at 300 K.

Both of these materials are exceptionally bright to α particle excitation at low temperature, ZnS(Ag)/^{6}LiF is 4.5 times brighter than BC408 at base temperature, and are therefore

Scintillator	300 K	200 K	100 K	7K
ZnS(Ag)	2.1	1.7	1.7	1.8
CaF_2(Eu)	1.1	1.3	1.4	1.3

Table 5.8: Inorganic scintillators ZnS(Ag) and CaF_2(Eu) light output at various temperature, (unit is fraction of $CaWO_4$ light output at room temperature)

quite suitable for use as a cryogenic UCN detector. This is the first measured and published scintillation light response of ZnS(Ag)/^{6}LiF over the temperature range 300 – 10 K [192]. It has been shown that temperature has no significant effect on the scintillation characteristics, with light output exhibiting only small changes with cooling, and likely would remain bright down to 500 mK. This confirms that ZnS(Ag)/^{6}LiF and CaF_2(Eu) are adequate scintillation detectors over a wide temperature range, meeting requirement (5.) in Table 5.1 for a cryoEDM UCN detector, as discussed in Section 5.1.

They both have their own challenges as materials. ZnS(Ag) is an opaque phosphor which means only a fraction of the light produced escapes the material to be further transferred through the light detection system. Its slow decay time at room temperature is incompatible with the fast repetition rates of cryoEDM, unless a detector is significantly segmented. Its decay time properties at low temperature are further studied in Section 5.4.3. CaF_2(Eu) is grown as a single crystal, and so faces the same difficulties as the cerium orthosilicates- prohibitive cost for medium to large size crystals, and limited geometries due to the difficulty of cutting and shaping. Its decay time properties at low temperature are also discussed in Section 5.4.3.

5.3 Luminescence from Vacuum Ultra Violet (VUV) Photons

Following α scintillation investigation, spectral studies of the shortlisted materials at low temperature was undertaken with VUV excitation. Selective VUV excitation is a powerful tool to study the spectroscopic properties of scintillation materials. By choosing the incident

energy of the excitation photons, the individual modes of luminescence may be identified. A scintillating material may have multiple modes of energy transfer from the host structure to the photon emitting centre, which can potentially contribute to scintillation. The selective study of these individual modes allows the energy levels and underlying physics of the material to be investigated. Used together with the scintillation analysis previously outlined, these techniques allow a comprehensive characterisation of scintillation properties of materials, and the evaluation of their worth as a cryogenic UCN detector material.

5.3.1 Experimental Setup & Analysis Methods

The data presented here was recorded at the SuperLumi station of the DORIS III storage ring at the DESY facility. The facility was designed to gather spectroscopic information on scintillators, and is described in detail by Zimmerer in [193]. A schematic diagram of the apparatus is shown in Figure 5.12, from the same paper. This facility was designed for comprehensive investigations of luminescence materials excited in the UV and VUV range, with photons in the energy range 3.7 – 40 eV from the DORIS III synchrotron radiation storage ring.

The excitation radiation is presented to the sample via the primary monochromator, which is a CGA/McPherson normal incidence monochromator, covering the full working UV spectral range. An aluminium grating with 1200 grooves/mm is used to select the incident energy in the data presented, which is optimised for the 4.2 – 24 eV range and has a resolution of 0.03 nm.

The beam intensity must be corrected for the relative tranmissivity of the primary monochromator for each wavelength. The standard procedure for such a correction is by illuminating a sample of Sodium Salycilate, which obeys the Kasha-Vavilov rule. The quantum yield of such a material is independent of the excitation energy, due to the fact that there is only one main relaxation mechanism, internal conversion and radiation [194]. Any variation in the luminescence intensity of Sodium Salycilate must be due to changes in the intensity of the arriving synchrotron radiation. The spectra in Figure 5.13 shows the inten-

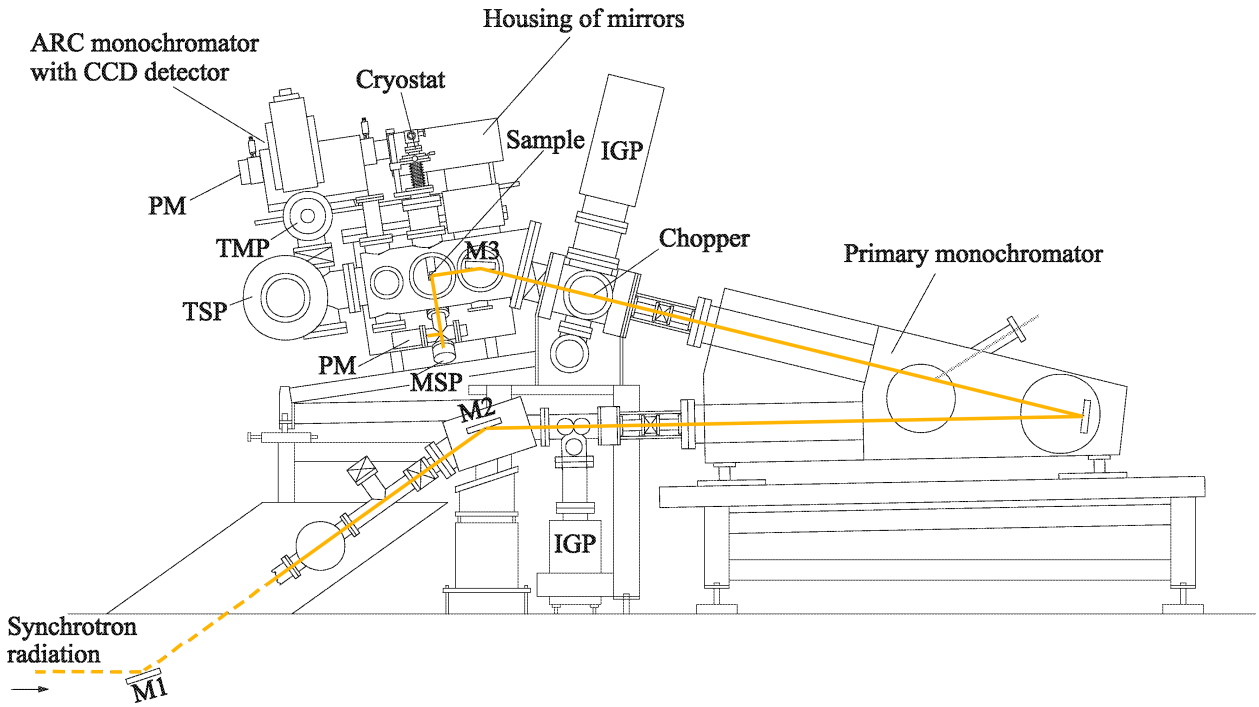

Figure 5.12: View of SuperLumi [193] with primary monochromator, sample and chopper chamber, ARC monochromator for luminescence analysis. M1, M2, M3: mirrors; TMP: turbo pump; TSP: titanium sublimation pump; IGP: ion getter pump; PM: photomultiplier; MSP: microsphere-plate detector. Yellow line shows the path of the sychrotron radiation.

sity of the synchrotron radiation let through by the grating. The entrance and exit slits used in this data were of 100 μm in width each, which corresponds to a resolution of 0.05 nm.

Samples of $5 \times 5 \times 1$ mm^3 were cut and polished to optical quality (except ZnS(Ag), a phosphor, which was just cut) and glued to the sample holder. The holder was placed in a vacuum chamber, which can be cooled to 6 K using a helium flow cryostat. The holder is translatable in a direction orthogonal to the beam, which allows for different samples to be presented to the excitation radiation. For each measurement, the sample position relative to the beam is optimised to detect the maximum intensity of synchrotron radiation reflected by the sample surface. For measurements where continuity across temperature range is required, the beam is focused at the first measurement, and not adjusted again through cooling. In this fashion, the fixed geometry of the experiment allows a direct comparison of the intensity of the light emitted at each temperature.

In order to examine the emission spectra of the sample, the emitted light is directed on a secondary monochromator which is used to narrow its bandwidth to approximately

200 nm before detection. The secondary monochromator is a SpectralPro 308 Czerny-Turner monochromator from Acton Research Company (ARC). The grating used is a 300 grooves/mm with 500 nm blazing (300/500).

The emission spectra were measured at fixed excitation wavelength using a liquid nitrogen cooled CCD camera (Princeton Instruments). To eliminate the second order effect of the grating monochromator, a WG295 or WG360 cut-off filter was placed in front of the entrance slit for the measurements in the spectral range greater than 295 nm or 360 nm respectively.

Similarly to the case of the primary monochromator, the secondary monochromator's reflectivity is not constant over the range of light detected, and so a correction curve is obtained, shown Figure 5.14. The curve includes the correction for the grating and the CCD and any other optical elements. The spectra presented here are corrected for the spectral response of the detection system.

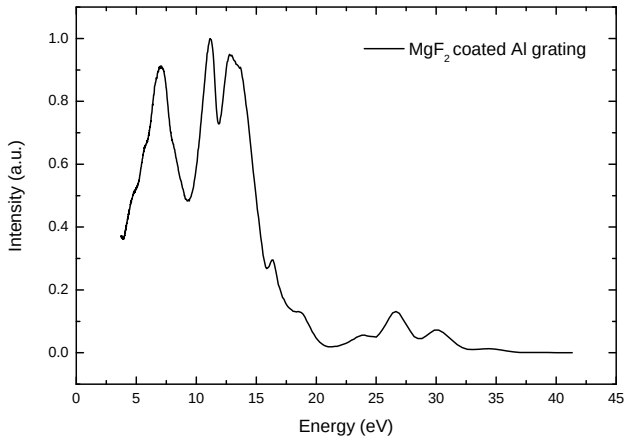

Figure 5.13: The incident VUV photon flux on the Sodium Salicylate sample with the MgF_2 coated Aluminium grating.

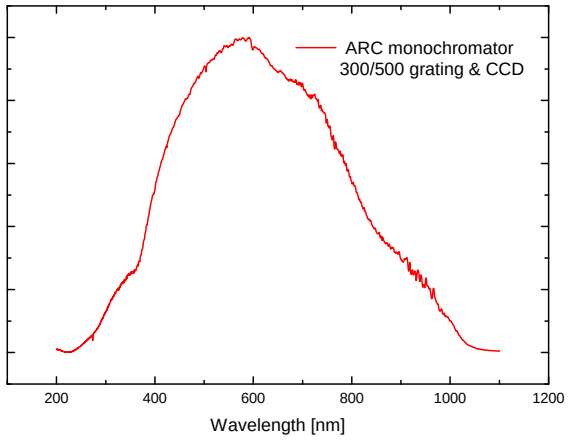

Figure 5.14: Transmission curve response of the secondary monochromator ARC SpectraPro with the 300/500 grating with CCD detector to a black-body emitting tungsten calibration lamp.

For the measurements of excitation spectra, the emission band is selected by the ARC monochromator and recorded with a Hamamatsu, R6358P Photomultiplier tube (PMT). The excitation spectra are normalized to equal quantum intensity of the synchrotron radiation by dividing for the response of a sample of sodium salicylate, as displayed in Figure 5.13, that has constant quantum yield over the energy range of interest. They are also corrected

for variation in beam current over time.

A schematic diagram of the SuperLumi sample holder chamber is displayed in Figure 5.15. The path of luminescence light in relation to these measurements described is shown in blue.

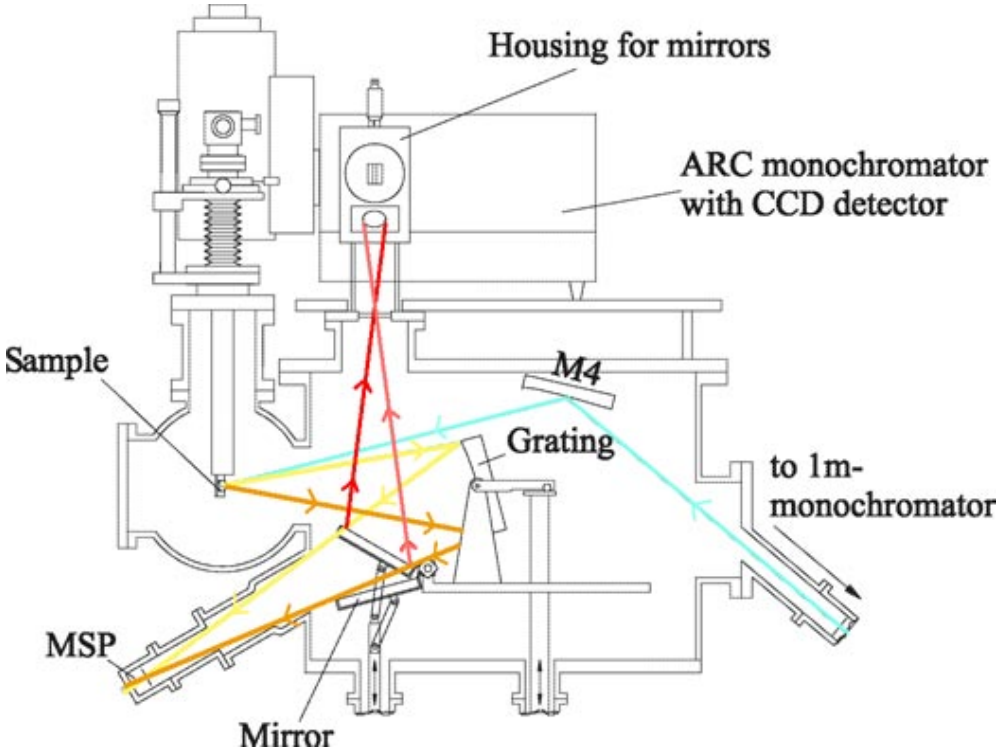

Figure 5.15: Side view of SuperLumi [193] with sample holder and chamber, ARC monochromator for luminescence analysis. M4: mirror; MSP: microsphere-plate detector. Blue line shows the path of the luminescence.

5.3.2 Emission Spectra

Plastic Scintillators

Figure 5.16 shows the luminescence spectra of St. Gobain Plastic Scintillator BC408. The spectra are corrected for the response of the experimental setup as was described previously. The excitation energy of the incoming photons were chosen to coincide with maxima as measured in the excitation spectra, presented later in Section 5.3.3.

The luminescence spectra of the other St. Gobain and Eljen Plastics scintillators are presented in Appendix A.1.1. Each manufacturer varies the chemical composition and fractional concentrations of the different types of plastic scintillator to produce changes in light yield, emission spectra, decay time and sensitivity to particular radiation. The spectral variation, as seen when comparing BC408 in Figure 5.16 to those of BC400 and BC418 presented in Appendix A in Figure A.1 and EJ204 and EJ254 in Figure A.2, is subtle. For all the materials involved, there is essentially no change in shape of the emission profile as a function of temperature, indicating that there is no change in the underlying processes. As the shape of the emission profile do not change as a function of temperature, variation is due to an increase or decrease in efficiency of the same emission method, rather than different methods becoming more or less dominant as a function of temperature. Similarly there is little discernible difference in emission spectra shape between excitation with $E_{ex} = 7.75$ eV and $E_{ex} = 5.2$ eV photons and we conclude that these energies excites the same mode.

The insets of the plot shown in Figure 5.16 gives the light yield as a function of temperature. This is calculated by integrating the area under the emission spectra. Comparing the trend to the light yield as a function of temperature for α scintillation in Figure 5.9, we can see in general agreement.

The light yield for BC408 and the other plastics presented in Appendix A.1 are summarised in Table 5.9. All St. Gobain materials show only a small decrease in light yield upon cooling, which is consistent with the α scintillation results presented in Figure 5.9. The Eljen plastics show a small increase upon cooling, which is also consistent with the more

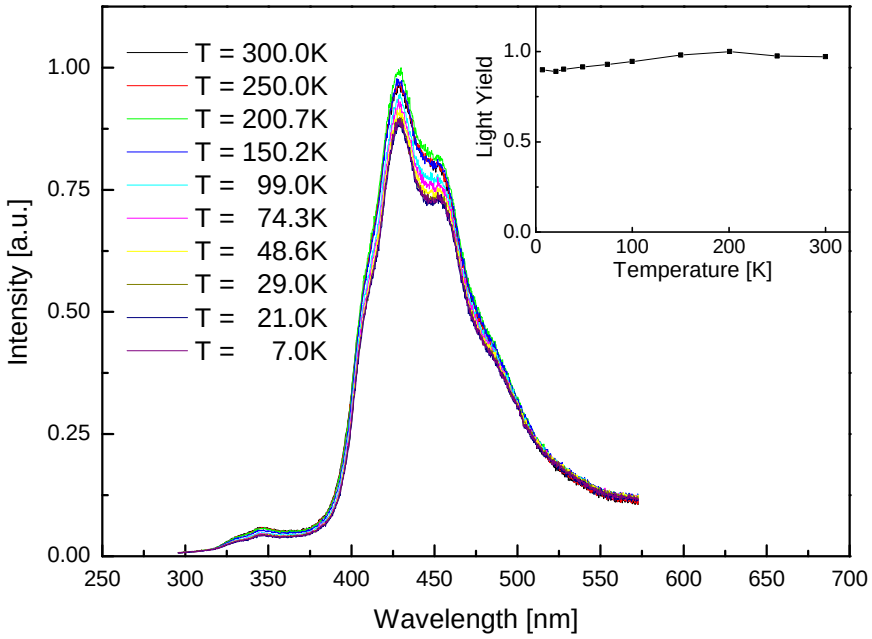

(a) BC408 E_{ex}=7.75 eV

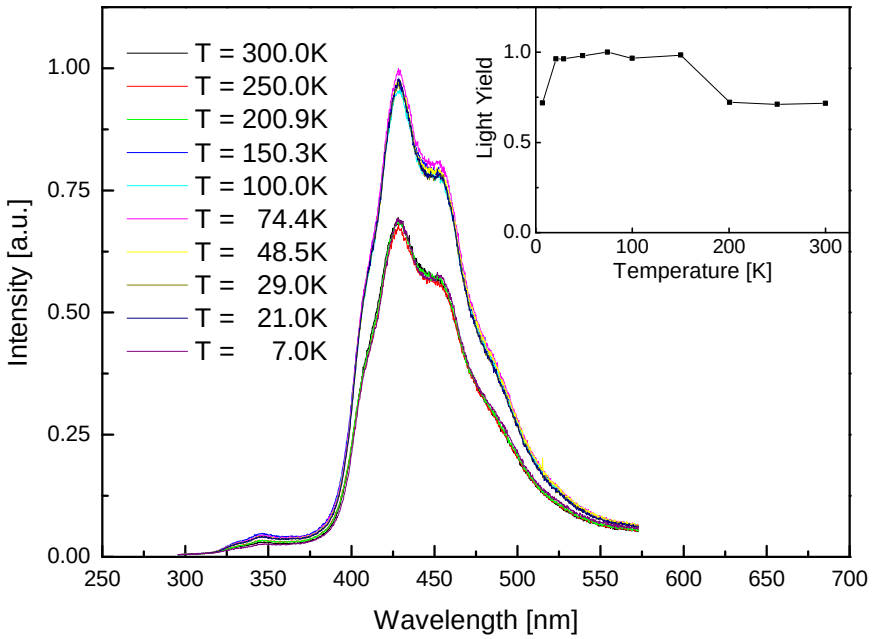

(b) BC408 E_{ex}=5.2 eV

Figure 5.16: St Gobain BC408 Plastic Scintillator Emission Spectra

limited α results. Once again, EJ204 and BC408 shows the most stable light yield across a wide temperature range for the excitation energy 7.75 eV.

Material	300 K	200 K	100 K	7K
	E_{ex} = 5.2 eV			
BC400	1	0.98	0.84	0.76
BC408	1	1.01	1.35	1
BC418	1	0.80	1.12	0.90
EJ204	1	1.28	1.16	1.42
EJ254	1	1.78	1.22	1.88
	E_{ex} = 7.75 eV			
BC400	1	0.93	0.83	0.79
BC408	1	1.03	0.97	0.93
BC418	1	0.75	1.09	1.03
EJ204	1	1.01	1.01	1.06
EJ254	1	0.94	0.93	0.91

Table 5.9: Plastic VUV Luminescence light output at various temperature, Normalised to their 300 K value.

ZnS(Ag)/^{6}LiF

The luminescence spectra of ZnS(Ag)/^{6}LiF are shown in Figure 5.17 measured in the temperature range 300 – 7 K under excitation with 4.1 eV (Figure 5.17b) and 6.5 eV (Figure 5.17a) photons. According to current understanding of the luminescence mechanism of ZnS(Ag) excitation, high-energy photons promote electrons to the conduction band and thus create holes in the valence band. The holes are then trapped by Ag^{+} which replaces regular Zn^{2+} ions on their sites, while electrons can be captured by shallow levels of charge-compensating sites associated with either impurities or intrinsic defects. Subsequent recombination of electrons with these holes results in the characteristic blue emission of ZnS(Ag) phosphor [195].

The shape of the emission spectra are temperature independent, however the intensity is not. The decrease of temperature results in an increase of the emission intensity that is a typical feature of recombination luminescence. The temperature variation of the luminescence is controlled by thermal quenching as the probability of non-radiative recombination increases with temperature. Due to the relatively high activation energy of thermal quenching in ZnS(Ag) the luminescence at room temperature remains at a relatively high intensity (see insets in Figure 5.17), and that facilitates the wide-ranging application of this material.

The quenching continues to be suppressed as the temperature is reduced to 7 K, and thus the light yield increases. These results are summarised in Table 5.10.

The temperature dependence of the scintillation response of ZnS(Ag)/^{6}LiF, measured using α particle excitation, was discussed in Section 5.2.3 and shown in Figure 5.11. It was found that the scintillation light yield showed little change over the temperature interval, 300 – 7 K, in contrast to the luminescence emission intensity under excitation with monochromatic VUV photons. Such a difference associated with excitation conditions is often observed in luminescence materials [196] [197]. It is generally interpreted as due to the difference in the distribution of excitation density over the volume of the material. Monochromatic VUV photons create electron-hole pairs in a thin surface layer (∼10 nm) with high concentration of non-radiative centres that facilitates quenching processes. On the other hand α particles can penetrate a few micrometers into materials. Taking into account typical diffusion lengths of electron-hole pairs (∼100 nm [198]) the majority of created pairs recombine within the bulk of the crystal where they are not affected by surface quenching processes.

Excitation (eV)	300 K	200 K	100 K	7K
6.5	1	2.6	3.6	3.2
4.1	1	1.8	1.9	2.1

Table 5.10: ZnS(Ag)/^{6}LiF VUV Luminescence light output at various temperature, Normalised to their 300 K value.

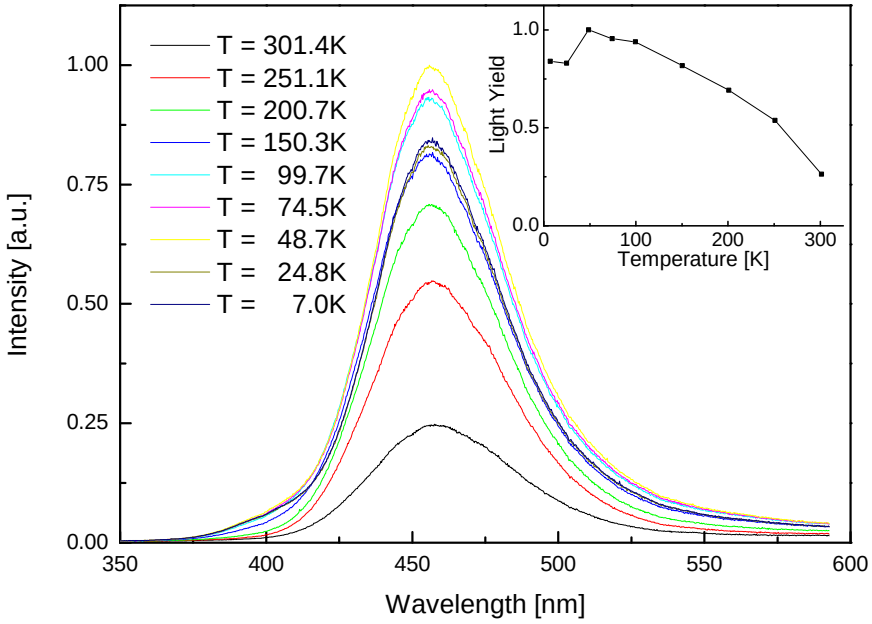

(a) ZnS(Ag)/^{6}LiF E_{ex}=6.5 eV

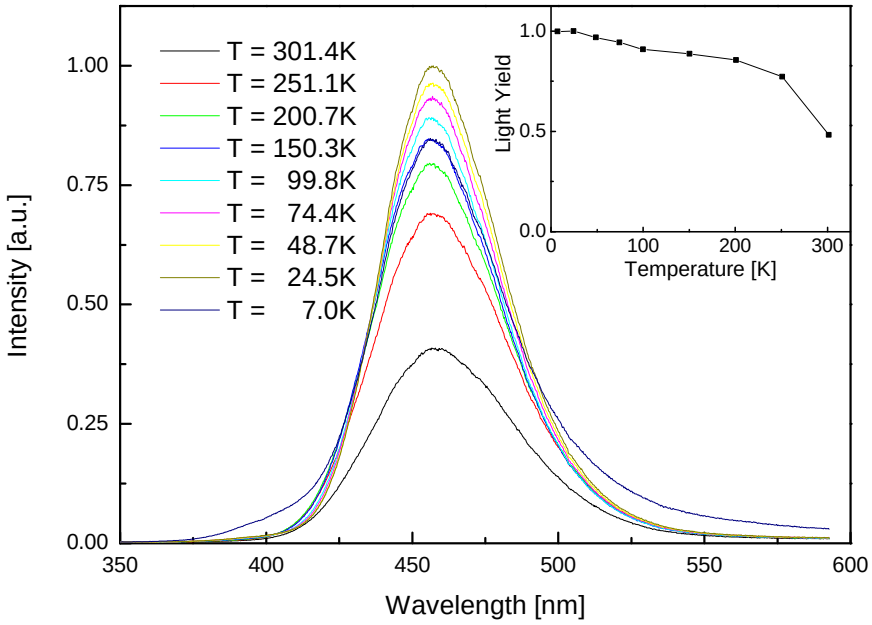

(b) ZnS(Ag)/^{6}LiF E_{ex}=4.1 eV

Figure 5.17: ZnS(Ag)/^{6}LiF Emission Spectra

Other Scintillators

Luminescence emission spectra of the cerium-doped oxides studied in Section 5.2.3, YSO(Ce), LYSO(Ce) and YAG(Ce), are presented in Appendix A.2. As these materials have been thoroughly studied under VUV excitation to low temperature previously, a comprehensive study was not repeated. A full discussion is given in Appendix A.2.1.

The luminescence emission spectra of ^{6}Li loaded neutron glass GS20 are presented in Appendix A.3. The luminescence emission spectra under UV excitation are essentially temperature independent, and therefore so is the light yield in the range 300 – 7 K, in marked contrast to the α particle results discussed in Section 5.2.3. The material has previously been studied by Spowart in [190] [179], which also showed significant light yield temperature dependence in response to ionising particles, but not to UV photons. They proposed an energy transfer model which is phonon assisted, and thus temperature dependant, unless the cerium activator is directly excited by UV photons. A full discussion of the results are given in Appendix A.3.1.

The temperature dependant luminescence emission spectra of CaF_2(Eu) are presented in Appendix A.4. The spectral characteristics of CaF_2(Eu) have also been published previously [199] [200], and therefore a comprehensive study was not repeated, instead there was a focus on low temperature measurements. A full discussion if these results are given in Appendix A.4.1.

5.3.3 Excitation Spectra

Plastic Scintillators

The excitation spectra at 300 and 7 K for the St Gobain plastic BC408 are presented in Figure 5.18. Results for the other plastics studied are presented in Appendix A.1.2. These excitation spectra were measured at the peak emission value for the given scintillator. At excitation energies lower than ∼5 eV, the base plastic PVT is almost transparent to this energy photon, and so the primary fluor is excited directly. This is the case for all the plastics studied, at all temperatures, where we see a high scintillation efficiency at low energies.

At excitation energies greater than ∼5 eV, the base PVT plastic absorbs the incident radiation. As previously discussed, the energy transfer mechanism from the base plastic to the primary fluor, is non-radiative, and depends on the square of concentration of the fluorescing chemical [126], and also on the frequency overlap integral between the base emission spectrum and the primary fluor absorption spectrum. As each commercial scintillator is a proprietary mixture of base plastic, primary fluor and secondary wavelength shifting fluor, we can only speculate as to the exact nature of the processes occurring.

The peak at ∼8 eV seen in the BC408 excitation spectra in Figure 5.18 (and for all the plastics) corresponds to the absorption peak of the PVT base plastic, which is common to them all. All spectra decrease in intensity slightly at 7 K relative to 300 K. We can assume that at $E_{ex} < 5$ eV this is due to decrease in efficiency of absorption, scintillation efficiency of the primary fluor or the efficiency of energy transfer to the wavelength shifter. At $E_{ex} > 5$ eV, a temperature dependant change in the Forster transfer between the base plastic and primary fluor may also contribute.

It is clear from these excitation spectra that the differences in these plastics are subtle and the luminescence mechanism is the similar for all of them and not very temperature dependant, as was the case for the temperature response of the α scintillation.

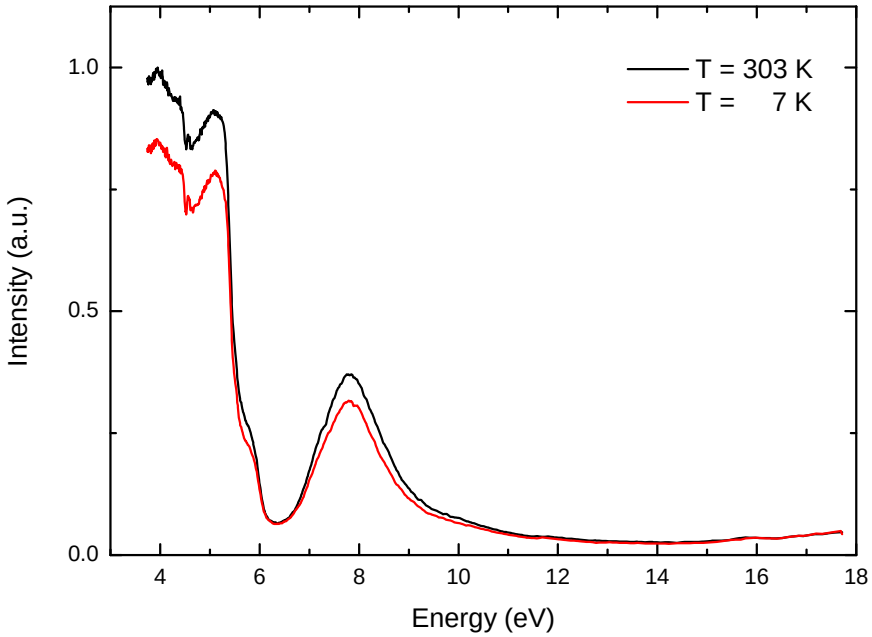

Figure 5.18: St Gobain BC408 plastic scintillator excitation spectra at 300 and 7 K. Recorded at emission wavelength 435 nm.

ZnS(Ag)/^{6}LiF

The excitation spectra of ZnS(Ag)/^{6}LiF at room temperature and 7 K are displayed in Figure 5.19. The results are in good agreement with earlier measurements of a ZnS(Ag) phosphor [201]. The main features of the excitation spectra can be explained on the basis of present knowledge of the band structure of ZnS as discussed in [202]. The maximum in the excitation spectra corresponds to the band gap energy of zinc sulphide between the conduction and valence bands, E_g, which is assigned to 3.8 eV [201]. As the energy of the excitation photons increase, the kinetic energy of the excited electrons increases, and hence the mean distance between the electrons and holes also increases. As the electrons taking part in the recombination must migrate to the luminescence centre they can be lost by decaying through non-radiative surface recombination [198]. This effect reduces the probability of luminescence recombination and explains the decrease of the light output over the 4 – 11 eV energy range.

The structure observed in the excitation spectra at higher energies can be related to the features of the valence band of ZnS. Measurements of the X-ray photo-electron emission spectra presented in [202] show that the valence band of ZnS consists of three bands

with maxima at around 2.6, 4.9 and 12.4 eV relative to the top of the valence band. By adding the band gap energy to these values one finds that the features in the excitation spectra of ZnS(Ag) marked A, B and C in Figure 5.19 correspond to the position of the valence-conduction band transitions at 6.4, 8.7 and 16.2 eV. Above 10 eV electron-hole pairs are created, which can can generate secondary excitations through a process called photon multiplication. In this process, the energy of the excitation photon is so high that it may create an energetic electron in the material, that loses some of its energy by creating a secondary electron-hole pair or a secondary excitation, in effect producing electronic excitation multiplication. The number of such excitations increases with the photon energy, causing a gradual rise of the luminescence yield at higher energies. All these features are more visible at 7 K rather than 300 K as the luminescence efficiency has increased. Emission spectra presented in Figure 5.17 were measured with the energies marked with "×".

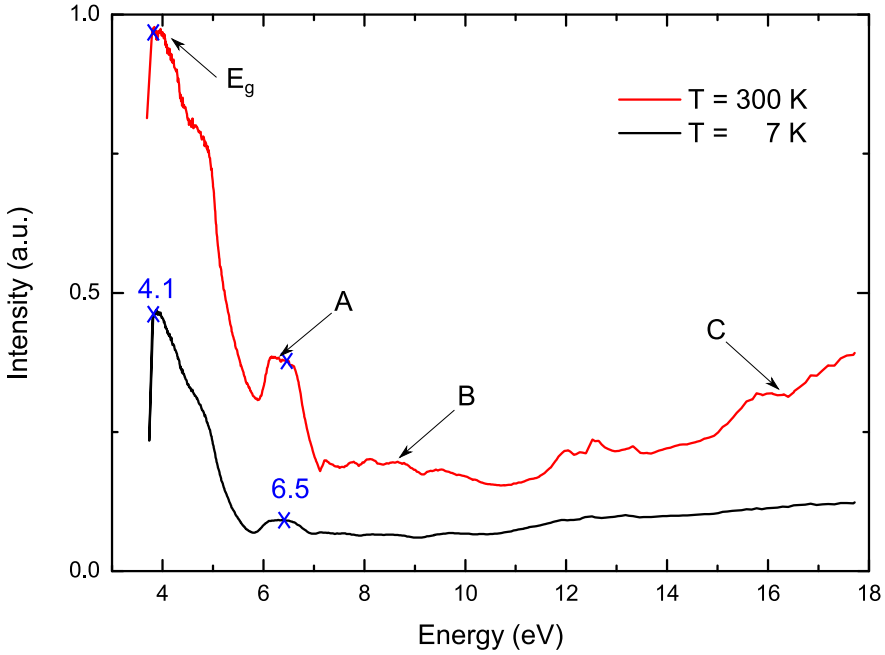

Figure 5.19: ZnS(Ag) Excitation spectrum at emission wavelength 455nm at 300 and 7 K. Emission spectra were recorded with energies marked in blue, 4.1 eV (Figure 5.17a) and 6.5 eV (Figure 5.17b).

Other Scintillators

Detailed spectra of other materials studied are available in Appendix A. Excitation spectra of the cerium-doped oxides, YSO(Ce), LYSO(Ce) and YAG(Ce), are presented in Ap-

pendix A.2. As the cerium doped oxide crystals have been well studied elsewhere, only 7 K excitation spectra were measured. Results are compatible with previous published studies and discussed further in Appendix A.2.2. Excitation spectra of GS20 glass are presented in Appendix A.3.2 and of CaF_2(Eu) in Appendix A.4.2.

5.4 Decay Time Measurements

VUV luminescence decay time measurements were made at Hasylab with the equipment outlined in Section 5.3.1. A fixed excitation energy and emission wavelength was used for each measurement. The transient decay trace was acquired by using 1024 channels for scanning a time interval of 192 ns between adjacent pulses. It was measured with the method of delayed coincidences. With a trigger pulse which is synchronized to the SR excitation pulses, a time-to-amplitude converter is started and then stopped with a single-photon event. The time delays between the excitation pulses and the events are analysed and converted into a decay curve, with a resolution of $\sim$1 ns. As the total recording window is $\mathcal{O}$(100 ns), only materials with decay times less than this can be analysed with this method. Decay curves were fitted with a one or two or three component exponential decay

$$y = y_0 + \sum_{i=1}^{n} A_i e^{-t/\tau_i} \tag{5.3}$$

The fit is performed with the Origin software non-linear curve fitting tool, which uses the Levenberg–Marquardt algorithm for Chi-squared minimisation.

Measurements of the kinetics of α scintillation decay were possible for some of the samples with slower decay times. This was done with the equipment outlined in Section 5.2.1 with the samples investigated under α illumination. This method was limited to the slower materials due to the electronics upper limit of the sampling rate at 20 ns, and is a complementary measurement to the VUV fast decay time measurements at SuperLumi.

5.4.1 Plastic Scintillators

Plastic scintillators are known to be fast materials with ns decay times at room temperature, however no published studies of their temporal luminescence characteristics at low temperature were found. Decay time measurements of the St Gobain plastics BC400, BC408 and BC418 and the Eljen plastics EJ205 and EJ254 were made at the SuperLumi facility. The results of BC408 are presented here and the others in Appendix A.1.3.

Decay time measurements at two excitation energies were made, 5.2 and 7.75 eV, in the temperature range 300 – 7 K. Normalised decay curves for BC408 with both excitations at 300 and 7 K are displayed in Figure 5.20. A two component exponent was fitted to the curves, with the faster component being dominant across all temperatures for both excitation energies. For E_{ex} = 5.2 eV, the two decay times from the fit to data are plotted as a function of temperature in Figure 5.21a. The fast component in black measures τ_f = 1.83 ± 0.01 ns at 300 K and τ_f = 1.77 ± 0.01 ns at 6.5 K. The slow component in red measures τ_s = 9.9 ± 0.26 ns at 300 and τ_s = 10.1 ± 0.26 ns at 6.5 K. τ_f dominates with $A_{fast} \sim 130 \cdot A_{slow}$ across all temperatures. For E_{ex} = 7.75 eV, the two decay times from the fit to data are plotted as a function of temperature in Figure 5.21b. The fast component quickens from τ_f = 1.98 ± 0.01 ns at 300 K to τ_f = 1.88 ± 0.01 ns at 6.5 K and the slow component slows from τ_s = 11.7 ns ± 0.15 at 300 K to τ_s = 12.3 ± 0.18 at 6.5 K. For this excitation, the fast component still dominates, but with a larger slow component, $A_{fast} \sim 40 \cdot A_{slow}$. These changes are subtle and the plastic remains a fast and useful scintillator at low temperature.

This analysis was repeated for the other plastics and summarised in Table 5.11. All these plastics show similar results decay times becoming slightly faster at low temperature, and dominated by the fast decay time component. BC418 is the fastest with τ_f = 1.34 ns at 6.5 K, and Eljen EJ204 has a fast decay component of τ_f = 1.67 ± 0.01 ns at 6.5 K, offering a middle ground between BC400/408 and BC418. All the plastic scintillators remain fast at low temperature, and so would be sufficiently fast to avoid pile-up if utilised in a UCN detector for cryoEDM.

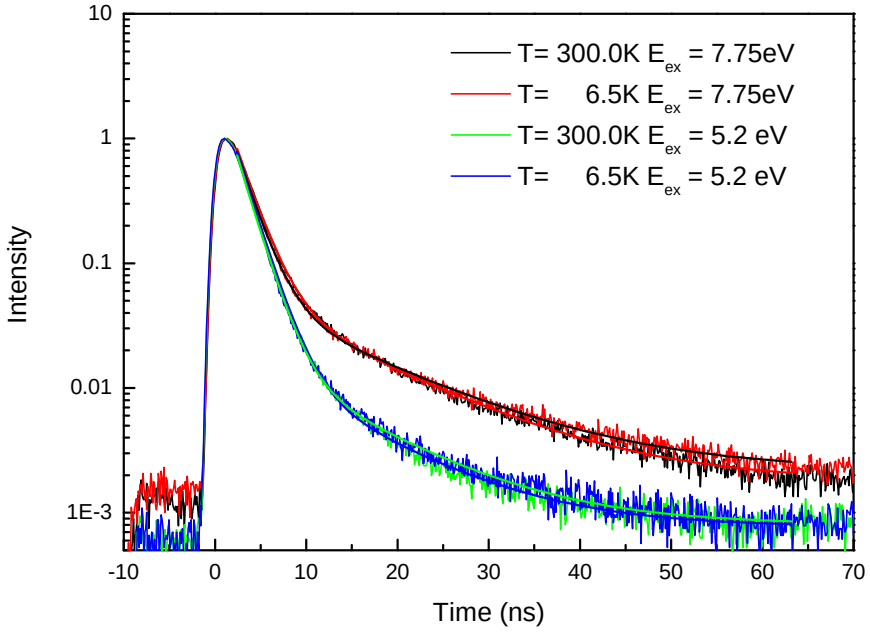

Figure 5.20: BC408 Decay Traces and Fits

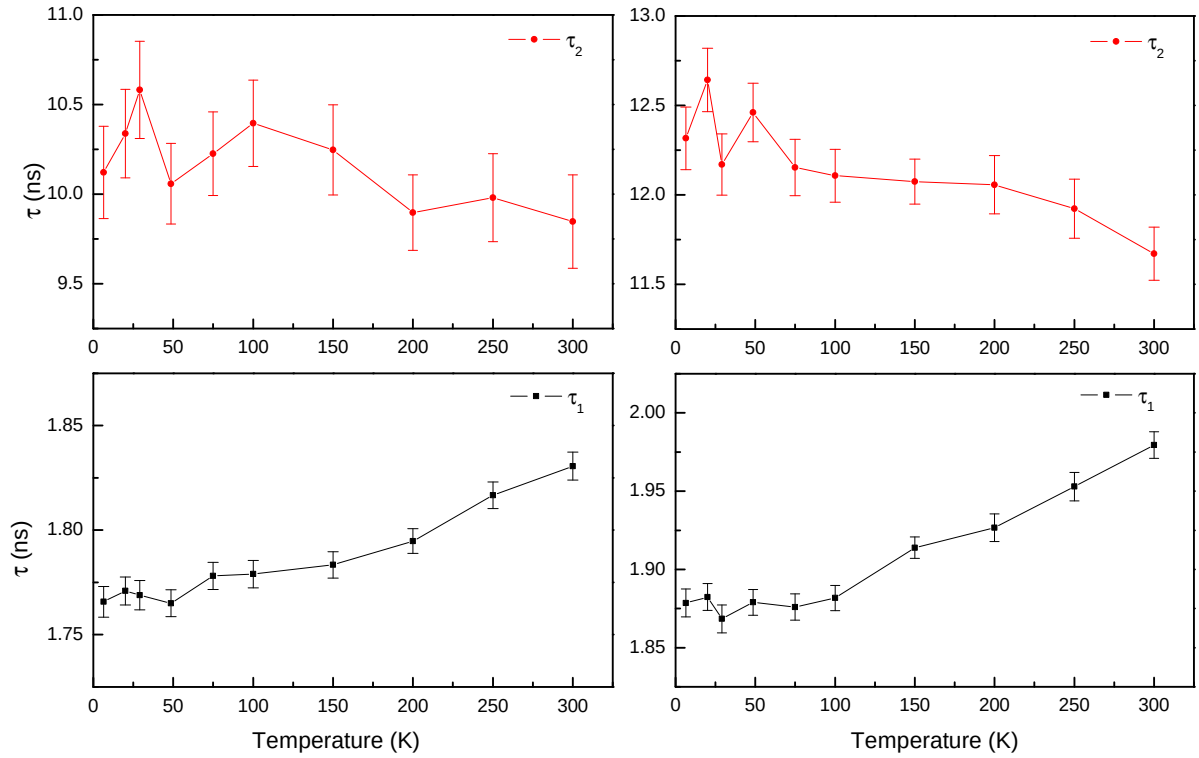

(a) BC408 E_{ex} = 5.2 eV E_{em} = 435 nm (b) BC408 E_{ex} = 7.75 eV E_{em} = 435 nm

Figure 5.21: BC408 Decay

Scintillator	τ_f 300 K (ns)	τ_f 6 K (ns)	τ_s 300 K (ns)	τ_s 6 K (ns)
	E_{ex} = 5.2 eV			
BC400	2.00 ± 0.01	1.96 ± 0.01	9.3 ± 0.17	9.3 ± 0.17
BC408	1.83 ± 0.01	1.77 ± 0.01	9.9 ± 0.26	10.1 ± 0.26
BC418	1.24 ± 0.004	1.22 ± 0.004	7.6 ± 0.16	7.7 ± 0.20
EJ204	1.7 ± 0.01	1.7 ± 0.01	10.3 ± 0.4	10.0 ± 0.3
EJ254	1.77 ± 0.01	1.66 ± 0.01	11.1 ± 0.71	9.67 ± 0.40
	E_{ex} = 7.75 eV			
BC400	2.1 ± 0.01	1.97 ± 0.01	12.6 ± 0.16	13.3 ± 0.17
BC408	1.98 ± 0.01	1.88 ± 0.01	11.7 ± 0.15	12.3 ± 0.18
BC418	1.37 ± 0.006	1.35 ± 0.007	10.1 ± 0.12	10.4 ± 0.14
EJ204	1.9 ± 0.01	1.9 ± 0.01	12.5 ± 0.2	12.7 ± 0.2
EJ254	2.00 ± 0.01	1.89 ± 0.01	10.4 ± 0.12	11.2 ± 0.11

Table 5.11: Plastic scintillator decay times at 300 and 6.5 K.

5.4.2 ZnS(Ag)/^{6}LiF

As ZnS(Ag)/^{6}LiF is a slow scintillator with a decay time of $\mathcal{O}(\mu s)$, it was not suitable for decay time measurements at the SuperLumi station. However it is sufficiently slow for decay time analysis with α excitation using the apparatus in Oxford described in Section 5.2.1. Figure 5.22 shows the α scintillation decay curves of ZnS(Ag)/^{6}LiF at 295 and 10 K. The shape of the scintillation curves is largely unaffected by cooling and they exhibit recombination characteristics over the full temperature range. A three component exponential was fitted to the decay curves, the fitted time and relative intensity of which are shown in Figure 5.23. Inspection of the data shows that cooling has only a very marginal effect on the scintillation decay kinetics of ZnS(Ag). It is only the first decay constant τ_1 which exhibits a decrease from 4.6 to 3.4 μs, while all other parameters remain constant within the error. Altogether this is consistent with the observed temperature stability of the scintillation light response since the changes in the decay kinetics and emission intensity are controlled by the same mechanisms.

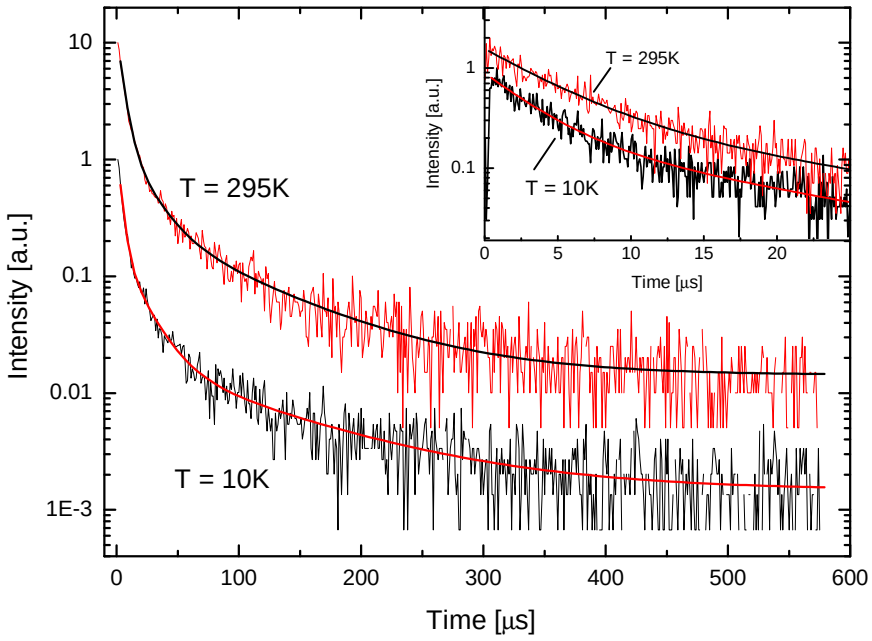

Figure 5.22: Normalised scintillation decay curves of ZnS(Ag)/^{6}LiF measured at T = 295 K and 10 K. The graphs are vertically shifted for clarity. Lines show the fit to the experimental data using the sum of three exponential functions. Parameters to the fit are graphed in Figure 5.23. The inset shows the initial part of the decay curves.

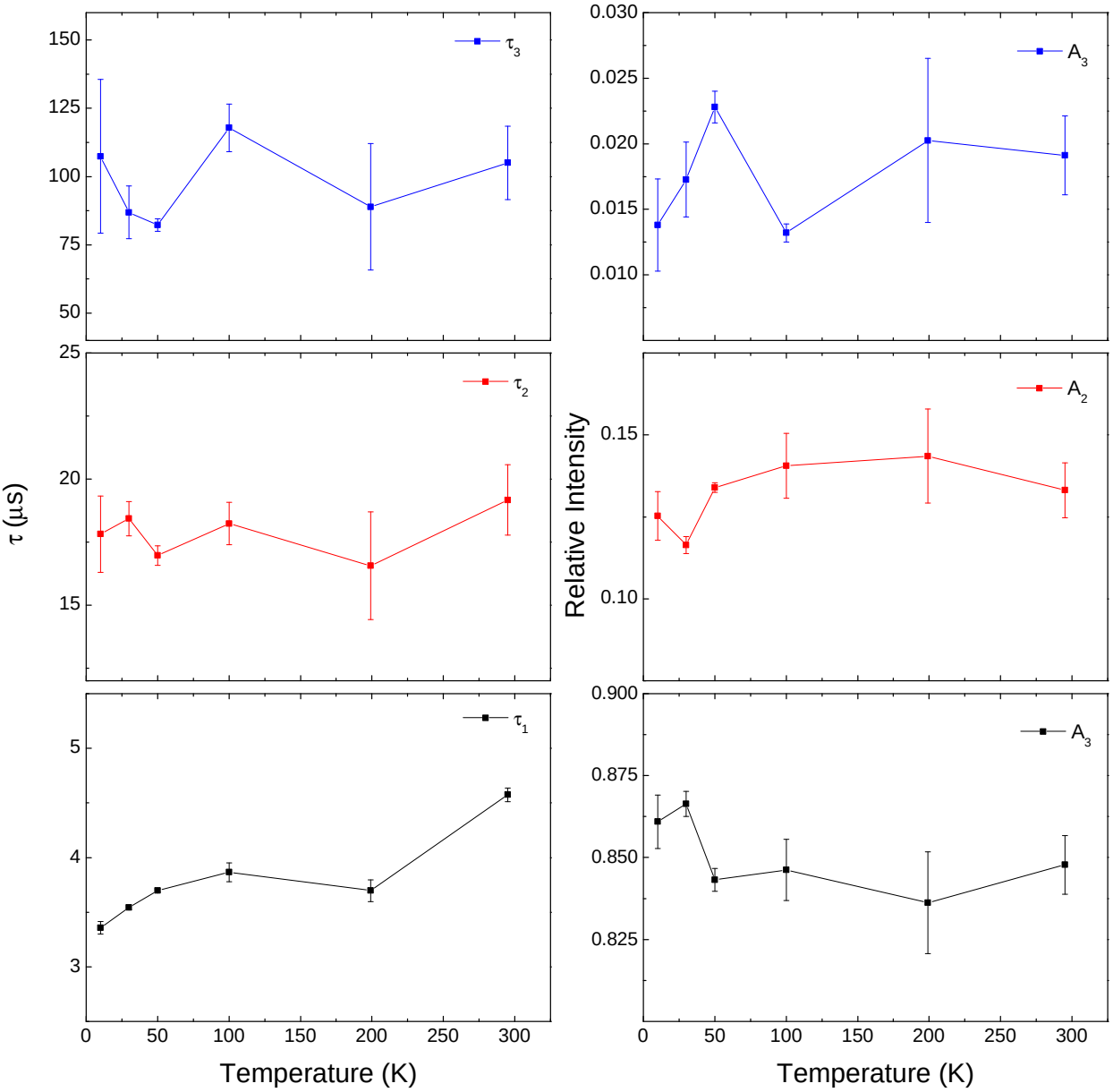

Figure 5.23: ZnS(Ag) Decay times to 3 component exponential fit vs. temperature

T (K)	τ_1	τ_2	τ_3	A_1	A_2	A_3
300	4.6 ± 0.06	19.2 ± 1.4	105.0 ± 13.5	0.85 ± 0.01	0.13 ± 0.01	0.019 ± 0.003
200	3.7 ± 0.10	16.6 ± 2.1	88.9 ± 23.1	0.84 ± 0.02	0.14 ± 0.01	0.020 ± 0.006
100	3.9 ± 0.09	18.2 ± 0.9	117.8 ± 8.7	0.85 ± 0.01	0.14 ± 0.01	0.013 ± 0.001
7.5	3.4 ± 0.06	17.8 ± 1.5	107.4 ± 28.2	0.86 ± 0.01	0.13 ± 0.01	0.014 ± 0.004

Table 5.12: ZnS(Ag)/^{6}LiF scintillator decay times τ_i and relative intensities A_i from 300 to 7.5 K.

5.4.3 Other Scintillators

A similar decay time analysis was performed on the cerium doped oxides and presented in Appendix A.2.3. The results are typical of cerium activated materials, with decay times in the range 34.1 – 62 ns, and this agrees with earlier published work. The decay time measurements of GS20 glass are presented in Appendix A.3.3, showing a single exponential decay time of 77.9 – 92.5 ns at 6.5 K, depending on excitation energy.

The slower decay time of CaF_2(Eu) meant it was unsuitable for the SuperLumi decay time measurements, however an analysis of the decay time from α scintillation results is presented in Appendix A.4.3. It indicates a slow component to the decay >2 ms, which may cause problems with pile-up and misidentification of neutron events in a cryoEDM UCN detector and for this reason, it is unsuitable for further application.

These decay time results are summarised below in Table 5.13.

Scintillator	300 K - τ (ns)	6 K - τ (ns)
LYSO(Ce)	-	34.1 – 37.0
YSO(Ce)	-	33.7 – 35.8
YAG(Ce)	-	48.7 – 61.9
GS20	60.0 (E_{ex} = 4.8 eV)	77.9
	82.5 (E_{ex} = 7.1 eV)	92.5
	75.7 (E_{ex} = 7.7 eV)	80.4
CaF_2(Eu) (α)	631 – 49	>2 ms

Table 5.13: Decay times of other scintillators.

5.5 Conclusion

This systematic study of potential scintillating materials for cryoEDM has revealed a number of materials that could be integrated into a prototype low temperature UCN detector for cryoEDM. A combination of scintillation studies with α particles and VUV excitation results at low temperature have shown that plastic scintillators remain bright and fast to 7 K. Their stable light output across the wide range from 300 K – 7 K indicates they would remain sufficiently bright down to 500 mK. Furthermore the light yield and decay time of ZnS(Ag)/^{6}LiF does not degrade at low temperature.

The cerium doped orthosilicates have been eliminated as potential materials for this application due to their relatively low light yield at cryogenic temperature, the variation in light yield as a function of temperature, the cost and their larger γ sensitivity relative to the other materials. The cerium activated lithium glass is not suitable as a cryogenic detector due to the large temperature quenching effect. CaF_2(Eu) is grown as a single crystal, and so faces the same difficulties as the cerium orthosilicates- prohibitive cost for medium to large size crystals, and limited geometries due to the difficulty of cutting and shaping. The long decay time at low temperature is also a prohibitive factor.

Plastic scintillators offer one of the easiest materials with which to use for the prototyping process, as they are cheap, easy and fast to machine for the iterative process of prototype production and testing. Although their light yield to 5.5 MeV α particles was $\sim$4.5 times less than ZnS(Ag)/^{6}LiF, their decay time remained less than 2 ns at low temperature, and will have no problem dealing with the high event rate that the cryoEDM experiment will produce. However plastic scintillators are sensitive to γ rays, and produce more light per unit energy for γ than α. With careful consideration during the detector design stage, the γ sensitivity of the plastic scintillator should not interfere with the UCN signal. This could be done with making a thin detector for minimal γ interaction, and significant shielding to reduce the γ energy.

For ZnS(Ag)/^{6}LiF, it has been shown that temperature has no significant effect on the

scintillation characteristics. Light output and decay curve exhibit small changes with cooling. Thus, it is now confirmed that it is an adequate scintillation detector that can be used over a very wide temperature range, and offers the advantage of incredibly low γ sensitivity. Furthermore the ^{6}Li is already incorporated in the material, removing one extra production process. However its decay time of 4 μs at low temperature would result in pile-up with a neutron interaction rate of 500 kHz, although it is not so slow that a well-designed segmented detector could be produced capable of counting the expected number of neutrons without pile-up issues. However at this time it was decided that plastic scintillator offers the easier solution.

In conclusion, plastics offer the most versatility to proceed with the process of designing and testing a prototype UCN detector while still meeting the detector requirements as outlined in Chapter 3 and Section 5.1. Of the plastics, BC408 is the brightest and most temperature stable of the St Gobain materials, and was less costly, and more readily available in large quantities than the Eljen materials. The boron loaded EJ254 is an interesting material which remained bright and fast at low temperature. However it was significantly more expensive than than the unloaded plastics, even taking into account the cost of ^{6}LiF surface deposition. For these reasons, BC408 has been chosen as the material most suitable for the detector prototyping process, the design and testing of which is discussed in the next chapter.

Chapter 6

Design Studies for a Prototype UCN Scintillation Detector

The process of designing and testing a prototype UCN detector for cryoEDM based on plastic scintillator and the ^{6}Li(n,α)^{3}H conversion reaction is carried out in this chapter. The aim is to prove that the scintillation detection technology and appropriate readout is viable for application to this experiment, and for a cryogenic neutron EDM experiment in general. This technology has the potential to have high UCN detection efficiency and low sensitivity to background and electronic noise, and careful consideration of the design process must be made to realise this potential. Key to this process is counting as many scintillation photons as possible for good particle recognition, within the constraints of the experiment, as was outlined in Chapter 3. A detector must be designed and tested; it must produce an acceptable neutron signal, clear from γ background, with high detection efficiency; it must be robust and operate reliably in liquid helium, and not interfere with the other sensitive sub-systems of the overall experiments, such as the neutron polarisation or magnetic field stability.

Wavelength shifting (WLS) optical fibres offer a number of advantages in the collection and transportation of light from the scintillator to the light detector. They offer one of the most efficient ways of collecting photons; they are compact; they can be spliced to clear

fibres for transportation of the light signal over a distance; and are easily coupled to a PMT or a more compact Silicon Photomultiplier which can be located at a convenient place in the experiment. Their operation at low temperature in liquid helium has not been studied before, and so is done as part of the design studies outlined in this chapter.

6.1 Losses in the Signal Transport Process

A scintillation counter relies on the detection of as many emitted photons as possible, as the larger the light signal due to a particle interaction, the more easily distinguished it will be from noise and background, thereby maximising the UCN detection efficiency. Unfortunately, a relatively large fraction of these photons are lost due to a number of mechanisms, before being detected. However, as this detector's primary function is good particle recognition, rather than a focus on good energy resolution of the counted particle, some photon loss can be tolerated, as long as a minimum light level requirement is met.

6.1.1 Sources of Photon Loss

Firstly, there is the effect of **optical self-absorption** within the scintillating material, whereby emitted photons are recaptured by the scintillator material. This is usually a significant consideration for the large calorimeters for high energy particle physics experiments, but for dimensions of a few centimetres as in this case, losses due to self-absorption are generally negligible in transparent scintillators.

Secondly, there are **losses within the light collection system**. This may be due to photons escaping at the scintillator surfaces, photon absorption in reflector materials, multiple reflections at the detector walls, absorption in any light guiding and coupling materials, and losses due to the PMT quantum efficiency (QE). PMT QE is a measure of the fraction of the photons that impinge on the photocathode of the PMT that are absorbed and converted to photoelectrons. Generally, these losses in the collection system are the

largest mechanism of loss, where design choices may be influential in minimising losses. The PMT QE may cause a loss of a factor of 2 – 5, depending on the particulars of the PMT and the wavelength of the impinging photon. This is unavoidable beyond choosing the best available PMT, matched to the spectrum of the scintillator. Photons may also be trapped inside the scintillator by multiple reflections, however this can also be reduced with careful consideration of geometry and surface finish. Scintillators are usually wrapped in a high performance reflector material, with reflectance higher than ∼95%. However, there may be a non-negligible absorption due to multiple reflections at this interface.

Photon collection becomes all the more complicated when dealing with a detector system that will be cooled to 500 mK. Established photon collection strategies at room temperature may no longer work as well at low temperature, due to variable material contraction, varying refractive indices and other temperature effects. It is precisely these considerations that must be taken into account when designing a prototype scintillation UCN detector for cryoEDM. With this in mind, an experimental investigation has been undertaken into the optimal detector design to maximise the photon collection efficiency.

6.1.2 Transportation of Scintillation Photons

There are three common methods employed to collect photons from a scintillator and transport them to the photocathode of a PMT or other photodetector. Firstly, the simplest way is for the scintillator and the PMT window to be in contact, often with an refractive index matching grease to couple the two for maximum light collection efficiency. Secondly, if that is not possible due to geometrical factors, a light guide can be used to transmit the light from the scintillator to the light detector. These are transparent solid materials in which the photons are totally internally reflected until they reach the photocathode. They can be easily manufactured in many geometries in order to match the detector geometry to the PMT face geometry. Thirdly, optical fibres can be coupled to the scintillator, a more flexible method of transporting photons to the PMT.

Clear fibres are limited in the number of photons they can collect by their acceptance

cone, leading to only a very small fraction $\big(\mathcal{O}(1\%)\big)$ of light produced in a scintillator being transported by the fibre. To overcome this limitation, wavelength shifting fibres are more commonly used. The advantage of these is that they are made from a photofluorescent material and absorb a higher frequency (blue) scintillation photon and re-emit multiple lower frequency (green) photons, which may be trapped inside the fibre and transported to the light detector. Thus in addition to acting as a light guide, they increase the light yield per interaction, and although only $\big(\mathcal{O}(5\%)\big)$ of the WLS photons emitted are also captured in the fibre, this remains a significant improvement on clear fibres. They are embedded in the scintillator giving them a much larger light collection area, along the whole embedded length. However, the self-absorption losses are significantly larger than in clear fibres, and therefore are typically used to collect photons from the scintillator before being coupled to clear fibres for transport over longer distances to the PMT. As fibres are compact and flexible, this enables them to be used in a limited experimental volume, transporting the signal to the PMT or other light detector at a more convenient place.

The transportation of photons in both light guides and clear optical fibres is constrained by Liouville's theorem on the time evolution of the phase space distribution of particles. This states that the density of particles evolving according to Hamilton's equations in phase space is a constant. In three dimensions, this means that the flux of photons per unit area and per unit solid angle is constant throughout a given medium. Consequently, no optical coupling scheme relying on reflection or diffraction alone can transmit photons from a large source, such as a scintillator, to a small detector, such as a PMT, with full efficiency. The implication of this theorem is that the light collection can never be more than the ratio of the area of the scintillator face to the light collector face. It is possible to overcome this limitation with wavelength shifting materials, which absorb the incident light and re-emit photons of a lower wavelength, thereby redefining the phase space element. This is the principle upon which WLS fibre readout scintillation detectors are based.

6.1.3 Collection of Scintillation Photons

The UCN measurement environment in cryoEDM is at the heart of the experiment, at the superfluid liquid helium level beneath many layers of thermal and magnetic shielding. The complications of operating a photo-detector at low temperature are numerous, although not impossible. The low temperature operation of PMTs has been proven to work at 1 K by the Oxford group [122]. However the desired location of the cryoEDM detectors is one of extremely sensitive magnetic field requirements (See Figures 2.1 and 3.3 for cryoEDM layout). The magnetic environment is highly controlled in order to preserve the polarisation of the neutron pre- or post- Ramsey resonance. It is controlled by the application of static and varying fields, which would curve electron paths inside the PMT and cause loss of gain. Usually PMTs in strong magnetic fields are operated with a μ-metal shield. However the effect of an extra μ-metal object in the highly controlled and precisely known magnetic environment would be too large of a unknown and risk for cryoEDM.

The development of Silicon Photomultipliers, SiPM, (also known as Multi Pixel Photon Counters, MPPCs) in the last years has been vast, and they are operated in conjunction with scintillators by many physics experiments, such as the T2K neutrino experiment [203]. Low temperature studies of SiPM have shown problems with operation below 77 K due to carrier freeze-out within the semiconductor [204], and so are not suitable for application inside the cryoEDM apparatus.

The most promising alternative is to place the light detector at a more suitable location, and couple the light from the in-situ scintillating detector via WLS optical fibres to the light detector, as they are thin and flexible, they could be made to fit more easily within the physical constraints of the detector area than a solid light guide. WLS fibres may be embedded in the scintillator, absorbing any photons passing through the entire embedded length. These fibres offer all the space advantages of clear optical fibres, but with a larger light collection efficiency. For travel of the light signal over larger distances, they can be spliced to clear fibres, and the signal easily coupled to a SiPM or PMT at a convenient location.

The optimisation of light collection efficiency from scintillators with WLS fibres has been studied [205] [206] and implemented in many scintillation detectors, including the LHCb calorimeter [207] and T2K neutron detector [208]. No low temperature investigation of the performance of WLS at cryogenic temperatures was found in the literature. To make informed design choices, a series of experimental tests needs to be performed to investigate the performance of WLS in liquid helium, the optimum optical coupling between fibre and scintillator for a good light yield and robustness at low temperature, and the particulars of the best geometry for this application.

6.2 Design Considerations

To produce a well characterised, reliable and consistent detector, some design questions first must be identified and answered. Maximising detection efficiency must be at the heart of the design process, with the aim being to count every neutron that interacts with the scintillator. As only a fraction of the scintillation light is collected via optical fibres, this fraction, i.e. the number of photons per neutron event that reach the light detector, must be maximised. This is in order to ensure a clean signal, clearly distinguishable from noise or a background event, for good particle recognition so that the maximum neutron counting efficiency can be obtained. To maximise the photon collection, we must optimise the geometry, finish and reflective coating of the scintillator in order to produce the largest signal for the light yield of the detector. The parameters involved in the design process are listed in Table 6.1 and outlined in this section.

The path of the scintillation photons will depend on the physical **geometry** of the scintillator. Photons may become trapped in a material due to repeated reflections, eventually being absorbed. This can be minimised with an appropriate choice of scintillator geometry.

Similarly, the **finish** of the scintillator will affect the reflected path of the photon and if photons are trapped. Typically scintillators are coated in a specular or a diffuse **reflector** in order to maximise collection efficiency. Various materials are available for this, such as

Detector Design Parameters
Shape of scintillator geometry
Finish of scintillator
Reflective coating
Volume of scintillator
Number and layout of optical fibres
Optical fibre coupling
Consistency of parts
Temperature robustness

Table 6.1: Parameters to consider during the detector design process.

Mylar, Teflon, Tyvek, Aluminium, Lumirror, VM2000.

While a low atomic weight scintillator would be ideal to minimise γ interactions, a small **volume** detector could also provide this functionality. The scintillator must be sizeable enough to stop the nuclei produced by neutron absorption, large enough for optimised optical fibre coupling, and to be robust and for ease of assembly, but minimised to reduce sensitivity to background γ rays.

Key to the design process is to decide how much light is sufficient to reliably identify and count the neutron signal. For this, the **fraction of light** carried from the scintillator to the PMT via an optical fibre must be quantified, and how this varies with the **number and layout** of fibres. The various losses must be minimised by investigating the best way to **couple** the fibre to the scintillator and to the PMT.

The **consistancy** and reliability of the detector components must be known in order to quantify the systematic error associated with it. For example, what is the variation in light yield from sample to sample of scintillator machined to the same standards. This involves measuring the consistency of light output of various pieces of scintillator in the same experimental conditions, and repetition of experiments to determine uncertainty due to reproducibility of the experimental conditions.

Finally, the reliability of components at **low temperature** must be ensured. The optical coupling of the fibres and the scintillator at helium temperatures must remain robust. The

light guide nature of the fibres, as well as the light emission characteristics of the WLS fibre must be sufficient at low temperature to count events.

All these design factors can then be combined to produce the best prototype. With this in mind, a series of test experiments were undertaken to quantify the variables and iterate towards a prototype design.

6.3 Experimental Design Investigation

A preliminary experimental investigation was undertaken to determine the light signal obtained from various samples of scintillator in order to make an estimation of the material's consistency, of the quality of the optical surfaces, of the coupling of the scintillator to the PMT or to the optical fibres.

6.3.1 Consistancy of Scintillator Pieces

Firstly the consistency of the scintillator output between different pieces of the the same specification was measured. Four pieces of plastic scintillator BC408 of dimensions 20 mm $\times$ 17.5 mm $\times$ 10 mm were machined and surfaces polished.

The sample's light yield was measured by coupling it directly to the face of the PMT with index refraction matching grease, known as optical coupling grease. It was covered with a reflective lid and exposed to 5.5 MeV α particles from a ^{241}Am source within a light tight box. The scintillation events for the different samples were recorded and a spectrum calculated using the same method as outlined in Chapter 5. The light yield, in arbitrary units, is the value of the mean of a Gaussian fitted to the α peak in the spectrum. The standard deviation of the light yield from the mean was 4.6%. In order to estimate the systematic error associated with changing each scintillator sample, this measurement was repeated ten times, and the standard deviation of the light output of these measurements was found to be 3%.

6.3.2 Polishing

The effect of polishing on light collection, and the variation in polishing quality, was measured by comparing the light yield of each sample with initially polished faces, and subsequently dulled. The results for most samples showed no difference in light yield depending on surface finish. For example, one piece had a peak position of the α peak at 0.00757 μV s with polished faces and 0.00705 μV s with dull faces, a decrease of 7%. On visual inspection, a crack was visible in the dull face, indicating that the drop in light yield in this case may be due to this imperfection rather than the type of finish. Another sample's light yield decreased by 5% from 0.00739 μV s to 0.00703 μV s and all others were less than 1%.

6.3.3 Coupling

The effect of the optical coupling grease was tested by measuring the light yield from a sample directly coupled to the PMT with and without the grease applied. The grease improves the light yield by 80%, for example one measurement of the peak integral position of the α peak increase from 0.00386 μV s to 0.00707 μV s, an increase of 83%. When light crosses a boundary between materials with different refractive indices, the light beam will be partially refracted, and partially reflected at the boundary surface. The fraction of light that is reflected at this boundary depends only on the two refractive indices, for example Plastic Scintillator, $n_s = 1.58$, and PMT Borosilicate glass $n_g = 1.49$. In reality, the boundary between a scintillator and PMT glass is not perfectly smooth and separated by a variable thin layer of air, with n = 1, which causes a much higher amount of total internal reflection. The introduction of a grease of similar refractive index thus reduces the reflections at the boundary, $n_{gr} = 1.46$, and increasing light transmission. The effect of a similar product, optical coupling glue was tested in the same manner, and also yielded an increase in light yield of at least 85%.

6.3.4 Sources of Light Yield Variation

These sources of variation in light yield are summarised in Table 6.2. The sum in quadrature of the sample placement, consistency and polishing uncertainties gives an experimental

uncertainty of 7.4%.

Source	Effect [%]
Sample Placement	3
Sample Consistency	4.6
Polishing	< 5
Grease	80

Table 6.2: Sources of Light Yield Variation

6.3.5 Wavelength Shifting Optical Fibres

Having characterised some basic quantities related to light collection mentioned above, an experimental investigation into the light collection efficiency of optical fibres was begun. We wish to find out how many fibres are necessary to collect sufficient photons to count each neutron/α/triton event, and what is the best way to couple these fibres to the scintillator to maximise the photons collected.

A first test of the light yield from a wavelength shifting fibre connected to a plastic scintillator was carried out. A small piece of plastic scintillator of dimensions $20 \times 20 \times 5$ mm^2 was cut and a hole drilled through the middle with clearance for a 1 mm diameter WLS fibre. The fibres are Kururay multiclad Y11 1 mm diameter plastic wavelength shifting fibres. A 30 cm length of WLS fibre was cut and optically polished at both ends. It was placed in the scintillator and coupled with some optical grease. The end of the fibre was covered with a small piece specularly reflective VM2000 foil, to reflect any photons travelling in this direction back towards the PMT. The scintillator was wrapped in PTFE tape for diffuse reflection, with a small hole left for the α particles from the ^{241}Am source to impinge on the scintillator without scattering in the wrapping. The WLS fibre was wrapped in a black sheath to prevent any cross talk and creation of background photons in the fibre from direct UV excitation. A plastic holder was machined to hold the fibre firmly in place perpendicularly to the PMT window and to avoid any strain on the fibre. The end of the fibre lies flush with this holder, which is bolted firmly in contact with the PMT window via some optical

Figure 6.1: WLS fibre to PMT coupling device.
Left: WLS fibres are glued into plastic holder for support and to couple to PMT face. Scintillator wrapped in light reflecting PTFE and fibres in black sheath seen in background. Right: Polished WLS fibres end flush with the surface of the plastic holder, which is then bolted onto the PMT holder and in contact with the PMT window, coupled with grease.

coupling grease. This is similar to that shown in the photographs in Figure 6.1.

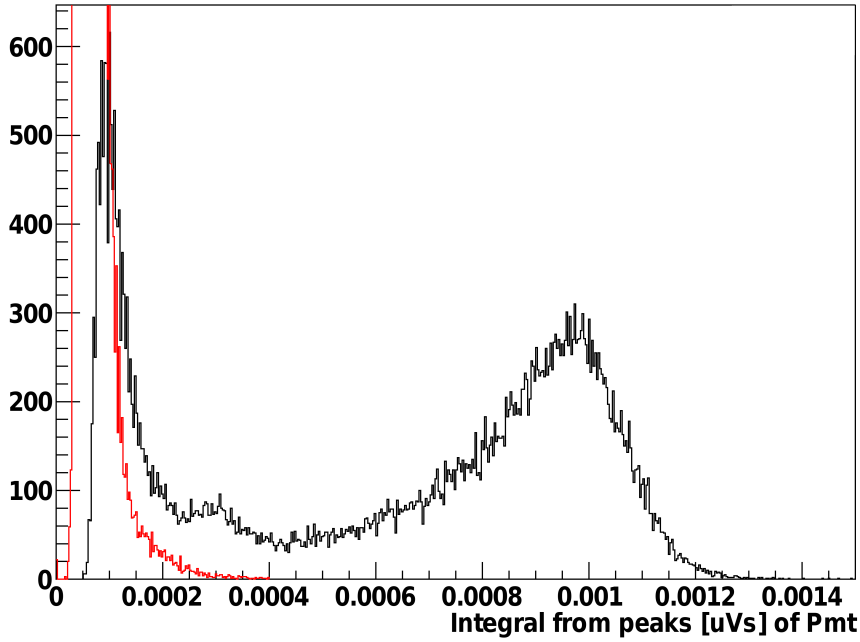

Figure 6.2: PHS for direct coupled (black) and WLS fibre coupled (red) scintillator.

The light yield from this test with 1 WLS fibre was compared to that from placing the scintillator in direct contact with the PMT window. The number of photons reaching the PMT via the WLS fibre was very small. For direct contact, the α peak in the pulse height spectrum (PHS) is clearly distinguished from γ and noise, as seen in the black trace of Figure 6.2. In the same figure, the much smaller pulse height spectrum of the WLS

fibre configuration can be seen, in the red trace. Any α signal is not distinguished from noise. Further improvements are now carried out by increasing the number of WLS fibres, with a larger and more carefully machined, polished and wrapped scintillator, and testing improvements to coupling the fibre to the scintillator with optical glue.

6.3.6 Quality & Volume of Scintillator

A larger scintillator piece machined of dimensions $35 \times 20 \times 10$ mm^3 (3.5 times the volume for the small piece) with a higher quality optical surface produced in the mechanical workshop rather than by hand, and its light yield with 1 WLS fibre tested in the same manner. A comparison of the PHS of this piece compared to the first piece is seen in Figure 6.3, with a clearer definition of the α peak from the background events seen in the newly machined sample. There is now some definition between the signal and background events, and background events could now by removed with a simple cut. For each event, it can be decided if it contained signal from a single photon or multiple photons. Events with a single photon signal were removed, leaving a PHS of mostly α events, as seen in Figure 6.4. A Gaussian was fitted to the peak, centred at 1.5×10^{-4} μV s.

The light yield value of the signal events remains small, and further improvements are needed to boost this. This can be done with better coupling between the scintillator and fibre, and with using multiple wavelength shifting fibres.

6.3.7 Optical Glue

The next attempt at improving the light yield was to use optical glue Norland NOA 61, a refractive index matching glue, and to carefully glue the WLS fibre in the drilled hole. This product is to seal any air gap between the scintillator and the WLS fibre with a material of similar refractive index, thus reducing the amount of light internally reflected at this interface, reducing light trapping and increasing the number of photons entering the WLS fibre and thus producing a larger signal. The fibre was glued in place using a thin syringe

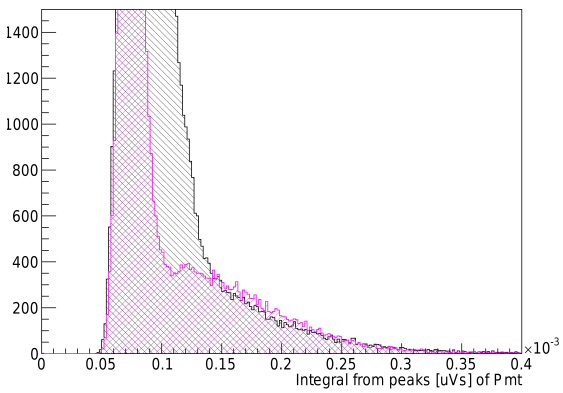

Figure 6.3: Comparison of PHS of small rough piece (black) to larger piece (magenta). Some signal is now distinct from the noise.

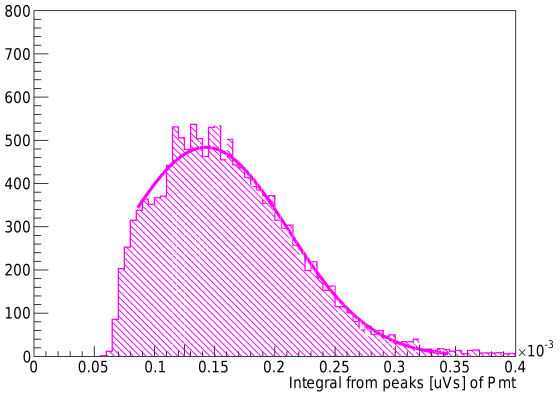

Figure 6.4: Extracted α signal from larger scintillator piece (magenta), fitted with a Gaussian centred at 1.5×10^{-4} μV s.

and needle, and no air bubbles were seen by eye. The light yield was improved by a factor of 2 to a peak position of 3.0×10^{-4} μVs, over the previous test whereby the fibre was only coated in grease, resulting in a peak position of 1.5×10^{-4} μVs. The α spectrum is shown in Figure 6.5 in red, relative to the light yield for directly coupling (black) and the grease coupled WLS fibre (blue).

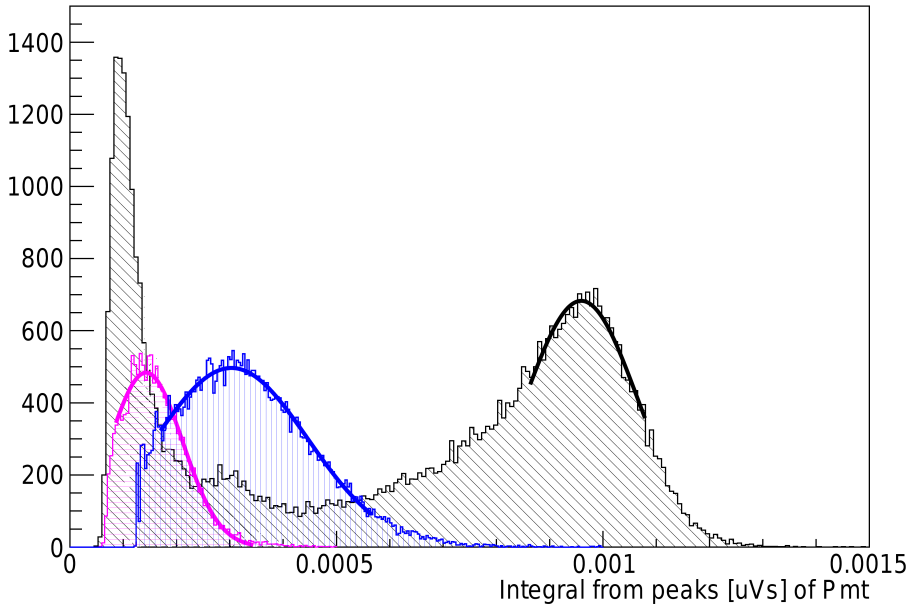

Figure 6.5: Pulse Height spectra of Scintillator and WLS Fibre tests. Direct coupling in black; Larger Scintillator 1 WLS grease coupled in magenta; 1 WLS glue coupled in blue. Values of α peak light yield given in Table 6.3.

6.3.8 Quantity of Fibres

Although the use of the optical glue improved the light yield, the signal is still small and insufficient. Therefore a second and subsequently third WLS fibre were glued into drilled holes in the scintillator. A photograph is seen in Figure 6.6 showing the scintillator piece with 3 WLS fibres embedded in drilled holes and glued in place. The light yield improved by a factor of 1.5 from 1 to 2 fibres to 4.7×10^{-4} μVs, and a factor of 1.3 from 2 to 3 fibres to 4.7×10^{-4} μVs. The pulse height spectra are shown in Figure 6.7 and the values of the light yield improvements listed in Table 6.3. The introduction of multiple fibres results in an α signal peak that is now clearly distinguishable from noise, and no cuts were required to remove background events.

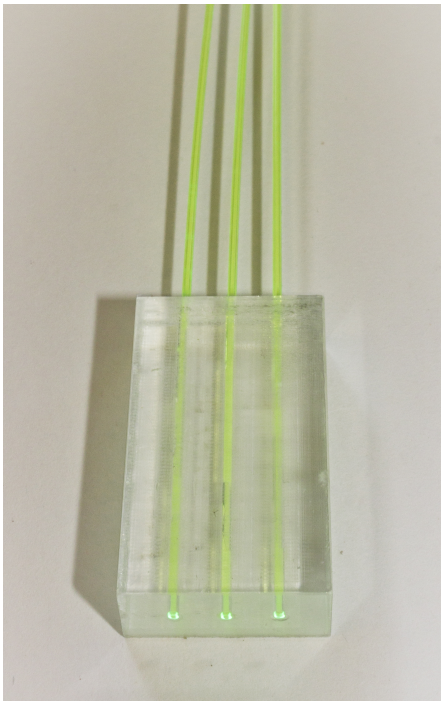

Figure 6.6: Photo of 3 WLS fibres glued into scintillator

6.3.9 Conclusion

A steady improvement of light yield was seen over the course of these tests, with the light yield results and resolution listed in Table 6.3 and plotted in Figure 6.8. The α peak is now clearly distinguished from PMT noise. It is important that the number of events that are

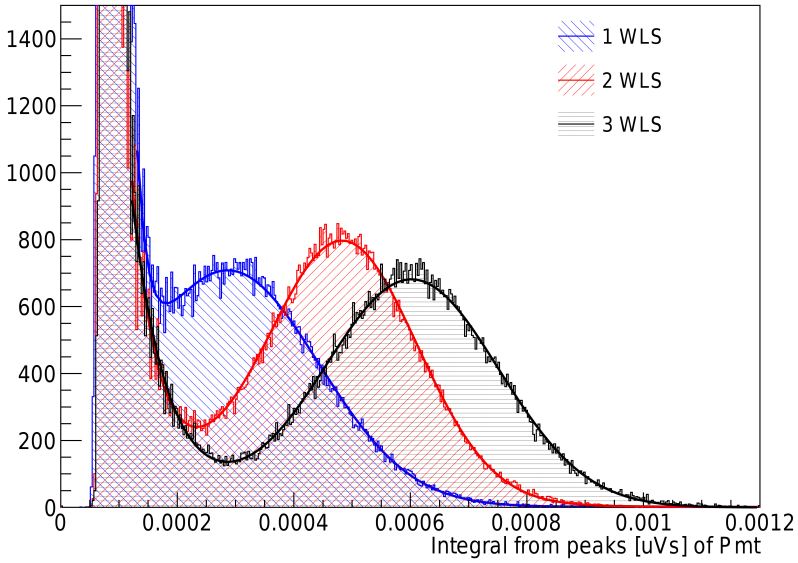

Figure 6.7: Comparison of PHS of one (blue), two (red), and three (black) WLS fibre readout.

removed by software cuts in order to improve the spectrum is kept to a minimum, as each signal event removed is a neutron not counted, thus defeating the purpose of improving the efficiency of neutron detection. The next stage is to design and construct a prototype α detector which can be operated in liquid helium.

Configuration	Peak [a.u.]	FWHM [a.u.]	
Small Piece on PMT	9.6	2.3	
Large Piece 1 WLS	1.5	1.6	Signal extracted by cutting events with single photon.
Large Piece 1 WLS glued	3.0	3.3	Signal extracted by cutting events with single photon.
Large Piece 2 WLS glued	4.7	2.9	No Cuts Required
Large Piece 3 WLS glued	6.1	3.5	No Cuts Required

Table 6.3: Improvements in Light Yield

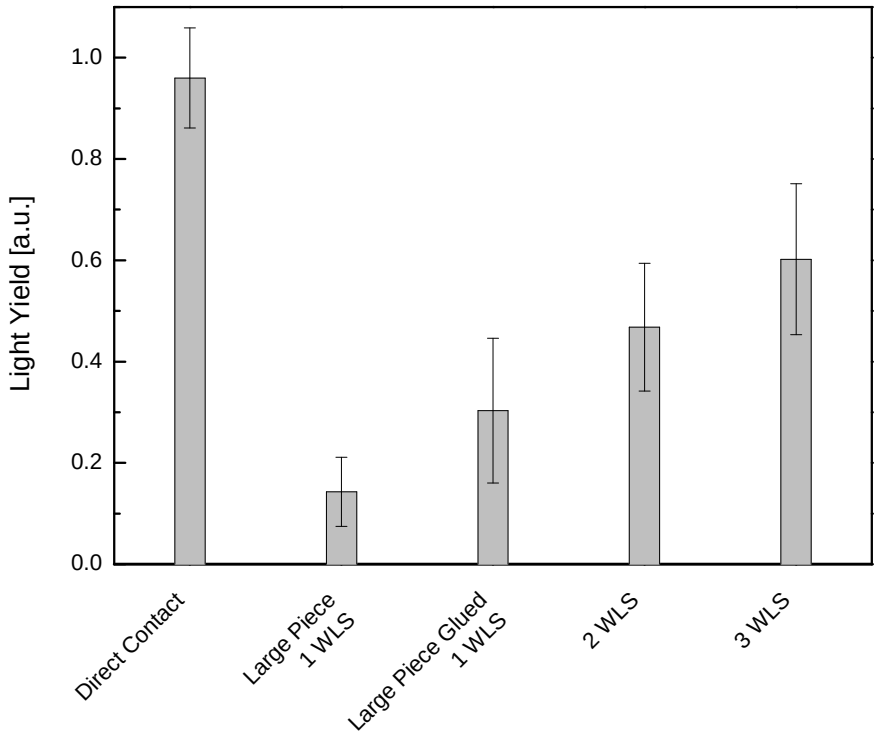

Figure 6.8: Light yields of the improvements to the prototype compared to direct PMT contact. Error is σ of Gaussian fit to α peak.

6.4 A Prototype Cryogenic Scintillation α Detector

Following the optimisation of the WLS fibre readout, the process of prototyping a module of a scintillating detector that could function at liquid helium temperature was begun. Although we know the scintillator performs as required at 4 K, the WLS fibre and the coupling between the scintillator and fibre has not been tested in these conditions. Light losses may occur due to relative thermal contraction of different materials, causing gaps or breaks. The wavelength shifting fluors involved in the WLS fibre have not been studied at low temperature, and so like a scintillator itself, the emitted light may be quenched or slow with reduced temperature.

6.4.1 Design

A liquid helium bath cryostat was used for designing and testing the prototype, with a 1 m long hollow dipstick used for this process. In general, the equipment to be tested in the cryostat is mounted at the end of the dipstick, and the readout cables travel up the centre

and out of the cryostat, where feedthrough and readout equipment is mounted outside at room temperature. In this case, a custom mounting plate was designed and machined to hold a scintillator piece and to hold the α source in contact with it. The WLS fibres travelled up the centre to the top of the dipstick where they were glued into a plastic feedthrough and PMT coupling piece, as was depicted in Figure 6.1. The PMT was then held in an aluminium holder that was bolted to this mount. This set-up is shown in Figure 6.9.

The prototype low temperature scintillating α detector consists of a $35 \times 20 \times 10$ mm^3 BC408 scintillator piece, machined to the same quality as the last piece tested in Section 6.3.5. All sides are polished to optical quality and three holes of diameter 1.1 mm were machined through the centre, as was shown in Figure 6.6. Three 1.2 m long WLS fibres were glued into these holes with NOA 61 optical glue, and the ends of the fibres polished. The scintillator piece was wrapped in 4 layers of PTFE tape of thickness 0.75 mm, with a small hole left for the α particles to impinge directly on the scintillator surface without scattering in the tape. The scintillator detector is then mounted in the dipstick holding plate, and the WLS fibres threaded through the centre of the dipstick. At the other end, the fibres are glued into holes in a solid plastic feedthrough, which bolts onto both the dipstick and the PMT holder, and forms a gas-tight seal. The polished ends of the fibres end flush with the plastic which is coupled to the PMT window using optical grease. The PMT is mounted here, outside the cryostat and operates as normal at room temperature. The dipstick is mounted on the helium bath, and can be lowered by 80 cm, so that the scintillator and a significant portion of the WLS fibres are in the 4.2 K liquid.

6.4.2 Characterisation

Firstly, the light yield with 5.5 MeV α particles from ^{241}Am was tested at room temperature, and found to be 4.1×10^{-4} μVs, which is 67 % that of the 3 WLS fibre test piece discussed previously, 6.1×10^{-4} μVs. This reduction in light yield may be due to the 3 fold increase in length of fibre, in which there is light attenuation, as well as small changes due to variation

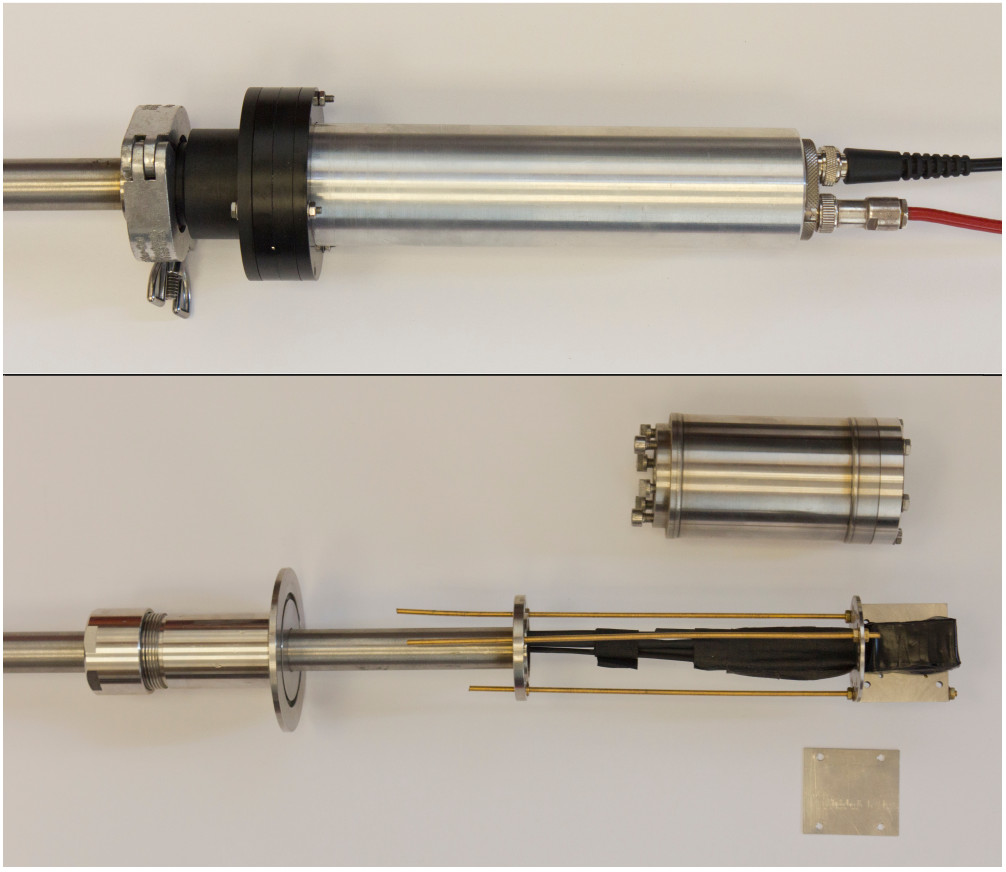

Figure 6.9: The cryogenic dipstick.
Top: Aluminium PMT holder which remains outside cryostat at room temperature. WLS fibres glued into black plastic holder are clamped flush with the PMT window.
Bottom: The scintillator and α source are wrapped in light tight black material and mounted on the bottom of the dipstick which is lowered into liquid helium. The WLS fibres also wrapped in black travel up the centre of the dipstick to the PMT outside the cryostat. A steel liquid-tight container may be mounted around the scintillator to allow the α particles to impinge on the scintillator unattenuated by the liquid.

in production quality of scintillator and fibre polishing. The specifications of the WLS fibre are such that there is attenuation of 1 dB/m at 500 nm, the peak of the green emission. Over 1.2 m this corresponds to a fractional loss of power of 25%, compared to 7% over 30 cm of fibre. For any significant length of signal travel, the WLS fibres would need to be spliced to clear fibres, which have only 0.02 dB/m attenuation at the same wavelength. This α pulse height spectrum is plotted in relation to that of the earlier tests in Figure 6.10.

It was then tested in a bath of liquid nitrogen at 77 K and subsequently in a liquid helium bath at 4.2 K. The range of α particles in water is less than 50 microns, and there will undoubtedly be liquid filling the small gap between the scintillator and the source. Thus

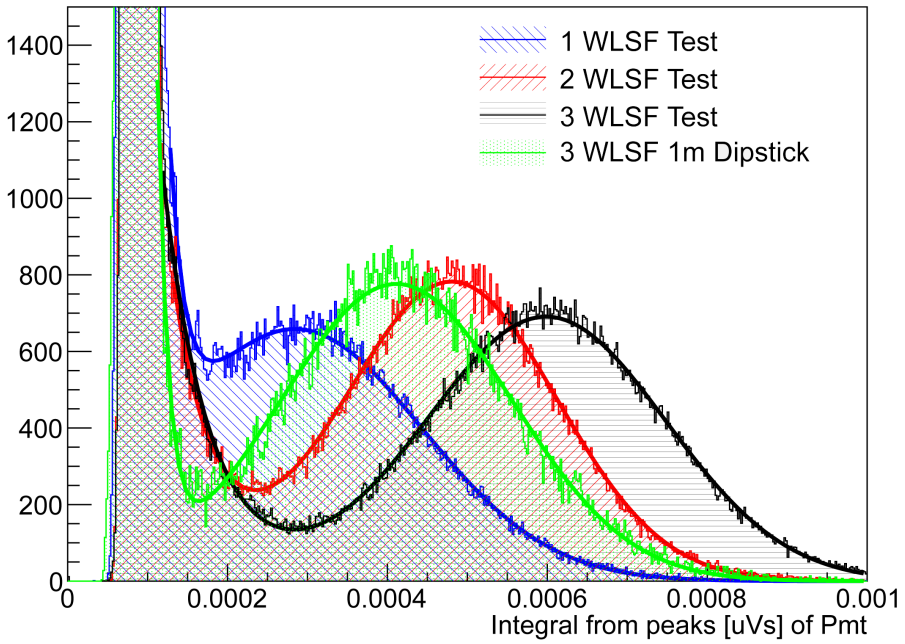

Figure 6.10: A comparison of the light yield of the 3 fibre dipstick scintillation module (green) to the earlier 1, 2 and 3 fibre test results.

a liquid tight container was mounted around the holder, which the scintillator was thermally connected to with a copper connector. At 77 K, hardware failure led to very high noise, and so data quality was low and therefore not presented. This was rectified for the 4.2 K test.

Once cooled in liquid helium, the light yield of the α peak was at $2.5 \pm 0.01 \times 10^{-4}$ μVs, 61% that at room temperature. The pulse height spectra for room temperature and 4.2 K are shown in Figure 6.11 and the peak positions listed in Table 6.4.

Configuration	Peak [a.u.]	FWHM [a.u.]
3 WLS fibre Test Piece	6.1	3.5
3 WLS fibre Dipstick 300 K	4.1	3.3
3 WLS fibre Dipstick 4 K	2.5	1.6

Table 6.4: Light yield results of the prototype α detector tested cryogenically.

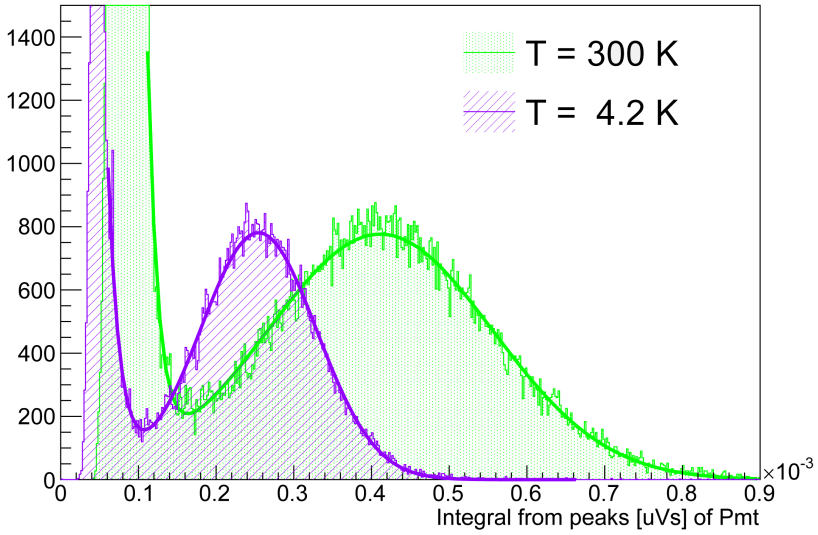

Figure 6.11: Comparison of signal at room temperature, 300 K (green), and liquid helium temperature, 4.2 K (purple), for the 3 fibre dipstick protoype α detector.

6.4.3 Further Improvements

To improve further on light yield, an alternative coupling mechanism between the scintillator and the WLS fibres was investigated. NOA 61 optical glue cures upon exposure to UV light, provided by an high power hand held device designed for this purpose. The design of the scintillator-fibre coupling method of holes through the plastic presented some problems for thorough curing of the glue. As the scintillator absorbs efficiently in the UV range, few photons were reaching the glue to cure it. Furthermore it was difficult to transfer the glue without creating air bubbles which will affect the transport of the photons from the fibre to the scintillator. The alternative is that instead of holes through the scintillator, 1.1 mm diameter grooves were cut from the surface, as shown in the photograph in Figure 6.12. This way, the glue can be laid with more reliability and with less air bubbles, and a more thorough enveloping of the WLS fibre in the refractive index matching material achieved. This method was tested with 3 $\times$ 1.2 m lengths of WLS fibres either glued in holes or grooves. It was found that the light yield from the groove method was $5.1 \pm 0.002 \times 10^{-4}$ versus $4.1 \pm 0.001 \times 10^{-4}$ μVs from the hole method, an increase of 24%. The comparison of these pulse height spectra is seen in Figure 6.13

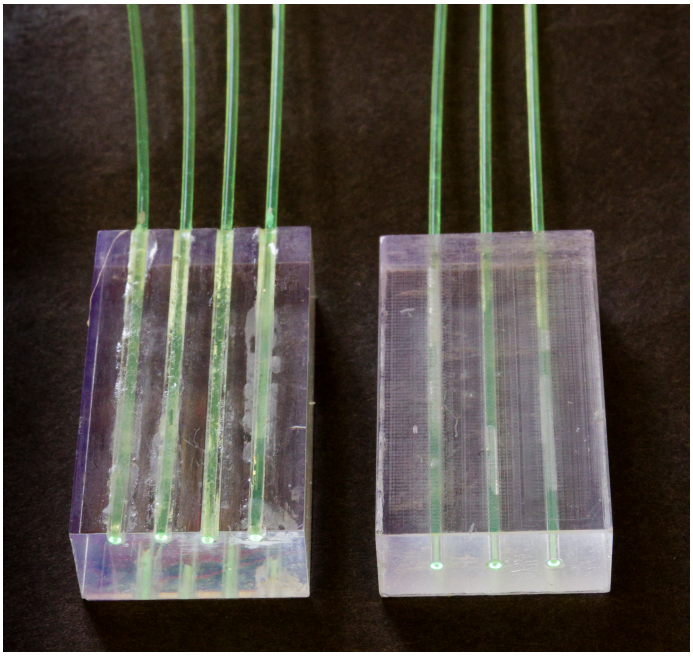

Figure 6.12: Scintillator coupled to WLS fibres via grooves in surface (left) versus holes through centre (right).

This method was then used to manufacture a full length scintillation α dipstick, with 3 and subsequently 4 WLS fibre readout, for further light yield improvement and even clearer separation of the α peak from the PMT noise floor. As the energy of the α and triton from the ^{6}Li capture reaction are 2.05 and 2.73 MeV respectively, rather than 5.5 MeV as used here, it was decided that the detector would benefit from clearer signal to noise separation, to ensure that the peak due to these lower energy particles is still separated from the noise floor. This was tested at room temperature and gave a light yield of 5.1 $\pm$ 0.02 $\times$ 10^{-4} μVs for the 3 fibre readout and 7.4 $\pm$ 0.02 $\times$ 10^{-4} μVs for the 4 fibre readout, as seen in Figure 6.14.

The 4 fibre prototype was then tested in liquid nitrogen and liquid helium. The light yield at 77 K and 4.2 K was the same, 4.7 $\pm$ 0.01 $\times$ 10^{-4} μVs, 64% that at room temperature. This is the same relative light loss as was found for the earlier 3 fibre model. The improvement of the light yield of this 4 fibre design over the 3 fibre design is seen at room temperature in Figure 6.15 and in liquid helium in Figure 6.16. The light yield of the 4 fibre detector at 300, 77 and 4.2 K is seen in Figure 6.17. The low temperature pulse height spectrum was deemed bright enough and sufficiently clear of the noise floor for development as a neutron

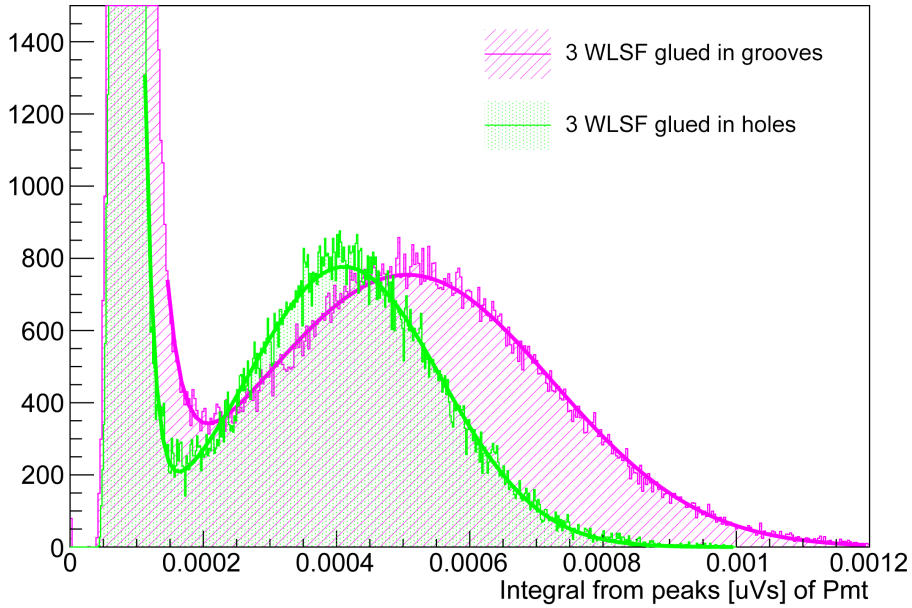

Figure 6.13: Comparison of signal from slotted design with 3 WLS fibres glued in (magenta), to hole design with 3 WLS fibres glued in (green).

detector.

Figure 6.17 indicates a successful prototype has been designed and tested. Some light loss was seen upon initial cooling from room temperature, and this may be due to a break in a light seal between the scintillator and WLS fibres, causing increased reflection losses. No further change in light output between 77 K and 4.2 K is seen, indicating no further mechanism of light losses, and showing that the detector prototype is rugged to the environment. This design can now be used to produce a prototype neutron detector. A summary of the improvement in light yield throughout this prototyping process is presented in Table 6.5.

Configuration	Peak [a.u.]	FWHM [a.u.]
3 WLS Fibres in Holes	4.1	3.2
3 WLS Fibres in Grooves	5.1	5.1
4 WLS Fibres in Grooves	7.4	5.9
4 WLS Fibres in 77 K	4.8	5.3
4 WLS Fibres in 4.2 K	4.8	5.1

Table 6.5: Light yield results of further improvements to prototype α detector, tested cryogenically.

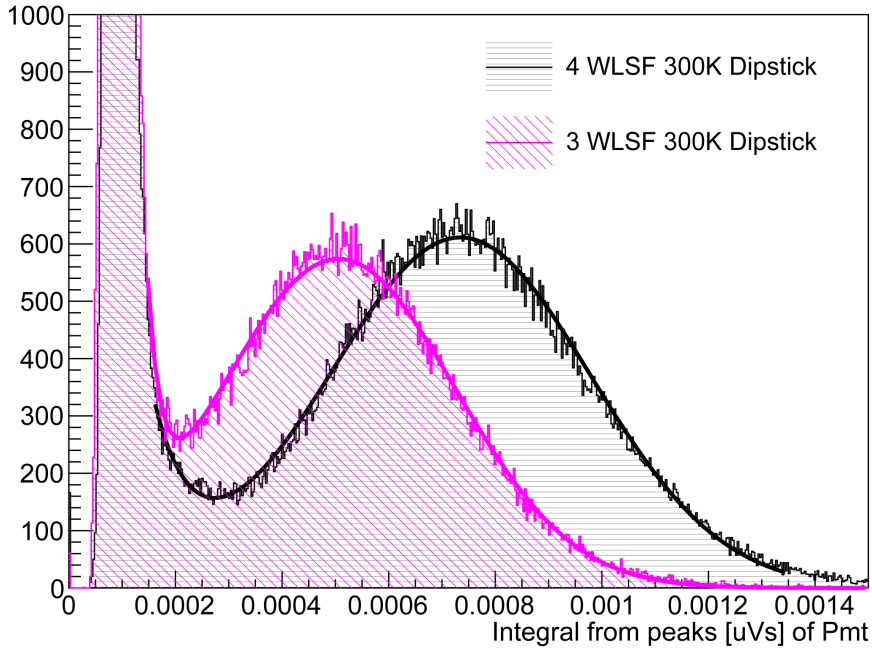

Figure 6.14: Comparison of signal from slotted design with 3 WLS fibres glued (magenta) vs 4 fibres glued (black).

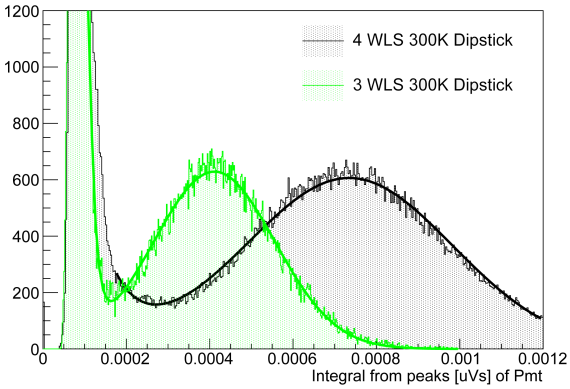

Figure 6.15: Comparing signal from prototype with 3 WLS fibres embedded at room temperature (green) to prototype with 4 WLS fibres in groove at room temperature (black).

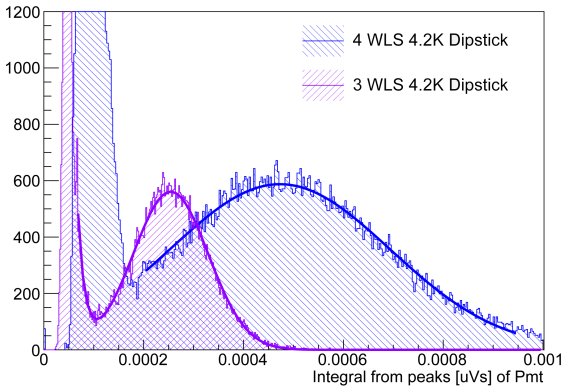

Figure 6.16: Comparing signal from prototype with 3 WLS fibres embedded at helium temperature (purple) to prototype with 4 WLS fibres in groove at helium temperature (blue).

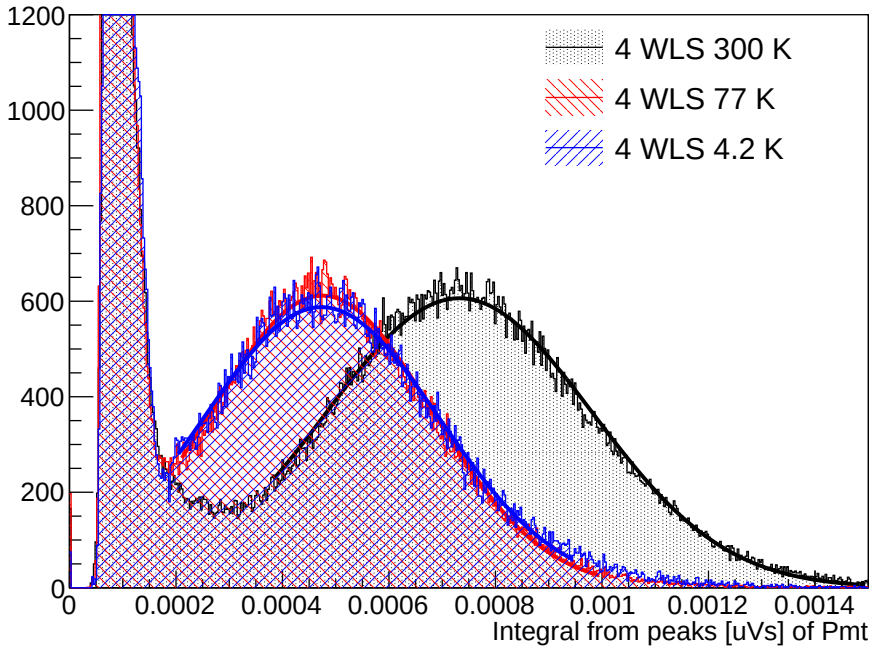

Figure 6.17: Successful prototype design with 4 WLS fibres glued in a groove. Comparison of signal at room temperature (black), liquid nitrogen temperature, 77 K (red), and liquid helium temperature, 4.2 K (blue). The prototype sees no further light loss between 77 and 4.2 K indicating the design is robust to the cryogenic environment.

6.5 A Prototype Neutron Detector

To convert the successful low temperature scintillation α prototype detector into a UCN detector, a thin film of ^{6}LiF must be deposited. The existing silicon UCN detectors have a 600 μg/cm^2 layer of ^{6}LiF deposited. The expected fraction of incident ultra cold neutrons that will be captured by the ^{6}Li can be calculated using the following equation

$$R_n = \frac{N_A}{m_A} L\rho\sigma_n \tag{6.1}$$

where N_A is Avogadro's Number (mol^{-1}), m_A is molecular mass (g mol^{-1}), L is the thickness of material (cm), ρ is the material density (g cm^{-3}) and σ is the capture cross section (cm^2). For the thin film ^{6}LiF deposited on the existing silicon detectors, $L\rho = 600\ \mu g\ cm^{-2}$, $\sigma = \mathcal{O}$(Mb) $= 1 \times 10^{-18}\ cm^2$, $m_A = 25$ g mol^{-1}, so $N_A/m_A = 2.41 \times 10^{22}\ g^{-1}$. However not all of the nuclei in ^{6}LiF will capture a neutron, only a fraction of 6/25 by mass, giving an additional factor of 0.24. This gives

$$R_n = (2.41 \times 10^{22}\, g^{-1}) \cdot (0.24) \cdot (600 \times 10^{-6}\, g\, cm^{-2}) \cdot (1 \times 10^{-18}\, cm^2) = 3.47 > 1 \tag{6.2}$$

which means there will be 100% UCN capture. This thickness of converter was optimised by Baker et. al. [101] for efficient conversion and minimal product scattering or loss in the layer, as was discussed in Chapter 3. The range of the 2.05 MeV α particles in ^{6}LiF is 1500 μg cm^{-2} and of the 2.73 MeV tritons is 5630 μg cm^{-2} [209].

This choice of thickness of ^{6}LiF was also used for the scintillator. This process was carried out by the thin films facility at Oxford using the Physical Vapour Deposition (PVD) process. The ^{6}LiF is heated and evaporated in a vacuum, this then condenses on the substrate which is mounted at the top of the chamber.

As the success of the deposition on a plastic surface has not been tested before, the first test was done using the piece of scintillator read out by 3 $\times$ 30 cm lengths of WLS fibre glued in holes, rather than with the α prototype. One 35 $\times$ 20 mm^2 face of the scintillator

was deposited with ^{6}LiF. The success of the adhesion of the deposit critically depends on the conditions of the surface properties itself or any contaminants. Upon visual inspection, the process was successful, and can be seen in Figure 6.18. The effect of the layer on the light collection efficiency and light yield of the scintillation test detector was tested with the ^{241}Am α source, impinging both on the coated and non-coated faces of the crystal. The light yield of the α peak was identical for both faces, indicating that scattering of the 5.5 MeV α particles was insignificant. The light yield results are shown in Table 6.6, whereby after deposition, the α light yield is 48% with 3 WLS fibre readout relative to direct coupling. This compares to 62% prior to deposition, thus a 14% decrease in light yield after the addition of the neutron conversion layer. Such a decrease when applied to the prototype α detector is acceptable and will still yield a peak clear of the PMT noise floor.

Figure 6.18: ^{6}LiF deposited on the surface of the scintillation module, read out with 4 WLS fibres glued in grooves. The iridescence is due to the ^{6}LiF thin film layer.

Sample	PI 3WLS	PI Face	Ratio
LiF	$2.1 \pm 0.6 \times 10^{-4}$	$4.3 \pm 0.5 \times 10^{-4}$	0.48
No LiF	$6.0 \pm 1.5 \times 10^{-4}$	$9.6 \pm 1.0 \times 10^{-4}$	0.62

Table 6.6: How LiF deposition affect light collection

Following the successful testing of the deposition process, the prototype low temperature scintillation α detector read out with 4 $\times$ 1 m WLS fibres was deposited with 600 μg cm^{-2} ^{6}LiF in the same manner as the test detector.

6.5.1 A Portable Scintillation Neutron Detector

A simple prototype of a cryogenic UCN scintillation detector has now been constructed. It was design and built in such a way that allowed for portability and ease of testing at neutron science facilities. The cryogenic dipstick has a KF50 flange mount which is easily connected to a wide-necked liquid helium dewar or a bath cryostat for ease of testing. The neutron sensitive scintillation module is mounted at the base of the dipstick, which can be placed in a neutron beam. The scintillator is wrapped in layers of PTFE reflective tape and black tape to encapsulate the scintillation photons and prevent light leaks. The scintillator is read out by four 1 m WLS fibres, wrapped in a black coating, which travel up the dipstick to a gas tight feedthough. This feedthrough acts as mount in which to glue the fibres, and as a PMT connector component. The end of the fibres are held in firm contact via optical coupling grease with the PMT window, whose holder is bolted to the top of the dipstick.

The PMT is powered by an Ortec Camac high voltage supply which provides 940 V for the PMT, connected by a simple HV coaxial cable. A significant improvement to the system was a new dedicated fast DAQ system for photon measurement designed and produced in-house. This system consists of a front-end fast digitisation electronics board with on-board FPGA, connected by a pair of fibre optics to a USB-interface box. The front-end is directly linked to the PMT using a BNC cable while the USB-interface is connected to a USB port of a Linux laptop PC. The USB box is interfaced with dedicated software that produces `.ox2` files compatible with the OxRop data analysis software. This DAQ system is pictured in Figure 6.19.

The PMT signal is digitized by a fast 12 bit ADC with 5 ns sampling interval that allows resolving individual photons, for slower scintillators. The signal trace is recorded in a buffer, until a scintillation event meets the trigger requirements, whereby the scintillation event and

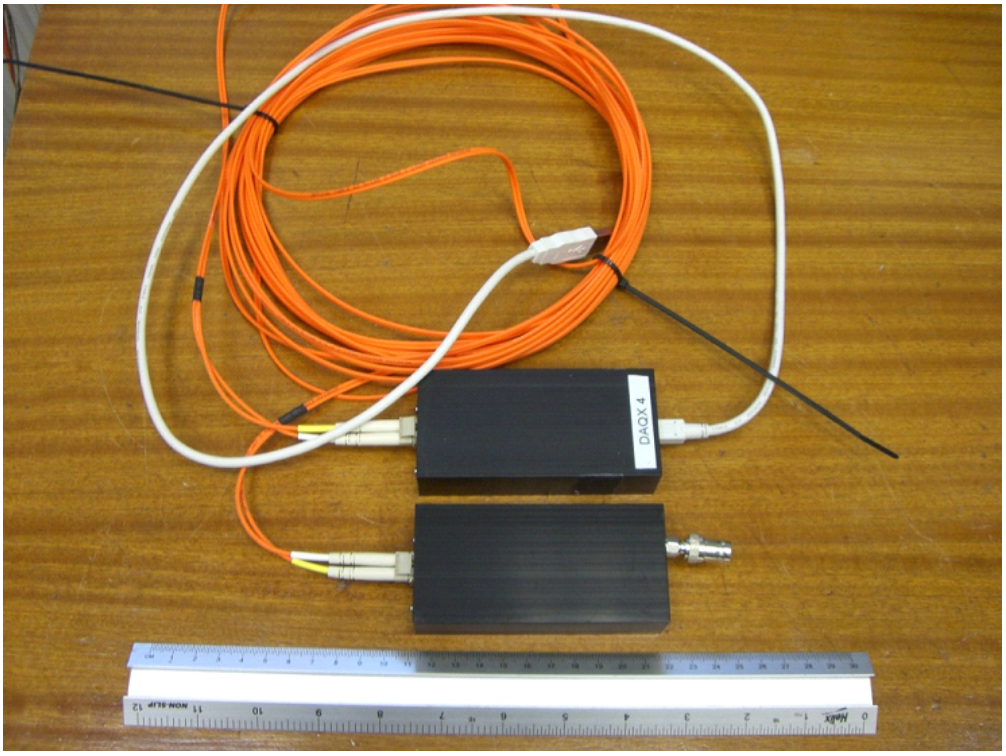

Figure 6.19: 200 MHz data acquisition system showing DAQ-front-end, USB-interface and connecting cables.

a pre-trigger region of data are retrieved from the buffer and recorded. The DAQ software interfaces with this hardware to produce event parameters as were discussed with the older system in Chapter 5. As before, it identifies individual photons in the event and derives their arrival time and the area under the peaks that is proportional to the intensity of light generated in the scintillation event. Furthermore, improvements to the OxRop software have now made many of the analysis procedures, including cuts, classification of events and decay time analysis part of the software package rather than separate analysis macros.

This has all contributed to a convenient portable and flexible cryogenic UCN scintillation detector that can be easily transported and tested at different neutron sources. A photograph of the complete system is seen in Figure 6.20.

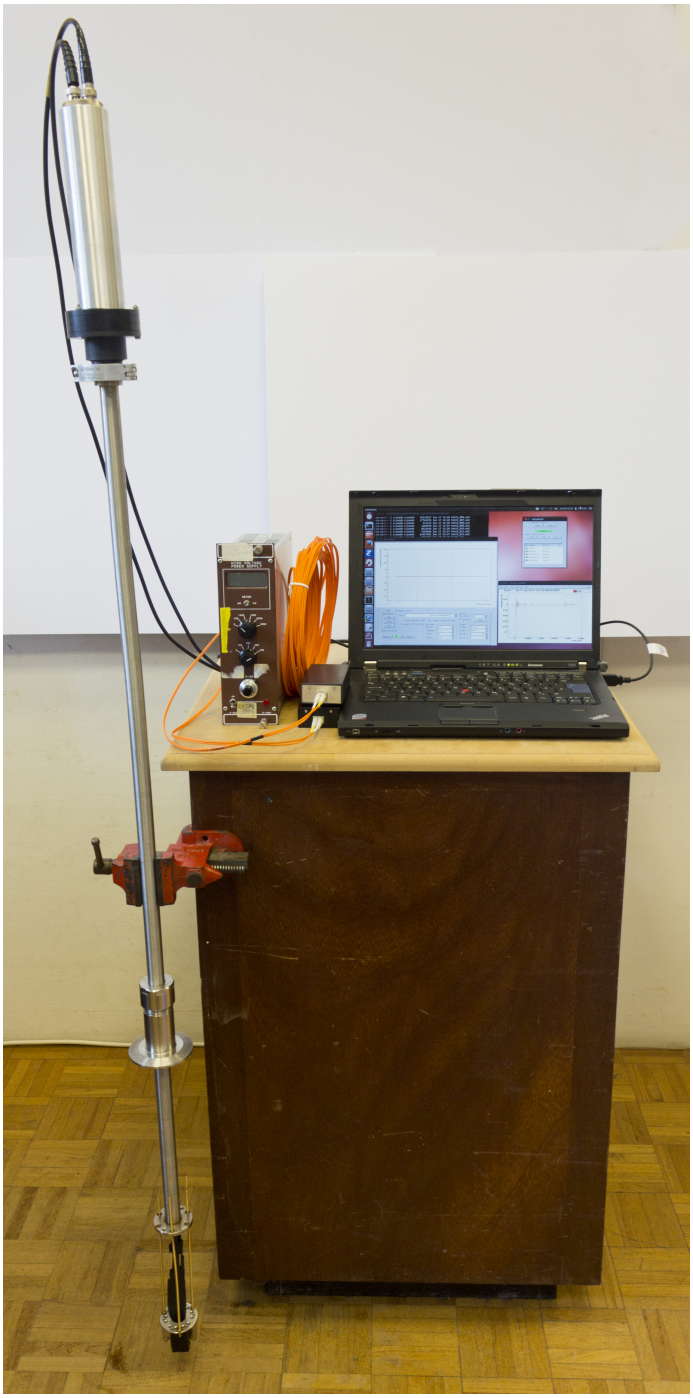

Figure 6.20: Cryogenic scintillation UCN detector system including scintillation module on cryogenic dipstick, WLS fibres, PMT and its high voltage, data acquisition system and PC.

6.5.2 Characterisation with AmBe Neutron Source at ISIS

At the time of this research the ILL was undergoing a long reactor shut-down until summer 2014 for fuel rod replacement and a significant upgrade program. The cryoEDM experiment was being moved to a new beamline and unfortunately no UCN source was available to test the prototype. In light of this, other neutron sources were considered in order to prove that the prototype would function as a neutron detector.

The portable prototype system was taken to the ISIS neutron scattering facility at Rutherford Appleton Laboratory in Oxfordshire, where a moderated AmBe neutron source was available for detector testing. ISIS is primarily a neutron scattering facility, with an active neutron detector research group to design build and test their suite of neutron detectors for the scattering experiments. As such, it has a range of sources and detector test facilities.

The AmBe source used consists of a mixture of ^{241}Am and ^{9}Be. The natural α emission of ^{241}Am produces 5.5 MeV α particles which bombard the Beryllium nuclei and are captured via the reaction $^{9}Be(\alpha, n)^{12}C$ to produce neutrons.

$$^{9}_{4}Be + ^{4}_{2}He \rightarrow ^{12}_{6}C^{*} + ^{1}_{0}n \tag{6.3}$$

$$^{12}_{6}C^{*} \rightarrow ^{12}_{6}C + \gamma\,(4.4MeV) \tag{6.4}$$

Fast neutrons are emitted with energies across a continuum in the range 3 – 6 MeV with an average of 5.5 MeV. Approximately 70 neutrons are emitted per MBq of ^{241}Am activity. Photons are emitted from the ^{241}Am at 60 keV and 14 keV, however the primary photon background comes from the high energy 4.4 MeV γ emitted from the excited state of ^{12}C following α capture. For each neutron emitted, a high energy photon is also emitted.

The AmBe source at ISIS is nominally 360 GBq neutron activity. Firstly, it is shielded by lead which reduces the γ flux, but has low neutron cross section. Next a 7 cm layer of water acts as a moderator of the fast neutrons, producing a flux of $80\,n\,s^{-1}\,cm^{-2}$ thermal neutrons of energy 25 meV at the detector position, on a fixed experimental platform. Additionally,

one expects a further contribution to the γ background from neutron reactions with any materials in the experimental area, particularly Copper or Cadmium. The γ emission of the ISIS source has not been characterised, but one can naively assume at least $\mathcal{O}(1)$ high energy γ per neutron, possibly significantly higher. Unfortunately the source room was not equipped for cryogen use, and so the UCN prototype detector was tested at room temperature only.

One can calculate the expected fraction of incident thermal neutrons that will be captured by the ^{6}Li using Eq. (6.2) as before. The significant difference is that the captured cross section is now 940 b for thermal neutrons rather than ∼1 Mb for UCN. Thus the expected fraction of incident thermal neutrons of energy 25 meV is 0.0033. So at the ISIS AmBe neutron source with a flux of $80\,n\,s^{-1}\,cm^{-2}$ on the $3.5\,cm \times 2\,cm$ face of the detector, one expects to capture ∼2 neutrons per second, which will emit a triton or α into the scintillator.

As the plastic scintillator is also sensitive to γ radiation, we can estimate the number of incident γ we expect to scatter in the material. BC408 consists primarily of Polyvinyl Toluene (PVT) which is a long chain hydrocarbon consisting of $(C_9H_{10})_n$. On average n = 3, giving a molecular mass of 354.5 g mol^{-1}. Data on the scattering and absorption coefficients of photons in materials is available from NIST [210]. The total attenuation coefficient for 4.44 MeV photons in PVT is $\frac{\mu}{\rho} = 3.1 \times 10^{-2}\,cm^2\,g^{-1}$. This comes primarily from Compton scattering, with about 5% pair production and negligible photo-absorption. The expected cross section for PVT plastic can be calculated from the absorption coefficient by

$$\sigma_\gamma = \frac{\mu}{\rho}\frac{m_A}{N_A} = 1.826 \times 10^{-23}\,cm^2. \tag{6.5}$$

Eq. (6.6) can be applied to γ interactions in plastic with $m_A = 354.5\,g\,mol^{-1}$, $\rho = 1.032\,g\,cm^{-3}$, L = 1 cm and σ from Eq. (6.5) to give the expected fraction of incident γ to interact in the plastic:

$$R_\gamma = \frac{N_A}{m_A} L\rho\sigma_\gamma = 0.032. \tag{6.6}$$

This is 10 times larger than the neutron capture fraction, and if one naively estimates there to be equal quantities of neutrons and γ, one would expect 20 γ per second interacting in

the plastic scintillator, emitting scintillation photons.

As the ISIS γ flux has not been characterised, it is difficult to estimate how many and of what energy γ escape the lead shield and water moderator and reach the experimental platform. However what can be said is that a continuum of γ with energies up to 4.4 MeV is expected at rates significantly above that of the thermal neutrons. With the given amount of ^{6}Li deposited and the thickness of plastic scintillator, it is no surprise that no neutron signal was seen at the ISIS AmBe source. The pulse height spectrum as seen by the detector remained unchanged when a Boron Carbide beam stop was placed in the beam, absorbing the thermal neutrons, but allowing the γ to continue, as seen in Figure 6.21.

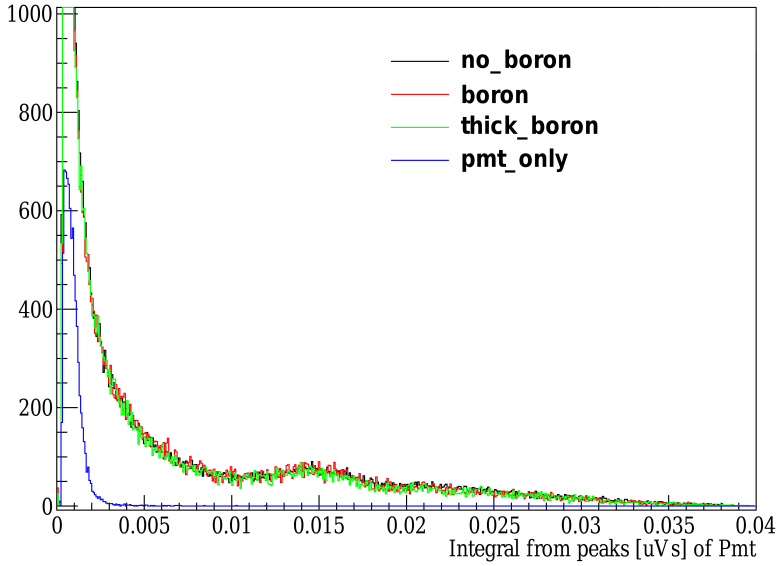

Figure 6.21: Prototype PHS from AmBe source. No change seen when enough Boron Carbide was placed in the source to remove all neutrons.

6.5.3 Characterisation with Thermal Neutron beamline at ISIS

Following these tests, it was decided to modify the detector to improve its sensitivity to thermal neutrons and decrease its sensitivity to γ. Although in cryoEDM, 600 $\mu g\, cm^{-2}$ has proved an optimal quantity of ^{6}Li for 100% UCN capture, due to the higher energy and lower capture cross section of thermal neutrons, this must be significantly increased to improve the thermal neutron capture, and to prove the operation of this detector system. As no

UCN source was available, the detector must be tested at the next best option, a thermal beamline.

The CRISP thermal neutron beamline [211] was available for testing at ISIS which produces a flux of $\sim 10^7\, n\, s^{-1}\, cm^{-2}$. ISIS is a spallation source, where protons are accelerated to 800 MeV and bombarded on a tungsten target at 50 Hz, producing neutrons by spallation. This gives an extremely intense neutron pulse, which is then moderated to thermal energies at a detector testing beamline. A typical energy spectrum of the neutrons at this beamline is seen in Figure 6.22. The γ flux is expected to be $\sim$2 orders of magnitude less than the neutron flux a short time ($\sim$1 ms) after the proton pulse. However during the proton pulse, the flux of γ and fast neutrons is expected to be high, and data recorded during this time window can be removed in post-analysis.

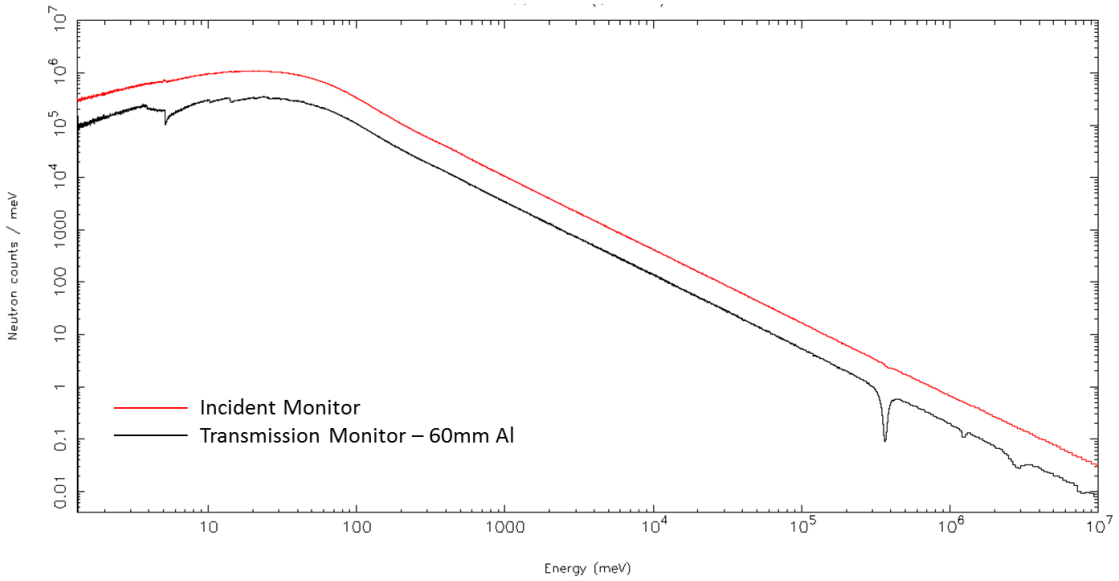

Figure 6.22: ISIS thermal neutron beamline flux.

In order to improve the fraction of captured neutrons by the detector, the thickness of the ^{6}LiF layer must be increased. However there is then a trade-off between the fraction of captured neutrons and attenuation of the reaction products in the thicker ^{6}LiF layer. As was mentioned, the thickness of $600\,\mu g\, cm^{-2}$ was optimised for this very reason. The range of 2.05 MeV α particles in ^{6}LiF is $1500\,\mu g\, cm^{-2}$ and of 2.73 MeV tritons is $5630\,\mu g\, cm^{-2}$ [209] [101]. Therefore a second prototype optimised for the thermal beam was designed with a thickness of ^{6}LiF of $1000\,\mu g\, cm^{-2}$. This is still less than the range of the α particle, although

scattering effects and losses may be seen.

With the current prototype, in the thermal neutron beam, we can expect $2.64 \times 10^3\, n\, s^{-1}$ absorbed in the detector. This is equivalent to one neutron every 4 μs, which is a perfectly acceptable rate, not too fast for the detection and DAQ system, but fast enough to quickly collect spectra.

The second prototype was designed with larger neutron capture capability and smaller γ capture cross-section. The scintillator in the first prototype was 1 cm in depth, with 4 $\times$ 1 mm diameter fibres. As the range of α and tritons in plastic is very short, $\sim$40 μm, the depth of the scintillator can be significantly decreased to reduce γ sensitivity. The only changes that can be made to reduce the γ sensitivity are to change the scintillator to one of lower density or to decrease the depth of the detector. One must also consider the amount of light emitted per γ by the scintillator chosen. If when changing to one of a lower density, it must be ensured that one with a higher relative γ light output is not chosen. The easiest change to implement is to make a slimmer prototype. This can easily be reduced by a factor of 4 while still maintaining sufficient depth for the triton and α to fully ionise, and with enough material to embed the fibres. This would cause the prototype a 4 fold reduction in γ sensitivity.

The new prototype was built with a 2.5 mm thick piece of scintillator with 3.5 $\times$ 2 cm face deposited with 1 mg cm^{-2} ^{6}LiF, read out with 4 $\times$ 1 m long WLS fibres. It is pictured in Figure 6.23. It was assembled in the same manner as the previous prototype described in Section 6.5.1. The light yield of the prototype was tested at room temperature in response to the 5.5 MeV α ^{241}Am source. The light yield was marginally higher than the previous prototype. The pulse integral α spectra are shown in Figure 6.24 and show a peak at 8.0×10^{-4} μVs versus a peak at 7.3×10^{-4} μVs for Prototype 1, an increase of 9%.

The prototype and the portable system was then taken to ISIS for testing at the CRISP thermal neutron beamline. Unfortunately this beamline was also not equipped for cryogens and so the detector was tested at room temperature. During the short time window when the proton beam is interacting with the tungsten target, a high flux of radiation is produced,

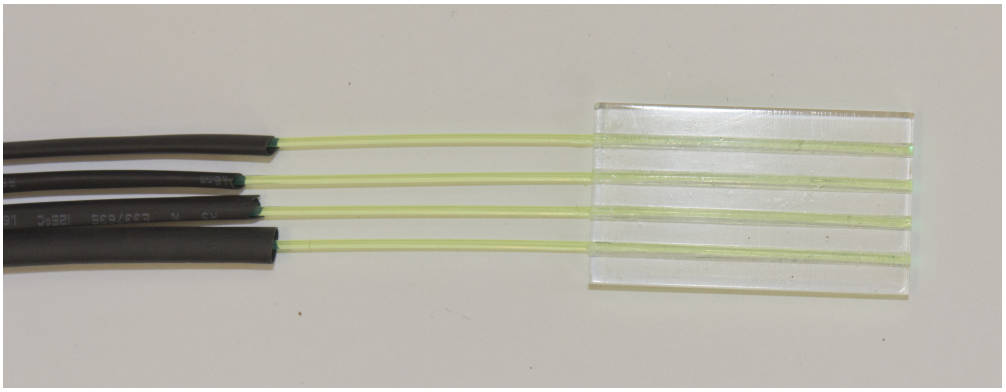

Figure 6.23: Second Prototype optimised for thermal neutron capture

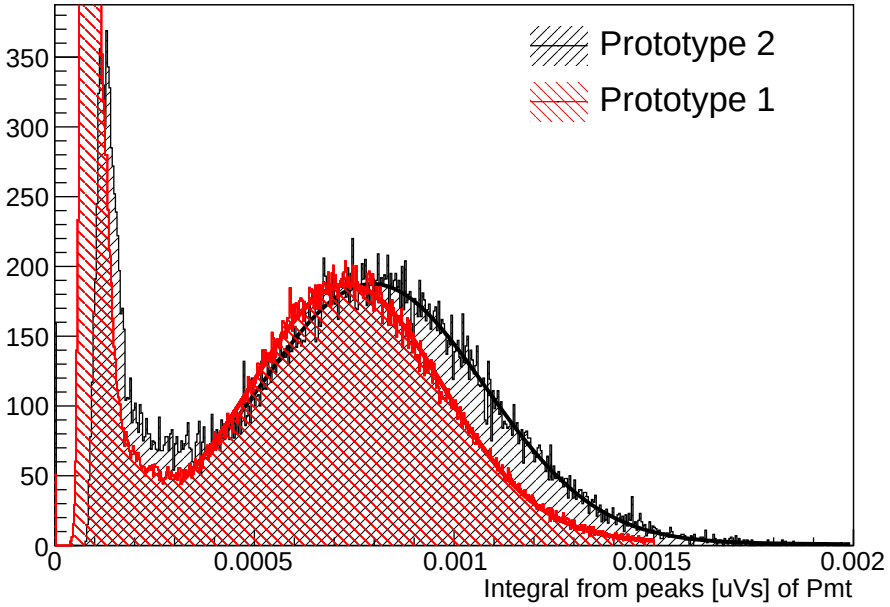

Figure 6.24: Pulse Integral spectra of Prototype 1 (black) and Prototype 2 (red) response to 5.5 MeV α from ^{241}Am.

including fast neutrons and γ. The timestamp of the proton gate signal was recorded by the same DAQ system as the detector signal. The proton gate signal is a 1 μs wide 0 – -5 V pulse at 50 Hz. This timestamp can then be cross-referenced against the timestamp of the recorded scintillation events, and used to veto those events arriving less than 1 ms after the protons have hit the target. This corresponds to the high radiation period, after which the background has subsided and the beam consists of mostly thermal neutrons.

A time-of-flight (ToF) spectrum of the neutron beam using the ISIS monitoring detectors was also recorded. This gives the neutron time of flight between the target, i.e. point of

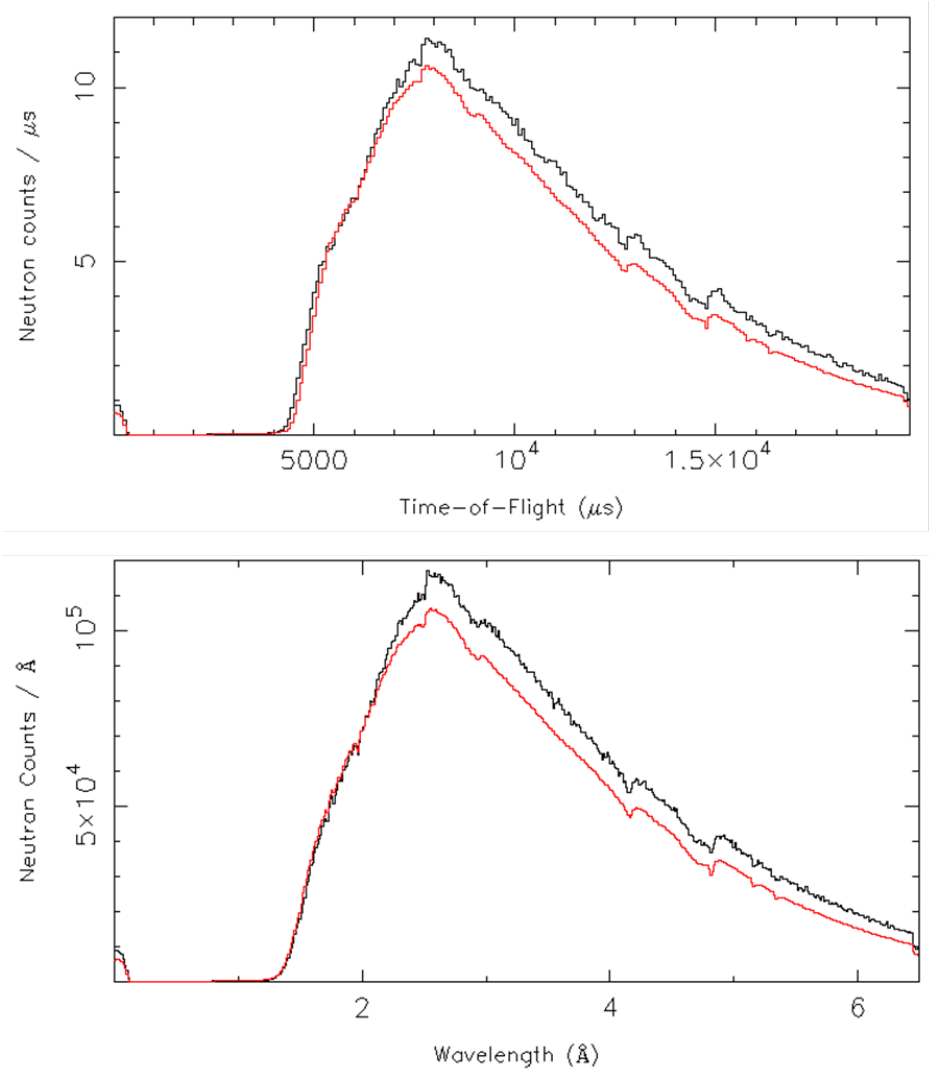

Figure 6.25: Top: Time of Flight spectrum from ISIS monitoring detectors before (black) and after (red) the UCN detector prototype. Bottom: Conversion from ToF to neutron wavelength.

production, and the detectors. Two detectors are installed 11 m and 12 m downstream of the target, just in front and behind the testing platform where the UCN prototype detector was mounted. The ToF spectra and equivalent neutron wavelength can be seen in Figure 6.25. The spectrum shows a broad range of neutron energies with the thermal peak at 2.5 Å (13 meV), and a cold tail to up to 6 Å (2.3 meV).

Neutrons are produced in an intense pulse at the moment the protons hit the target and continue to travel in the beam to the detector with decreasing intensity for 20 ms until the next pulse. If events are selected that arrive at least 15 ms after the proton gate signal was recorded, this will correspond to cold neutrons energies less than 3.3 meV or wavelengths

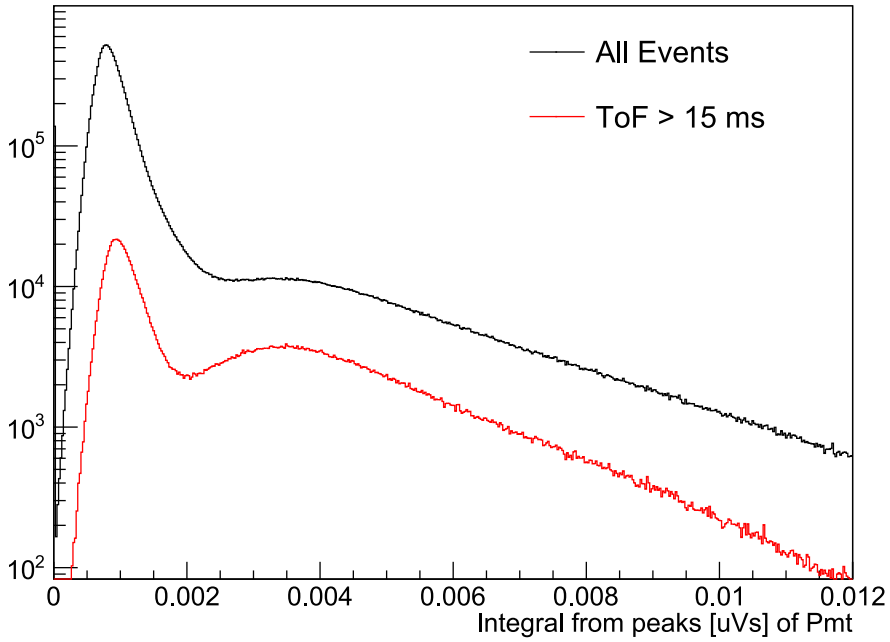

Figure 6.26: Removal of events arriving less than 15 ms after proton pulse, selecting only cold neutrons with $E < 3.3$ meV, $\lambda > 5$ Å.

greater than 5 Å. Discarding 3/4 of the time available for collecting neutron data is only possible due to the high intensity source and long collection time– events were collected for 18 hours. This cut also immediately removes events within the high-background period following the proton pulse on target.

The pulse height spectrum measured by the UCN prototype is seen in Figure 6.26, with all events measured in the 18 hour period in black and only those that arrive at least 15 ms after the proton pulse in red. The response of the UCN prototype detector following this cold-neutron-cut is displayed in Figure 6.27, in black. This consists of the scintillation light created by the 2.05 and 2.73 MeV α and tritons, which are unresolved due to the broad intrinsic resolution of the scintillator. The data was fit with a sum of an exponential for the low energy γ background and a constant offset to account for any high energy neutrons, high energy prompt γ and pile-up, and a skewed Gaussian for the signal from the 2.05 MeV α and 2.73 MeV triton. The signal $s(x)$ and background $b(x)$ are described by the following equations:

$$s(x) = c_0\, exp\left(-\frac{1}{2}\left(\frac{x-\mu}{\sigma+\alpha\ (x-\mu)}\right)^2\right) \qquad \alpha = 0 for x > \mu \tag{6.7}$$

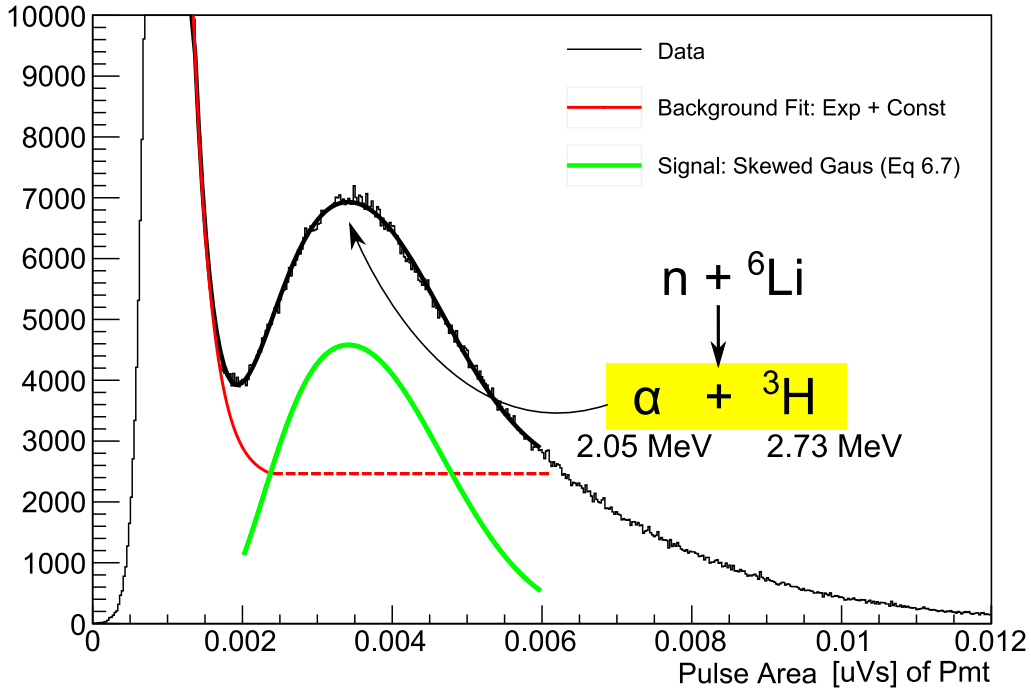

Figure 6.27: Pulse height spectrum of the ^{6}LiF/Plastic Scintillator UCN detector in response to cold neutrons (λ >6 Å) at ISIS. The recorded data in black is fit with a sum of an exponential decay (τ = -4019 μV^{-1} s^{-1}) for the background γ (red) and a skewed Gaussian (Eq. (6.7)) for the unresolved 2.05 MeV α and 2.73 MeV triton signal peak (green), and a constant ($c = 2347$) to account for further background and pile-up in the region $x < 0.006$. The fitted peak is at 3.4×10^{-3} μVs with $\sigma = 1.2 \times 10^{-3}$ μVs.

$$b(x) = c_1\, e^{-\tau\, x} + c_2 \tag{6.8}$$

where μ, and σ refer to the mean and standard deviation of the skew Gaussian distribution, the parameter α modifies the shape of the tail for $x < \mu$ to produce a skewed shape, and the background is characterised by an exponential decay with rate τ and a constant offset c_2.

The result to the fit yielded a Gaussian peak at $3.4 \pm 0.01 \times 10^{-3}$ μVs with $\sigma = 1.2 \pm 0.01 \times 10^{-3}$ μVs, and skew-scale parameter $\alpha = 0.29$, giving a FWHM resolution of 83%. The background and signal fit results are also plotted separately in red and green respectively in Figure 6.27. It must be noted that the absolute value of the *Integral from Peaks* parameter (x-axis value), is no longer directly comparable to that recorded for previous experiments in Section 6.5.2 and Section 6.4, due to an amplifier upgrade in the DAQ system.

Below $x = 0.002$ μV s, the detector shows significant γ background, likely from 480 keV

γ produced from neutron capture by the ^{10}Bo contained in the slits and shielding at the beamline. This reaction was given in Eq. (3.2); the excited ^{7}Li reaction product de-excites with the emission of a 480 keV γ. The light yield from these events is below the neutron signal, however it is not completely distinct from the α/triton peak. There is a minimum in the PHS at 0.002 μVs, where the exponential fit to this background overlaps with the signal Gaussian. This corresponds to 1.67 σ, and therefore 88% of the thermal neutron peak is above this point and clear of this background. For quantitative detection efficiency estimation, the detector would need to be compared to a ^{3}He gas detector or to the cryoEDM silicon detectors, which can be done once the ILL reactor is operational again.

In the region above the α and triton signal, $x > 0.006$, the background is no longer well described by the sum of the constant offset and exponential; it overestimates the background in this region. In this region, the background may have a contribution from a higher energy γ continuum in the experimental area. Cadmium that is present in the shielding and beamline slits may capture neutrons and emit γ in the 2 –7 MeV region. There may be a further contribution in this region of the spectrum from other sources γ emission by neutron capture, and detector pile-up that has not been effectively eliminated in the analysis. These background contributions are specific to the ISIS beamline this experiment was performed at, and any background would need to be characterised and eliminated at a cryogenic UCN source.

6.6 Recommendations for Further Development

This promising technology has delivered a functional detector prototype capable of counting UCN within a liquid helium environment. It has been shown separately to be sensitive to 5.5 MeV α particles within a 4.2 K liquid helium environment, and to cold neutrons via their conversion to α and tritons through the ^{6}Li(n,α)^{3}H reaction. Unfortunately due to the ongoing reactor upgrade at ILL, it was not possible to utilise the UCN source, nor test the detector with a neutron source at low temperature. Nonetheless the separate experi-

mental investigation of its α sensitivity at low temperature and neutron sensitivity at room temperature was deemed sufficient to demonstrate the technology works for this application.

The scintillator has been proven to be bright and fast even to low temperature, and the wavelength shifting fibres have been shown to function within liquid helium. The coupling between the scintillator and readout remains robust at low temperature and although we see a decrease of 36% in light transport efficiency upon cooling, the signal remains distinct from noise. The deposition of thin film ^{6}LiF on a plastic scintillator has been demonstrated and tested with multiple cycling to cryogenic temperature without any visible degradation of the surface quality.

It has been shown that this detector principle could be applied to the cryoEDM experiment to provide a detector that is free from electrical noise and less sensitive to γ background than the silicon detectors, and could deliver a higher UCN detection efficiency, thereby improving the sensitivity of the experiment and the limit on the EDM of the neutron. Comparing the response of this scintillation prototype to neutrons in Figure 6.27 to a recent UCN spectrum from the silicon detectors in Figure 3.6, it is clear that this prototype is a viable alternative low temperature UCN detector to the silicon detectors with the potential to improve on the current UCN detection efficiency and signal quality.

Perhaps plastic scintillator is not the most ideal scintillator choice, due to the non-negligible γ sensitivity and lack of PSD capability. In this regard, ZnS:Ag may be more appropriate, however a program of research to optimise the best detector segmentation to allow for fast signal repetition would have to be carried out. Research is ongoing to minimise the long decay time component and afterglow of ZnS(Ag) with novel manufacturing methods [212], which would make the material more useful in the future for this application with high UCN count rates. Neutron scintillators are an active area of research with innovative new materials being reported all the time and becoming commercially available. A fast bright material with low γ sensitivity that fits the detector criteria as outlined in Chapter 3 may become available very soon.

More generally, this technology demonstration project would be applicable to any num-

ber of the next generation cryogenic nEDM experiments discussed in Chapter 1. It has been shown that the detector elements function within the difficult cryogenic environment, and could be engineered to integrate with the particulars of any given nEDM experiment. Although there are some room temperature nEDM experiments within the current generation, the future of increasing the sensitivity of this measurement undoubtedly lies with the cryogenic experiments. The Superthermal UCN Production Method can produce unrivalled UCN densities over any other production method, and unrivalled statistical sensitivity. Developing UCN detectors that operate efficiently and reliably at low temperature is an essential part of the research and development necessary to advance this field and the sensitivity of the nEDM limit and reach a non-zero measurement.

Conclusion

The process of the research and development of a cryogenic UCN detector has been outlined in this thesis, right from the idea that there may be a better way to detect UCN at low temperature, to investigating different technologies, to studying the behaviour of materials at low temperature, and then finally producing and testing an affordable fast scintillation detector for neutrons that operates successfully and reliably in liquid helium. To place a limit on the electric dipole moment of the neutron, a cryogenic nEDM experiment requires a reliable and efficient UCN detector. Although ^{6}Li silicon charged particle detectors have been developed for cryoEDM, their signal degrades significantly upon cooling, they exhibit only 41% UCN detection efficiency and are subject to electrical interference, γ background and are not as mechanically robust as desired. And so the question was asked "Can we produce an alternative high-efficiency UCN detector that operates within a cryogenic helium environment and is insensitive to background and noise?".

Firstly, Cryogenic Phonon Scintillation Detectors, developed for WIMP searches, were investigated for their application as UCN detectors at cryogenic temperatures, in Chapter 4. These detectors have excellent resolution, pulse shape discrimination capability and background rejection and may be a good solution for UCN detection at $\sim$500 mK. The operation and stabilisation of a phonon detector was demonstrated with a titanium TES sensor operating in its superconducting transition at 350 mK. I successfully demonstrated the detector's capability to measure an α spectrum, and its characterisation and calibration, proving that this technology can work at this elevated temperature. This investigation demonstrated the novel technique of detector stabilisation with infra-red light, and even with primitive

hardware could produce up to an hour of continuous stable data taking. Thermal feedback shortened the response time from $\mathcal{O}(10$ ms) for CRESST detectors to $\mathcal{O}(100$ μs). With further investigation into shortening this time with feedback or alternative crystals, it may be a viable technology for cryogenic UCN detection at high rates. Operation of the detector certainly has its limitations; with the basic stabilisation system used here, stabilisation at the working point in the transition was very susceptible to squid resets, flux jumps or noise spikes. As extremely fine resolution is not paramount to counting UCN, an alternative readout could be investigated. For example, a semiconductor thermistor sensor could be investigated as a temperature sensor instead of the TES, which does not need SQUIDs and may be easier to stabilise and operate. Ultimately, as these detectors require a vacuum in which to operate, it was decided that it would be difficult to retrofit such a detector in the cryoEDM apparatus, and a scintillation detector would be an easier and less costly option. In particular, a neutron window into a vacuum can would cause an undesirable loss of detection efficiency, although low loss windows have been reported in the literature. These cryogenic detectors certainly offer a viable UCN detection technology with good background rejection and with some further research and attention to engineering and design, they would be applicable to future cryogenic nEDM experiments.

Scintillators were identified as the most promising technology for application as a low temperature UCN detector, and plastic scintillators and ZnS(Ag) were identified as the most suitable materials. In particular, a fast, bright scintillator with high α sensitivity and low γ sensitivity was required. A systematic study of a variety of fast scintillators at low temperature was performed in Chapter 5 to determine the relative light yield and decay times across a wide range of temperatures, with excitation from both α particles and VUV photons. The approach of studying the materials' spectroscopic properties provides an understanding of the underlying mechanism that produces the scintillation light. This is interesting in and of itself, but it also provides useful knowledge about competing emission mechanisms which may contribute to pulse shape discrimination capability. This research was the first low temperature study of the light yield, kinetic properties and spectroscopic properties of a wide variety of plastic scintillators and of the phosphor ZnS(Ag), and this research is a new

addition to knowledge in the field. ZnS(Ag) results have been published [192] and a paper on plastic scintillators is in preparation. The study revealed the scintillation from plastics to be extremely stable across a wide range of temperatures, indicating that they are an extremely useful material for cryogenic detectors. Convenient and affordable, it was chosen as the most suitable material for the prototyping process. Interestingly, ZnS(Ag), an inorganic phosphor, also remained extremely bright and fast at low temperature. In combination with ^{6}LiF it is one of the most commonly used neutron scintillators, with negligible γ sensitivity. Its decay time of $3 - 5$ μs means it is somewhat slow for count rates of 500 kHz as expected in cryoEDM and at other high density cryogenic UCN sources. However a segmented detector design could still exploit this extremely bright material in a future cryogenic UCN detector.

The plastic scintillator BC408 was then used to produce a prototype an affordable and robust detector that operated well within in liquid helium. The scintillation light was read out using wavelength shifting fibres, and the materials and optical coupling were shown to remain robust even after multiple cycles from room temperature to 4.2 K. This method of readout allows the scintillator to be in the heart of the cryogenic nEDM experiment, in a sensitive volume where magnetic stability is of utmost importance and impurities must be minimised. This design allows for the photon detector to be operated away from this sensitive region and at room temperature. The successful deposition of ^{6}LiF neutron converter film on the plastic scintillator transformed it from an α detector to a neutron detector, and was tested at the ISIS thermal beamline with good results. What needs to be demonstrated next is its operation within superfluid helium at a UCN source, which was not possible at this time due to the ILL upgrade. This technology demonstration project is applicable to any future cryogenic neutron electric dipole moment experiment. A ^{6}LiF/plastic scintillator UCN detector read out with wavelength shifting fibres is an elegant solution to the challenges of operating a neutron detector in the sensitive cryogenic environment of an nEDM experiment.

All future cryogenic nEDM experiments will require instrumentation of as high performance as possible to improve on measured neutron counts and minimise systematic effects on this measurement. This includes a UCN detector that can deal with high neutron count

rates, that can operate at cryogenic temperatures, and has low sensitivity to the γ background that is at all neutron source facilities. Following the recommendation in 2014 from the Science & Technology Facilities Council for a withdrawal from the cryoEDM project, the future for the experiment in its current form is uncertain, although it is hoped that the knowledge and expertise will become integrated with another nEDM collaboration. In particular, I hope that this demonstration of a low-cost cryogenic scintillation UCN detector is incorporated into a future experiment.

What is certain is that scientific case for the measurement of the neutron EDM is as strong as ever. It is an active and competitive field worldwide with at least seven different experiments operational or in development. Undoubtedly the future of improving the sensitivity of this measurement lies in cryogenic techniques, due to the unrivalled densities of UCN produced by the superthermal production method in helium, and thus statistical sensitivity. Future cryogenic nEDM experiments will face the same technical challenges and research questions outlined in this thesis in the context of cryoEDM. In particular the next generation experiments that will operate in superfluid will also require high efficiency low-temperature UCN detectors, for which the research outlined here is relevant and applicable. The measurement of the neutron electric dipole moment remains one of the most fascinating, and most sensitive paths to discovering new physics beyond the standard model, and to solving the mysteries of the universe.

Appendix A

Hasylab Spectra

A.1 Plastic Scintillators

A.1.1 Emission Spectra

Figures A.1 and A.2 show the luminescence spectra of St. Gobain Plastic Scintillators and Eljen Plastic scintillators. The spectra are corrected for the response of the experimental setup as was described previously. The excitation energy of the incoming photons were chosen to coincide with maxima as measured in the excitation spectra, presented later in Section 5.3.3.

Each manufacturer varies the chemical composition and fraction concentrations of the different types of plastic scintillator to produce changes in light yield, emission spectra, decay time and sensitivity to particular radiation. The spectral variation, as seen when comparing the BC400 and BC418 in Figure A.1, BC408 earlier in Figure 5.16 and EJ204 and EJ254 Figure A.2, is subtle. For all the materials involved, there is essentially no change in shape of the emission profile as a function of temperature, indicating that there is no change in the underlying processes. As the shape of the emission profile do not change as a function of temperature, variation is due to an increase or decrease in efficiency of the same emission method, rather than different methods becoming more or less dominant as a

function of temperature. Similarly there is little discernible difference in emission spectra shape between excitation with E_{ex} = 7.75 eV and E_{ex} = 5.2 eV photons and we conclude that these energies excites the same mode.

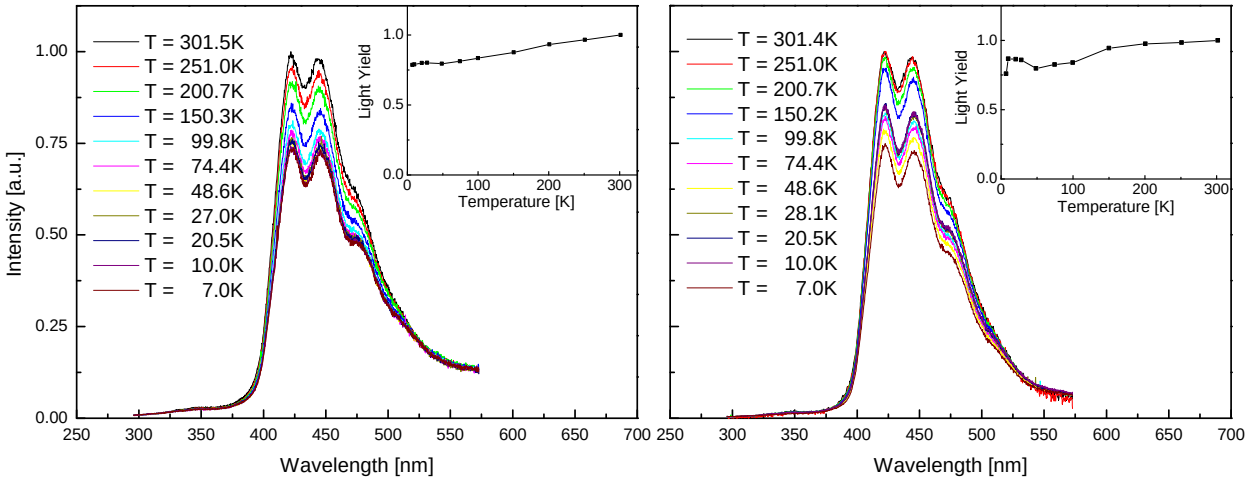

(a) BC400 E_{ex}=7.75 eV

(b) BC400 E_{ex}=5.2 eV

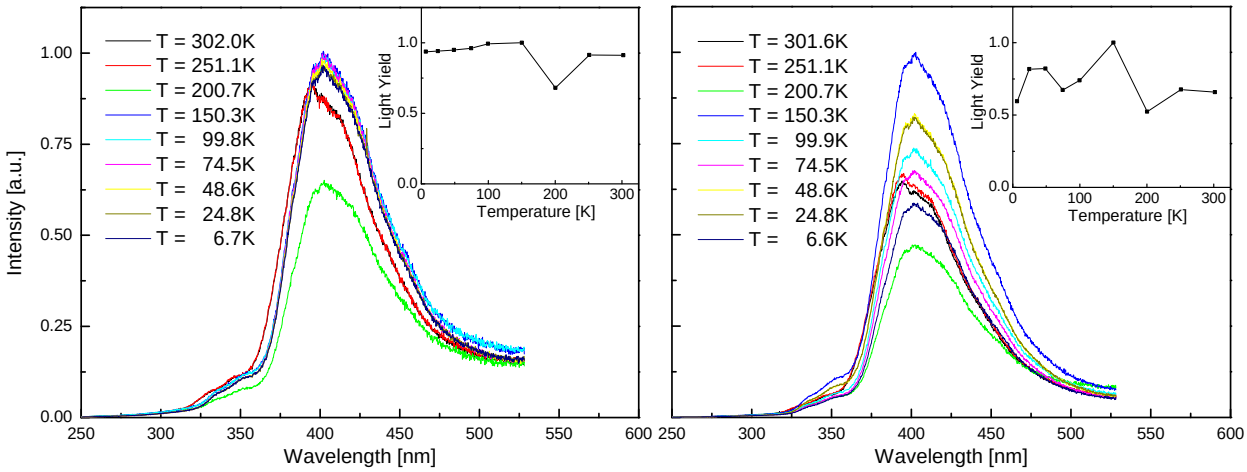

(c) BC418 E_{ex}=7.75 eV

(d) BC418 E_{ex}=5.2 eV

Figure A.1: St Gobain Plastic Scintillator Emission Spectra

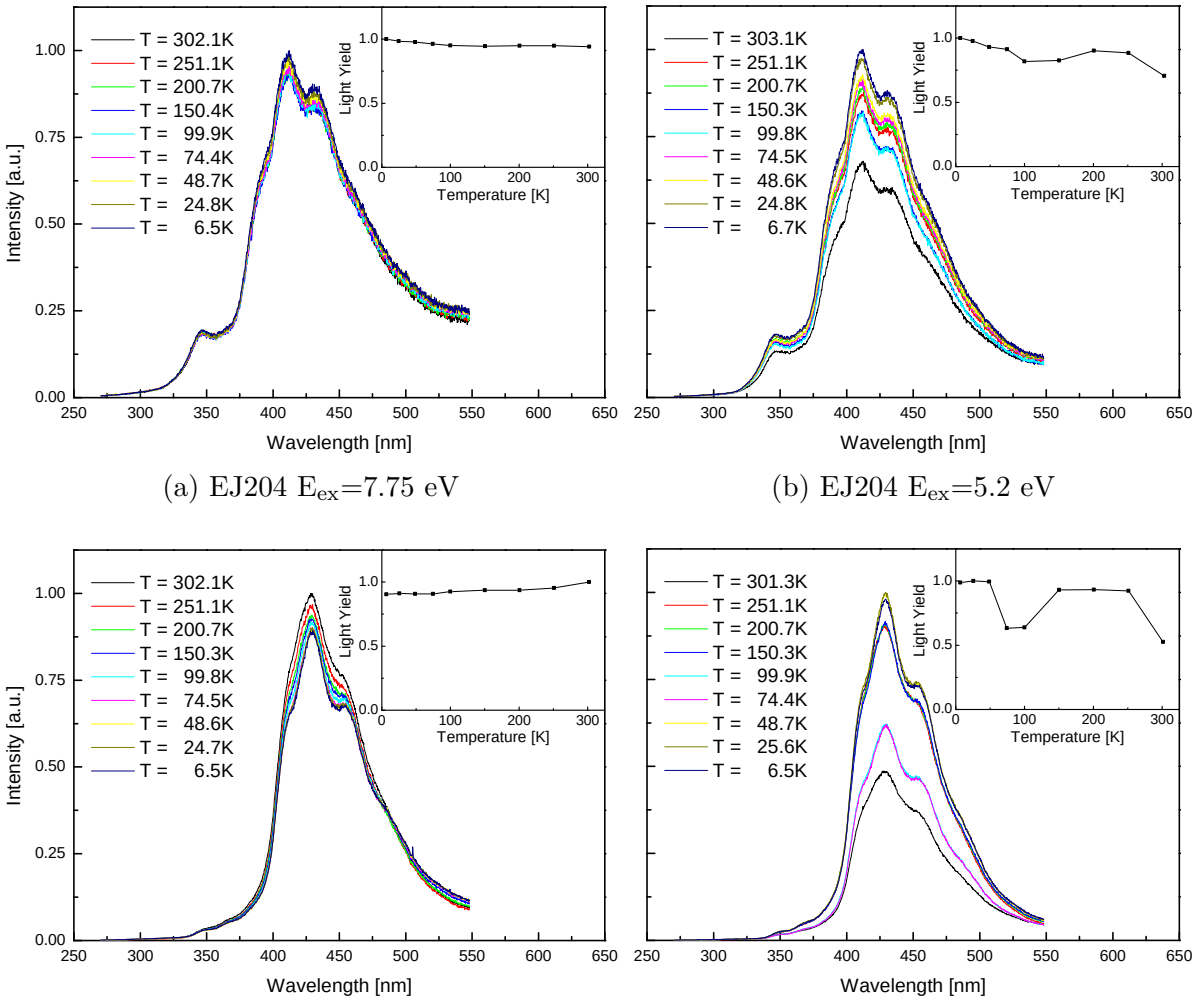

(a) EJ204 E_{ex}=7.75 eV

(b) EJ204 E_{ex}=5.2 eV

(c) EJ254 Boron Plastic E_{ex}=7.75 eV

(d) EJ254 Boron Plastic E_{ex}=5.2 eV

Figure A.2: Eljen Plastic Scintillator Emission Spectra

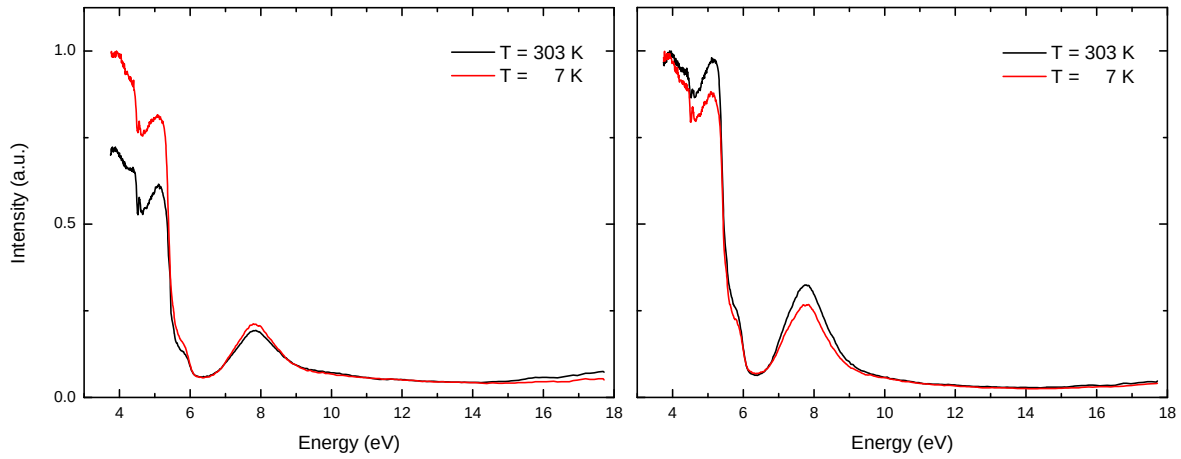

(a) BC400 Excitation spectrum

(b) BC418 Excitation spectrum

Figure A.3: St Gobain BC plastic scintillator excitation spectra at 300 and 7 K. Recorded at emission wavelength 435 nm (BC400) and 390 nm (BC418) for maximum light output.

A.1.2 Excitation Spectra

The excitation spectra at 300 and 7 K for the St Gobain plastics are presented in Figure A.3 and the Eljen plastics in Figure A.4. These were measured at the peak emission value for the given scintillator. At excitation energies lower than ∼5 eV, the base plastic PVT is almost transparent to this energy photon, and so the primary fluor is excited directly. At excitation energies greater than ∼5 eV, the base PVT plastic absorbs the incident radiation, and the energy is transferred non radiately from the base plastics to the primary fluor.

The peak at ∼8 eV seen in the excitation spectra for all the plastics corresponds to the absorption peak of the PVT base plastic which is common to them all. All spectra decrease in intensity slightly at 7 K relative to 300 K, due to decrease in efficiency of absorption, scintillation efficiency of the primary fluor or the efficiency of energy transfer to the wavelength shifter; or due to a temperature dependant change in the Forster transfer between the base plastic and primary fluor.

It is clear from these excitation spectra that the differences in these plastics are subtle and the luminescence mechanism is the similar for all of them and not very temperature dependant, as was the case for the temperature response of the α scintillation.

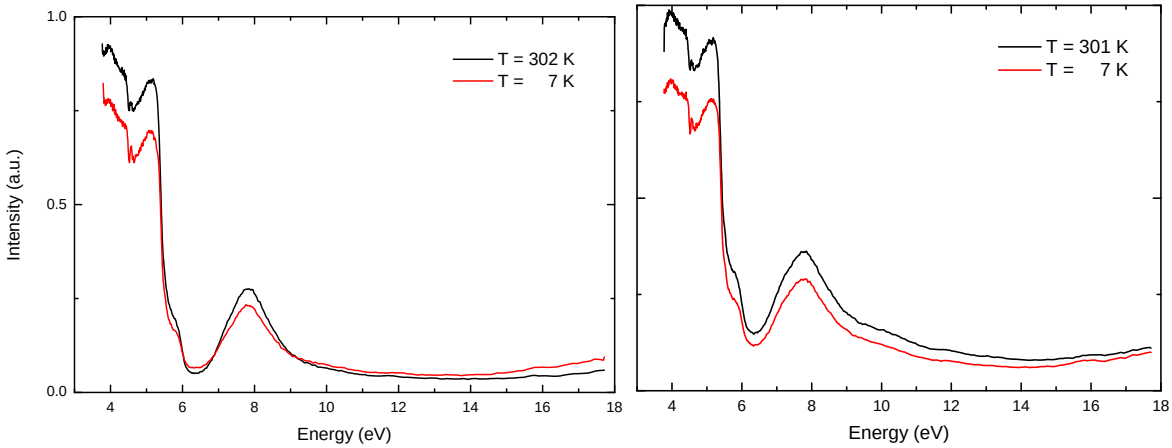

(a) EJ204 Excitation Spectrum (b) EJ254 Excitation Spectrum

Figure A.4: Eljen Plastic Scintillator Excitation Spectra at 300 and 7 K. Recorded at emission wavelengths 410 nm (EJ204) and 435 nm (EJ254) for maximum light output.

A.1.3 Decay Times

Decay time measurements at two excitation energies were made, 5.2 and 7.75 eV, in the temperature range 300 – 7 K. Normalised decay curves for BC400 with both excitations at 300 and 7 K are displayed in Figure A.5. A two component exponent was fitted to the curves, with the faster component being dominant across all temperatures for both excitation energies. For E_{ex} = 5.2 eV, the two decay times from the fit to data are plotted as a function of temperature in Figure A.6a, and in Figure A.6b for E_{ex} = 7.75 eV, and were tabulated earlier in Table 5.11. This analysis was repeated for BC418 and presented in Figures A.7 and A.8. The changes with temperature are subtle and the plastics remains fast and useful scintillators at low temperature, with decay times remaining less than 2 ns.

The Eljen plastic materials are presented in Figures A.9 and A.10 for EJ204 and Figures A.11 and A.12 for EJ254. Similarly to the St Gobain materials, there is little change with temperature, the plastics remaining fast at 6.5 K. EJ204 has a fast decay component of τ_f = 1.67 ± 0.01 ns at 6.5 K, offering a middle ground between BC400/408 and BC418. The boron loaded plastic EJ254 base scintillator is EJ200, which is Eljen's equivalent to BC400. It is not surprising that the decay curves and decay times for both excitation are very similar to BC400.

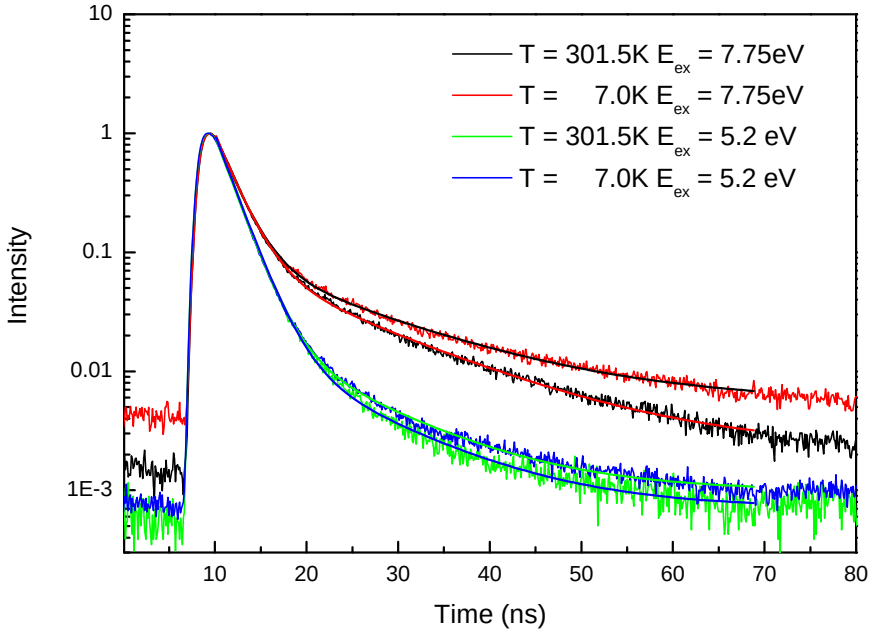

Figure A.5: BC400 Decay Traces and Fits

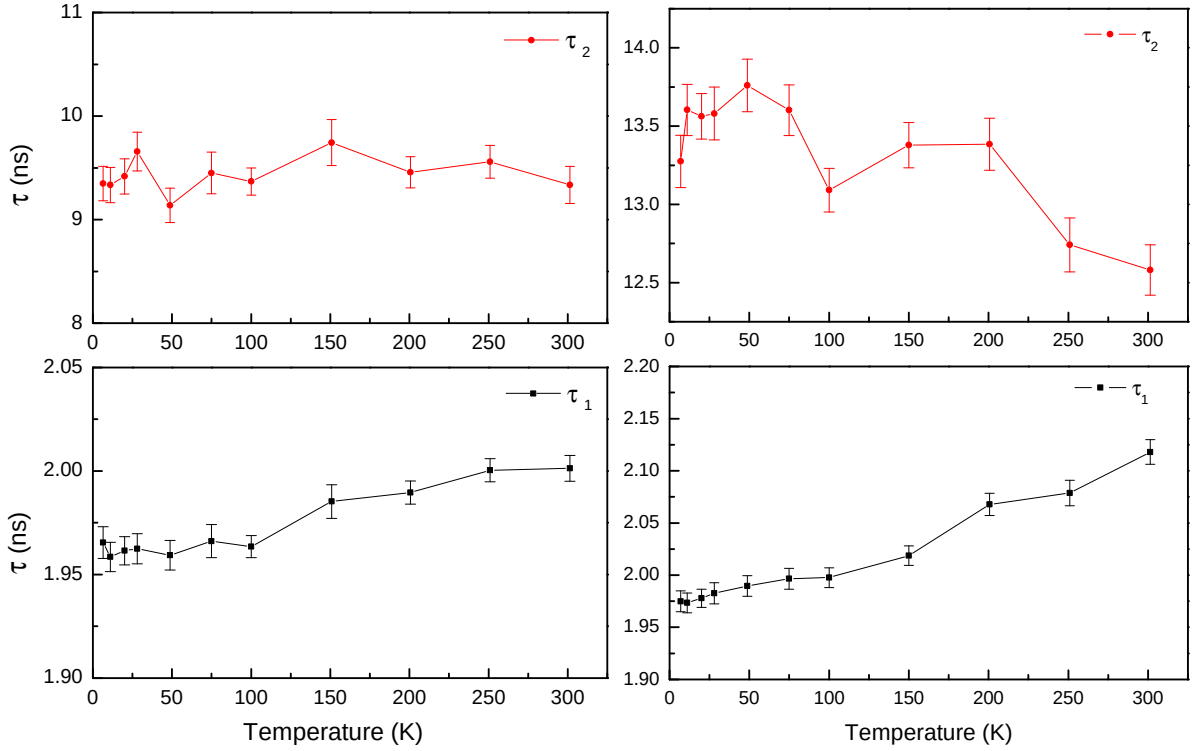

(a) BC400 E_{ex} = 5.2 eV E_{em} = 435 nm (b) BC400 E_{ex} = 7.75 eV E_{em} = 435 nm

Figure A.6: BC400 Decay

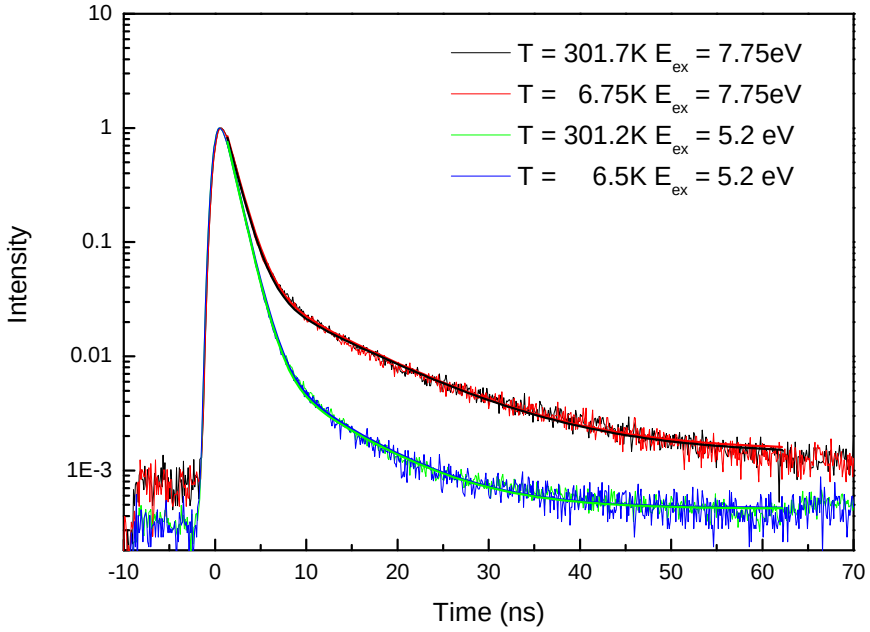

Figure A.7: BC418 Decay Traces and Fits

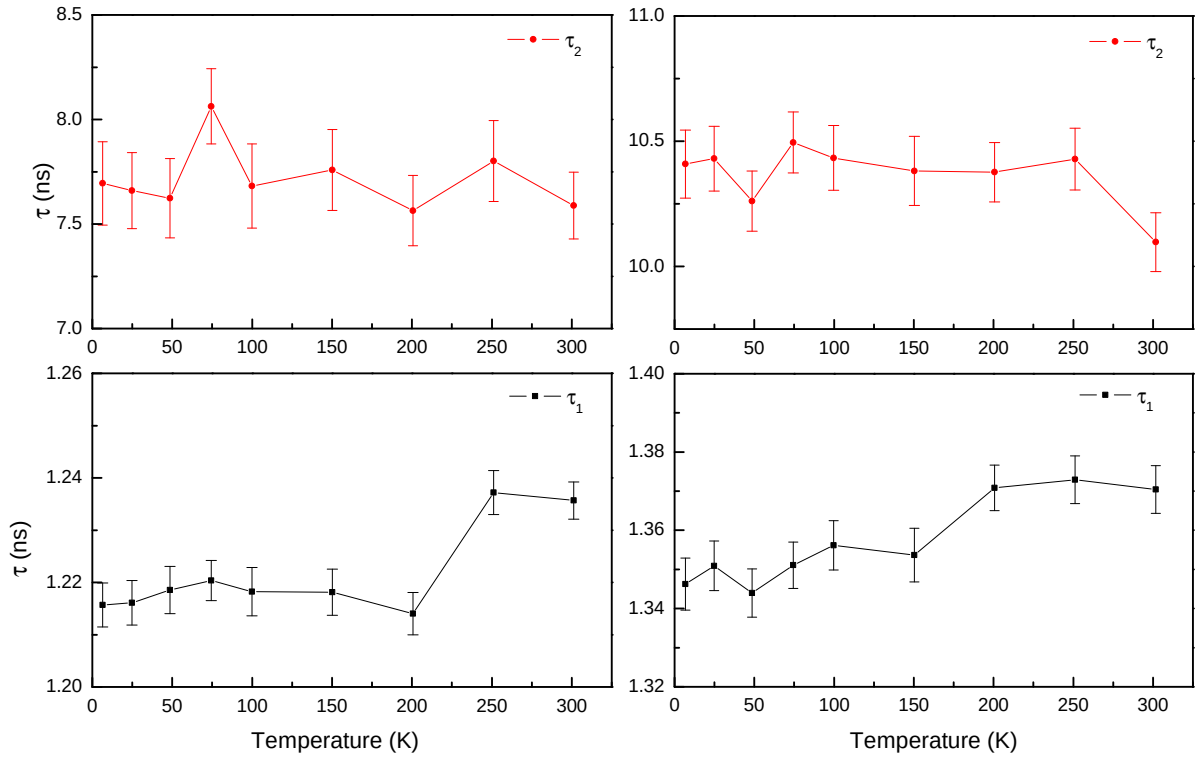

(a) BC418 E_{ex} = 5.2 eV E_{em} = 390 nm (b) BC418 E_{ex} = 7.75 eV E_{em} = 390 nm

Figure A.8: BC418 Decay

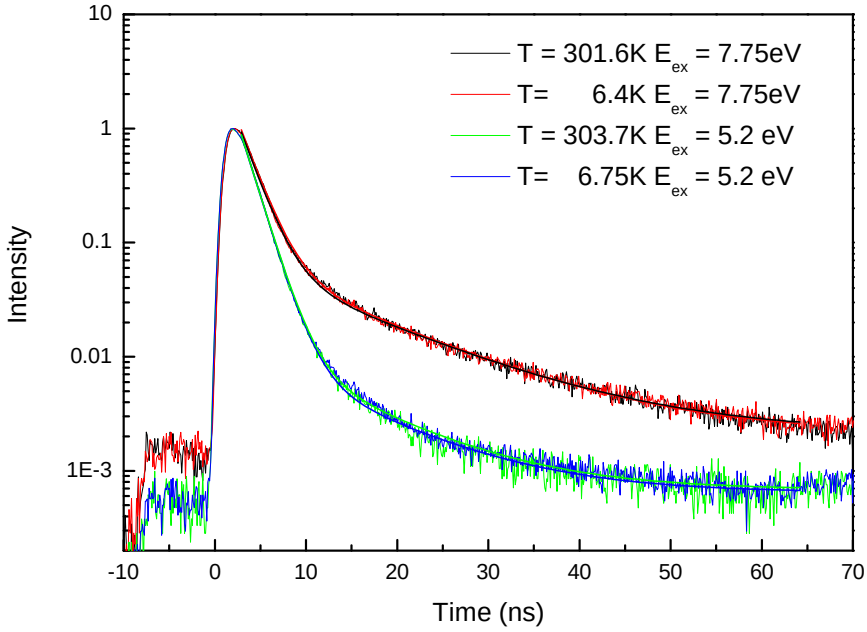

Figure A.9: EJ204 plastic Decay Traces and Fits

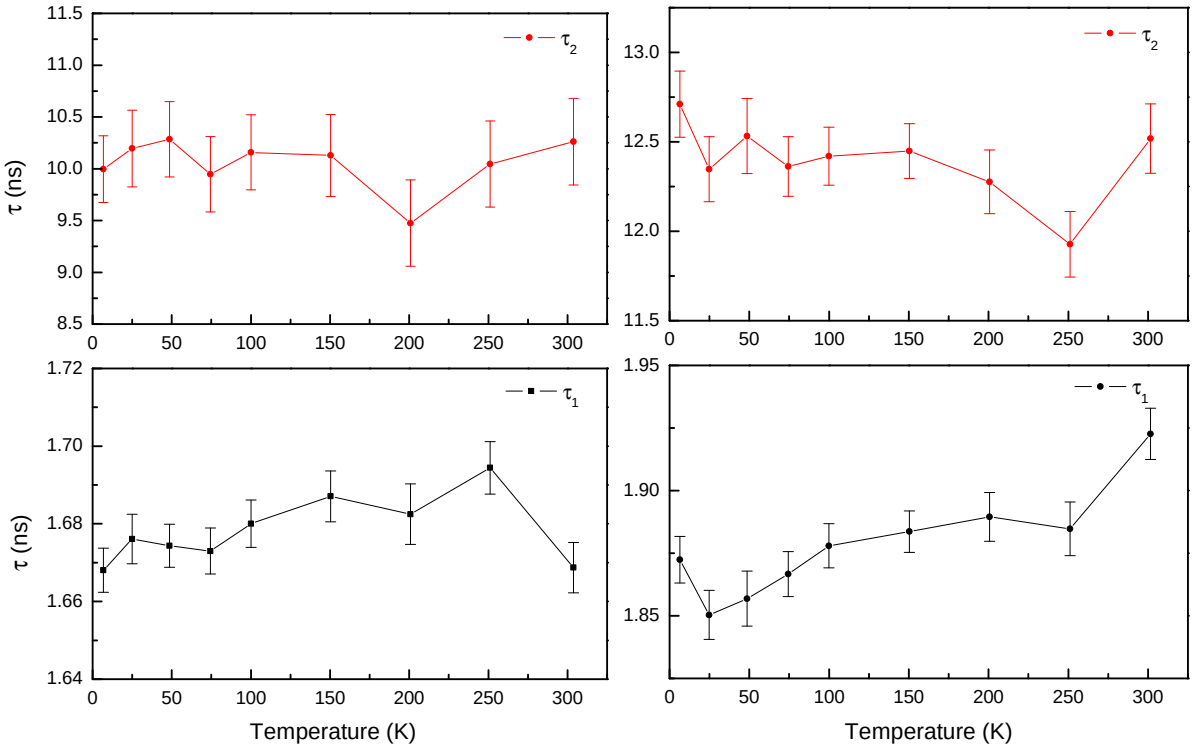

(a) EJ204 E_{ex} = 5.2 eV E_{em} = 410 nm (b) EJ204 E_{ex} = 7.75 eV E_{em} = 410 nm

Figure A.10: EJ204 Decay

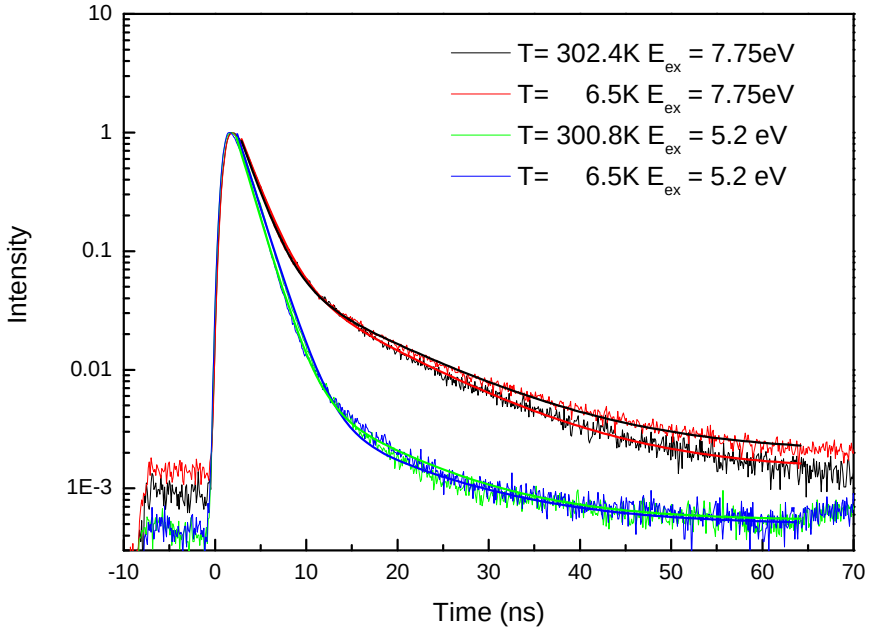

Figure A.11: EJ254 Decay Traces and Fits

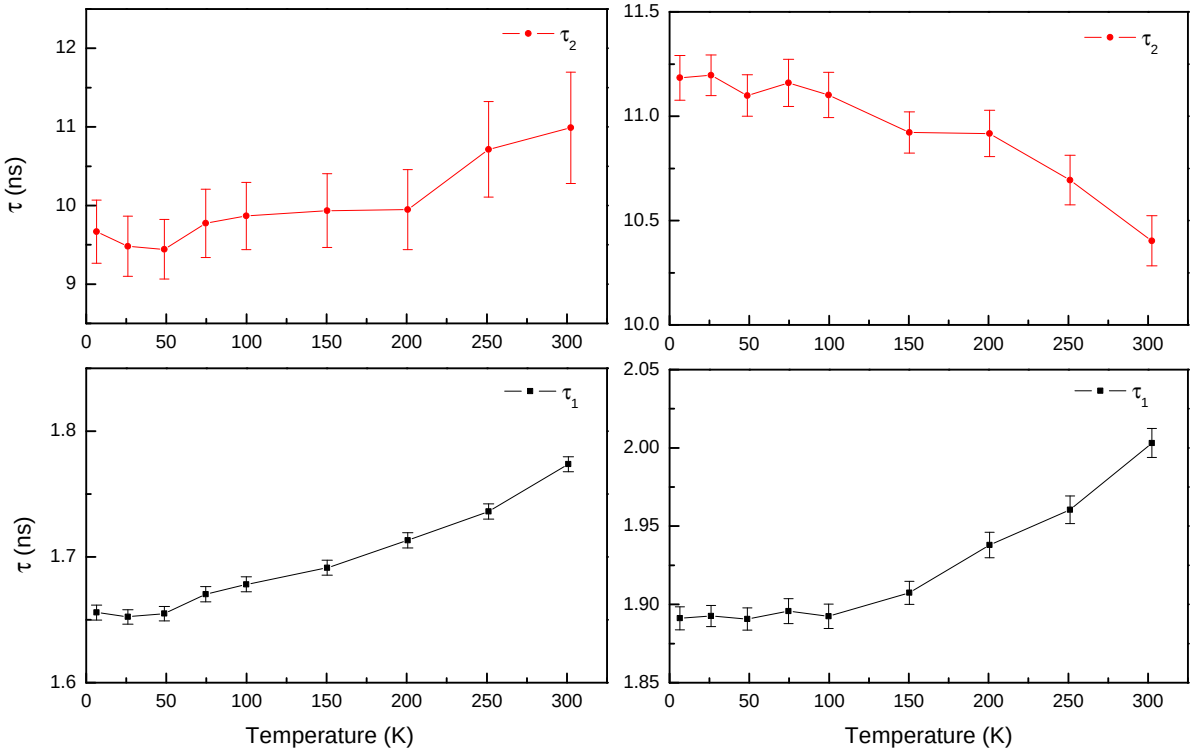

(a) EJ254 E_{ex} = 5.2 eV E_{em} = 425 nm (b) EJ254 E_{ex} = 7.75 eV E_{em} = 425 nm

Figure A.12: EJ254 Decay

A.2 Cerium Doped Oxides

A.2.1 Emission Spectra

Cerium doped oxide single crystals including LYSO(Ce), YSO(Ce) and YAG(Ce) have been thoroughly studied under VUV excitation to low temperature previously, and therefore a comprehensive study was not repeated. LYSO has two crystallographically independent lutetium sites, and therefore when it is doped with cerium, these two sites become substituted with Ce^{+3} ions, known as activation centres. The two sites are known in the literature as Ce1 and Ce2, and have different luminescence characteristics. The Ce^{+3} ion has one electron in the 4f shell, and the light emission is based on the electronic transition from the lowest 5d energy level to two 4f ground levels.

The emission spectra of LYSO(Ce) at 7 K with various excitation energies can be seen in Figure A.13a. The excitation energies of 4.1 and 4.8 eV correspond to maxima for exciting the cerium centres directly, and so these emission spectra are characteristic of any cerium doped crystals. This is where the cerium ions themselves absorb the incident radiation, rather than the host crystal molecules. The excitation energy of 7.1 eV corresponds to the band gap energy of the LYSO crystal and thus there is a contribution from the host lattice luminescence. The emission spectra show peaks at 400 nm and 430 nm which correspond to the Ce1 site and agrees with previously published characterisation studies [164]. The Ce1 site is dominant, and the Ce2 site has a characteristic emission spectrum peaking at 470 nm and is largely masked by the strong Ce1 emission at all excitations energies, but contributes to the tail at higher wavelengths. In general, high energy ionising radiation such as α excites both Ce1 and Ce2 and so the scintillation spectral profiles would be some combination. The emission spectra of YSO(Ce) are presented in Figure A.13b. It is a very similar crystal to LYSO(Ce) and also contains the two cerium sites, Ce1 and Ce2. At an excitation energy of 4.1 eV, again the crystal is dominated by direct Cerium ion excitation. At the higher energy of 4.7 eV there is some contribution also from Ce2 emission, seen as a shoulder at higher wavelength, and at 6.7 eV the host lattice is excited directly. This agrees with the

low temperature excitation and emission spectra published previously [169] [213].

The emission spectra of YAG(Ce) are presented in Figure A.13c. YAG(Ce) also has characteristic doublet 5d – 4f Ce^{3+} transitions, which correspond to peaks in the emission spectrum in the green region at 525 nm and 575 nm for this crystal. The strong bright excitation due to 5.6 eV and 6.7 eV photons correspond to direct excitation of the Ce^{3+} centres. YAG(Ce) has been heavily developed recently for white LEDs, in the form of ceramics, nano-particles and phosphors rather than as a single crystal, with similar luminescence characteristics in the visible region, as published by Zorenko in [178], [214], [215].

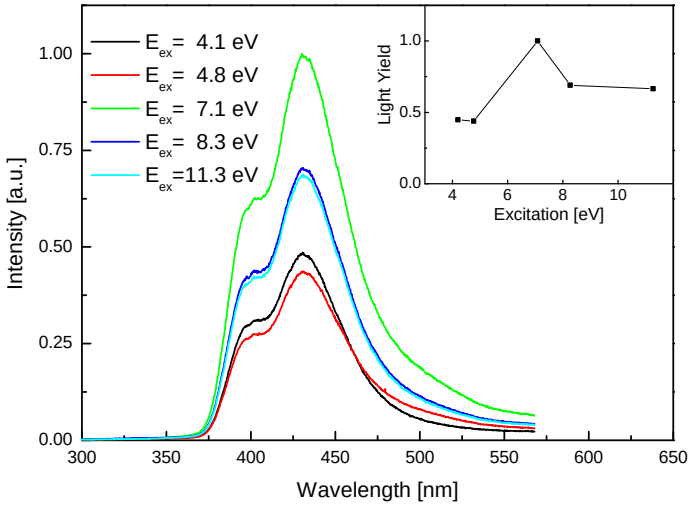

(a) LYSO(Ce) emission spectra at 6.5 K with 4 different excitation energies.

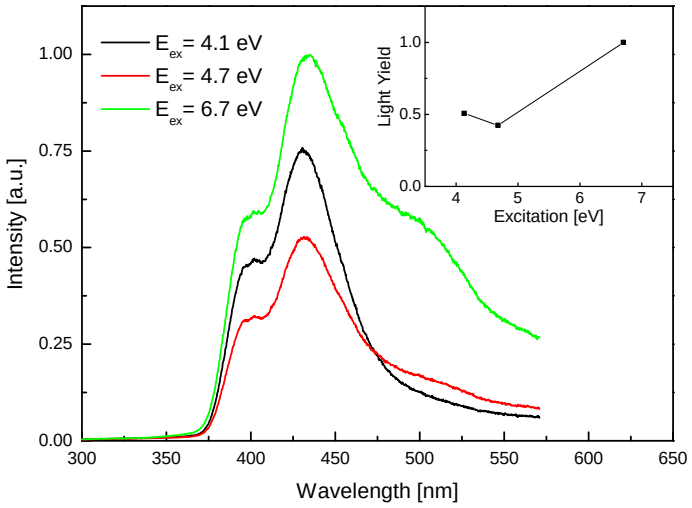

(b) YSO(Ce) emission spectra at 6.5 K with 3 different excitation energies.

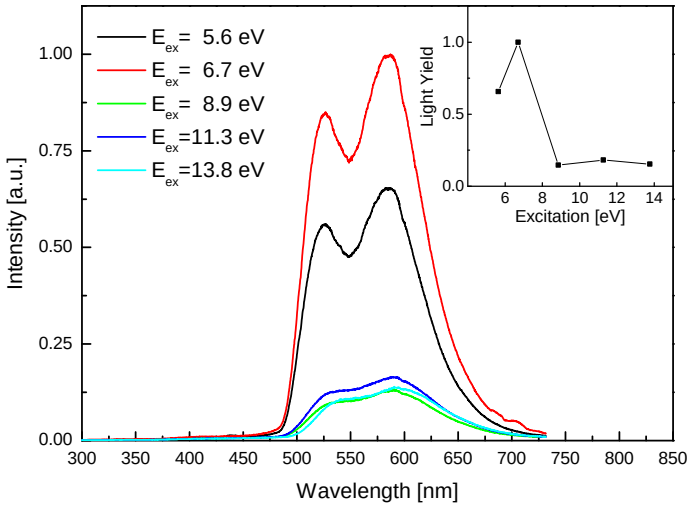

(c) YAG(Ce) emission spectra at 6.5 K with 5 different excitation energies.

Figure A.13: Emission Spectra of Cerium-activated LYSO, LYSO and YAG crystals at 6.5 K with various excitation energies. Inset: Light yield vs. Excitation energy

A.2.2 Excitation Spectra

The excitation spectra of the cerium doped oxide single crystals, LYSO(Ce), YSO(Ce) and YAG(Ce) are presented in Figure A.14. These were recorded at the peak emission wavelength for each material. The excitation energies at which the emission spectra in Section **??** were presented are marked with "×".

As the cerium doped oxide crystals have been well studied elsewhere, only 7 K excitation spectra were measured. The strong double absorption peaks characteristic of Ce^{3+} are visible at 4.3 and 4.8 eV for both LYSO(Ce) and YSO(Ce). The broader absorption peaks around ∼7.4 eV for LYSO(Ce) and ∼6.7 eV for YSO(Ce) correspond to the bandgap energy of the host crystal, which agrees with previous studies [164] [216]. For YAG(Ce), the host band gap energy is at 8 eV [217], which is seen only as a small shoulder on the much larger Ce^{3+} peak at 6.7 eV.

A.2.3 Decay Times

The decay time traces of LYSO(Ce) at 8 K at E_{em} = 430 nm with four different excitation energies are presented in Figure A.15a. At 4.2 and 4.8 eV, direct excitation into the absorption bands of the Ce^{3+} ions is occurring, at the Ce1 luminescence site. A single exponential can be fitted to these traces with a decay time of 34.2 ± 0.3 ns and 34.1 ± 0.4 ns for 4.2 eV and 4.8 eV excitation respectively. This is consistent with pure Ce1 emission [164]. Ce2 emission has a characteristic decay time of 56 ns at 11 K as published by [164]. We measure the decay times due to the higher excitation energies of 7.1 and 11.3 eV to be 35.7 ± 0.4 ns and 37.0 ± 0.4 ns respectively, concluding that this is primarily Ce1 site emission with a small component of Ce2.

Results of YSO(Ce) decay traces at 6.5 K at emission wavelength of 433 nm are presented in Figure A.15b. These traces were fitted with a single exponential of decay time 33.7 ± 0.3 ns for excitation energy of 4.1 eV and 34.5 ± 0.3 ns for 4.7 eV, corresponding to direct Ce1 excitation. At 6.7 eV excitation, the decay time is 35.8 ± 0.3 ns. Rothfuss [170] examined the

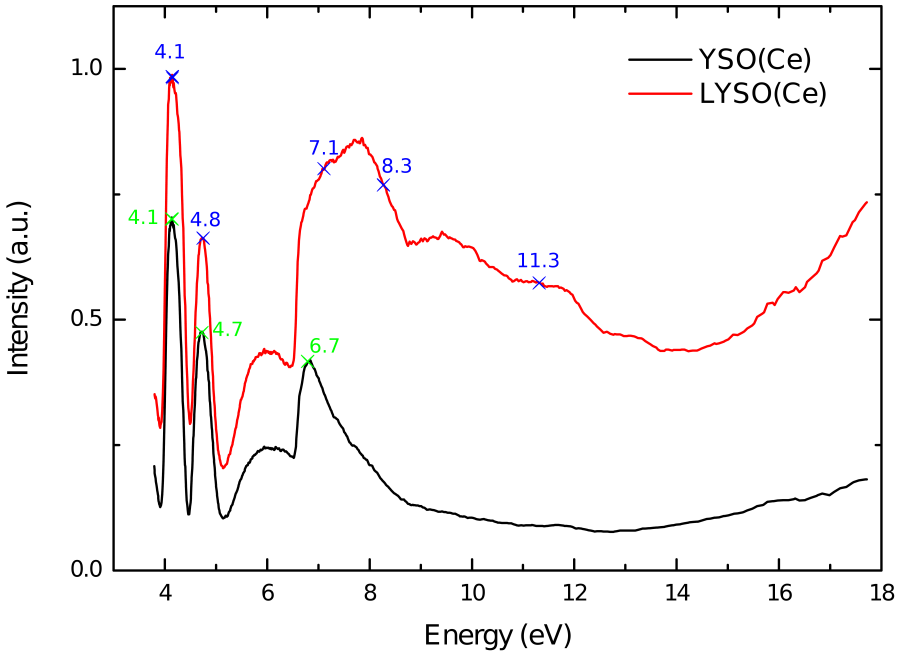

(a) YSO(Ce) and LYSO(Ce) Excitation spectrum at emission wavelength 430 nm at 7 K

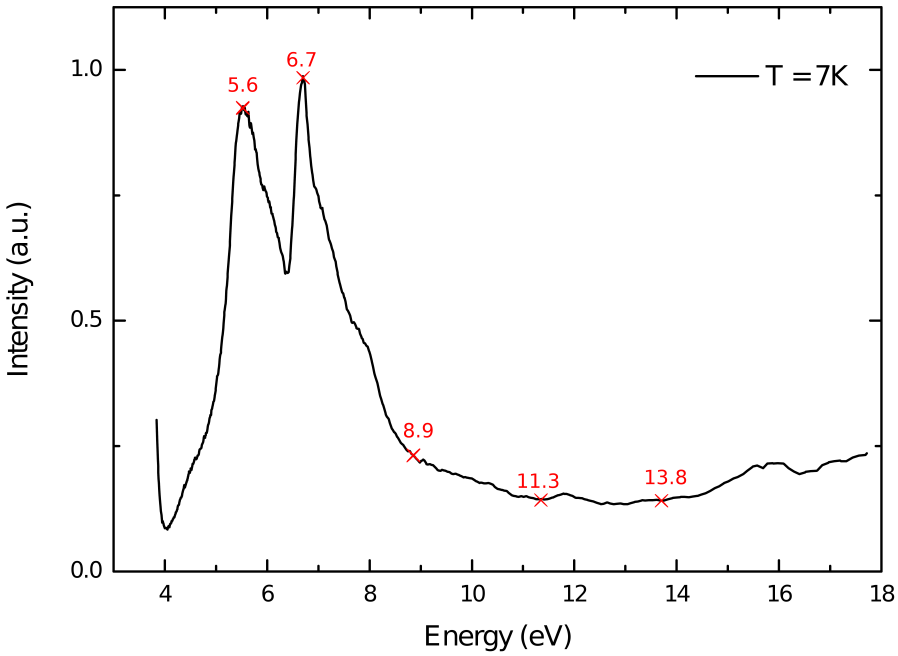

(b) YAG(Ce) Excitation spectrum at emission wavelength 595 nm at 7 K

Figure A.14: Cerium activated scintillators' excitation spectra.

decay time kinetics of YSO(Ce) under α and γ excitation at room temperature. They found that the decay time with γ excitation at 300 K to be 60 ns, however it was not perfectly fitted by a single exponent. They showed that the decay time for α excitation to be longer than 60 ns. However at 40 K, the γ response was reduced to a single exponential of 27 ns, close to

the results presented here. They concluded that the slower and more complex decay time of YSO(Ce) at room temperature relative to pure Ce^{3+} emission to be due to the presence of high intensity, low temperature electron traps. At 40 K these traps are saturated, allowing a faster decay time, approaching that of the cerium transition time from the 5d – 4f level of 32 ns. The 6.5 K results presented here confirms that there are no traps present to slow the scintillator, as exist at room temperature, and the decay time is consistent with pure Ce^{3+} emission.

The decay time traces of YAG(Ce) at 6.5 K at $E_{em} = 595$ nm with four different excitation energies are presented in Figure A.15c. The lifetime of pure Ce^{3+} decay in YAG(Ce) is 60 – 65 ns [171] at room temperature, and it was measured to be 48 – 56 ns in this sample. The pure Ce^{3+} emission corresponds to the 5.6 and 6.7 eV excitation energies with decay times of 55.7 ± 2.8 ns and 48.7 ± 1.1 ns respectively. The decay time with excitation energies of 11.3 and 13.8 eV are 52.3 ± 6.9 ns and 61.9 ± 8.1 ns, and as this is above the band gap of the crystal (8 eV) and has contributions to its emission from host and Ce2 emission, possibly contributing to the slightly longer decay time.

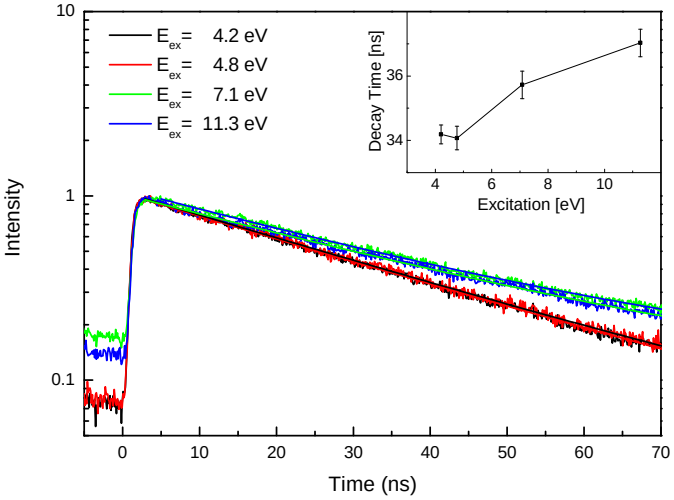

(a) LYSO(Ce) Decay time traces measured at 8 K with E_{em} = 430 nm and with four different excitations energies.

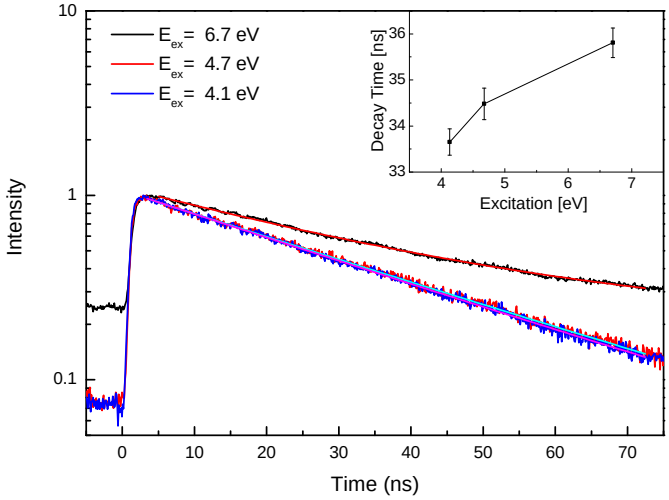

(b) YSO(Ce) Decay time traces measured at 6.5 K with E_{em} = 433 nm and with four different excitations energies.

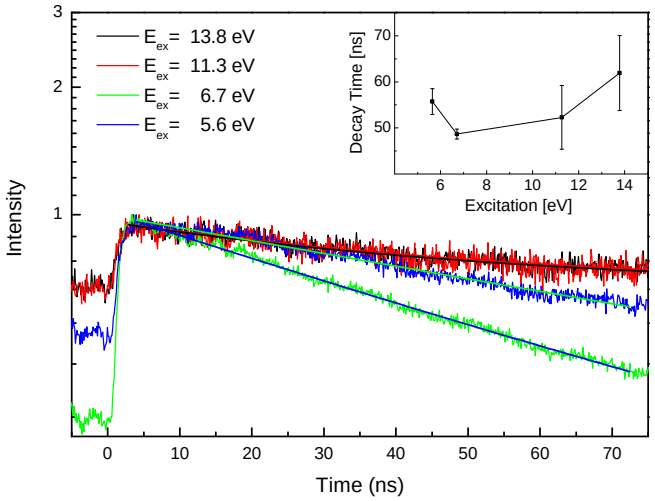

(c) YAG(Ce) Decay time traces measured at 6.5 K with E_{em} = 595 nm and with four different excitations energies.

Figure A.15: Decay time measurements of Cerium doped oxide scintillators

A.3 GS20 Neutron Glass Scintillator

A.3.1 Emission Spectra

The Ce^{3+} activated silicate glass thermal neutron scintillator GS20 has been studied previously by Spowart [190] [179]. The emission spectra presented in Figure A.16 are due to 5.8, 7.1 and 7.75 eV photons, in the temperature range 300 – 7 K. When excited by UV photons below 5 eV, the Ce^{3+} sites directly absorb the incident radiation, bypassing any transfer mechanism between the absorbing glass material and the luminescence centre. However when the scintillator is irradiated by higher energy photons, ionising particles (α) and γ rays, electron-hole pairs are created which must migrate to the Ce^{3+} sites, where the pair recombine and luminescent photons are emitted. When the scintillator is irradiated by thermal neutrons, the ionisation occurs internally by the emitted α and triton, again causing electron hole pairs in the bulk material which must migrate to the activation centre for the emission of luminescence.

No temperature dependence is seen in the UV emission spectra, which indicates from Figure A.16a that the direct Ce^{3+} emission is temperature independent. This is in agreement with previous studies by Spowart [190] to 50 K with UV photons and β particles, and is consistent with a theory of phonon assisted energy migration from the glass molecules to the cerium activator sites, which is necessary for ionising particle energy migration but not so in the case of direct UV excitation.

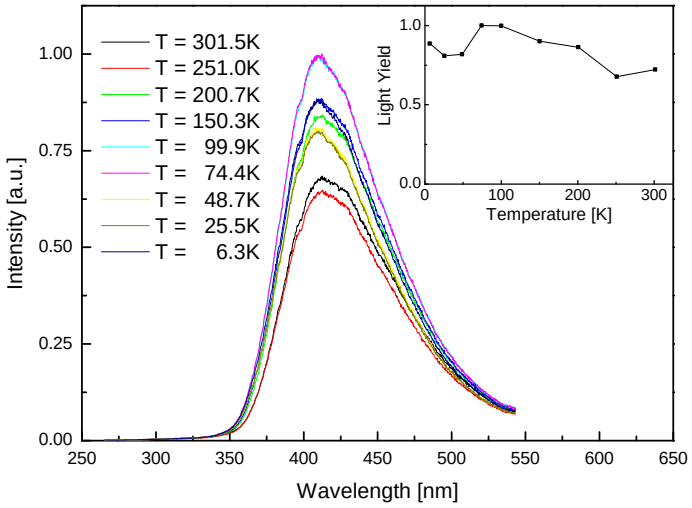

(a) GS20 Lithium-6 Glass E_{ex}=4.8 eV

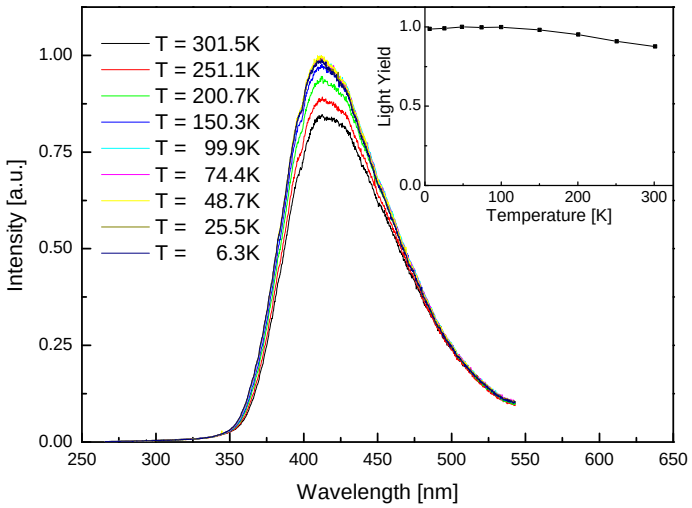

(b) GS20 Lithium-6 Glass E_{ex}=7.1 eV

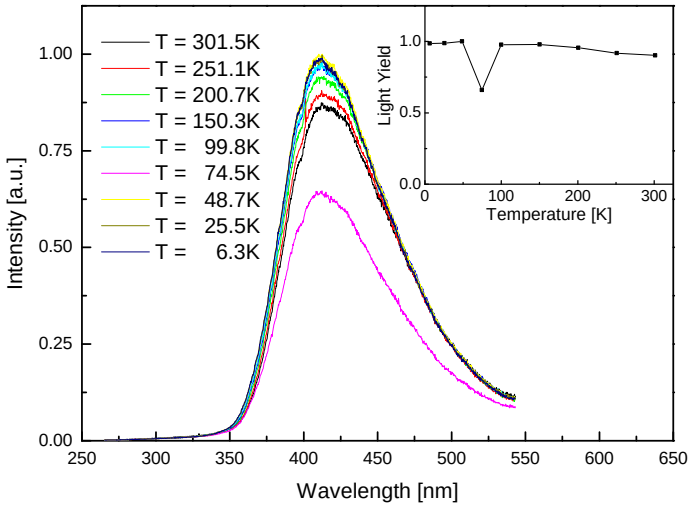

(c) GS20 Lithium-6 Glass E_{ex}=7.75 eV

Figure A.16: GS20 Lithium-6 Doped Glass Emission Spectra

A.3.2 Excitation Spectra

The excitation spectra of cerium activated lithium glass GS20 at 300 and 7 K are presented in Figure A.17 The spectra show the broad band direct Ce^{+3} excitation below 5 – 6 eV at both room temperature and 7 K, with an increased absorption band at 7 eV at low temperature. [190] reports temperature independence of direct UV excitation and emission of GS20 glass to below 50 K, which agrees generally with our findings.

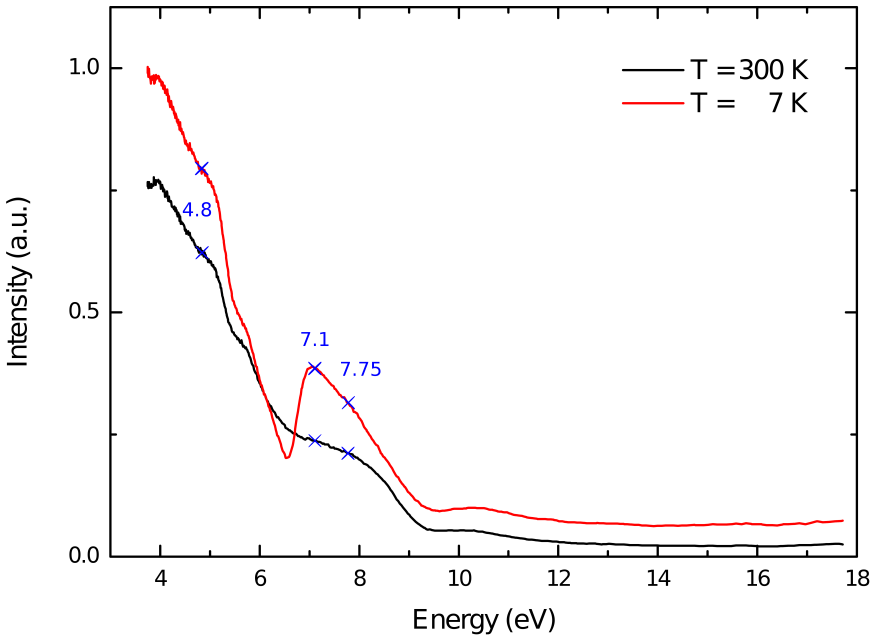

Figure A.17: GS20 Excitation spectrum at emission wavelength 400 nm at 300 K and 7 K

A.3.3 Decay Times

The decay time traces of GS20 glass at 300 and 6.5 K at E_{em} = 595 nm with three different excitation energies are presented in Figure A.18. A single exponent was fitted to data recorded in the range 300 – 6.5 K at excitation energies of 4.8, 7.1 and 7.75 eV. The decay time of these fits as a function of temperature are plotted in Figure A.19. For E_{ex} = 4.8 eV the decay time slows from 60.0 ± 1.3 ns at 300 K to 77.9 ± 2.0 ns at 6.5 K. For E_{ex} = 7.1 eV the decay time slows from 82.5 ± 3.2 ns at 300 K to 92.5 ± 3.4 ns at 6.5 K. For E_{ex} = 7.75 eV the decay time slows from 75.7 ± 2.9 ns at 300 K to 80.4 ± 2.9 ns at 6.5 K. These changes are subtle, and as discussed in Section **??**, the emission from the absorption of 4.8

eV UV photons is due to direct excitation of the Ce^{3+} centres.

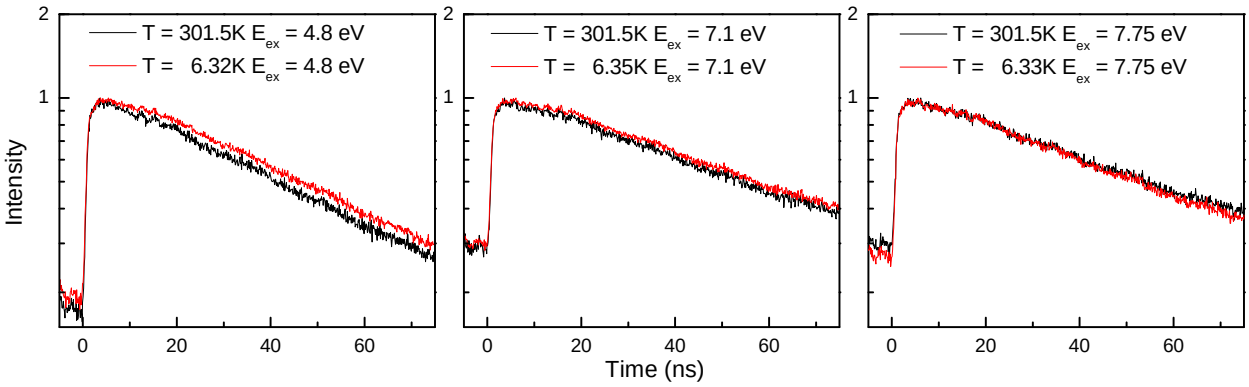

Figure A.18: GS20 Decay Traces and Fits at 300 and 6.5 K.

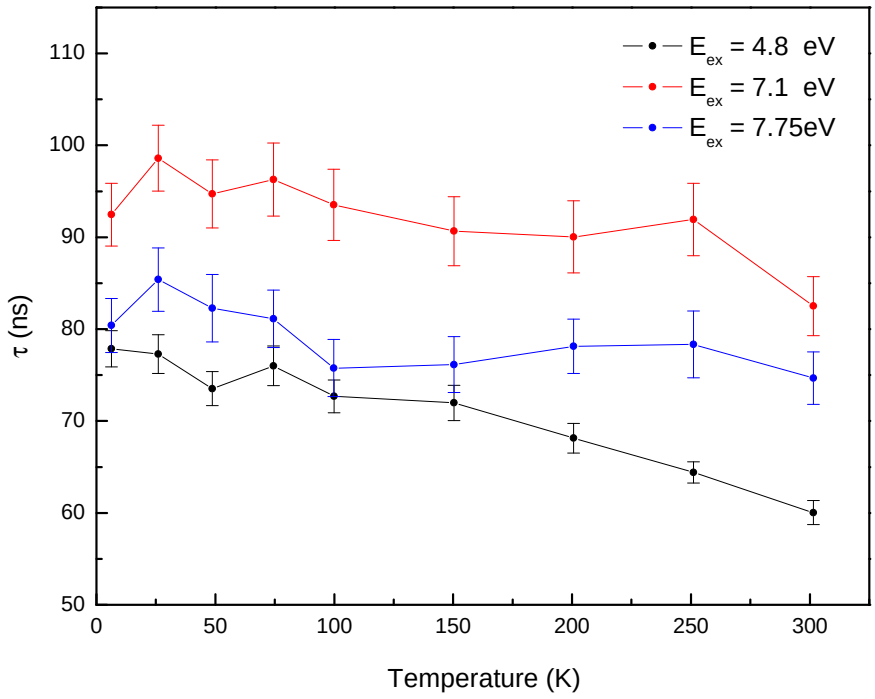

Figure A.19: GS20 Decay time as a function of temperature.

A.4 CaF_2(Eu)

A.4.1 Emission

As previous measurements of the spectral characteristics of CaF_2(Eu) have been published [199] [200], a comprehensive study was not repeated, instead there was a focus on low temperature measurements. The luminescence spectra of CaF_2(Eu) are shown in Figure A.20 measured at room temperature and base temperature, 6.5 K. The slight shifting of the peak between room temperature to low temperature as shown in Figure A.20a and the narrowing agrees with low temperature emission results with laser excitation discussed in [218]. Various excitation energies were investigated from 5.8 – 13.1 eV shown in Figure A.20b, with the most luminescence seen at 5.8 eV, showing a broad strong luminescence at 425 nm, which agrees with the known properties [219] [218] and is attributed to the 5d – 4f transition of the Eu^{2+} ion. Like the cerium-doped crystals, europium, also a lanthanide, has a similar electronic structure, with Eu^{2+} ions replacing Ca^{2+} ions at its lattice point to produce the luminescence centre. No change in spectral shape is seen with the different excitation energies, only a change in light yield, indicating there is no other mode of excitation visible with these higher excitation energies.

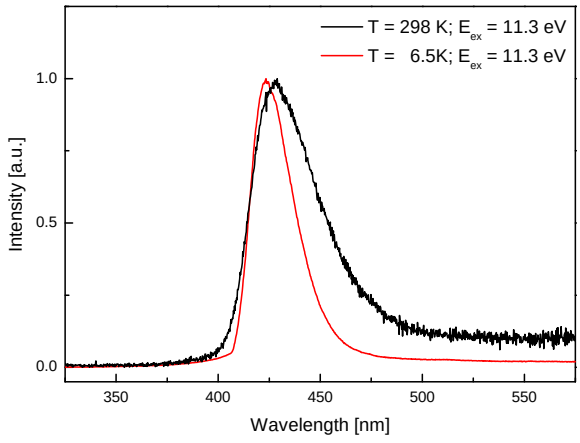

(a) Emission spectra with E_{ex} = 11.3 eV at 298 K and 6.5 K

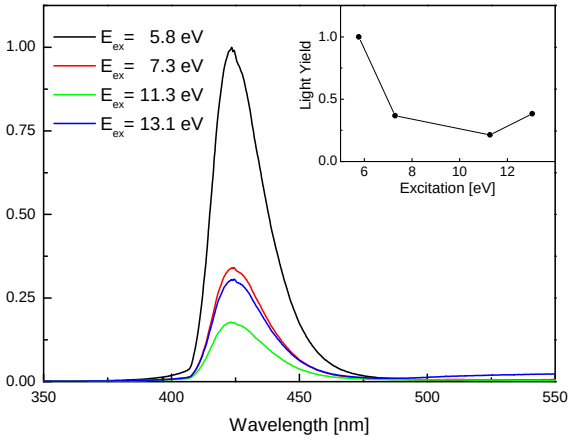

(b) Emission spectra at 6.5 K with 4 different excitation energies. Inset: Light yield vs Excitation energy.

Figure A.20: CaF_2(Eu) Emission Spectra

A.4.2 Excitation

The excitation spectrum of CaF_2(Eu) measured at 6.4 K at the peak emission wavelength of 425 nm is displayed in Figure A.21. CaF_2(Eu) is known to have two absorption bands centred at 3.4 eV and 5.5 eV at room temperature [218], and reported as becoming narrower with decreasing temperature. The prominent absorption peak in the data reported here corresponds to 5.8 eV at 6.4 K, the higher of the two Eu^{2+} absorption bands. The lower is not within our measurement window, but the edge of which appears to be seen below 4 eV. Emission spectra presented in Figure A.20 were measured with the energies marked in blue.

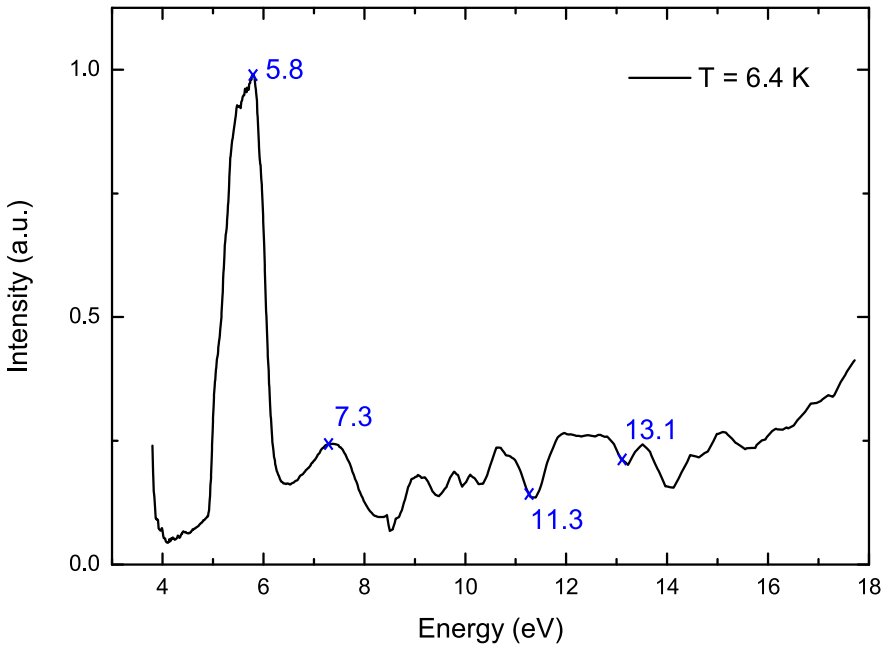

Figure A.21: CaF_2(Eu) Excitation spectrum at emission wavelength 425nm at 7K

A.4.3 Decay Times

Similarly, the slower decay time of CaF_2(Eu) meant it was unsuitable for the SuperLumi decay time measurements, however an indication of the decay time can be made by inspecting typically events from α scintillation at 300 and 6.5 K, as displayed in Figure A.22. At 300 K, Figure A.22a, the primary decay time is measured to be 631 $\pm$ 49 ns and at 6.5 K, Figure A.22b, this is similar. However with an expanded view of the time axis of a low temperature event, as displayed in Figure A.22c, there is a very long decay time component. This scale shows photons emitted for 2 ms after the fast component emission. While this component is significantly less bright than the fast component, which has not slowed at low temperature, the presence of this decay may cause problems with pile-up and misidentification of neutron events in a cryoEDM UCN detector and for this reason, it is unsuitable for further application.

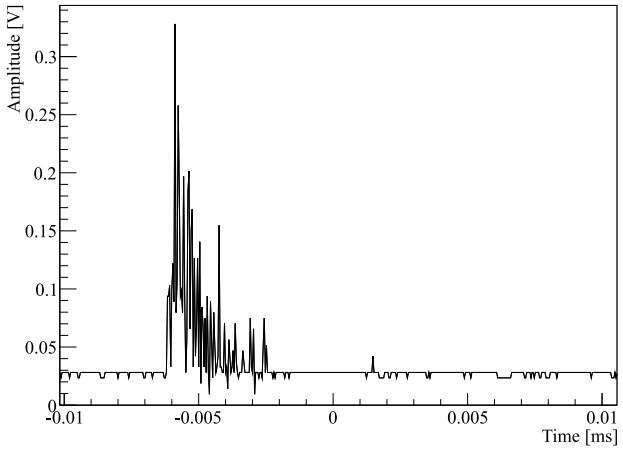

(a) 300 K

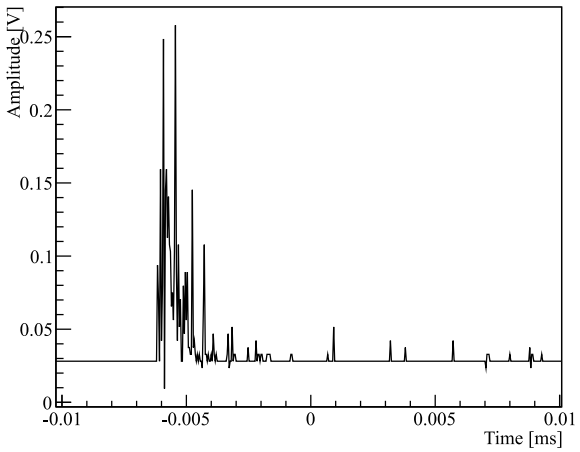

(b) 6.5 K

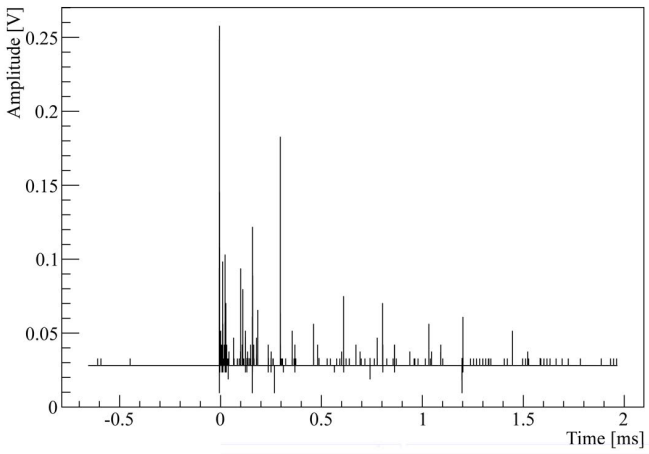

(c) 6.5 K: A wide time axis shows a long component to the scintillation.

Figure A.22: Scintillation events from CaF_2(Eu) to α radiation, to indicate the decay time scale

Appendix B

Luminescence Processes in Organic & Inorganic Materials

Scintillation materials come in a wide variety of forms, but can essentially be divided into two categories: Inorganic and Organic materials. These two categories have very different underlying physics mechanism responsible for the absorption of radiation and emission of scintillation photons. This appendix outlines the physical principles underlying the scintillation in these materials for reference in the discussion of light yield measurement, kinetic measurements and spectroscopic properties of scintillators in Chapter 5.

B.1 Organic Scintillators

Luminescence in organic materials arises from transitions in the energy level structure of a single molecule, and therefore it can occur in a number of different states of matter of that molecule, e.g. crystalline solid, liquid, solution. This is in complete contrast to inorganic luminescent materials that depend wholly on the crystal lattice and its energy levels for photon emission.

The structure of organic molecules is largely determined by the electronic structure of the carbon atom, which has six electrons, that form hybridised shells, depending on the

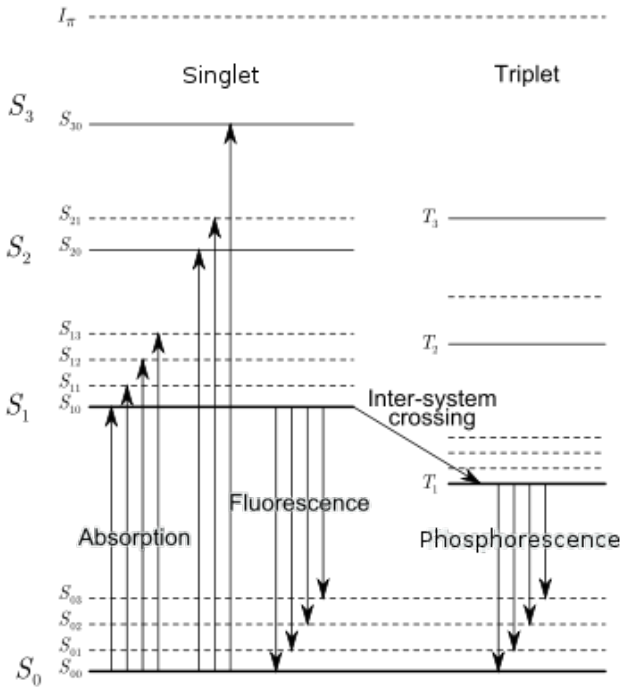

Figure B.1: Energy levels of a molecule with π electron structure.

chemical bond taking place. These hybrid shells form what is known as π molecular bonds to form aromatic material. This type of bond allows for the de-localisation of electrons, and π electronic energy levels are formed, as depicted in Figure B.1. Excitation and de-excitation between these energy levels is the source of luminescence in organic materials.

Absorbed radiation excites electrons from the singlet ground state S_0 to a singlet excited state S_1, (usually separated by 3 or 4 eV) or higher S_2, S_3 etc. States contain fine structure consisting of vibrational transitions of order 0.15 eV, annotated with S_{10}, S_{11} etc. At room temperature, most electrons are in the ground state S_0, as thermal vibration does not produce enough energy for excitation (0.025 eV). Absorption of radiation causes the population of the higher singlet states. This is a fast process of order picoseconds, and the higher excited states de-excite through non-radiative internal conversion to the S_1 state, and further vibrational relaxation to S_{10}. After a negligibly short amount of time the excitation process has produced a population of excited molecules in the S_1 state. The principle scintillation light is then emitted between this state and one of the vibrational states of the ground state, S_{0x}. It is precisely the energy spread in these vibration states which causes the intrinsic resolution of a scintillator, and the characteristic fluorescence spectrum of a material. The fluorescence

intensity at a time t following excitation is given by:

$$I = I_0 e^{-t/\tau} \tag{B.1}$$

where τ is of the order nanoseconds for organic molecules.

There is also a sequence of π electron triplet states, lower in energy than their corresponding singlet states. Absorption from S_0 to T_1 is forbidden, but the triplet states can be populated by other means, known as inter-system crossing. The lifetime of an excited triplet state is much longer than a singlet, as much as milliseconds, due to the spin-forbidden transition. Thus this radiation is characteristically long, and is of longer wavelength. Some molecules in T_1 may be thermally excited back to S_1 and subsequently emit photons in a process known as delayed fluorescence.

Organic materials are transparent to their own fluorescence due to the larger energy gap in the $S_{0x} \rightarrow S_{1x}$ absorption transitions than the $S_{10} \rightarrow S_{0x}$ transitions. Usually there is little overlap between the optical absorption and emission spectra, often called the Stokes shift, as depicted in Figure B.2. Therefore there is little self absorption of the fluorescence by the scintillator material. The scintillation efficiency is the fraction of incident particle energy that is converted into visible light. As there are many alternative de-excitation modes available, most energy is usually transformed to heat, and only a small fraction of order 0.04 to fluorescence light. In organic materials, the excitation energy may transfer from molecule to molecule before de-excitation. This allows for the production of solutions of multiple molecule types, utilised in the production of plastic and liquid organic scintillators.

When excited by heavy or slow particles, which produce a higher ionization and excitation density within the scintillator than high energy electrons, the scintillation efficiency is reduced. This ionization quenching effect causes the relative output of electrons to protons to α of the same energy to be approximately 10:5:1. The *alpha-to-beta ratio* is a common parameter used which relates the light output of a scintillator when ionised with an α particle or an electron of the same energy. For organic scintillators, the light output from electron

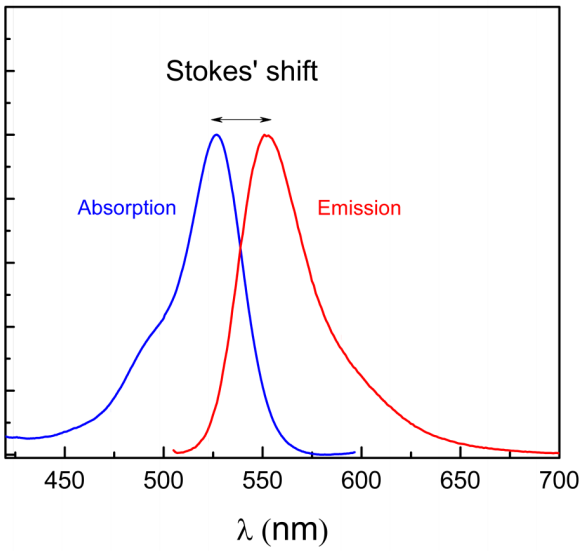

Figure B.2: The optical absorption and emission spectra for a typical organic scintillator usually overlap very little, with the difference in wavelength of the maxima of the two spectra known as the Stokes shift.

excitation is always greater than α and so this parameter is always less than 1.

For the vast majority of organic scintillators, prompt fluorescence represents most of the observed scintillation light. Sometimes a longer lived component is seen due to delayed fluorescence, and the decay time characteristics of the material will have a sum of two exponential decays with a fast and a slow component. A very useful property is that the fraction of light that appears in the slow component often depends on the nature of the exciting particle. One can make use of this by differentiating between incident particle based on the pulse shape produced, known as pulse shape discrimination.

The quenching due to heavy ions affects the intensity of the fast component mainly, and has much less of an impact on the intensity of the slow component. The decay times are unaffected. Hence the overall shape of the scintillation pulse is changed by this quenching and therefore the pulse shape depends on the nature of the incident particle. This is exploited in pulse shape discrimination techniques.

Organic scintillators may be found as pure crystals such as stilbene, or as binary systems, whereby the scintillating molecule is a solute in a plastic or liquid. This allows for the

absorption of radiation by the solvent, and the transfer of energy from the solvent molecules to the solute molecules where the luminescence occurs. Furthermore, a liquid or plastic solution with two solvents may be produced, either to allow ease of transfer of energy from the primary absorbing solvent to the emitting solute, or where one acts as a wavelength shifting material, absorbing the luminescence of the first solute and emitting radiation at a longer wavelength.

B.1.1 Plastic Scintillators

When an organic scintillator is dissolved in a solvent that is then polymerized, a solid plastic scintillator is produced. Typical plastic matrices are polyvinyltoluene (PVT) or polymethylmethacrylate (PMMA). They have become extremely popular due to the ease with which they can be shaped and fabricated, and their affordable cost. The combination of a scintillator dissolved in a plastic solvent, is known as a binary system. Sometimes a third solute is used for its wavelength shifting properties, and is known as a ternary system.

In these cases, energy is absorbed by the primary solvent, and then competing processes dissipate this energy through emission by the primary solvent, transfer to the solute(s) through internal conversion, non-radiative quenching processes and fluorescence. These competing energy migration processes create the characteristic spectroscopic and kinetic properties of plastic scintillators.

Energy is predominantly transferred non-radiately from the excited solvent molecules to the scintillator molecule. It is thought to occur by a resonance interaction between segments of the same or adjacent polymer chains, a mechanism known as Forster transfer. There is often also a radiative component of energy transfer from the solvent to the scintillator, where the plastic emits a UV photon which is then absorbed by the scintillator and subsequently emitted as fluorescence. The efficiency of a plastic scintillator depends on its mode of preparation as well as its constituents.

B.2 Inorganic Scintillators

The scintillation mechanism in inorganic materials depends on the energy levels determined by the crystal lattice of the material. The overall potential an electron experiences in a crystal lattice is a repetition of periodic potentials. The solution of the Schroedinger equation for such a periodic potential results in a wavefunction of the same period with discrete allowed energy eigenvalues, corresponding to a structure of allowed and forbidden energy bands. Electrons bound at lattice sites may be excited by incident radiation from the valence band to the conduction band, where they can move freely in the lattice. A corresponding hole is left in the valence band.

In a pure crystal, the return of the electron from the conduction band to the valence band is an inefficient process, and with an energy difference usually greater than the visible range. Often, an impurity is introduced to the lattice to produce allowed donor sites in the forbidden band. These impurities are known as activators, and modify the band structure so that an electron can de-excite from this donor site to the valence band with the emission of a luminescence photon. The energy is less than the forbidden gap, giving rise to visible photons. These de-excitation sites are called luminescence centres.

An ionising particle passing through the lattice will form a large number of electron-hole pairs. The hole quickly drifts to the activator site and ionizes it, as the ionization energy of the impurity is usually less than a typical lattice site. The electron is free to migrate through the crystal until is encounters an ionized activator. The electron will drop into the activator site and create a neutral configuration. Recombination of the electron hole pair can then occur, typically with lifetime in the 30 – 500 ns range, with the emission of a visible photon can then occur. This process is illustrated in Figure B.3.

Competing processes include radiationless transitions, known as quenching, excited states with a forbidden transition, causing characteristic slow emission, known as phosphorescence. The electron-hole pair may migrate together in a configuration known as an exciton, and move together until they meet an activator site, giving rise to scintillation emission with

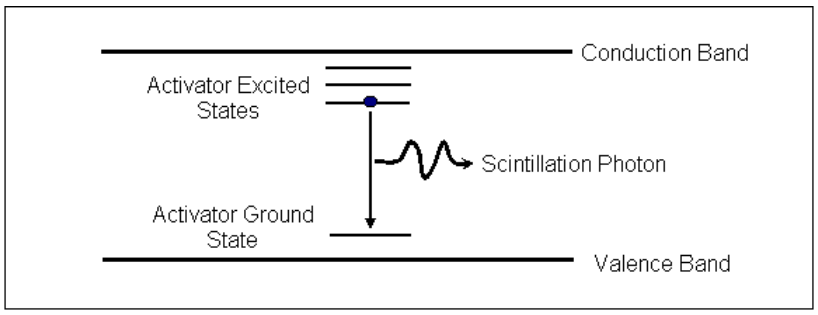

Figure B.3: Energy band structure of an activated crystalline scintillator.

different decay time characteristics.

Luminescence through activator sites means that the crystal can be transparent to its own luminescence as the energy gap for the absorption process between the conduction and valence band is larger than that emitted from a transition at an activator site.

For many common inorganic scintillator, the light yield is nearly proportional to the deposited radiation energy, more so than in common organic scintillators. As with organics, heavy charged particles produce less light per unit energy than an electron. However they usually have a much higher alpha-to-beta ratio than organics.

Bibliography

[1] M. Dine and A. Kusenko. "Origin of the matter-antimatter asymmetry." *Rev. Mod. Phys.* **76** (2003) 1–30.

[2] D. E. Morrissey and M. J. Ramsey-Musolf. "Electroweak baryogenesis." *New Journal of Physics* **14** (12) (2012) 125003.

[3] G. R. Farrar and M. E. Shaposhnikov. "Baryon asymmetry of the Universe in the standard model." *Phys. Rev. D* **50** (1994) 774–818.

[4] O. W. Greenberg. "CPT." *Phys. Rev. Lett.* **89** (2002) 231602.

[5] F. W. Stecker. "Baryon Symmetric Big Bang Cosmology." *Nature* **273** (1978) 493–497.

[6] J. Beringer et al. "Review of Particle Physics." *Physical Review D* **86** (1) (2012) 1504.

[7] R. J. Cooke et al. "Precision Measures of the Primordial Abundance of Deuterium." *The Astrophysical Journal* **781** (1) (2014) 31.

[8] A. S. Beach et al. "Measurement of the Cosmic-Ray Antiproton-to-Proton Abundance Ratio between 4 and 50 GeV." *Phys. Rev. Lett.* **87** (2001) 271101.

[9] A. Yamamoto et al. "Search for Primordial Antiparticles with BESS." *Advances in Space Research* **42** (3) (2008) 442 – 449.

[10] Planck Collaboration et al. "Planck 2013 results. XVI. Cosmological parameters." *ArXiv e-prints* `1303.5076`.

[11] A. G. Cohen, A. D. Rjula, and S. L. Glashow. "A Matter-Antimatter Universe?" *The Astrophysical Journal* **495** (2) (1998) 539.

[12] I. V. Moskalenko et al. "Secondary Antiprotons and Propagation of Cosmic Rays in the Galaxy and Heliosphere." *The Astrophysical Journal* **565** (1) (2002) 280.

[13] A. Sakharov. "CP Symmetry Violation, C-Asymmetry and Baryonic Asymmetry of the Universe." *JETP Letters* **5** (1967) 24–27.

[14] A. Riotto and M. Trodden. "Recent Progress in Baryogenesis." *Annual Review of Nuclear and Particle Science* **49** (1) (1999) 35–75.

[15] S. Davidson, E. Nardi, and Y. Nir. "Leptogenesis." *Physics Reports* **466** (45) (2008) 105 – 177.

[16] M. Shaposhnikov. "Baryon asymmetry of the universe in standard electroweak theory." *Nuclear Physics B* **287** (0) (1987) 757 – 775.

[17] V. Cirigliano et al. "MSSM baryogenesis and electric dipole moments: an update on the phenomenology." *Journal of High Energy Physics* **2010** (1) (2010) 1–23.

[18] C. S. Wu et al. "Experimental Test of Parity Conservation in Beta Decay." *Phys. Rev.* **105** (1957) 1413–1415.

[19] J. H. Smith, E. M. Purcell, and N. F. Ramsey. "Experimental Limit to the Electric Dipole Moment of the Neutron." *Phys. Rev.* **108** (1957) 120–122.

[20] J. H. Christenson et al. "Evidence for the 2π Decay of the K_2^0 Meson." *Phys. Rev. Lett.* **13** (1964) 138–140.

[21] M. Kobayashi and T. Maskawa. "CP-Violation in the Renormalizable Theory of Weak Interaction." *Progress of Theoretical Physics* **49** (2) (1973) 652–657.

[22] BABAR Collaboration. "Direct CP Violating Asymmetry in $B_0 \to K^+\pi^-$ Decays." *Phys. Rev. Lett.* **93** (2004) 131801.

[23] LHCb Collaboration. "Evidence for CP Violation in Time-Integrated $D_0 \to h^-h^+$ Decay Rates." *Phys. Rev. Lett.* **108** (2012) 111602.

[24] C. A. Baker et al. "Improved Experimental Limit on the Electric Dipole Moment of the Neutron." *Phys. Rev. Lett.* **97** (2006) 131801.

[25] J. S. Nico and W. M. Snow. "Fundamental Neutron Physics." *Annual Review of Nuclear and Particle Science* **55** (1) (2005) 27–69.

[26] I. Khriplovich and A. Zhitnitsky. "What is the value of the neutron electric dipole moment in the Kobayashi-Maskawa model?" *Physics Letters B* **109** (6) (1982) 490 – 492.

[27] M. Gavela et al. "Intermediate states in the calculation of the neutron electric dipole moment." *Physics Letters B* **109** (12) (1982) 83 – 88.

[28] Belle Collaboration. "Evidence for direct CP violation in the decay $B^\pm \to D^{(*)}K^\pm, D \to K_S^0\pi^+\pi^-$ and measurement of the CKM phase θ_3." *Phys. Rev. D* **81** (2010) 112002.

[29] V. Baluni. "CP-nonconserving effects in quantum chromodynamics." *Phys. Rev. D* **19** (1979) 2227–2230.

[30] M. Pospelov and A. Ritz. "Theta vacua, QCD sum rules, and the neutron electric dipole moment." *Nuclear Physics B* **573** (12) (2000) 177 – 200.

[31] R. Crewther et al. "Chiral estimate of the electric dipole moment of the neutron in quantum chromodynamics." *Physics Letters B* **91** (34) (1980) 487.

[32] J. E. Kim and G. Carosi. "Axions and the strong CP problem." *Rev. Mod. Phys.* **82** (2010) 557–601.

[33] R. D. Peccei and H. R. Quinn. "Constraints imposed by CP conservation in the presence of pseudoparticles." *Phys. Rev. D* **16** (1977) 1791–1797.

[34] C. Amsler et al. "Review of Particle Physics (Section: Axions)." *Physics Letters B* **667** (15) (2008) 1 – 6. Review of Particle Physics.

[35] T. D. Lee and C. N. Yang. "Question of Parity Conservation in Weak Interactions." *Phys. Rev.* **104** (1956) 254–258.

[36] G. Chardin. "CP violation and antigravity (revisited)." *Nuclear Physics A* **558** (0) (1993) 477 – 495.

[37] M. Holzscheiter et al. "Antihydrogen production and precision experiments." *Nuclear Physics B - Proceedings Supplements* **56** (12) (1997) 336 – 348. Proceedings of the Fourth Biennial Conference on Low Energy Antiproton Physics.

[38] H. Nilles. "Supersymmetry, supergravity and particle physics." *Physics Reports* **110** (12) (1984) 1 – 162.

[39] M. Pospelov and A. Ritz. "Electric dipole moments as probes of new physics." *Annals of Physics* **318** (1) (2005) 119 – 169. Special Issue.

[40] S. Khalil. "CP Violation in Supersymmetric Theories." *International Journal of Modern Physics A* **18** (10) (2003) 1697–1732.

[41] S. A. Abel and O. Lebedev. "Neutron-electron EDM correlations in supersymmetry and prospects for EDM searches." *Journal of High Energy Physics* **2006** (01) (2006) 133.

[42] M. Ramsey-Musolf and S. Su. "Low-energy precision tests of supersymmetry." *Physics Reports* **456** (12) (2008) 1 – 88.

[43] D. Dubbers and M. G. Schmidt. "The neutron and its role in cosmology and particle physics." *Rev. Mod. Phys.* **83** (2011) 1111–1171.

[44] S. Barr. "A Review of CP Violation in Atoms." *International Journal of Modern Physics A* **08** (02) (1993) 209–236.

[45] W. C. Griffith et al. "Improved Limit on the Permanent Electric Dipole Moment of 199-Hg." *Phys. Rev. Lett.* **102** (2009) 101601.

[46] The ACME Collaboration et al. "Order of Magnitude Smaller Limit on the Electric Dipole Moment of the Electron." *Science* **343** (6168) (2014) 269–272.

[47] G. W. Bennett et al. "Improved limit on the muon electric dipole moment." *Phys. Rev. D* **80** (2009) 052008.

[48] K. Inami et al. "Search for the electric dipole moment of the τ lepton." *Physics Letters B* **551** (12) (2003) 16 – 26.

[49] H. Abele. "The neutron. Its properties and basic interactions." *Progress in Particle and Nuclear Physics* **60** (1) (2008) 1 – 81.

[50] J. J. Hudson et al. "Improved measurement of the shape of the electron." *Nature* **473** (2011) 493– 496.

[51] W. Bernreuther and M. Suzuki. "The electric dipole moment of the electron." *Rev. Mod. Phys.* **63** (1991) 313–340.

[52] E. D. Commins. "Electric Dipole Moments of Leptons." vol. 40 of *Advances In Atomic, Molecular, and Optical Physics*, pp. 1 – 55. Academic Press (1999).

[53] J. Ginges and V. Flambaum. "Violations of fundamental symmetries in atoms and tests of unification theories of elementary particles." *Physics Reports* **397** (2) (2004) 63 – 154.

[54] B. L. Roberts and New Muon (g – 2) collaboration. "Status of the Fermilab muon (g – 2) experiment." *Chinese Physics C* **34** (6) (2010) 741.

[55] The Storage Ring EDM Collaboration. "A Proposal to Measure the Proton Electric Dipole Moment with 10^{-29} e cm Sensitivity." `http://www.bnl.gov/edm/files/pdf/Proton_EDM_proposal_20111027_final.pdf`.

[56] E. M. Purcell and N. F. Ramsey. "On the Possibility of Electric Dipole Moments for Elementary Particles and Nuclei." *Phys. Rev.* **78** (1950) 807–807.

[57] N. F. Ramsey. "A Molecular Beam Resonance Method with Separated Oscillating Fields." *Phys. Rev.* **78** (1950) 695–699.

[58] I. Altarev et al. "A search for the electric dipole moment of the neutron using ultracold neutrons." *Nuclear Physics A* **341** (2) (1980) 269 – 283.

[59] N. F. Ramsey. "Electric-Dipole Moments of Particles." *Annual Review of Nuclear and Particle Science* **32** (1982) 211–233.

[60] N. F. Ramsey. "Electric-Dipole Moment of the Neutron." *Annual Review of Nuclear and Particle Science* **40** (1990) 1–14.

[61] J. M. Pendlebury. "Fundamental Physics with Ultracold Neutrons." *Annual Review of Nuclear and Particle Science* **43** (1993) 687–727.

[62] R. Golub and S. K. Lamoreaux. "Neutron electric-dipole moment, ultracold neutrons and polarized ^{3}He." *Physics Reports* **237** (1) (1994) 1 – 62.

[63] A. Steyerl et al. "A new source of cold and ultracold neutrons." *Physics Letters A* **116** (7) (1986) 347 – 352.

[64] P. G. Harris and J. M. Pendlebury. "Dipole-field contributions to geometric-phase-induced false electric-dipole-moment signals for particles in traps." *Phys. Rev. A* **73** (2006) 014101.

[65] R. Golub and J. Pendlebury. "Super-thermal sources of ultra-cold neutrons." *Physics Letters A* **53** (2) (1975) 133 – 135.

[66] R. Golub and J. Pendlebury. "The interaction of Ultra-Cold Neutrons (UCN) with liquid helium and a superthermal UCN source." *Physics Letters A* **62** (5) (1977) 337 – 339.

[67] C. Baker et al. "Experimental measurement of ultracold neutron production in superfluid ^{4}He." *Physics Letters A* **308** (1) (2003) 67 – 74.

[68] P. R. Huffman et al. "Magnetic trapping of neutrons." *Nature* **403** (6765) (2000) 62–64.

[69] S. K. Lamoreaux and R. Golub. "Experimental searches for the neutron electric dipole moment." *Journal of Physics G: Nuclear and Particle Physics* **36** (10) (2009) 104002.

[70] D. Budker et al. "A New Search for The Neutron Electric Dipole Moment." `http://p25ext.lanl.gov/edm/pdf.unprotected/EDM_proposal.pdf`. Accessed: 2014-04-20.

[71] T. M. Ito and the nEdm Collaboration. "Plans for a Neutron EDM Experiment at SNS." *Journal of Physics: Conference Series* **69** (1) (2007) 012037.

[72] J. Zenner. *The search for the neutron electric dipole moment.* Ph.D. thesis, Johannes Gutenberg-Universitat, Mainz (2013).

[73] E. Pierre. *Developpement et optimisation dun systeme de polarisation de neutrons ultra froids dans le cadre dune nouvelle mesure du moment dipolaire electrique du neutron.* Ph.D. thesis, Universite de Caen (2012).

[74] G. Ban et al. "UCN detection with ^{6}Li-doped glass scintillators." *Nuclear Instruments and Methods in Physics Research Section A: Accelerators, Spectrometers, Detectors and Associated Equipment* **611** (23) (2009) 280 – 283. Particle Physics with Slow Neutrons.

[75] A. Anghel et al. "The PSI ultra-cold neutron source." *Nuclear Instruments and Methods in Physics Research Section A: Accelerators, Spectrometers, Detectors and Associated Equipment* **611** (23) (2009) 272 – 275. Particle Physics with Slow Neutrons.

[76] I. Altarev et al. "An improved measurement of the electric dipole moment of the neutron." *Nuclear Physics A* **844** (14) (2010) 47c – 52c. Proceedings of the 4th International Symposium on Symmetries in Subatomic Physics.

[77] A. Serebrov et al. "New measurements of neutron electric dipole moment." *ArXiv e-prints* 1310.5588v2.

[78] A. Serebrov et al. "Ultracold-neutron infrastructure for the PNPI/ILL neutron {EDM} experiment." *Nuclear Instruments and Methods in Physics Research Section A: Accelerators, Spectrometers, Detectors and Associated Equipment* **611** (23) (2009) 263 – 266. Particle Physics with Slow Neutrons.

[79] A. Serebrov et al. "Preparation of facilities for fundamental research with ultracold neutrons at PNPI." *Nuclear Instruments and Methods in Physics Research Section A: Accelerators, Spectrometers, Detectors and Associated Equipment* **611** (23) (2009) 276 – 279. Particle Physics with Slow Neutrons.

[80] I. Altarev et al. "A next generation measurement of the electric dipole moment of the neutron at the FRM II." *Il Nuovo Cimento C* **35** (2012) 122–127.

[81] Y. Masuda et al. "Spallation Ultracold-Neutron Production in Superfluid Helium." *Phys. Rev. Lett.* **89** (2002) 284801.

[82] Y. Masuda et al. "Spallation UCN Production for nEDM." *Physics Procedia* **51** (0) (2014) 89 – 92. ESS Science Symposium on Neutron Particle Physics at Long Pulse Spallation Sources, 2013.

[83] J. Martin et al. "Canadian Spallation Ultracold Neutron Source." http://nuclear.uwinnipeg.ca/ucn/triumf/post-acot-5-26-8/ucn-post-acot-may08.pdf. Accessed: 2014-04-20.

[84] V. Fedorov et al. "Measurement of the neutron electric dipole moment via spin rotation in a non-centrosymmetric crystal." *Physics Letters B* **694** (1) (2010) 22 – 25.

[85] S.N.Balashov et al. "A Proposal for a Cryogenic Experiment to Measure the Neutron Electric Dipole Moment (nEDM)." arXiv:0709.2428v1[hep-ex].

[86] C. Baker et al. "The search for the neutron electric dipole moment at the Paul Scherrer Institute." *Physics Procedia* **17** (0) (2011) 159 – 167. 2nd International Workshop on the Physics of fundamental Symmetries and Interactions.

[87] E. Aleksandrov et al. "A new Precision Measurement of the Neutron Electric Dipole Moment (EDM)." http://nrd.pnpi.spb.ru/LabSereb/edm_proposal.pdf.

[88] J. Ellis et al. "Grand unification, the neutron electric dipole moment and galaxy formation." *Nature* **293** (1981) 41– 43.

[89] P. G. Harris et al. "New Experimental Limit on the Electric Dipole Moment of the Neutron." *Phys. Rev. Lett.* **82** (1999) 904–907.

[90] N. Ramsey. *Molecular Beams*, vol. Reprint Edition of *Oxford Classic Texts in the Physical Sciences*. Oxford University Press (1986).

[91] R. Golub, D. Richardson, and S. Lamoreaux. *Ultra Cold Neutrons*. Taylor & Francis (1991).

[92] F. E. Wietfeldt and G. L. Greene. "The neutron lifetime." *Rev. Mod. Phys.* **83** (2011) 1173–1192.

[93] W. Schott et al. "UCN production in superfluid helium." *The European Physical Journal A* **16** (2003) 599.

[94] M. Raso-Barnett. *A new Monte-Carlo based Simulation for the CryoEDM Experiment*. M.Phil. thesis, University of Sussex (2013).

[95] F. Pobell. *Matter and Methods at Low Temperatures*. Springer-Verlag, first edn. (1992).

[96] A. G. Katsika. *Magnetic Aspects of the Cryo-nEDM experiment*. Ph.D. thesis, University of Sussex (2013).

[97] P. Ripka. "Advances in fluxgate sensors." *Sensors and Actuators A: Physical* **106** (13) (2003) 8 – 14. Proceedings of the 4th European Magnetic Sensors and Actuators Conference.

[98] M. Schmelz et al. "Field-stable SQUID magnetometer with sub-fT $\mathrm{Hz}^{-1/2}$ resolution based on sub-micrometer cross-type Josephson tunnel junctions." *Superconductor Science and Technology* **24** (6) (2011) 065009.

[99] M. A. McCann. *Magnetometry for cryoEDM*. D.Phil. thesis, University of Oxford (2012).

[100] A. J. Davidson. *High voltage breakdown in the Ramsey cell of the CryoEDM experiment: an experimental study of some relevant parameters*. Ph.D. thesis, University of Sussex (2013).

[101] C. A. Baker et al. "Development of solid-state silicon devices as ultra cold neutron detectors." *Nuclear Instruments and Methods in Physics Research Section A: Accelerators, Spectrometers, Detectors and Associated Equipment* **487** (3) (2002) 511 – 520.

[102] C. A. Baker and others. "Development of low temperature solid state detectors for ultra-cold neutrons within superfluid ^{4}He." *Nuclear Instruments and Methods in Physics Research Section A: Accelerators, Spectrometers, Detectors and Associated Equipment* **501** (2-3) (2003) 517 – 523.

[103] A. T. Yue et al. "Improved Determination of the Neutron Lifetime." *Phys. Rev. Lett.* **111** (2013) 222501.

[104] J. M. Pendlebury et al. "Geometric-phase-induced false electric dipole moment signals for particles in traps." *Phys. Rev. A* **70** (2004) 032102.

[105] G. F. Knoll. *Radiation Detection and Measurement*. Wiley, second edn. (1989).

[106] G. Archibald et al. "Characterization of Scintillation Light produced in Superfluid Helium - 4." *AIP Conference Proceedings* **850** (1) (2006) 143–144.

[107] ORTEC. "ORTEC ULTRA Ion-Implanted-Silicon Charged-Particle Detector Data Sheet." `http://www.ortec-online.com/download/ULTRA.pdf`.

[108] V. F. Sears. "Neutron scattering lengths and cross sections." *Neutron scattering lengths and cross sections* **3** (3) (1992) 26 – 37.

[109] N. W. Ashcroft and D. N. Mermin. *Solid State Physics*. Thomson Learning, 1 edn. (1976).

[110] G. Ban et al. "A novel fast UCN detector based on the ^{6}Li doped glass scintillators." In "8th International Workshop on Ultra Cold & Cold Neutrons. Physics & Sources," (2011).

[111] A. N. Caruso. "The physics of solid-state neutron detector materials and geometries." *Journal of Physics: Condensed Matter* **22** (44) (2010) 443201.

[112] G. Breit and E. Wigner. "Capture of Slow Neutrons." *Phys. Rev.* **49** (1936) 519–531.

[113] U. of Cambridge. "Cross Sections." `http://www.doitpoms.ac.uk/tlplib/nuclear_materials/cross_section.php`. Accessed: 2014-04-20.

[114] R. T. Kouzes et al. "Neutron detection alternatives to ^{3}He for national security applications." *Nuclear Instruments and Methods in Physics Research Section A: Accelerators, Spectrometers, Detectors and Associated Equipment* **623** (3) (2010) 1035 – 1045.

[115] M. Lasakov et al. "A large area silicon UCN detector with the analysis of UCN polarization." *Nuclear Instruments and Methods in Physics Research Section A: Accelerators, Spectrometers, Detectors and Associated Equipment* **545** (12) (2005) 301 – 308.

[116] J. Uher et al. "Characterization of 3D thermal neutron semiconductor detectors." *Nuclear Instruments and Methods in Physics Research Section A: Accelerators, Spectrometers, Detectors and Associated Equipment* **576** (1) (2007) 32 – 37. Proceedings of the 8th International Workshop on Radiation Imaging Detectors.

[117] S. Bellinger et al. "Characteristics of 3D Micro-Structured Semiconductor High Efficiency Neutron Detectors." *Nuclear Science, IEEE Transactions on* **56** (3) (2009) 742–746.

[118] S. Bellinger et al. "Improved High Efficiency Stacked Microstructured Neutron Detectors Backfilled With Nanoparticle ^{6}LiF, year=2012, month=Feb, volume=59, number=1, pages=167-173, doi=10.1109/TNS.2011.2175749, ISSN=0018-9499,." *Nuclear Science, IEEE Transactions on* .

[119] D. S. McGregor, S. L. Bellinger, and J. K. Shultis. "Present status of microstructured semiconductor neutron detectors." *Journal of Crystal Growth* **379** (0) (2013) 99 – 110. Compound Semiconductors and Scintillators for Radiation Detection Applications: A Special Tribute to the Research of Michael Schieber.

[120] G. Angloher et al. "Commissioning run of the CRESST-II dark matter search." *Astroparticle Physics* **31** (4) (2009) 270 – 276.

[121] V. B. Mikhailik and H. Kraus. "Performance of scintillation materials at cryogenic temperatures." *Physica Status Solidi (B)* **247** (7) (2010) 1583–1599.

[122] H. Kraus and V. Mikhailik. "First test of a cryogenic scintillation module with a $CaWO_4$ scintillator and a low-temperature photomultiplier down to 6 K." *Nuclear Instruments and Methods in Physics Research Section A: Accelerators, Spectrometers, Detectors and Associated Equipment* **621** (13) (2010) 395 – 400.

[123] H. Kraus et al. "Feasibility study of a $ZnWO_4$ scintillator for exploiting materials signature in cryogenic {WIMP} dark matter searches." *Physics Letters B* **610** (12) (2005) 37 – 44.

[124] V. B. Mikhailik et al. "Luminescence of $CaWO_4$, $CaMoO_4$, and $ZnWO_4$ scintillating crystals under different excitations." *Journal of Applied Physics* **97** (8) 083523.

[125] P. Sibczynski et al. "Properties of NaI(Tl) scintillator at liquid nitrogen temperature." In "Nuclear Science Symposium and Medical Imaging Conference (NSS/MIC), 2011 IEEE," pp. 1616–1620 (2011).

[126] J. B. Birks. *The Theory and Practice of Scintillation Counting.* Pergamon Press (1964).

[127] Saint Gobain Crystals. "BC-454 Natural Boron-loaded Premium Plastic Scintillator." `http://www.crystals.saint-gobain.com/uploadedFiles/SG-Crystals/Documents/SGC%20BC454%20Data%20Sheet.pdf`.

[128] Eljen Technology. "EJ-254." `http://www.eljentechnology.com/index.php/products/loaded-scintillators/78-ej-254`.

[129] N. Rhodes et al. "Pixelated neutron scintillation detectors using fibre optic coded arrays." *Nuclear Instruments and Methods in Physics Research Section A: Accelerators, Spectrometers, Detectors and Associated Equipment* **392** (13) (1997) 315 – 318. Position-Sensitive Detectors Conference 1996.

[130] M. G. Rogel. *Developpement de detecteurs de neutrons ultra-froids et d'un systeme d'analyse de polarisation pour la mesure du moment electrique dipolaire du neutron.* Ph.D. thesis, Universite de Caen Basse-Normandie (2009).

[131] M. Bravin et al. "Simultaneous measurement of phonons and scintillation light for active background rejection in the CRESST experiment." *Nuclear Instruments and Methods in Physics Research Section A: Accelerators, Spectrometers, Detectors and Associated Equipment* **444** (12) (2000) 323 – 326.

[132] C. M. Lavelle et al. "Ultracold-neutron production in a pulsed-neutron beam line." *Phys. Rev. C* **82** (2010) 015502.

[133] P. C. Miranda. "Ultra-cold neutron transmission of clear and metal-coated polypropylene windows." *Journal of Physics D: Applied Physics* **21** (9) (1988) 1326.

[134] M. Klein, J. Schmidt, and U. Schmidt. "Cascade-U: A 10-Boron high count rate area detector for UCN." `http://pmle.web.psi.ch/poster1/posterfiles/klein_martin.pdf` (2007). Poster Presentation at Workshop on Precision Measurements at Low Energy at PSI.

[135] F. Probst et al. "Model for cryogenic particle detectors with superconducting phase transition thermometers." *Journal of Low Temperature Physics* **100** (1-2) (1995) 69–104.

[136] R. McGowan. *Data Analysis and Results of the Upgraded CRESST Dark Matter Search*. D.Phil. thesis, University of Oxford (2008).

[137] J. Hellmig et al. "The CDMS II Z-sensitive ionization and phonon germanium detector." *Nuclear Instruments and Methods in Physics Research Section A: Accelerators, Spectrometers, Detectors and Associated Equipment* **444** (12) (2000) 308 – 311.

[138] H. Kraus. "Superconductive bolometers and calorimeters." *Superconductor Science and Technology* **9** (10) (1996) 827.

[139] H. Kraus. "Superconducting Radiation Detectors and Their Future Perspectives." *Japanese Journal of Applied Physics* **37** (12R) (1998) 6273.

[140] H. P. Myers. *Introductory solid state physics*. Taylor & Francis, first edn. (1990).

[141] J. Clarke and A. I. Braginski. *The SQUID Handbook Vol. I Fundamentals and Technology of SQUIDs and SQUID Systems*. Wiley (2004).

[142] A. Brown. *Analysis and modelling for CRESST - II*. D.Phil. thesis, University of Oxford (2011).

[143] S. Cebrian et al. "First results of the ROSEBUD dark matter experiment." *Astroparticle Physics* **15** (1) (2001) 79 – 85.

[144] OSRAM Opto Semiconductors. "SFH 4503 Data Sheet." `http://catalog.osram-os.com/catalogue/catalogue.do?act=showBookmark\&favOid=000000000003d0970001003a`.

[145] E. Armengaud et al. "Final results of the EDELWEISS-II {WIMP} search using a 4-kg array of cryogenic germanium detectors with interleaved electrodes." *Physics Letters B* **702** (5) (2011) 329 – 335.

[146] P. Coulter. *Cryogenic phonon-scintillation detectors with NTD germanium readout*. D.Phil. thesis, University of Oxford (2013).

[147] J. Valentine et al. "Temperature dependence of absolute CsI(Tl) scintillation yield." In "Nuclear Science Symposium and Medical Imaging Conference, 1991., Conference Record of the 1991 IEEE," pp. 176–182 vol.1 (1991).

[148] V. B. Mikhailik et al. "Scintillation studies of $CaWO_4$ in the millikelvin temperature range." *Phys. Rev. B* **75** (2007) 184308.

[149] J. Gironnet et al. "Scintillation studies of $Bi_4Ge_3O_{12}$ (BGO) down to a temperature of 6K." *Nuclear Instruments and Methods in Physics Research Section A: Accelerators, Spectrometers, Detectors and Associated Equipment* **594** (3) (2008) 358 – 361.

[150] C. W. van Eijk. "Neutron PSDs for the next generation of spallation neutron sources." *Nuclear Instruments and Methods in Physics Research Section A: Accelerators, Spectrometers, Detectors and Associated Equipment* **477** (13) (2002) 383 – 390. 5th Int. Conf. on Position-Sensitive Detectors.

[151] T. Nakamura et al. "A half-millimetre spatial resolution fibre-coded linear position-sensitive scintillator detector with wavelength-shifting fibre read-out for neutron detection." *Nuclear Instruments and Methods in Physics Research Section A: Accelerators, Spectrometers, Detectors and Associated Equipment* **606** (3) (2009) 675 – 680.

[152] C. L. Wang et al. "Wavelength-shifting-fiber scintillation detectors for thermal neutron imaging at SNS." In "Nuclear Science Symposium and Medical Imaging Conference (NSS/MIC), 2011 IEEE," pp. 4877–4882 (2011).

[153] Department of Physics, University of Oxford. "Mars Project." `http://www2.physics.ox.ac.uk/research/mars-project/`.

[154] A. Vacheret et al. "Apparatus and Method for Radiation Detection." `http://patentscope.wipo.int/search/en/WO2013027069` (2013).

[155] C. van Eijk, A. Bessiere, and P. Dorenbos. "Inorganic thermal-neutron scintillators." *Nuclear Instruments and Methods in Physics Research Section A: Accelerators, Spectrometers, Detectors and Associated Equipment* **529** (1- 3) (2004) 260 – 267.

[156] T. Tojo and T. Nakajima. "Preparation of thermal neutron scintillators based on a mixture of ZnS(Ag), ^{6}LiF and polyethylene." *Nuclear Instruments and Methods* **53** (0) (1967) 163 – 166.

[157] W. Y. S. Shionoya. *Phosphor Handbook*. CRC Press, Boca Raton (1999).

[158] S. Umehara et al. "Neutrino-less double- β decay of ^{48}Ca studied by CaF_2(Eu) scintillators." *Phys. Rev. C* **78** (2008) 058501.

[159] A. Alessandrello et al. "A scintillating bolometer for experiments on double beta decay." *Physics Letters B* **420** (12) (1998) 109 – 113.

[160] C. Bobin et al. "Alpha/gamma discrimination with a CaF_2(Eu) target bolometer optically coupled to a composite infrared bolometer." *Nuclear Instruments and Methods in Physics Research Section A: Accelerators, Spectrometers, Detectors and Associated Equipment* **386** (23) (1997) 453 – 457.

[161] V. Mikhailik et al. "Scintillation properties of pure CaF_2." *Nuclear Instruments and Methods in Physics Research Section A: Accelerators, Spectrometers, Detectors and Associated Equipment* **566** (2) (2006) 522 – 525.

[162] Hilger Crystals. "Materials Index." `http://www.hilger-crystals.co.uk/materials.asp`.

[163] C. Amsler et al. "Temperature dependence of pure CsI: scintillation light yield and decay time." *Nuclear Instruments and Methods in Physics Research Section A: Accelerators, Spectrometers, Detectors and Associated Equipment* **480** (23) (2002) 494 – 500.

[164] A. J. Wojtowicz et al. "Scintillation properties of selected oxide monocrystals activated with Ce and Pr." *Optical Materials* **28** (1 - 2) (2006) 85 – 93.

[165] Crytur. "Scintillation Materials." `http://www.crytur.cz/pages/67/crytur-materials`.

[166] M. Weber. "Scintillation: mechanisms and new crystals." *Nuclear Instruments and Methods in Physics Research Section A: Accelerators, Spectrometers, Detectors and Associated Equipment* **527** (12) (2004) 9 – 14. Proceedings of the 2nd International Conference on Imaging Technologies in Biomedical Sciences.

[167] C. Pepin et al. "Properties of LYSO and recent LSO scintillators for phoswich PET detectors." *Nuclear Science, IEEE Transactions on* **51** (3) (2004) 789–795.

[168] H. Feng et al. "Temperature dependence of luminescence characteristics of $Lu_{2(1-x)}Y_{2x}SiO_5$: Ce^{3+} scintillator grown by the Czochralski method." *Journal of Applied Physics* **108** (3) 033519.

[169] W. Drozdowski et al. "VUV spectroscopy and low temperature thermoluminescence of LSO:Ce and YSO:Ce." *Journal of Alloys and Compounds* **380** (1-2) (2004) 146 – 150. Proceedings of the 4th International Spring Workshop on Spectroscopy, Structure and Synthesis of Rare Earth Systems.

[170] H. Rothfuss et al. "Scintillation kinetics of YSO:Ce." In "Nuclear Science Symposium Conference Record, 2007. NSS '07. IEEE," vol. 2, pp. 1401 –1403 (2007).

[171] M. Moszynski et al. "Properties of the YAG:Ce scintillator." *Nuclear Instruments and Methods in Physics Research Section A: Accelerators, Spectrometers, Detectors and Associated Equipment* **345** (3) (1994) 461 – 467.

[172] E. Zych, C. Brecher, and J. Glodo. "Kinetics of cerium emission in a YAG:Ce single crystal: the role of traps." *Journal of Physics: Condensed Matter* **12** (8) (2000) 1947.

[173] A. Dalton. "Light conversion efficiency of small lithium scintillators for electrons, protons, deuterons and alpha particles." *Nuclear Instruments and Methods in Physics Research Section A: Accelerators, Spectrometers, Detectors and Associated Equipment* **254** (2) (1987) 361 – 366.

[174] N. Rhodes, E. Schooneveld, and R. Eccleston. "Current status and future directions of position sensitive neutron detectors at ISIS." *Nuclear Instruments and Methods in Physics Research Section A: Accelerators, Spectrometers, Detectors and Associated Equipment* **529** (13) (2004) 243 – 248.

[175] F. Markley et al. "Development of radiation hard scintillators." *Radiation Physics and Chemistry* **41** (12) (1993) 135 – 152.

[176] N. Zaitseva et al. "Plastic scintillators with efficient neutron/gamma pulse shape discrimination." *Nuclear Instruments and Methods in Physics Research Section A: Accelerators, Spectrometers, Detectors and Associated Equipment* **668** (0) (2012) 88 – 93.

[177] H. Feng et al. "Temperature dependence of luminescence characteristics of $Lu_{2(1-x)}Y_{2x}SiO_5$: Ce^{3+} scintillator grown by the Czochralski method." *Journal of Applied Physics* **108** (3) 033519.

[178] Y. Zorenko et al. "Single-crystalline films of Ce-doped YAG and LuAG phosphors: advantages over bulk crystals analogues." *Journal of Luminescence* **114** (2) (2005) 85 – 94.

[179] A. Spowart. "Neutron scintillating glasses: Part II: The effects of temperature on pulse height and conductivity." *Nuclear Instruments and Methods* **140** (1) (1977) 19 – 28.

[180] C. Coceva. "Pulse-shape discrimination with a glass scintillator." *Nuclear Instruments and Methods* **21** (0) (1963) 93 – 96.

[181] A. Alessandrello et al. "Development of a thermal scintillating detector for double beta decay of ^{48}Ca." *Nuclear Physics B - Proceedings Supplements* **28** (1) (1992) 233 – 235.

[182] P. Belli et al. "Search for a decay of natural Europium." *Nuclear Physics A* **789** (1-4) (2007) 15 – 29.

[183] C. Bacci et al. "Dark matter search with calcium fluoride crystals." *Astroparticle Physics* **2** (2) (1994) 117 – 125.

[184] S. Oguri, Y. Inoue, and M. Minowa. "Pulse-shape discrimination of CaF_2(Eu)." *Nuclear Instruments and Methods in Physics Research Section A: Accelerators, Spectrometers, Detectors and Associated Equipment* **622** (3) (2010) 588 – 591.

[185] Oxford Instruments. "Optistat CF-V liquid helium (LHe) continuous flow optical spectroscopy cryostat product guide." `http://www.oxford-instruments.com/products/low-temperature/opticaland-spectroscopy/optistatcf-v/Documents/OptistatCF-V-liquid-helium-continuous-flow-optical-spectroscopy-cryostat-product-guide.pdf`.

[186] Electron Tube Enterprises. "Electron Tubes 9125 Series PMT Data Sheet." `http://my.et-enterprises.com/pdf/9125B.pdf`.

[187] H. Kraus, V. Mikhailik, and D. Wahl. "Multiple photon counting coincidence (MPCC) technique for scintillator characterisation and its application to studies of $CaWO_4$ and $ZnWO_4$ scintillators." *Nuclear Instruments and Methods in Physics Research Section A: Accelerators, Spectrometers, Detectors and Associated Equipment* **553** (3) (2005) 522 – 534.

[188] S. Moser et al. "Principles and practice of plastic scintillator design." *Radiation Physics and Chemistry* **41** (12) (1993) 31 – 36.

[189] L. Pidol et al. "High efficiency of lutetium silicate scintillators, Ce-doped LPS, and LYSO crystals." *Nuclear Science, IEEE Transactions on* **51** (3) (2004) 1084–1087.

[190] A. R. Spowart. "Energy transfer in cerium-activated silicate glasses." *Journal of Physics C: Solid State Physics* **12** (16) (1979) 3369.

[191] J. Menefee, C. F. Swinehart, and E. W. O'Dell. "Calcium Fluoride as an X-Ray and Charged Particle Detector." *Nuclear Science, IEEE Transactions on* **13** (1) (1966) 720 –724.

[192] V. Mikhailik et al. "Investigation of luminescence and scintillation properties of a ZnS–Ag/^{6}LiF scintillator in the 7–295 K temperature range." *Journal of Luminescence* **134** (0) (2013) 63 – 66.

[193] G. Zimmerer. "SUPERLUMI: A unique setup for luminescence spectroscopy with synchrotron radiation." *Radiation Measurements* **42** (45) (2007) 859 – 864. Proceedings of the 6th European Conference on Luminescent Detectors and Transformers of Ionizing Radiation.

[194] R. Allison, J. Burns, and A. J. Tuzzolino. "Absolute Fluorescent Quantum Efficiency of Sodium Salicylate." *J. Opt. Soc. Am.* **54** (6) (1964) 747–750.

[195] Y. Uehara. "Electronic structure of luminescence center of ZnS:Ag phosphors." *The Journal of Chemical Physics* **62** (8) (1975) 2982–2994.

[196] V. B. Mikhailik et al. "Luminescence of $CaWO_4$, $CaMoO_4$, and $ZnWO_4$ scintillating crystals under different excitations." *Journal of Applied Physics* **97** (8) 083523.

[197] A. E. R. Malins et al. "Luminescence excitation characteristics of Ca, Na and K-aluminosilicates (feldspars) in the stimulation range 5–40eV: determination of the band-gap energies." *Journal of Physics D: Applied Physics* **37** (10) (2004) 1439.

[198] E. L. Benitez et al. "A surface recombination model applied to large features in inorganic phosphor efficiency measurements in the soft x-ray region." *Journal of Applied Physics* **70** (6) (1991) 3256–3260.

[199] J. L. Merz and P. S. Pershan. "Charge Conversion of Irradiated Rare-Earth Ions in Calcium Fluoride. I." *Phys. Rev.* **162** (1967) 217–235.

[200] U. Caldino, A. F. Munoz, and J. O. Rubio. "Luminescence and energy transfer in CaF_2 slightly doped with europium and manganese." *Journal of Physics: Condensed Matter* **2** (27) (1990) 6071.

[201] J. Berkowitz and J. Olsen. "Investigation of luminescent materials under ultraviolet excitation energies from 5 to 25 eV." *Journal of Luminescence* **50** (2) (1991) 111 – 121.

[202] L. Ley et al. "Total valence-band densities of states of III-V and II-VI compounds from x-ray photoemission spectroscopy." *Phys. Rev. B* **9** (1974) 600–621.

[203] P. A. Amaudruz et al. "The T2K fine-grained detectors." *Nuclear Instruments and Methods in Physics Research Section A: Accelerators, Spectrometers, Detectors and Associated Equipment* **696** (0) (2012) 1 – 31.

[204] G. Collazuol et al. "Studies of silicon photomultipliers at cryogenic temperatures." *Nuclear Instruments and Methods in Physics Research Section A: Accelerators, Spectrometers, Detectors and Associated Equipment* **628** (1) (2011) 389 – 392. VCI 2010 Proceedings of the 12th International Vienna Conference on Instrumentation.

[205] C. Ankenbrandt and E. Lent. "Increasing the light collection efficiency of scintillation counters." *Review of Scientific Instruments* **34** (6) (1963) 647–651.

[206] G. Keil. "Design principles of fluorescence radiation converters." *Nuclear Instruments and Methods* **89** (0) (1970) 111 – 123.

[207] The LHCb Collaboration. "LHCb Calorimeters, Technical Design Report." `http://lhcb-calo.web.cern.ch/lhcb-calo/html/TDR/calotdr/node14.html`.

[208] S. Aoki et al. "The T2K Side Muon Range Detector (SMRD)." *Nuclear Instruments and Methods in Physics Research Section A: Accelerators, Spectrometers, Detectors and Associated Equipment* **698** (0) (2013) 135 – 146.

[209] M. Berger et al. "ESTAR, PSTAR, and ASTAR: Computer Programs for Calculating Stopping-Power and Range Tables for Electrons, Protons, and Helium Ions (version 1.2.3), National Institute of Standards and Technology, Gaithersburg, MD." `http://physics.nist.gov/Star`.

[210] M. Berger et al. "XCOM: Photon Cross Section Database (version 1.5), National Institute of Standards and Technology, Gaithersburg, MD." `http://physics.nist.gov/xcom`.

[211] J. Penfold, R. C. Ward, and W. G. Williams. "A time-of-flight neutron reflectometer for surface and interfacial studies." *Journal of Physics E: Scientific Instruments* **20** (11) (1987) 1411.

[212] J. Sykora. "Scintillators: Basics and Practical Aspects." In "International Neutron Scattering Instrumentation School (INSIS), INFN - Laboratori Nazionali di Frascati, Rome Italy," (2012).

[213] H. Suzuki et al. "UV and gamma-ray excited luminescence of cerium-doped rare-earth oxyorthosilicates." *Nuclear Instruments and Methods in Physics Research Section A: Accelerators, Spectrometers, Detectors and Associated Equipment* **320** (12) (1992) 263 – 272.

[214] Y. Zorenko et al. "Single crystalline film scintillators based on Ce- and Pr-doped aluminium garnets." *Radiation Measurements* **42** (45) (2007) 521 – 527. Proceedings of

the 6th European Conference on Luminescent Detectors and Transformers of Ionizing Radiation (LUMDETR 2006).

[215] Y. Zorenko et al. "Luminescence and scintillation characteristics of YAG:Ce single crystalline films and single crystals." *Radiation Measurements* **45** (36) (2010) 389 – 391. Proceedings of the 7th European Conference on Luminescent Detectors and Transformers of Ionizing Radiation (LUMDETR 2009).

[216] Y. Zorenko et al. "Intrinsic luminescence of Lu_2SiO_5 (LSO) and Y_2SiO_5 (YSO) orthosilicates." *Journal of Luminescence* **137** (0) (2013) 204 – 207.

[217] M. Kirm et al. "Investigation of luminescence properties of pure and Ce^{3+} doped $Y_3Al_5O_{12}$ crystals using VUV radiation." In "ECS Proceedings Physics and Chemistry of Luminescent Materials," vol. 40, pp. 113–122 (1999).

[218] J.Rubio. "Doubly-valent rare-earth ions in halide crystals." *Journal of Physics and Chemistry of Solids* **52** (1) (1991) 101 – 174.

[219] T. Tsuboi and P. Silfsten. "The lifetime of Eu^{2+} fluorescence in $CaF_2 : Eu^{2+}$ crystals." *Journal of Physics: Condensed Matter* **3** (46) (1991) 9163.